Molecular self-assembly of organic molecules on coinage metal surfaces

Baker, Brian

DOI:
10.33612/diss.169358947

Molecular Self-Assembly of Organic Molecules on Coinage Metal Surfaces

Brian David Baker Cortés

university of groningen / faculty of science and engineering / zernike institute for advanced materials

Molecular Self-Assembly of Organic Molecules on Coinage Metal Surfaces

Brian David Baker Cortés

PhD Thesis

University of Groningen

The work presented in this thesis was performed in the research group Surfaces and Thin Films of the Zernike Institute for Advanced Materials at the University of Groningen and financially supported by the University's PhD Scholarship Programme.

Cover design by Brian David Baker Cortés. Front: Artistic view of the Dutch landscape at night. Back: Artistic view of the Great Pyramid of Cholula in San Andrés Cholula, Puebla, Mexico (top) and Waikiki Beach in Washington State, USA (bottom).

Zernike Institute for Advanced Materials PhD-thesis series 2021-10

ISSN: 1570-1530

Printed by: ProefschriftMaken

university of groningen

Molecular Self-Assembly of Organic Molecules on Coinage Metal Surfaces

PhD thesis

to obtain the degree of PhD at the
University of Groningen
on the authority of the
Rector Magnificus Prof. C. Wijmenga
and in accordance with
the decision by the college of Deans.

This thesis will be defended in public on

Friday 4 June 2021 at 11:00 hours

by

Brian David Baker Cortés

born on 20 October 1990
in Puebla, Mexico

Supervisors
Prof. M.A. Stöhr
Prof. P. Rudolf

Assessment Committee
Prof. S. Maier
Prof. H.J.W. Zandvliet
Prof. G. Palasantzas

To my parents, wife
and brother

Table of Contents


chapter 1

1 Introduction

1.1 Motivation

"And God saw everything that he had made, and, behold, it was very good. And the evening and the morning were the sixth day".[1] In the beginning of time, the Big Bang allowed matter to expand across the universe and consequently, triggered by nucleosynthetic phenomena, the lightest and heaviest elements were able to form. As time progressed over a period of billions of years, evolutionary biology paved its history, leading to the appearance of the earliest civilizations of humankind. From the early stages of ancient civilization there has been a profound link between human activity and the usage of matter expressed in various forms and pertaining different purposes. The chronology of human history presents a series of artifacts that span from cave drawings made with natural pigments to the creation of tools from precious metals such as gold and silver.

The development of civilization has been characterized by mankind's fascination and curiosity towards the unknown. For instance, the Maya studied astronomical bodies and the Greek philosophers coined the term atom for the first time. Later, the course of history led to the Scientific Revolution and the Age of Enlightenment, an era of scientific discovery and sociological progress, where Galileo Galilei established the scientific method as it is known today,[2] Hans and Zacharias Janssen created the first microscope[3] and Isaac Newton postulated the law of universal gravitation.[4] These pioneering events – along with the first and second industrial revolutions – inspired humankind to develop even further, in search of new technologies to improve its quality of life.

The advent of new technologies in the second half of the twentieth century transformed the scope of all fields of applied sciences. The creation of the first transistor in 1947 by John Bardeen, Walter Brattain and William Schockley,[5] and the invention of the first integrated circuit at the end of the 1950s by Jack Kilby and Robert Noyce[5] became landmarks of the birth of a new intriguing field nowadays known as nanotechnology. The central concept of nanotechnology was envisioned by Richard Feynman in 1959 in his lecture "There's Plenty of Room at the Bottom", where he predicted the miniaturization of the already existing technological devices and the storing of incredible amounts of information in a small space.[6] However, the term nanotechnology was first mentioned by Norio Taniguchi until 1974.[7]

Nanotechnology is an interdisciplinary and multidisciplinary field that utilizes a series of tools to study matter at the nanoscale. This field makes use of two approaches for the fabrication of nanostructures and so-called nanodevices: *top-down* and *bottom-up* approaches. The *top-down* approach makes use of bulk materials to scale them down to nanometer length objects through the usage of techniques such as nanolithography. On the other hand, the *bottom-up* approach concerns the formation of nanoscale objects by assembling atoms and/or molecules together.[8] Both of these approaches are supported by the invention of cutting-edge technological devices. For instance, the invention of the scanning tunneling microscope (STM) in 1981 by Binnig and Rohrer, has granted real-space imaging at the nanoscale.[9–11] In analogy to the cave paintings performed thousands of years ago by our ancestors, nowadays, following a *bottom-up* approach, the scientific community can design archetypal patterns by positioning single atoms and molecules on surfaces by means of STM.[10,11]

In the last three decades, the usage of *bottom-up* techniques has gained substantial interest within the scientific community, among others due to the ability to form nanoscale devices by following concepts of supramolecular chemistry.[12,13] Supramolecular chemistry is a field of study that designs molecular systems that are stabilized by non-covalent intermolecular interactions between two or more chemical entities[13,14] and provides promising applications in catalysis, gas storage, molecular electronics and spintronics.[10,11,15–20] Its relevance awarded the Nobel Prize in Chemistry in 1987 to Donald J. Cram, Jean-Marie Lehn and Charles J. Pedersen. A fundamental concept within this field is the term self-assembly, which is defined, according to Whitesides et al. as "the spontaneous association of molecules under equilibrium conditions into stable, structurally well-defined aggregates joined by non-covalent bonds".[12] In particular, molecular self-assembly is a process that is observed at the nanoscale and can be studied on different surfaces by a variety of surface sensitive techniques.[21,22,23] By linking organic molecules to metal-atoms on a surface, so-called metal-organic coordination networks (MOCNs) can be fabricated. These 2D nanoscale systems offer promising applications in gas storage and catalysis. In addition, they offer a route towards the understanding of the underlying mechanisms that drive molecular self-assembly on surfaces.[15,23]

In this thesis, the controlled synthesis and characterization of MOCNs is presented, where special detail is given to the 2D structure, i.e., topography, of the self-assembled MOCNs. The molecule-molecule and molecule-substrate interactions are addressed. Most of the work presented is related to MOCNs fabricated from porphyrin molecules, since they have shown to be stable and flexible building blocks used for the fabrication of 2D networks on

metal surfaces.[24–26] In summary, this thesis outlines the usage of self-assembly in the formation of well-ordered MOCNs on noble metal surfaces.

1.2 Thesis outline

Herein, an introduction to surface sensitive techniques employed for the characterization of nanoscale systems and molecular self-assembly on surfaces is given in Chapters 2 and 3, respectively. The usage of porphyrins and the influence of molecular coverage in the fabrication of MOCNs is presented in Chapter 4. In Chapter 5, the substitution of the already existing metal-atom in the porphyrin core by deposition of a different metal-atom (better known as atom-exchange reaction) is given. Then, a study of the modification of the electronic structure of a 2D porphyrin-based network by transforming it to a MOCN via addition of metal-atoms is addressed in Chapter 6. Finally, in Chapter 7, the formation of a MOCN triggered by the self-assembly between a triarylamine derivative and Cu-native atoms is shown. A more detailed description of each chapter can be found in the following.

Chapter 2 provides an overview of the experimental techniques used to carry out the measurements presented in this thesis. The experimental set-up and theoretical description of STM, scanning tunneling spectroscopy (STS), X-ray photoelectron spectroscopy (XPS) and low energy electron diffraction (LEED) is explained and supported with schematics. The chapter concludes with the importance of using ultra-high vacuum (UHV) in surface science.

Chapter 3 gives insight on the fundamentals of molecular self-assembly, followed by a summary of the self-assembly of porphyrins on metal

surfaces and their usage as molecular building blocks in the fabrication of MOCNs. Finally, the chapter concludes with an adaptation from our previous publication on the role of cyano endgroups in the self-assembly of organic molecules on metal surfaces.

Chapter 4 presents a study of the influence of molecular coverage on the self-assembly process of a Co-substituted tetracyanophenyl porphyrin (Co-TCNPP) before and after the deposition of Co-atoms on Au(111) by means of STM and LEED. Upon deposition on Au(111), Co-TCNPP formed a close-packed H-bonded network that was independent of molecular coverage. However, upon deposition of Co-atoms, a coverage-dependent structural transformation took place. At submonolayer coverage, the coexistence of two Co-coordinated MOCNs stabilized by fourfold and threefold Co-coordination motifs was revealed by the STM measurements. Upon increasing the molecular coverage to a monolayer, the fourfold MOCN was observed as one exclusive phase. This study demonstrates that a subtle interplay between the chemical nature of the building blocks and molecular coverage can steer the formation of structurally different MOCNs.

Chapter 5 reports on the influence of Fe-deposition on the self-assembly of a Co-substituted tetracyanophenyl porphyrin (Co-TCNPP) and Zn-substituted tetrapyridyl porphyrin (Zn-TPyP) on Au(111) by means of STM under UHV conditions. The deposition of Fe-atoms onto a submonolayer of either porphyrin derivative prompted the formation of two structurally different Fe-coordinated MOCNs stabilized by three and fourfold in-plane coordination nodes, respectively. In addition, the presence of a molecular species with a brighter STM contrast compared with the molecular appearance of bare Co-TCNPP and Zn-TPyP, suggested that a new molecular

species was formed due the replacement of the preexisting metal-atom (in the porphyrin core) by the co-deposited Fe-atoms. However, the molecular appearance of the bright Co-TCNPP molecules differed from that of the bright Zn-TPyP molecules, i.e., an off-centered brightness in some Co-TCNPP molecules suggested that the Fe-atoms did not replace the Co-atom but instead bonded on top of the porphyrin core. On the other hand, the bright Zn-TPyP molecules resembled the molecular appearance of Fe-TPyP – meaning that the Fe-atoms atoms replaced the Zn-atoms via an atom exchange reaction. This study presents the first detailed STM study of an atom exchange reaction under UHV conditions for a long-range ordered porphyrin-based MOCN on a metal surface.

Chapter 6 shows a complementary study on the self-assembly process of a nickel-porphyrin (Ni-DPPyP) before and after the addition of Co-atoms under UHV on Au(111) by means of STM, XPS and LEED. Ni-DPPyP is functionalized with two pyridyl endgroups – acting as coordinating sites – and two pentyl chains at trans *meso* positions. Deposition of Ni-DPPyP onto Au(111) gave rise to a close-packed network as revealed by STM and LEED. Subsequent deposition of cobalt atoms onto the close-packed network led to the formation of a Co-coordinated hexagonal porous network. As confirmed by XPS measurements, the porous network is stabilized by metal-ligand interactions between one cobalt atom and three pyridyl ligands, each pyridyl ligand coming from a different Ni-DPPyP molecule. In addition, the influence of the Co-coordination on the atoms that constitute the porphyrin backbone could be revealed with XPS, thereby providing detailed measurement on how the electronic properties of the porphyrin are affected.

Chapter 7 describes the influence of post-deposition annealing on the self-assembly process of a pyrimidinyl-functionalized triarylamine derivative under UHV on Cu(111) by means of STM and XPS. The deposition of the triarylamine derivative on Cu(111) at room-temperature led to the formation of a close-packed 2D network stabilized by H-bonds and twofold Cu-coordination motifs via the peripheral N-atoms bonded to H-atoms from neighboring molecules and Cu-native atoms, respectively. However, upon annealing the close-packed 2D network to 150°C, the molecules rearranged into a MOCN exhibiting a hexagonal porous structure that was stabilized by twofold metal-coordination motifs between the peripheral N-atoms and Cu-native atoms. The XPS measurements confirmed the presence of metal-coordination in both networks and that upon annealing – the increased concentration of Cu-native atoms provided by the Cu(111) surface – the formation of a MOCN exclusively stabilized by Cu-coordination motifs could be achieved.

1.3 References

1. Genesis 1:31, Holy Bible: King James Version.
2. Gower, B. Scientific Method: A Historical and Philosophical Introduction. Routledge, **2012**.
3. Croft, W. J. Under the Microscope: A Brief History of Microscopy. World Scientific, **2006**.
4. Stanford Encyclopedia of Philosophy: Newton's *Philosophiae Naturalis Principia Mathematica*. https://seop.illc.uva.nl/entries/newton-principia/ (accessed April 4, 2020).
5. Lojek., B. History of Semiconductor Engineering. Springer Science & Business Media, **2007**.
6. Feynman. R. P. There's Plenty of Room at the Bottom. *Eng. Sci.* **1960**, *23*, 22–36.
7. N. Taniguchi, "On the Basic Concept of 'Nano Technology," In *Proc. Intl. Conf. Prod. Eng. Tokyo, Part II*, Tokyo: Japan, Society of Precision Engineering, 1974.
8. Gates, B. D.; Qiaobing, X.; Stewart, M.; Ryan, D.; Wilson, C. G.; Whitesides. G. M. New Approaches to Nanofabrication: Molding, Printing, and Other Techniques. Chem. Rev. **2005**, *105*, 1171–1196.
9. Binnig, G.; Rohrer, H.; Gerber, C. et al. Surface Studies by Scanning Tunneling Microscopy. Phys. Rev. Lett. **1982**, *49*, 57–61.
10. Barth, J. V. Molecular Architectonic on Metal Surfaces. *Annu. Rev. Phys. Chem.* **2007**, *58*, 375–407.
11. Dong, L.; Gao, Z. A.; Lin, N. Self-Assembly of Metal-Organic Coordination Structures on Surfaces. *Prog. Surf. Sci*. **2016**, *91*, 101–135.
12. Whitesides, G. M.; Mathias, J. P.; Seto, C. T. Molecular Self-Assembly and Nanochemistry: A Chemical Strategy for the Synthesis of Nanostructures. *Science* **1991**, *254*, 1312–1319.
13. Lehn. J.-M. Supramolecular Chemistry. *Proc. Indian Acad. Sci. (Chem. Sci.)* **1994**, *106*, 915–922.
14. Lehn. J.-M. Supramolecular Chemistry: Receptors, Catalysts and Carriers. *Science.* **1985**, *227*, 849–856.
15. Gutzler, R.; Stepanow, S.; Grumelli, D.; Lingenfelder, M.; Kern, K. Mimicking Enzymatic Active Sites on Surfaces for Energy Conversion Chemistry. *Acc. Chem. Res*. **2015**, *48*, 2132–2139.
16. Stepanow, S.; Lin, N.; Barth, J. V. Modular Assembly of Low-Dimensional coordination architectures on metal surfaces. *J. Phys.: Condens. Matter* **2008**, *20*, 184002.
17. Kuang, G.; Zhang, Q.; Lin. T.; Shi, X.; Xu, H.; Lin, N. Mechanically-Controlled Reversible Spin Crossover of Single Fe-Porphyrin Molecules. *ACS Nano* **2017**, *11*, 6295–6300.

18. Moreno Pineda, E.; Komeda, T.; Katoh, K.; Yamashita, M.; Ruben, M. Surface Confinement of $TbPc_2$-SMMs: Structural, Electronic and Magnetic Properties. *Dalton Trans*. **2016**, *45*, 18417–18433.
19. Ishikawa, N.; Sugita, M.; Ishikawa, T.; Koshihara, S.-Y., Kaizu, Y. Lanthanide Double-Decker Complexes Functioning as Magnets at the Single-Molecular Level. *J. Am. Chem. Soc*. **2003**, *125*, 8694–8695.
20. Sosa-Vargas, L.; Kim, E.; Attias, A.-J. Beyond ‘‘Decorative’’ 2D Supramolecular Self-Assembly: Strategies Towards Functional Surfaces for Nanotechnology. *Mater. Horiz*. **2017**, *4*, 570.
21. Vickerman, J. C.; Gilmore. I. S. Surface Analysis – The Principal Techniques. *John Wiley and Sons* 2009.
22. Hofmann, P. *Surface Physics: An Introduction*. (ebook) **2013**. http://philiphofmann.net/Philip_Hofmann/SurfacePhysics.html.
23. Barth, J. V.; Constantini, G.; Kern, K. Engineering Atomic and Molecular Nanostructures at Surfaces. *Nature* **2005**, *437*, 671–679.
24. Gottfried, J. M. Surface Chemistry of Porphyrins and Phthalocyanines. *Surf. Sci. Rep*. **2015**, *70*, 259–379.
25. Auwärter, W.; Écija, D.; Klappenberger, F.; Barth, J. V. Porphyrins at Interfaces. *Nat. Chem*. **2015**, *7*, 105–120.
26. Baker Cortés, B. D.; Stöhr, M. Role of Cyano Groups in the Self-Assembly of Organic Molecules on Metal Surfaces. In *Encyclopedia of Interfacial Chemistry*; Wandelt, K., Ed.; Elsevier, **2018**; *Vol. 4*, pp 153–165.


chapter 2

2 Experimental Techniques

The following chapter provides an overview of the experimental techniques used to carry out the measurements presented in this thesis. The experimental set-up and theoretical description of scanning tunneling microscopy (STM), scanning tunneling spectroscopy (STS), X-ray photoelectron spectroscopy (XPS) and low energy electron diffraction (LEED) is explained and supported with schematics. The chapter concludes with the importance of using ultra-high vacuum (UHV) in surface science.

2.1 Introduction: Scanning Probe Microscopy (SPM)

Before the invention of the STM, the microscopes available allowed the observation of features in matter that were limited by the size of the wavelength of the source employed for imaging.[1] For instance, the resolution limit given by the photons (from visible light) used in optical microscopy hampered the observation of (topographical) features of matter with atomic resolution. However, this resolution limit was overcome by the usage of electrons in electron microscopes, which allowed real space imaging at the nanoscale.[2] In addition, the invention of the STM aided to this as well.

The first STM was developed in 1981 by Gerd Binnig, Heinrich Rohrer and co-workers at the IBM Research Laboratory in Zurich, Switzerland.[3] In 1986, Binnig and Rohrer[4] were awarded half of the Nobel Prize in Physics for their discovery, while the other half was given to Ernst Ruska for the development of the first electron microscope.[5]

The discovery of the STM was performed after the IBM research team of Binnig and Rohrer had performed some experiments concerning the measurement of the tunneling current[6,7] between a metallic tip and a

conducting sample at a distance of about 1 nm. This gave rise to the idea of taking advantage of such an effect to scan conducting surfaces and obtain useful topographical information in real space of different systems.

Later on, both developers worked on the improvement of the performance of the STM set-up to be able to perform measurements with atomic scale resolution, which lead to the development of a stable vibration isolation system as well as a controlled displacement of the scanning tip.[3] The invention of the STM was the first step in the creation of a new family of microscopes known as scanning probe microscopes (SPM).

The SPM family was extended in 1986 with the creation of the atomic force microscope (AFM).[8] Binnig et al. built the first AFM by creating an instrument capable of measuring the force given by the interaction between a STM tip and a sample. The birth of the SPM family defined the starting point for the study of matter at the atomic scale.

2.2 Scanning Tunneling Microscopy (STM)

2.2.1 STM experimental set-up and description

The schematic of an STM is shown in Figure 2.1 and will be used to describe its functional principle. A metallic tip (depicted in gray) is brought in proximity (few Å) to a sample (purple spheres in Figure 2.1) and when a bias voltage (V_{bias}) is applied between them, a tunneling current I_t (highlighted by the red dotted arrow) will flow. A piezoelectric tube moves the tip across the sample (depicted by the blue line) in *x*-*y* direction, while I_t is constantly monitored. As the tip is scanned across the surface, I_t might deviate from the set reference value due to irregularities found on the surface, such as a step edge. However, the control electronics adjust the tip-sample distance (*z*-

direction) so that I_t can remain constant during data acquisition, i.e., a feedback loop adjusts the tip in z-direction until the measured I_t matches the reference value. After collecting several line scans (x-y direction), the STM image is constructed, which reflects the z-position (movement) of the tip across the scanned surface. The above-mentioned process takes place when the STM is operated in the so-called constant current mode and the line scan depicts the line profile (Figure 2.1e) obtained in this mode across the x-direction. On the other hand, when performing a constant height mode scan, the height (z-position) of the tip is fixed by keeping constant the bias voltage applied to the piezoelectric tube (in z-direction) and the fluctuation of I_t is recorded as the tip scans across x-y direction, i.e., the variation of the distance to the surface leads to changes of I_t.

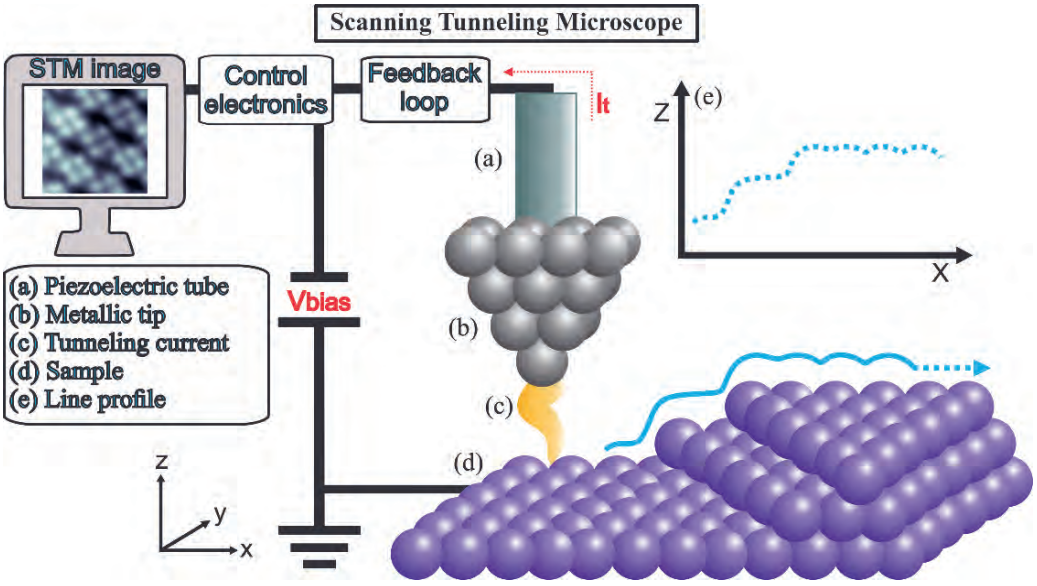

Figure 2.1. Schematic of the experimental set-up of the STM with labels of its main components.[9]

2.2.2 STM theoretical description
Quantum tunneling effect

The STM principle is based on the quantum mechanical tunneling effect that takes place between the metallic tip and sample.[6,10] In the following sections, the theoretical description of the STM will be addressed by taking the fundamentals of quantum tunneling into account. As a starting point, the fundamental one-dimensional (1D) rectangular potential barrier will be briefly explained.[11,12] In classical mechanics, an electron would not be able to penetrate a potential barrier with height U when its energy E is $E < U$, i.e., the barrier would reflect the incoming wave. However, in quantum mechanics, the electron is described by a wave function Ψ and its probability density $|\Psi|^2$ to penetrate (tunnel) through the barrier is nonzero. Such a phenomenon is known as quantum tunneling and the wave function Ψ inside (and outside) the barrier is described by the time-independent Schrödinger equation

$$H\Psi(z) = \left[-\frac{\hbar^2}{2m}\frac{\partial^2}{\partial z^2} + U(z)\right]\Psi(z) = E\Psi(z), \qquad (1)$$

where H is the 1D Hamiltonian operator, ħ the reduced Planck constant, m the mass of the electron, and E the energy of the electron.

The tunneling of an electron through a 1D rectangular potential barrier (depicted in orange) with height U and width d is illustrated in Figure 2.2a and b, where three main sections can be distinguished along z (*I*, *II* and *III*). As shown in Figure 2.2b, an incoming electron with energy $E < U$ – described as an oscillatory wave function Ψ_I (blue line) – reaches the rectangular potential barrier from the left (section *I*), which is partly reflected and transmitted at this stage. In the barrier (Ψ_{II} in section *II*), the electron wave

function decays exponentially as it passes through z. Finally, the outgoing wave function (Ψ_{III} in section *III*) leaves the barrier with reduced amplitude. Based on such an exponential behavior across the barrier, the tunneling of the electron can be expressed as a measurable tunneling current I_t

$$I_t \, \alpha \, e^{-2kd}, \text{ where } k = \sqrt{\frac{2m(\Phi - E)}{\hbar^2}} \qquad (2)$$

is the decay constant across the tunneling barrier ϕ.

The exponential relationship between the tunneling current I_t and the distance d is given in equation 2 and shows why the STM is so sensitive to variations in the tip-sample distance (z-direction). In the following section, the tunneling that takes place in the STM (between a metallic tip and a sample) will be addressed.

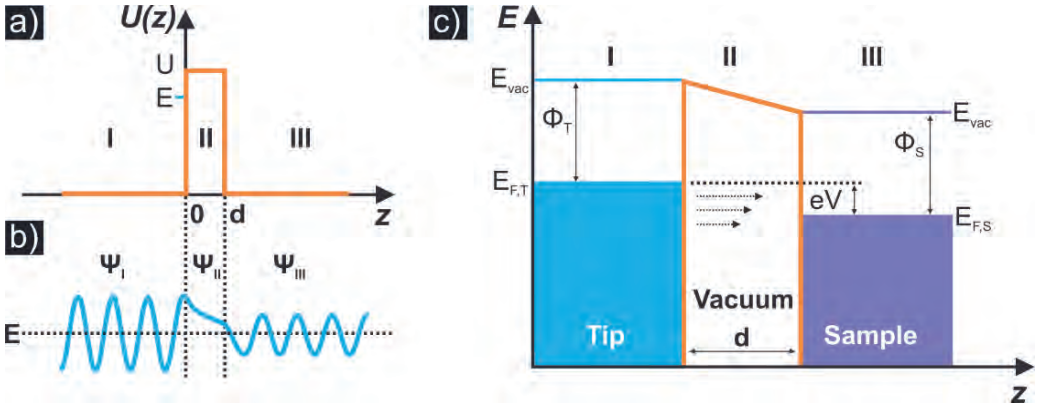

Figure 2.2. Different schematics describing quantum tunneling. a) Schematic of the fundamental 1D rectangular potential barrier (depicted in orange) with height U and width d. The roman numerals (*I*, *II* and *III*) highlight three different sections in which the potential of the barrier is 0 (regions *I* and *III*) or U (region *II*). b) Schematic of the wave function (blue line) of an electron penetrating (from left to right) the potential barrier that is shown in a). An oscillatory incoming wave function Ψ_I (with energy $E < U$) reaches the barrier at $z = 0$. An exponentially decaying wave function Ψ_{II} is found inside the barrier at $0 < z < d$. A wave function Ψ_{III} with a reduced amplitude is found outside the barrier at $z > d$. c) Schematic of quantum tunneling through a vacuum barrier represented by a tip–vacuum–sample junction along the z-direction, where d represents the distance between a tip and sample, i.e., the vacuum between them (region highlighted in orange). The roman numerals (*I*, *II* and *III*) highlight regions that are equivalent to those depicted in a) and b). The tip and sample are represented in blue and violet, respectively. Additionally, the work functions of the tip Φ_T and sample Φ_S, i.e., the separation between the vacuum level E_{vac} and the Fermi levels of the tip $E_{F,T}$ and sample $E_{F,S}$ are also shown. By considering a grounded tip, when a positive bias voltage eV has been applied to the sample, electrons can tunnel from occupied states of the tip to unoccupied states of the sample. The length of the black dashed arrows highlights the tunneling probability that an electron possesses at different energies.

Quantum tunneling in an STM

In a STM, quantum tunneling takes place between a metallic tip and a conducting sample that are separated by a vacuum barrier *d* (highlighted in orange) along the *z*-direction as shown in Figure 2.2c. The tip and sample are represented in blue and violet, respectively. The work functions of the tip Φ_T and sample Φ_S represent the minimum energy required to remove an electron from the bulk to the vacuum level E_{vac}. As shown in Figure 2.2c, by considering a grounded tip and assuming that Φ_T and Φ_S are equal, when a positive bias eV is applied to the sample, a net tunneling current will flow between tip and sample, where electrons can tunnel from occupied states of the tip to unoccupied states of the sample. The tunneling probability that an electron has at a given energy is highlighted by the black dashed arrows. The abovementioned description relates to the 1D rectangular potential barrier (shown in Figure 2.2a and b) expressed in terms of a tip–vacuum–sample junction along the *z*-direction.

In order to properly understand I_t across a metal–vacuum–metal junction (comparable to Figure 2.2), Bardeen developed a theory that considers the electronic structure between two planar electrodes (separated by an insulating layer) by describing them separately with two stationary one-particle Schrödinger equations. Time-dependent perturbation theory was used to calculate the rate of electron transfer. Additionally, he introduced the tunneling matrix element $M\mu\nu$ (equation 3) to calculate I_t. Such a quantity relates the overlap between the wave functions of both electrodes ($\Psi\mu$ and sample $\Psi\nu$) which have an exponential decay across the potential barrier. The matrix element $M\mu\nu$ is determined by a surface integral that is evaluated over a surface placed within the vacuum barrier as shown in equation (3)[13]

$$M_{\mu\nu} = -\left(\frac{\hbar^2}{2m}\right)\int_S \left(\Psi_\mu^* \nabla \Psi_\nu - \Psi_\nu \Psi_\mu^*\right) \cdot dS\,, \quad (3)$$

where $M\mu\nu$ is the tunneling matrix element proposed by Bardeen, $\Psi\mu$ and $\Psi\nu$ are the wave function of the tip and sample, respectively and S is the surface separation term within the vacuum barrier between two electrodes.

Following Bardeen's model, I_t can be evaluated as

$$I = \left(\frac{2\pi e}{\hbar}\right) \sum_{\mu\nu} f(E_\mu)[1 - f(E_\nu + eV)] \times \left|M_{\mu\nu}\right|^2 \delta(E_\mu - E_\nu), \quad (4)$$

in which $f(E)$ is the Fermi function, $M\mu\nu$ the tunneling matrix between the state $\Psi\mu$ of the tip and $\Psi\nu$ of the sample surface, $E\mu$ is the energy of the state $\Psi\mu$ in absence of tunneling and eV is the bias voltage at the sample.

In the limits of small voltage and temperature equation 4 becomes

$$I = \left(\frac{2\pi e^2}{\hbar}\right) V \sum_{\mu\nu} \left|M_{\mu\nu}\right|^2 \delta(E_\nu - E_F)\delta(E_\mu - E_F), \quad (5)$$

where E_F and δ are the Fermi energy and the Kronecker delta function, respectively.

Since the tip geometry (as in an STM set-up) is not considered in Bardeen's approach of I_t, Tersoff and Hamann[14,15] proposed a simple model – based on Bardeen's contribution – where the wave function of the outermost atom of the tip is assumed to be an atomic s-wave function. The model is shown in Figure 2.3, where the tip apex (depicted by the dashed green circle) is regarded to be locally spherical (with a radius R and center r_0) and the tip–sample distance is denoted by d.

The assumptions made by Tersoff and Hamann[14] lead to a new formulation to calculate I_t; where the angular dependency of the wave function of the tip $\Psi\mu$ was neglected

$$I = \left(\frac{32\pi^3 e^2}{\hbar}\right) V\varphi^2 D_\mu(E_F)\frac{R^2}{K^4} e^{2kR} \sum_v |\Psi_v(r_0)|^2 \delta(E_v - E_F), \quad (6)$$

in which $D_\mu(E_F)$ is the density of states (DOS) per unit volume at the tip and φ denotes the work function of the tip and sample.

In equation 6, the summation refers to the local density of states (LDOS) $\rho_v(r_o, E_F)$ of the sample's surface at the Fermi level and the tip's position (r_o)

$$\rho_v(r_o, E_F) = \sum_v |\Psi_v(r_o)|^2 \delta(E_v - E_F) \qquad (7)$$

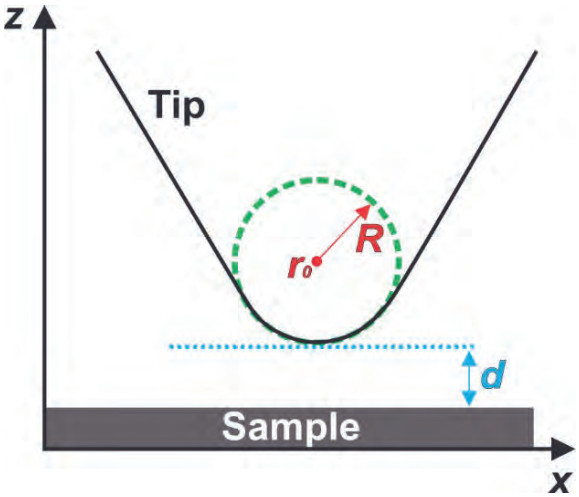

Figure 2.3. Schematic of the tunneling geometry at the tip apex as described by Tersoff and Hamann. The tip apex (shown as a dashed green circle) centered at r_0 has a radius R and is separated by a distance d from the sample.[14]

The relation between the tunneling current and the density of states of the sample and tip is given by the Tersoff-Hamann expression, which is a simplified version of equation 6

$$I \, \alpha \, V_{bias} D_{\mu}(E_F) \rho_{\nu}(r_o, E_F) \exp\left[-2kd\right] \qquad (8)$$

Since the tip is metallic, it is assumed that the DOS of the tip ($D_{\mu}(E_F)$) remains constant and the scanning (tip) probes the silhouette of constant density of states $\rho_{\nu}(r_o, E_F)$ of the sample. Therefore, the image obtained upon scanning depends only on the LDOS of the sample's surface. Additionally, equation 8 demonstrates the decaying exponential dependence (*exp[-2kd]*) of the tunneling current with respect to the tip-sample distance *d*. Therefore, for simplicity, the exponential dependence of the tunneling current I_t to the tip-sample distance can be expressed as I_t α *exp[-2kd]*. A small change in the tip-sample distance of ~1 Å will change the tunneling current by one order of magnitude.[10]

The lateral resolution *L* of the STM described by Tersoff and Hamann is based on the radius *R* of the tip and the tip-sample distance *d*

$$L = \sqrt{\frac{2\,(R+d)}{k}}, k = \sqrt{\frac{(2m_e\varphi)}{\hbar^2}} \qquad (9)$$

where *k* (on the right) denotes the minimum inverse decay length for the wave functions in vacuum.

For typical values in metals $2k^{-1}$ = 1.6 Å and if $R + d$ = 15 Å as assumed by Tersoff and Hamann, the lateral resolution according to equation 9 is about 5 Å.[14] However, lateral resolutions of 0.1 Å and vertical resolutions of 0.01 Å are achievable with the STM.[9] The detailed description of the lateral

resolution was given by Chen, where the localized p_z and d_{z^2} orbitals of the tip were considered.[16]

In summary, the actual STM image is obtained by convolution of the topography and electronic structure of the sample's surface. The tip-sample distance must be a couple Å so electrons are able to travel from the tip's apex to the sample (or vice versa), in this manner; the wave functions of the tip and sample overlap across the vacuum potential barrier.[14]

2.2.3 Scanning Tunneling Spectroscopy (STS)

The tunneling current depends on the LDOS close to the Fermi energy for small bias voltages as shown in eq. 8. For lager voltages (eV << Φ), the tunneling current is proportional to the combined density of the states of tip and sample integrated up to the bias voltage. According to this relation a technique known as scanning tunneling spectroscopy (STS) can be performed, which was demonstrated by Feenstra et al. for the first time.[17] STS is performed when the STM tip is positioned at a constant distance over the sample surface. To experimentally achieve this, a value of current *I* is selected and the feedback-loop is switched off. Then, a bias voltage is swept at a given range (e.g., -2 V to 2 V) in small steps (e.g., 0.01 V) while the current *I* is recorded, resulting in an *I-V* curve. Finally, by differentiating the *I-V* curves, i.e., dI/dV plots, a mapping that is proportional to the LDOS of the sample at that position is obtained.[18]

Hence, STS probes the electronic structure of occupied and unoccupied states of the sample. It should be noted that both electronic states (of the sample and tip) contribute to the results observed in the spectra. For such a reason, the condition of the scanning tip governs the sensitivity of the

technique.[19,20,21] Moreover, STS is suitable for studying adsorbates on surfaces[22,23] and confinement effects of surface state electrons.[24,25]

2.3 X-ray Photoelectron Spectroscopy (XPS)

The photoelectric effect was discovered by Hertz in 1887.[26] A decade later, the electron was discovered by J. J. Thomson, who also observed that these subatomic particles could be emitted from a zinc plate by irradiating it with light.[27,28] Then, Albert Einstein explained the photoelectric effect in 1905, stating that photons can transfer their energy to electrons in an atom, which results in the emission of electrons to the continuum states. This awarded him the Nobel Prize in Physics in 1921.[29] These pioneering discoveries served as a basis for the development of a group of analytical methods known as photoemission spectroscopy (PES). Herein, the focus will be given to X-ray photoelectron spectroscopy (XPS). XPS is a type of PES that uses X-rays to study the chemical composition of a sample by providing quantitative and qualitative information.

The first high-resolution photoelectron spectrometer was created in the second half of the 20th century by Kai Siegbahn and co-workers.[30] The importance of this work awarded him the Nobel Prize in Physics of 1981 and set the basis for the XPS experimental set-up and theory that is used in nowadays.[31] The XPS experimental set-up is shown in section 2.3.1 and the photoemission process is explained in section 2.3.2.

2.3.1 XPS experimental set-up and description

The basic set-up of an XPS instrument (Figure 2.4a) consists of a photon source (X-ray source shown in gray) that can produce photons with a

fixed energy *hv* (highlighted by the red arrow). The X-ray beam is produced by striking a metal target (highlighted in green) – or anode made of Al or Mg – with electrons coming from a thermionic emission electron source. The electrons are produced from a filament (highlighted in orange) and focused to the anode by a shield (highlighted in blue). The energy of the X-rays produced depends on the anode material, for instance, with Al as an anode, the Al-Kα line with an energy of *hv* = 1,486.6 eV can be acquired. The X-ray intensity can be tuned by the electron flux striking the anode.[32,33] In addition, synchrotrons provide high brilliance radiation that can be tuned over a wide range of wavelengths by making use of a monochromator (grating).[34]

The X-rays imping on the sample (depicted in purple) can produce photoelectrons from the core levels of the atoms. The photoelectrons (shown in blue) are expelled into vacuum with a certain kinetic energy E_{kin} and guided by a set of lenses (shown in brown) towards a hemispherical analyzer. The hemispherical electron analyzer – by applying a bias between the inner and outer hemisphere – deflects and separates the photoelectrons according to their E_{kin}. Finally, they are detected by a micro-channel plate (depicted in green) that detects the photoelectrons according to their energy, i.e., it registers a current that is proportional to the number of detected photoelectrons. Since XPS is used as a surface sensitive technique due to the small electron inelastic mean free path (few Å) that photoelectrons have at the E_{kin} range (10 to 2,000 eV) of interest, the measurements are usually performed under UHV conditions to avoid surface contaminations.[33]

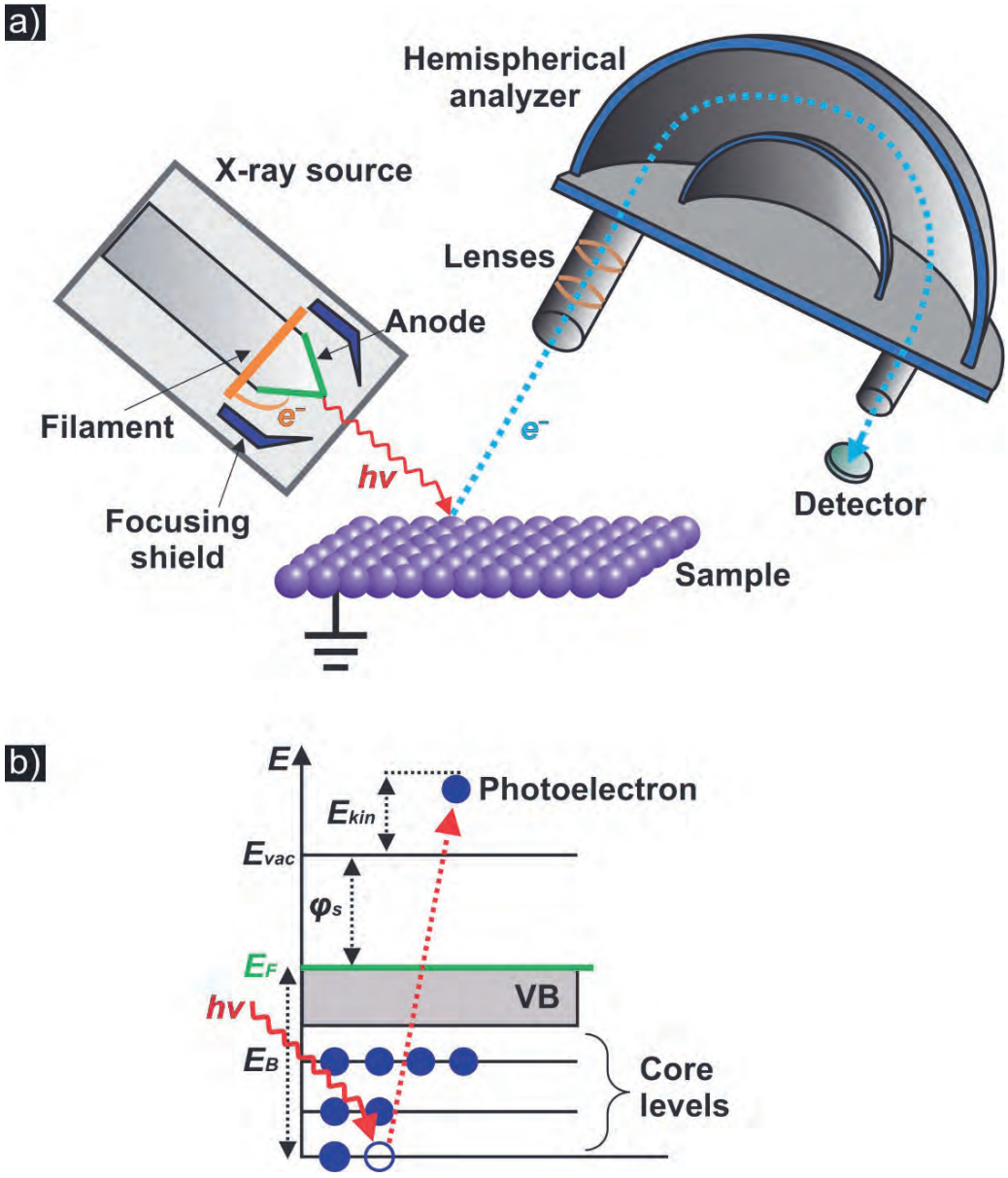

Figure 2.4. Schematics of the experimental setup for X-ray photoelectron spectroscopy (a) and of the energy level diagram of the photoemission process (b). For details see text. It should be noted that the E_{kin} shown in b) is different than the E_{kin} measured in the analyzer in a).

2.3.2 XPS theoretical description

As previously mentioned, this technique detects photoelectrons that are produced by the excitation of core level electrons in the sample that are sent into vacuum with a certain kinetic energy E_{kin} as shown in the schematic of the photoemission process in Figure 2.4b. The core level electrons (shown in purple) are characterized by being bonded to the nucleus in atomic orbitals by a fixed energy known as binding energy E_B. In order to excite core level electrons above the vacuum level E_{vac} with a certain E_{kin}, the energy hv of the incoming photons (highlighted by the red arrow) must be higher than the sum of the E_B of the core level electrons and the work function of the sample ϕ_s

$$E_{kin} = hv - \phi_s - E_B \qquad (10)$$

So, the E_{kin} of the photoelectron depends on the energy of the incoming photons hv. However, since the E_B is independent of hv, the values of E_B serve as fingerprints of the elements in the material being analyzed.[33] It should be noted that the sample and detector must be in electrical contact so that their Fermi levels E_F are aligned. This means that the measured E_{kin} at the detector can be an indirect measure of the E_B of the photoelectron by considering the work function of the analyzer ϕ_a. Therefore, equation 10 can be rewritten as

$$E_{kin} = hv - \phi_a - E_B \qquad (11)$$

For this reason, based on equation 11, the XPS spectrum is plotted as a function of E_B along the abscissa and photoemission intensity (number of emitted photoelectrons) along its ordinate.

2.4 Low Energy Electron Diffraction (LEED)

The diffraction of electrons was discovered by Davisson and Germer in 1927 by striking a nickel single crystal with low energy electrons.[35] Low energy electrons (20 to 500 eV) are surface sensitive due to their short inelastic mean free path, i.e., they are scattered at the surface or within the first few layers of the sample. Additionally, they possess low kinetic energy which confers them a de Broglie wavelength that is comparable to interatomic distances, i.e., a few Å.[36] Therefore, diffraction experiments with low energy electrons, due to their small wavelength λ, must be carried out under UHV conditions. The diffraction of low energy electrons coming from a surface provides information of its structure. The low energy electron diffraction (LEED) experimental set-up and theoretical description are addressed in the following sections.

2.4.1 LEED experimental set-up and description

The LEED experimental set-up is shown in Figure 2.5. The electron gun produces a beam of low energy electrons < 500 eV (highlighted by the solid red arrow) by thermally exciting a filament when a bias is applied to it. A Wehnelt cylinder (shown in blue) aids in confining the electron beam that is accelerated towards an anode (shown in black), which is able to extract the electron beam since it is held at a positive potential. The electron beam is guided by a set of lenses (shown in green) towards a sample (shown in purple) that is grounded. At the sample surface, the electron beam is elastically and inelastically backscattered (highlighted by the dashed red arrows). Then, these electrons travel towards the first of a set of four hemispherical grids, where the first grid is grounded to ensure a field-free region around the

sample. The electrons continue to travel to the second and third grids that possess a retarding voltage (highlighted in blue), i.e., a smaller bias than the E_{kin} of the elastic electrons, to suppress the inelastically scattered electrons. Finally, the fourth (grounded) grid allows the elastically scattered electrons to impinge onto the fluorescent screen by screening the sample and the other grids from the high voltage (~kV) that is applied to the fluorescent screen.[18,36]

In summary, the LEED experiment renders a diffraction pattern (as bright spots) of elastically scattered electrons that can be analyzed in a qualitative and quantitative manner. The former case – based on the position of the diffraction spots on the measured LEED pattern – gives information of the symmetry and periodicity of the sample's surface, as well as its quality, i.e., bright diffraction spots indicate that the surface is clean. The latter one consists in recording the diffraction intensities as a function of the electron kinetic energy of the incident beam to compare them with theoretical models and obtain information of the atomic positions of the sample surface. Additional information regarding the analysis of LEED patterns can be found in suitable textbooks.[9,18,34]

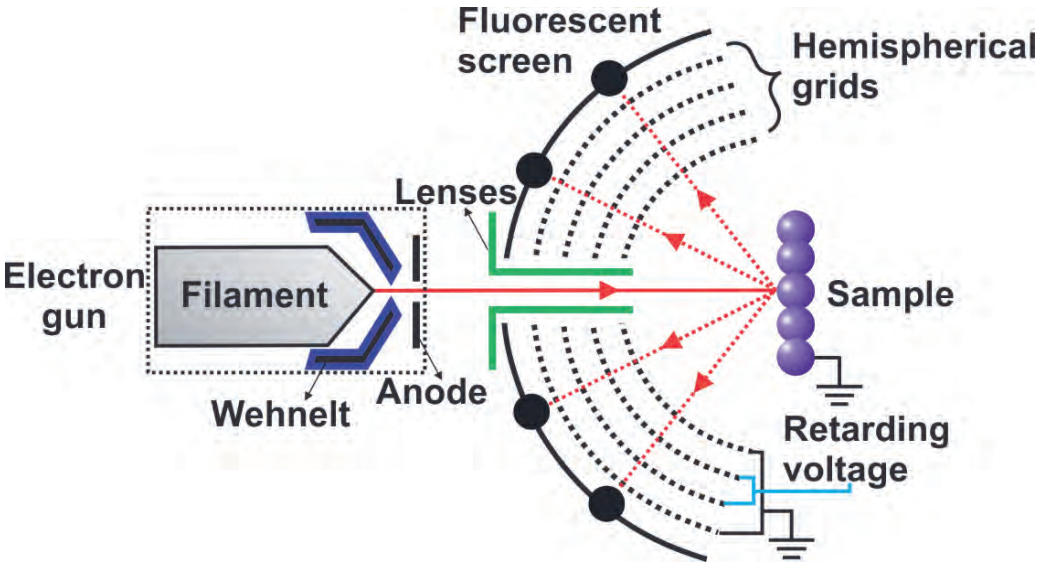

Figure 2.5. LEED experimental set-up including the essential components for its operation: an electron gun, lenses, four hemispherical grids and a fluorescent screen.

2.4.2 LEED theoretical description

As previously mentioned, the LEED measurement renders a diffraction pattern of elastically scattered electrons from a 2D grid of atoms. For elastic scattering to take place, the law of energy conservation is taken into account – meaning that the wave vectors of the incident k_0 and scattered k' beams must have the same magnitude

$$|k_0| = |k'|, \qquad (12)$$

In addition, the Laue condition must be fulfilled for diffraction to occur. In the 2D case it can be written as

$$g = k' - k_0, \qquad (13)$$

where g is a surface reciprocal lattice vector, while k_0 and k' are the incident and scattered wave vectors, respectively.

The Ewald sphere construction (shown in Figure 2.6) will be used to illustrate the diffraction from a surface. In reciprocal space, an incident wave vector k_0 (shown in red) with a given magnitude terminates at what can be regarded as the origin (Point O) of the reciprocal lattice. It should be noted that the reciprocal lattice points are replaced by rods that are perpendicular to the surface, since the dimension perpendicular to the surface is removed in the 2D case, i.e., the periodicity in z-direction is infinite. To construct the Ewald sphere, a circle with radius $r = k_0$ (highlighted by the blue dashed line) and center at the origin (point i) of k_0 is drawn. When the circle intersects any rod (shown with black lines) of the reciprocal lattice, the Laue condition (equation 13) for diffraction will be satisfied. Therefore, a scattered wave vector k' (shown in red) fulfilling the condition for elastic scattering (equation 12) can be drawn from point i to that specific intersection. Finally, the reciprocal lattice vector g can be drawn from the origin (point O) to the intersection between k' and the Ewald sphere. The distance between consecutive rods ($2\pi/d$) is inversely proportional to the corresponding distance in real space.[18,34]

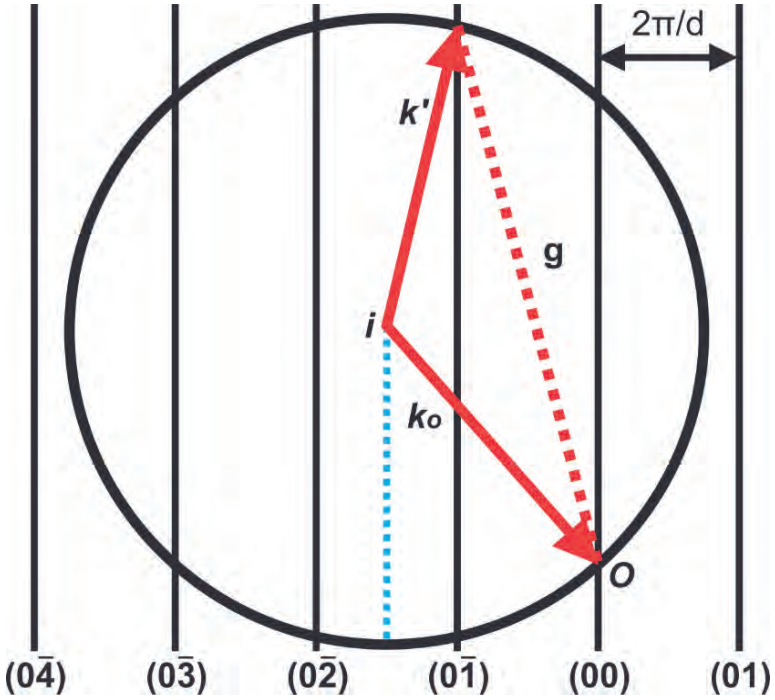

Figure 2.6. Schematic of the Ewald sphere construction in reciprocal space when diffraction occurs on a surface. Where *g* is the reciprocal lattice vector, k_0 and *k'* are the incident and scattered wave vectors, respectively. Diffraction spots will be visible in the LEED pattern when the condition $g = k' - k_0$ is satisfied.

2.5 Ultra-High Vacuum (UHV)

Experiments performed in surface science are usually carried out under UHV at pressure values between $1x10^{-9}$ to 10^{-12} mbar. Surfaces in ambient conditions are exposed to contaminants from the surrounding environment, i.e., unwanted particles may adsorb to it. Therefore, measurements performed under UHV will benefit from the cleanliness of the surface to be studied. Additionally, techniques that measure electrons such as LEED and XPS require UHV due to the relatively small electron inelastic

mean free path. Without UHV, contaminants in the gas phase can scatter the electrons that carry useful information of the sample.[9] Therefore, with UHV the electrons can travel to the analyzer without colliding with the molecules of the residual gas atmosphere that would be present at higher pressure values.

A dedicated pumping system must be used to achieve UHV.[18] A roughing pump is used as the first stage (also known as pre-vacuum) of the pumping system since it can achieve pressure values in the order of 10^{-3} mbar. Two common types of roughing pumps are the oil-sealed rotary vane pump and so-called membrane pumps. Membrane pumps can only achieve pressure values in the order of 10^{-1} mbar. Once the pre-vacuum has been established another type of pump is required to further reduce the pressure. The second stage of the pumping system typically uses a turbomolecular pump that can reach pressure values in the mid 10^{-11} mbar region. The turbomolecular pump has a rotor composed of blades spinning at high speed that transfer momentum to the gas molecules that collide with them and guide them towards the roughing pump. The turbomolecular pump can operate in the 10^{-3} to 10^{-11} mbar region; however, higher pressures will reduce its lifetime considerably.

Finally, a third type of pump known as ion pump can be used to maintain the UHV when the low-pressure regime has been achieved. This pump ionizes the rest gas by a plasma discharge formed between an anode and a cathode. A magnetic field deflects the charged particles in a spiral trajectory, which increases the ionization probability. The ions strike the titanium cathode and attach (react) to it. In addition, the ion pump can be supported by a so-called titanium sublimation pump (TSP), which evaporates titanium from a filament in order to create a getter film on the inner walls of the chamber. This film captures gas molecules that impinge on it by forming

stable compounds with the previously evaporated titanium ions. It should be noted that the TSP is used for a short interval of a couple minutes while the ion pump can be operated continuously.[9]

2.6 References

1. Abbe, E. *Beiträge zur Theorie des Mikroskops und der mikroskopischen Wahrnehmung (Contributions to the Theory of the Microscope and Microscopic Perception)*; University library Johann Christian Senckenberg: Frankfurt, Germany. **1873**, *9*, 413–468.
2. Knoll, M.; Ruska, E. Beitrag zur Geometrischen Elektronenoptik I und II. (Contribution to Geometrical Electron Optics). *Ann. Phys*. **1932**, *12*, 607–640.
3. Binnig, G.; Rohrer, H.; Gerber, C. et al. Surface Studies by Scanning Tunneling Microscopy. Phys. Rev. Lett. **1982**, *49*, 57–61.
4. Binnig, G.; Rohrer, H. *Scanning Tunneling Microscopy - From Birth to Adolescence*. Nobel lecture. Physics College. Park. Md. 1986.
5. Ruska, E. *The Development of the Electron Microscope and of Electron Microscopy. Nobel lecture*. Physics College. Park. Md. 1986.
6. Nordheim, L.; Fowler, R. H. Electron Emission in Intense Electric Fields. *Proc. R. Soc. London* **1928**, *119*, 173–181.
7. Binnig, G.; Hoenig, H. Tunneling Investigation of Superconducting (SN)x. *Z. Phys. B* **1978**, *32*, 23–26.
8. Binnig, G.; Quate, C. F.; Gerber, C. Atomic Force Microscopy. *Phys. Rev. Lett*. **1986**, *56*, 930–933.
9. Vickerman, J. C.; Gilmore, I, S. *Surface Analysis - The Principal Techniques*. Wiley Online Library: Manchester, U.K., **2009**.
10. Binnig, G.; Rohrer, H.; Gerber, C.; Weibel, E. Tunneling Through a Controllable Vacuum Gap. *Appl. Phys. Lett*. **1982**, *40*, 178–180.
11. Chen, J. *Introduction to Scanning Tunneling Microscopy*. Oxford University Press: Yorktown Heights, NY. **1993**, 1–379.
12. Wiesendanger, R. *Scanning Probe Microscopy and Spectroscopy: Methods and Applications*. Cambridge University Press. **1994**. 1–518.
13. Bardeen, J. Tunneling From a Many-Particle Point of View. *Phys. Rev. Lett.* **1961**, *6*, 57-59.
14. Tersoff, J.; Hamann, D. R. Theory and Application for The Scanning Tunneling Microscope. *Phys. Rev. Lett*. **1983**, *50*, 1998–2001.
15. Tersoff, J.; Hamann, D. Theory of the Scanning Tunneling Microscope. *Phys. Rev. B* **1985**, *31*, 805–813.
16. Chen. J. C. Origin of Atomic Resolution on Metal Surfaces in Scanning Tunneling Microscopy. *Phys. Rev. Lett.* **1990**, *65*, 448–451.
17. Feenstra, R.; Stroscio, J. A.; Fein, A. Tunneling Spectroscopy of the Si(111)2 × 1 Surface. Surf. Sci. **1987**, *181*, 295–306.
18. Hofmann, P. *Surface Physics: An Introduction*. (ebook) **2013**. http://philiphofmann.net/Philip_Hofmann/SurfacePhysics.html.
19. Toerker, M.; Fritz, T.; Proehl, H.; Gutiérrez, R.; Großmann, F.; Schmidt, R. Electronic Transport Through Occupied and Unoccupied States of an Organic

Molecule on Au: Experiment and Theory. *Phys. Rev. B: Condens. Matter Mater. Phys.* **2002**, *65*, 245422.
20. Hipps, K. W. *Scanning Tunneling Spectroscopy (STS)*. In Vijs D. (eds) Handbook of Applied Solid State Spectroscopy. Springer: Boston, MA. **2005**, 305–350.
21. Lang, N. D. Spectroscopy of Single Atoms in the Scanning Tunneling Microscope. *Phys. Rev. B* **1986**, *34*, 5947–5960.
22. Stipe, B.; Rezaei, M.; Ho, W. Single-Molecule Vibrational Spectroscopy and Microscopy. *Science* **1998**, *280*, 1732–1735.
23. Gross, L.; Moresco, F.; Savio, L.; Gourdon, A.; Joachim, C.; Reider, K.-H. Scattering of Surface State Electrons at Large Organic Molecules. *Phys. Rev. Lett.* **2004**, *93*, 56103.
24. Crommie, M. F.; Lutz, C. P.; Eigler, D. M. Imaging Standing Waves in a 2-Dimensional Electron-Gas. *Nature* **1993**, *363*, 524–527.
25. Pennec, Y.; Auwärter, W.; Schiffrin, A.; Weber-Bargioni, A.; Riemann, A.; Barth, J. V. Supramolecular Gratings for Tuneable Confinement of Electrons on Metal Surfaces. *Nat. Nanotech*. **2007**, *2*, 99–103.
26. Hertz, H. Über einen Einfluss des ultravioletten Lichtes auf die elektrische Entladung (About the Influence of Ultraviolet Light on Electrical Discharge). *Ann. Phys*. **1887**, *267*, 983–1000.
27. Thomson, J. J. Cathode Rays. *Lond. Edinb. Dubl. Philos. Mag.* **1897**, *44*, 293–316.
28. Thomson, J. J. On the Masses of the Ions in Gases at Low Pressures**.** *Phil. Mag*., **1899**, *48*, 547–567.
29. Einstein, A. Über einen die Erzeugung und Verwandlung des Lichtes betreffenden heuristischen Gesichtspunkt (On a Heuristic Point of View about the Creation and Conversion of Light). *Ann. Phys*. **1905**, *322*, 132–148.
30. Siegbahn, K.; Edvarson, K. β-Ray Spectroscopy in the Precision Range of 1:105. *Nucl. Phys.* **1956**, *1*, 137–159.
31. Siegbahn, K. Electron spectroscopy for Atoms, Molecules and Condensed Matter. Physics College. Park. Md. 1981.
32. Hüfner, S. *Photoelectron Spectroscopy: Principles and Application*. Springer: Berlin, **2003**.
33. Suga, S.; Sekiyama, A. *Photoelectron Spectroscopy: Bulk and Surface Electronic Structure*. Springer: Japan, **2004**.
34. Oura, K.; Lifshits, V.; Saranin, A.; Zotov, A.; Katayama, C. *Surface Science: An Introduction*. Springer: Berlin, **2003**.
35. Davisson, C.; Germer, L. H. Diffraction of Electrons by a Crystal of Nickel. *Phys. Rev*. **1927**, *30*, 705-740.
36. VanHove, M. A.; Weinberg, W. H.; Chan, C.-M. *Low-Energy Electron Diffraction*. Springer: Berlin, **1986**.

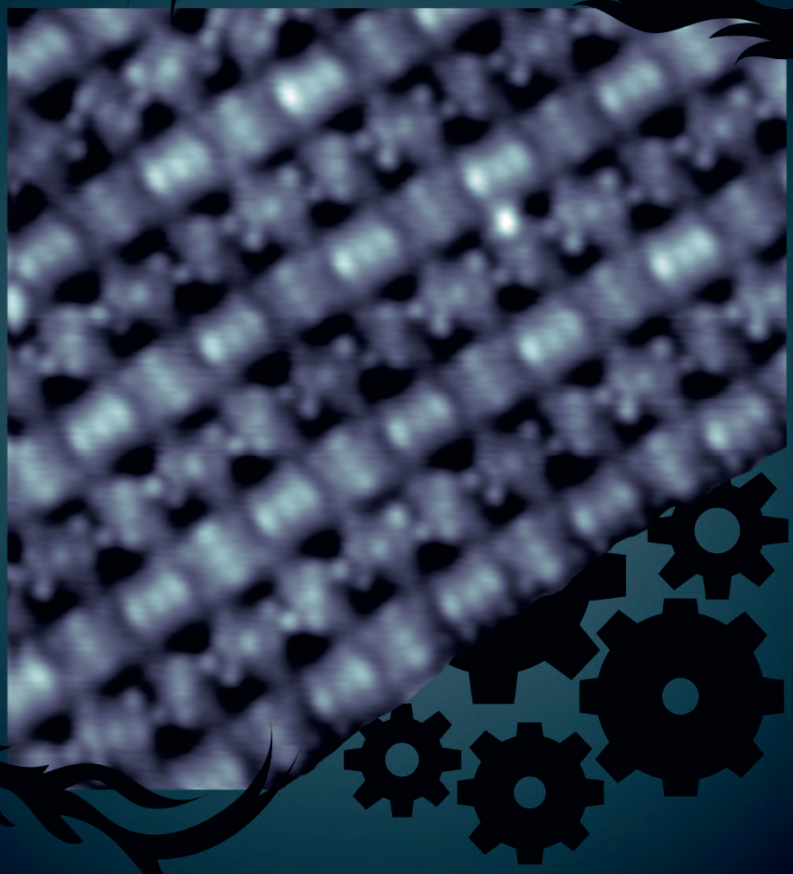

Chapter 3

3 Molecular Self-Assembly on Metal Surfaces[1]

The fundamentals of molecular self-assembly are introduced in the following chapter. In particular, we present a summary of the self-assembly of porphyrins on metal surfaces and their capacity to host a variety of 3d transition metals in their core. Then, the usage of porphyrins as molecular building blocks in the fabrication of metal-organic coordination networks (MOCNs) is addressed. Finally, an adaptation from our previous publication on the role of cyano endgroups in the self-assembly of organic molecules on metal surfaces is given.[1]

3.1 Introduction and Fundamentals

The field of supramolecular chemistry studies molecular systems that are stabilized and organized by non-covalent intermolecular interactions between two or more chemical entities.[2,3] These molecular systems are frequently encountered in nature, especially in biological processes such as the assembling of proteins, enzyme-substrate binding as well as cellular recognition.[2] The relevance of supramolecular chemistry was recognized in 1987, when the Nobel Prize in Chemistry was awarded to Donald J. Cram, Jean-Marie Lehn and Charles J. Pedersen for their work in this field. One of the essential concepts in supramolecular chemistry is the term molecular self-assembly, which is the process that steers the formation of well-ordered nanostructures. Whitesides et al. defines self-assembly as “the spontaneous

[1] The results presented in chapter 3.3 have been published as Baker Cortés, B. D.; Stöhr, M. in *Encycl. Interfacial Chem.* (Ed.: K. Wandelt), Elsevier, **2018**, *4*, pp 153–165.

association of molecules under equilibrium conditions into stable, structurally well-defined aggregates joined by non-covalent bonds".[4]

The development of supramolecular chemistry has provided the tools necessary for the fabrication of 2D networks driven by molecular self-assembly on metal surfaces under ultra-high vacuum (UHV) conditions and at the solid-liquid interface. In recent years, this bottom-up fabrication method has gained special attention in the scientific community owing to their promising applications in catalysis, gas storage, molecular electronics and spintronics.[5–12] In addition, the ability to carefully tailor organic molecules with a variety of functional endgroups such as pyridyl, cyano, phenyl, carboxylic and thiol moieties, has allowed the formation of structurally different 2D networks supported on a wide range of, especially noble metal surfaces.[5–8,13]

In order to understand the molecular self-assembly process on a surface, different energy contributions must be taken into account as shown in Figure 3.1. A low flow of molecules is deposited (indicated by the black arrow) with a given kinetic energy E_{kin} on a surface (depicted with the gray spheres). The molecules will adsorb on the surface when E_{kin} is smaller than the adsorption energy E_{ad} between the molecules and the surface. The adsorbed molecules will able to diffuse on the surface by rotation and migration, only if their E_{kin} is large enough to overcome the migration E_m and rotation E_{rot} energy barriers. As the molecules diffuse across the surface, they will be able to form ordered structures when the intermolecular energy E_{lat}, i.e., the energy given by the non-covalent lateral interactions between them, is slightly stronger or equal than E_{kin}. So far, the case when $E_{kin} < E_{ad}$ was described. However, in the opposite case, when $E_{kin} > E_{ad}$, the molecules will

desorb from the surface. Thus, the self-assembly of 2D networks on a surface may take place when $E_{ad} > E_{lat} \geq E_{kin} > E_{m,rot}$.[6,13,14]

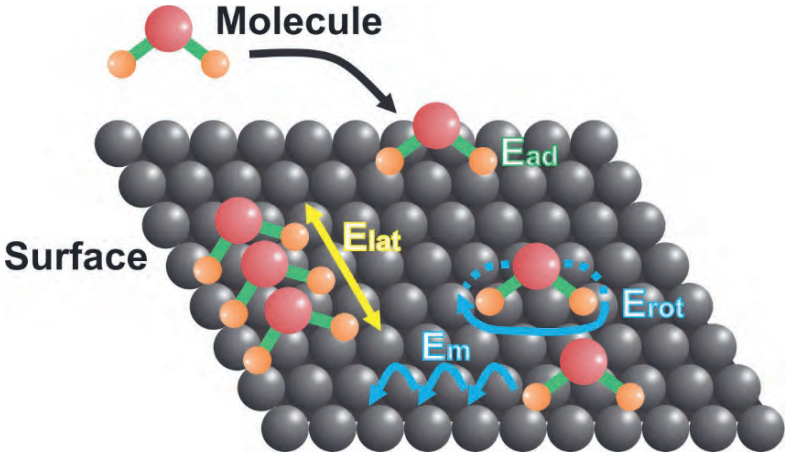

Figure 3.1. Schematic of the self-assembly of molecules on a surface with the different energy contributions that must be considered for the process to take place. Molecules are deposited with a low flux (indicated by the black arrow) on a surface (depicted with gray spheres) with a given kinetic energy E_{kin}. The molecules will adsorb on the surface if their E_{kin} is lower than the adsorption energy E_{ad} between the molecules and the surface. Once the molecules adsorb on the surface, they can diffuse on it by rotation and migration, only if their E_{kin} is large enough to overcome the migration E_m and rotation E_{rot} energy barriers. As the molecules diffuse, they will interact laterally with neighboring molecules and will be able to form ordered structures when the intermolecular energy E_{lat} between them is slightly stronger than E_{kin}.[6,13,14]

The self-assembly process (described in Figure 3.1) forms a structure that is in thermodynamic equilibrium, since the process is governed by high diffusivity and thermodynamics when the molecules are deposited at a low flux. However, if a high flux of molecules is used, the diffusivity will be limited and the structure will be kinetically trapped, i.e., the structure will be driven by kinetics instead of thermodynamics. This process is known as self-organization.[13,14] As previously mentioned, the non-covalent lateral interactions between the molecules that are adsorbed on the surface will determine the stability of the self-assembled structure. A common classification of these interactions according to their strength, bond distance and character is shown in Table 3.1.[6,14]

Interaction	**Strength (eV)**	**Bond distance (Å)**	**Character**
Van der Waals	0.02 – 0.1	< 10	Nonselective
Hydrogen bonding	0.05 – 0.7	1.5 – 3.5	Selective, directional
Dipole – dipole	0.1 – 0.5	2 – 3	Directional
Electrostatic ionic	0.05 – 2.5	Long range (nm)	Nonselective
Metal – ligand	0.5 – 2	1.5 – 2.5	Selective, directional

Table 3.1. Classification of the different non-covalent interactions with their respective energy range and bond distance.[6,14]

In summary, the electronic, chemical and structural properties of these 2D self-assembled networks is determined by the interplay between: (i) the electron affinity between the organic molecules used as building blocks, (ii) the interaction with the supporting metal substrate and in some cases, (iii) the elementary nature of the co-deposited metal-atoms. In the following section, the usage of porphyrins in the formation of 2D self-assembled networks on metal surfaces is given.

3.2 Porphyrins as Building Blocks in Molecular Self-Assembly

Porphyrins are a class of organic molecules that have shown to be stable and flexible building blocks used for the fabrication of 2D networks on metal surfaces.[1,15,16] As shown in Figure 3.2, porphyrins are tetrapyrrole macrocycles (the green rectangle highlights the pyrrole building block) with a central cavity that can remain in its free-base form (Figure 3.2a) or host a metal ion (in the formal +II oxidation state) through metal-ligand interactions (Fig 3.2b). The porphyrin core is also known as porphin and can be functionalized – at the β and *meso* positions (highlighted in blue and red in Fig3.2a, respectively) – with specific molecular endgroups, which influence the structure and bonding strength of the 2D networks. Porphyrins play vital roles in nature, but they also allow the development of nanoscale electronic devices and applications such as dyes in solar cells or in catalysis.[1,5,15,16] For instance, bioinspired porphyrin-based 2D networks that mimic catalytically active sites for the reduction of molecular oxygen have been reported. In the following, a series of porphyrin-based 2D networks on metal surfaces stabilized by different types of non-covalent interactions will be presented and illustrated by scanning tunneling microscopy (STM) images.

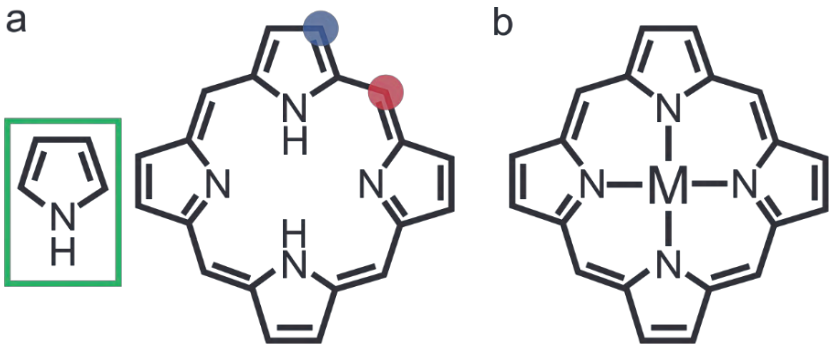

Figure 3.2. Schematic of the chemical structure of the porphyrin core also known as porphin. (a) Free-base porphyrin core with its main building block (pyrrole group) highlighted by the green rectangle. The blue and red circles refer to the *β* and *meso* positions, respectively, where functional endgroups can be attached to. (b) Metal-substituted porphyrin core or metalloporphyrin, where M can be a variety of 3d transition metal or lanthanide atoms.[15,16]

Porphyrins in Two-Dimensional (2D) Networks on Coinage Metal Surfaces

Auwärter et al. reported the formation of a long-range ordered network of Co-substituted tetraphenyl porphyrins (Co-TPP) on Ag(111) as shown in the overview STM image in Figure 3.3a.[17] The zoom-in STM image (Figure 3.3b) reveals submolecular features of Co-TPP within the 2D network, where the three main maxima observed along the porphyrin core were attributed to the central Co-atom (maxima located in the center) and to the saddle-shape adsorption geometry that the Co-TPP molecules adapted upon adsorption on the Ag(111) substrate (two outer maxima). In addition, the four dim protrusions in the surrounding belong to the phenyl endgroups. A square unit cell (highlighted in red in Figure 3.3a and b) was constructed based on the STM images. As depicted in the structural model (Figure 3.3c), the 2D network was stabilized by aromatic non-covalent T-type interactions

between the H-atom from a phenyl endgroup that points towards the ring of an adjacent phenyl endgroup from a neighboring molecule. Several reports of long-range ordered porphyrin-based 2D networks can be found in the literature.[1,15,16]

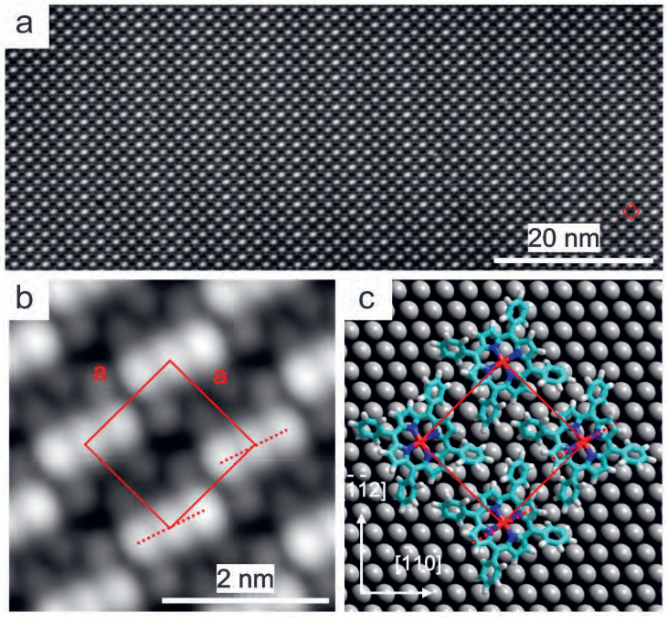

Figure 3.3. Self-assembly of Co-TPP on Ag(111). (a) Overview STM image of the 2D network formed by Co-TPP, where every bright protrusion is a Co-TPP molecule. (b) Zoom-in STM image displaying submolecular features of Co-TPP within the 2D network. Three main maxima can be observed along the porphyrin core and four dim protrusions in the surrounding. (c) Structural model of the assembly shown in (b), where carbon, nitrogen, hydrogen and cobalt atoms are shown in turquoise, blue, white and red, respectively. Scanning parameters in: (a) (U_{bias} = -0.48 V, I_{set} = 97 pA) and (b) (U_{bias} = -0.9 V, I_{set} = 0.12 nA). Reprinted (figure) with permission from [Auwärter. W.; Seufert, K.; Klappenberger, F.; Reichert, J.; Weber-Bargioni, A.; Verdini, A.; Cvetko, D.; Dell'Angela, M.; Floreano, L.; Cossaro, A.; Bavdek, G.; Morgante, A.; Seitsonen, A. P.; Barth, J. V. Phys. Rev. B, 81, 245403-3, 2010] Copyright (2010) by the American Physical Society.

As previously mentioned, the porphyrin core can host a variety of 3d transition metals (Figure 3.2b).[15,16,18,19] The addition of metal-atoms in the porphyrin core – known as metalation – is usually achieved by incorporating metal ions into free-base porphyrins following well-known solution-based protocols.[15,16] Moreover, the metalation of free-base porphyrins supported on a metal surface can be also achieved under UHV conditions by the co-deposition of metal-atoms or by a so-called self-metalation process, i.e., when the underlying metallic substrate supplies the metal-atoms.[18,19] For instance, Auwärter et al. reported the formation of a well-ordered network of free-base tetrapyridyl porphyrins (H_2-TPyP) on Ag(111) as shown in Figure 3.4a.[20] The appearance of individual H_2-TPyP molecules is distinguished by a dark depression in its core and four bright protrusions in its surrounding, which are given by the pyridyl endgroups. The structural model is superimposed and highlights the orientation of individual H_2-TPyP molecules within the network. In addition, a rectangular unit cell was obtained (highlighted in white in Figure 3.4a, b and c). The lateral non-covalent interactions that stabilized the 2D network were H-bonds given by the interaction between a N-atom from a pyridyl endgroup and a H-atom bonded to a pyridyl endgroup from a neighboring molecule.

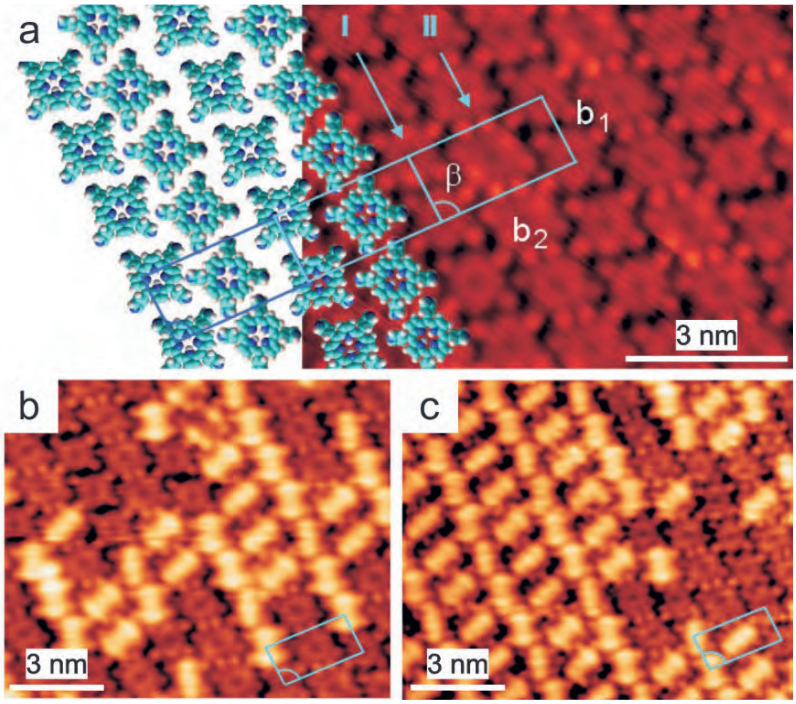

Figure 3.4. Self-assembly of H_2-TPyP on Ag(111). (a) STM image of the 2D network formed by H_2-TPyP. Its structural model is superimposed, where carbon, nitrogen and hydrogen atoms are shown in turquoise, blue and white, respectively. The STM images in (b) and (c) highlight the metalation reaction between H_2-TPyP and Fe-atoms. Increasing the dosage of Fe-atoms, i.e., going from image (b) to (c), the metalation can be tuned from few metalated porphyrins to a full saturation. Scanning parameters in: (a) (U_{bias} = -1.2 V, I_{set} = 0.7 nA) and (b), (c) (U_{bias} = -0.3 V, I_{set} = 0.85 nA). Reprinted from Auwärter, W., Weber-Bargioni, A., Brink, S., Riemann, A., Schiffrin, A., Ruben, M. and Barth, J.V. (2007), Controlled Metalation of Self-Assembled Porphyrin Nanoarrays in Two Dimensions. ChemPhysChem, 8: 250-254. doi:10.1002/cphc.200600675 with permission through Wiley.

The addition of Fe-atoms at 320 K modified the appearance of the porphyrins under STM investigation as shown in Figure 3.4b. The formation of brighter molecules with an increased apparent height was attributed to the

metalation of the porphyrin core by Fe-atoms, i.e., Fe-substituted porphyrins (Fe-TPyP) were synthesized from the free-base precursor on the Ag(111) surface. By increasing the dosage of Fe-atoms, the metalation of additional H_2-TPyP molecules also increased as shown in Figure 3.4c.[20]

The metalation of free-base porphyrins on metal surfaces has been reported for a variety of 3d transition metals such as Co, Fe, Cu and Zn-atoms.[18,19] However, the replacement of a preexisting metal-atom in the porphyrin core by a different metal – also known as atom exchange reaction – has been rarely reported under UHV conditions.[21–23] A detailed study of the atom-exchange reaction between Fe-atoms and Zn-atoms in Zn-substituted porphyrins on Au(111) is presented in Chapter 5.

Porphyrins in Metal-Organic Coordination Networks on Coinage Metal Surfaces

The fabrication of metal-organic frameworks (MOFs) in three-dimensions (3D) provided the toolbox necessary for the synthesis of similar frameworks on surfaces.[24,25] In particular, the synthesis and characterization of 2D metal-organic coordination networks (MOCNs) on surfaces steered by self-assembly has become a vibrant research field owing to their promising applications in gas storage and catalysis.[5,13] MOCNs are prepared by linking organic molecules and metal-atoms on a surface.[5–8] Porphyrins are building blocks of excellence for the construction of MOCNs because they allow the formation of various coordination geometries depending on the functional endgroups that constitute their backbone.[5,15,16]

Li et al. reported the self-assembly of a close-packed 2D MOCN formed by the deposition of H_2-TPyP followed by the addition of Cu-atoms

on Au(111) after annealing at 450 K (Figure 3.5).[26] The zoom-in STM image (Figure 3.5b) reveals intramolecular features of the assembly, where individual porphyrins can be distinguished by two bright lobes. It should be noted that the annealing step at 450 K activated the dehydrogenation of the porphyrin core (i.e., the removal of two H-atoms from the porphyrin core), which allowed the incorporation of a single Cu-atom in its core that exhibited two different oxidation states: (i) The brighter molecules were attributed to porphyrins bearing one Cu-atom in an oxidation state of 0 (Cu^0 highlighted in green), (ii) while the dim molecules coordinated to one Cu-atom in an oxidation state of 2 (Cu^{2+} highlighted in yellow). In addition, the structural model is overlaid to highlight the twofold Cu-coordination between neighboring molecules (highlighted in green between neighboring porphyrins) and the metalation (highlighted in yellow and green in the porphyrin core) of their core by a single Cu-atom. Upon increasing the annealing temperature up to 520 K, only metalated porphyrins with Cu^{2+} were observed within the twofold Cu-coordinated MOCN. Therefore, the Cu^0-atoms were considered as an intermediate state of the Cu-atom prior to oxidizing to the Cu^{2+} state. i.e., bearing the Cu(II)-TPyP derivative. The formation of structurally different porphyrin-based MOCNs has been reported for a variety of porphyrins on different metal substrates.[15,16,27]

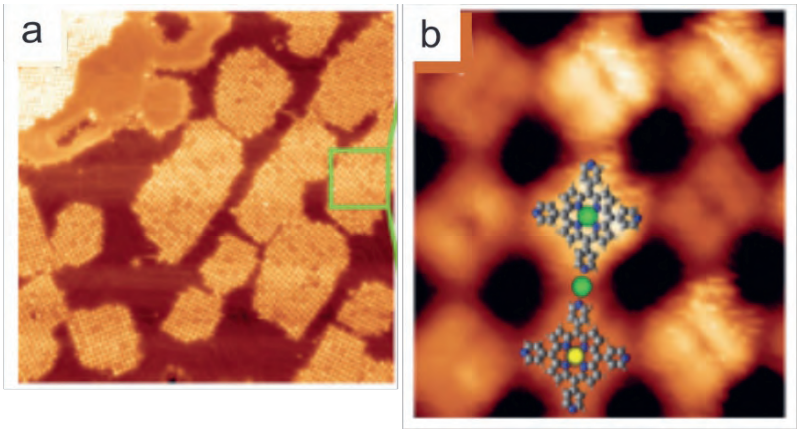

Figure 3.5. Self-assembly of H_2-TPyP on Ag(111) after annealing at 450 K. (a) Overview STM image of the close-packed MOCN formed by the deposition of H_2-TPyP followed by the addition of Cu-atoms. (b) Zoom-in STM image of the twofold MOCN, where a simple structural model (the carbon, nitrogen, hydrogen, cupper(0) and cupper(II) atoms are shown in gray, blue, white, green and yellow, respectively) was overlaid to highlight the metalation of the porphyrin core by Cu-atoms and coordination between neighboring molecules via a twofold Cu-coordination motif. Scanning parameters in: (a) (150 x 150 nm^2, U_{bias} = -1.31 V, I_{set} = 0.25 nA) and (b) (6.5 x 7 nm^2, U_{bias} = 1.21 V, I_{set} = 0.32 nA). Reprinted (adapted) with permission from (Y. Li, et al. Coordination and Metalation Bifunctionality of Cu with 5, 10, 15, 20-Tetra(4-pyridyl)porphyrin: Toward a Mixed-Valence Two-Dimensional Coordination Network. *J. Am. Chem. Soc*. **2012**, *134*, 6401-6408). Copyright (2012) American Chemical Society.

So far, the usage of porphyrins in the formation of 2D self-assembled networks on metal surfaces has been addressed. Furthermore, an adaptation from our previous publication on the role of cyano endgroups in the self-assembly of organic molecules on metal surfaces is given in the following section.

3.3 Role of Cyano Groups in the Self-Assembly of Organic Molecules on Metal Surfaces

A commonly accepted strategy to steer the molecular self-assembly process towards a desired structure on a surface is to tailor the molecular building blocks with certain functional endgroups that can engage in predefined bonding motifs having directionality and specific bonding strength. A frequently used functional endgroup towards this end is the cyano group (N≡C). Its negatively charged N-atom can interact through different bonding motifs with neighboring molecules. These are the weak interactions single H-bonding, H-bonding in a cyclic trimeric motif and antiparallel dipolar coupling and the substantially stronger interaction metal-ligand bonding.[28] From the mere number of interactions cyano groups can participate in together with the relative weak interaction strength for the first three motifs, it becomes obvious that the rational design of molecular networks as well as the formation of them on surfaces can be quite challenging.

Two prominent classes of molecules, namely porphyrin[16] and polyphenyl derivatives[29] substituted with cyano groups have been frequently studied for the formation of 2D supramolecular architectures. As previously mentioned in Section 3.2, porphyrins play vital roles in nature, but they also open the gap for the development of nanoscale electronic devices and applications such as dyes in solar cells or in catalysis. On the other hand, polyphenyls are linear molecular structures of varying length that are composed of a sequence of phenyl rings connected via single C-C bonds to which functional groups can be attached to at each end.

In the following, the influence of different cyano-substituted molecular building blocks is discussed for the formation of 2D assemblies merely stabilized by hydrogen bonding and dipolar coupling. Additionally, instructive examples for metal-ligand bonding are presented which also cover the effect of the type of metal-atom on the created molecular structures. In the last part the usage of cyano groups for controlling chirality on surfaces is detailed. The structural arrangement of the resulting self-assembled supramolecular architectures is depicted in detail by scanning tunneling microscope images. In addition, the usage of cyano groups for the formation of 2D networks on metal surfaces is presented in Chapters 4 and 5 of the present work.

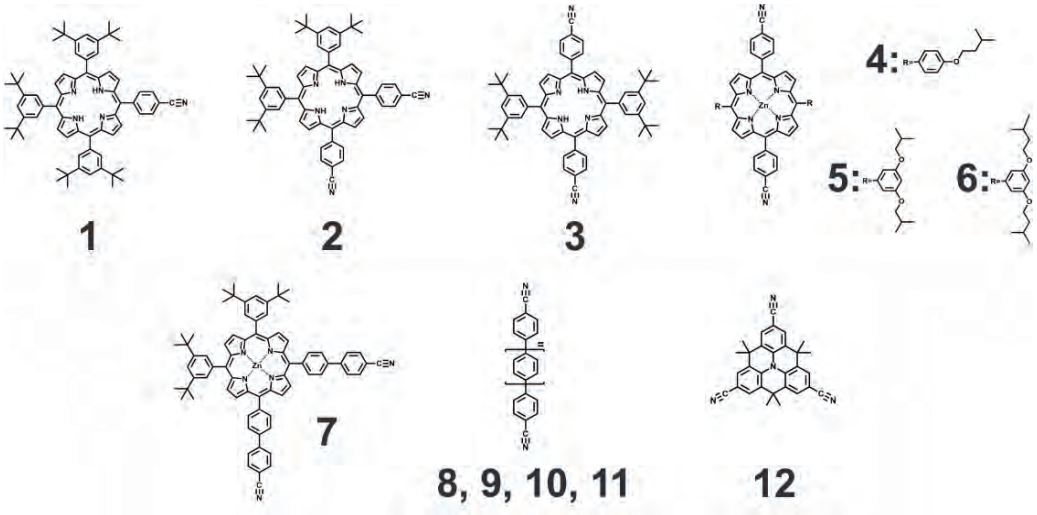

Figure 3.6. Summary of the chemical structures of each cyano-terminated molecule discussed in Chapter 3.3.[1]

3.3.1 Self-assemblies based on hydrogen bonding and dipolar coupling

Yokoyama et al. reported the directed self-assembly of surface-supported supramolecular structures for the first time by adequately choosing the functional endgroups –namely cyano groups–, which in turn control the non-covalent interactions of the structure.[30] In Figure 3.7a the scanning tunneling microscopy (STM) image of the self-assembly of *trans*-bis(cyanophenyl)-bis(di-tertiarybutylphenyl) porphyrin (molecule **3** in Figure 3.6) on Au(111) displays a linear arrangement in a supramolecular wire-like form stabilized by antiparallel dipolar coupling between the cyanophenyl substituents (Figure 3.7d). The bright lobes in Figure 3.7a correspond to the *tert*-butyl substituents, while the cyanophenyl substituents are found in the dimmer mid-region of the elongated structure. The maximum length of the supramolecular wire was reported to be slightly above 100 nm and the estimated length of the methine-cyano (CH…NC) contacts between neighboring cyanophenyl groups is of 2.6 Å, which in turn suggests the additional presence of hydrogen bonding interactions.

A very different scenario happens when this porphyrin derivative is deposited onto Cu(111), as observed in Figure 3.7b. An ordered two-dimensional porous network is arranged by windmill-like structures, each one consisting of six porphyrin molecules. Each windmill structure has a core in its center with a diameter of (18±1) Å, the cores extend throughout the network with a pore-pore distance of (32±1) Å.[31] The bright lobes belong to the *tert*-butyl substituents once again and each molecule **3** is shared among two windmill structures. Molecules **3** interact via hydrogen bonds arranged in the trimeric cyclic motif between the hydrogen atoms of the cyanophenyl

rings and the nitrogen atoms of the cyano endgroups as illustrated in Figure 3.7e. Comparison of the assembly structures from **3** on Au(111) and Cu(111) indicates that the substrate is a parameter that plays an essential role in the self-assembly of cyano-substituted molecules. In a similar case with the network from molecules **3**, a porphyrin derivative with cyanophenyl and alkoxyphenyl substituents at *trans meso* positions (molecule **6** in Figure 3.6) was deposited onto Cu(111) giving again rise to a nanoporous network (Figure 3.7c). The network exhibits a pore-pore distance of (48.0±1.4) Å (indicated by a yellow arrow in Figure 3.7c), which is significantly larger than the one for the network from molecules **3**. This is due to the alkoxyphenyl substituents which directly influence the interaction motif of the cyanophenyl groups: the trimeric motif is varied by replacing one cyanophenyl with an alkoxyphenyl group. In contrast to the previous nanoporous network (Figure 3.7b), where one porphyrin unit is shared among two pores, each pore is formed by six porphyrin units that are not shared among other pores. Subsequently, this increases the pore-pore distance.[32]

The structural model in Figure 3.7f illustrates the bonding motifs that stabilize this network. Basically, the cyanophenyl substituent acts as a hydrogen bond donor and acceptor. A trimeric bonding motif is formed (central region of the model) by the interaction of the cyano group from one of the cyanophenyl substituents via hydrogen bonding with the hydrogen of the *ortho* C-H moiety of one of the alkoxy substituents from another porphyrin. Analogously to this interaction, the same cyanophenyl group forms a hydrogen bond between the hydrogen of one of its nearest C-H moieties with the nitrogen of the cyanophenyl substituent of a neighboring porphyrin. Moreover, van der Waals interactions among two or three alkoxy chains of neighboring porphyrins provide further stabilization of the network.

Molecules **4** and **5** (Figure 3.6), which are substituted with different alkoxyphenyl groups compared to molecule **6**, also form nanoporous networks (STM images not shown) similar to the one of molecule **6**. The pore to pore distance increases from 30.9 to 33.5 Å for the network of molecules **4** and **5**, respectively. The pores of both networks are surrounded by alkoxy substituents from six different molecules and each molecule is shared among two pores. In comparison to the network of Figure 3.7c, a trimeric bonding motif involving three and not only two cyanophenyl groups stabilizes the networks of molecules **4** and **5**, only the intermolecular interaction is slightly modified. For molecule **4** the trimeric motif is given by the interaction between the cyano groups and the β-hydrogen atoms from three neighboring porphyrins. Meanwhile, the trimeric motif of molecule **5** is similar to the one for molecules **3** on Cu(111). The alkoxy groups in terms of size, amount and spatial orientation give access to control the dimensions of the porous networks, such as the pore-to-pore distance.[32]

As shown in Figure 3.7, porphyrin derivatives substituted by cyanophenyl groups at *trans meso* positions display different structural arrangements depending on the metallic substrate they are deposited onto. By either selecting a Au(111) or Cu(111) substrate different structural arrangements of the same molecule can be formed upon self-assembly. Furthermore, by carefully selecting the substituents (as in Figures 3.7b and c) the intramolecular interactions modify the self-assembly process and provide the formation of a myriad of two-dimensional networks.

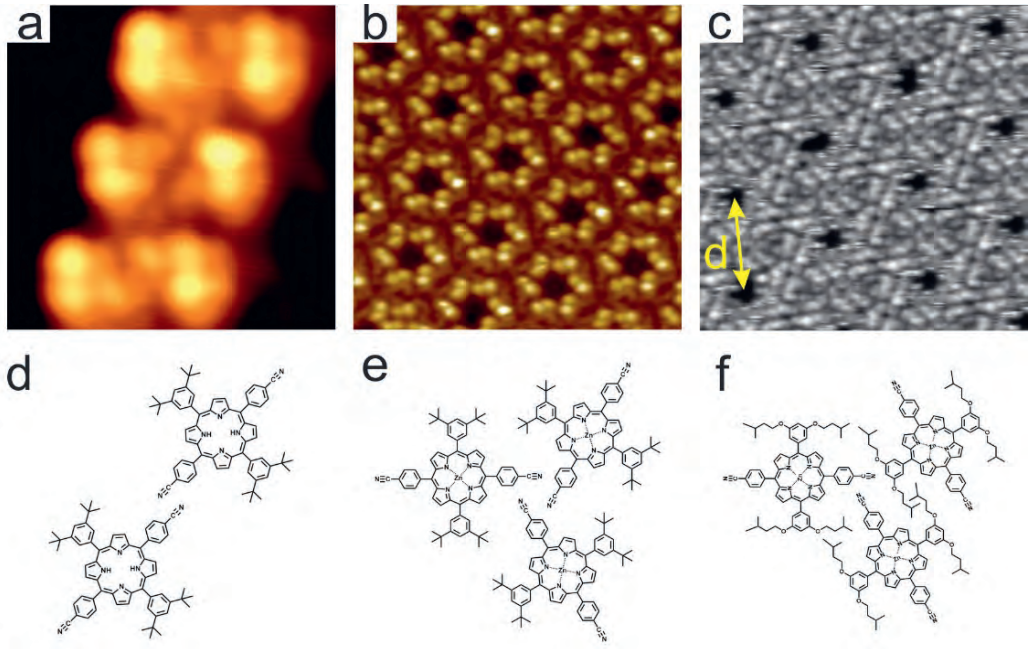

Figure 3.7. *Top:* STM images of the self-assembly of *trans*-cyano-substituted porphyrin derivatives. (a) Supramolecular aggregation in a wire-like form of molecule **3** on Au(111) (scan area = 5.3 x 5.3 nm^2). Nanoporous network of: (b) molecule **3** on Cu(111) (scan area = 12.5 x 12.5 nm^2) and (c) molecule **6** on Cu(111) (scan area = 15 x 15 nm^2). *Bottom* (d–f): Respective tentative structural models of each network displaying the bonding motifs involved.[30–32]

Varying the substitution pattern from *trans* to *cis* for molecule **3** gives rise to molecule **2** in (Figure 3.6), i.e. the cyanophenyl and di(tertbutyl)phenyl substituents are located at right angles, results in the formation of tetrameric units on Au(111) (Figure 3.8a).[30] The tetramers are stabilized via a combination of antiparallel dipolar coupling of the cyano groups and weak H-bonding between the cyano groups and the CH moieties of the cyanophenyl substituents from neighboring porphyrins. The H-bonding distance is approximately 2.6 Å, which is similar to the distance in the wire-like form in Figure 3.7a. Again, the bright lobes observed in the STM image correspond

to the *tert*-butyl substituents. In contrast, molecule **1** (Figure 3.6) has only one cyanophenyl substituent and is responsible for the formation of a cyclic configuration assembled in a trimeric structure (STM image not shown).

Molecule **7** (Figure 3.6) is obtained when replacing the cyanophenyl with a cyanobiphenyl group. Deposition of this molecule on Cu(111) resulted in the formation of cyclic oligomeric structures ranging from dimers up to hexamers.[33] This structural diversity is in contrast to the exclusive formation of tetramers from **3** on Au(111). The main reason was assigned to the change in substrate. The Cu(111) substrate is known to generally interact more strongly with organic molecules and thus, the interplay of intermolecular and molecule-substrate interactions is altered with the molecule-substrate interactions becoming more important for the final assembly structure. For the present case, the existence of the latter interactions can be seen by a closer inspection of the STM images displayed in Figures 3.8b)-d). The dark bending line originating from the saddle shape conformation of the porphyrin core leads to two conformational isomers labelled as type A and type B. For type A, the bending line separates the cyanobiphenyl from the di(*tert*-butyl)-phenyl substituents while for type B the bending line is parallel to the symmetry axis of the molecule. The bending line was for all molecules found to be parallel to a principal Cu direction, i.e., the rotational molecular arrangement dictates which types of intermolecular interactions can develop.

The trimer and tetramer shown in Figures 3.8b) and d), respectively, are (partly) held together by weak H-bonds between a hydrogen bonded to a sp^2-hybridized carbon atom and the nitrogen atom of the cyano group of an adjacent molecule. This bond is weaker than usual hydrogen bonds and lacks directionality. In turn this provides the possibility to adapt to different geometries. For the trimer (Figure 3.8b), always consisting of the same

conformational isomers, antiparallel CN-CN interactions accompanied by CN-HC H-bonds take place. The rectangular tetrameric structure (Figure 3.8c) assembled from alternating conformational isomers is similarly to the trimer stabilized by antiparallel CN-CN bonds and CN-HC H-bonds. Finally, the interaction involved in the all-type A (or B) tetramer is different and is based on non-directional H-bonding.

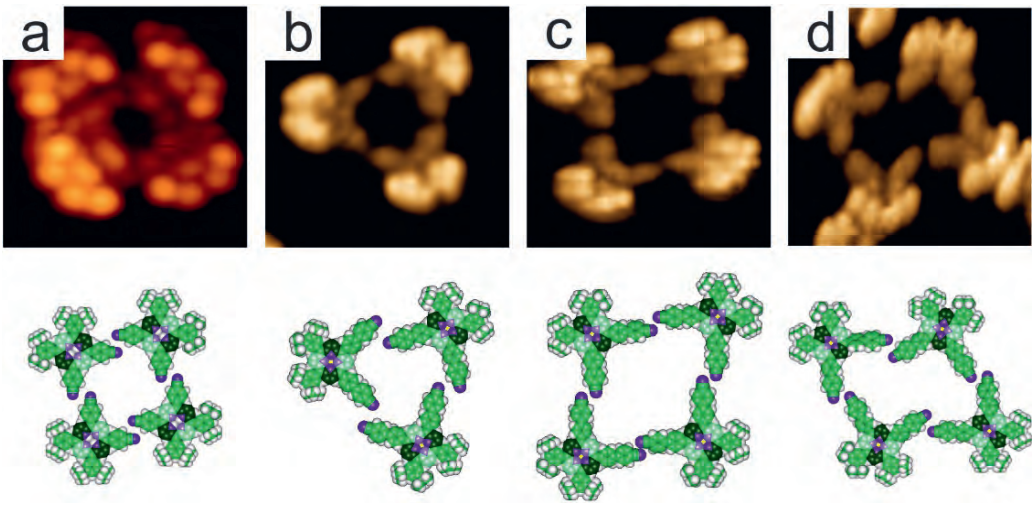

Figure 3.8. Top: STM images of the self-assembly of *cis*-cyano-substituted porphyrin derivatives. (a) Tetramer of molecule **2** on Au(111) (scan area = 5.3 x 5.3 nm^2).[30] Molecule **7** on Cu(111): (b) all-type A trimer (scan area = 6.3 x 6.3 nm^2), (c) tetramer formed by both conformational isomers (A and B) (scan area = 6.4 x 6.4 nm^2) and (d) all-type B tetramer (scan area = 6.2 x 6.2 nm^2).[33] *Bottom:* Respective tentative structural models of each arrangement displaying the bonding motifs involved.

The self-assembly of linear dicarbonitrile-polyphenyl molecules of varying length on Ag(111) has been intensively investigated by Barth and co-workers. The molecules employed have one cyano group attached to each end (NC-Ph_n-CN for n = 3, 4, 5 and 6) and correspond to molecules **8** to **11** from

Figure 3.6. The length of the rod-like molecules, which varies from 1.66 to 2.96 nm (N-N distance) for the molecules with n = 3, 4, 5 and 6, was found to influence their structural arrangement.[34,35]

A densely-packed arrangement of molecule **8** is depicted in the STM image of Figure 3.9a, the rod-like building blocks align in a V-shape manner or so-called chevron pattern. The overall alignment of the self-assembly clearly shows that the molecules lie in two directions parallel to the $[1\bar{1}0]$ and $[7\bar{3}\bar{4}]$ directions of the Ag substrate. In terms of bonding motifs, molecule **8** undergoes two types of interactions, N-N repulsive interactions from the cyano endgroups of neighboring molecules and an attractive one given by the cyano endgroups and H-atoms of the phenyl groups.[34] Later it was discovered that this type of interaction does not qualify for a classical H-bond and thus, was named PARI (proton acceptor-ring interaction).[36]

If one more phenyl ring is added to the central part of rod-like molecule **8** (molecule **9**, Figure 3.6), the self-assembly process creates an open rhombic network that comprises a fourfold chiral bonding motif (Figure 3.9b) leading to organizational chirality. Similarly to **8**, molecule **9** aligns along two Ag directions, namely the $[1\bar{1}0]$ and $[3\bar{5}8]$ direction and the molecular arrangement is suggested to be commensurate to the underlying Ag substrate. Due to the increased molecular length combined with the preference for parallel alignment along certain substrate directions, the formation of the chevron pattern is no longer possible. Thus, the molecular patterns are now stabilized by single H-bonds between the cyano groups and phenyl hydrogen atoms. This means the intermolecular interactions adapt to the dominant molecule-substrate interactions.[34]

The 2D kagomé lattice shown in Figure 3.9c forms when the even longer rod-like molecule **10** is deposited on Ag(111) (Figure 3.6). The nodes of the quasi-hexagonal structure connect four neighboring molecules and small triangular features surrounding each pore can be discerned. This structure is again chiral but much more complex compared to the other two previous ones. The hierarchical ordering levels that the subunits organize in the kagomé lattice, range from linear rod-like building blocks to triangular structures that interconnect in a hexagonal pattern. The terminal phenyl rings are rotated 20° with respect to the molecular axis. For such reason, the kagomé lattice does not lie completely flat on the Ag(111) surface, instead the fourfold nodes exhibit a non-planar geometry. In order to corroborate this assumption, X-ray absorption spectroscopy (XAS) measurements were carried out.[34]

Finally, molecule **11** (Figure 3.6) self-assembles into three kinds of two-dimensional structures as observed in the STM images shown in Figures 3.9d-f. For all three structures, there is a nodal binding motif that connects four molecular units together. The main interaction in between the molecules for all the different arrangements is given by hydrogen bonding in between the cyano groups and the hydrogen atoms from adjacent phenyl rings.[35] The rhombic phase (Figure 3.9e) and kagomé network (Figure 3.9f) are comparable to the ones obtained from **9** and **10** (Figures 3.9b and c), respectively. The main difference is the length of the molecular building block. By taking a closer look at the rhombic network (Figure 3.9e), two nodal configurations can be discerned, an open and a compact node. All three phases exhibit organizational chirality and are commensurate to the Ag surface. The H-N bond length in the kagomé lattice for **11** varies from 2.3 to 3.2 Å,[35] compared to the 1.5 Å reported for the kagomé lattice of molecule

10.[34] Summarizing, it can be stated for the self-assembly of cyano-substituted polyphenyls **8** – **11** on Ag(111) that the molecule-substrate interactions prevail and the flexibility of the cyano group to be involved in different intermolecular interactions (H-bonding, dipolar coupling, PARI) is the key for the formation of long-ranged well-ordered architectures.

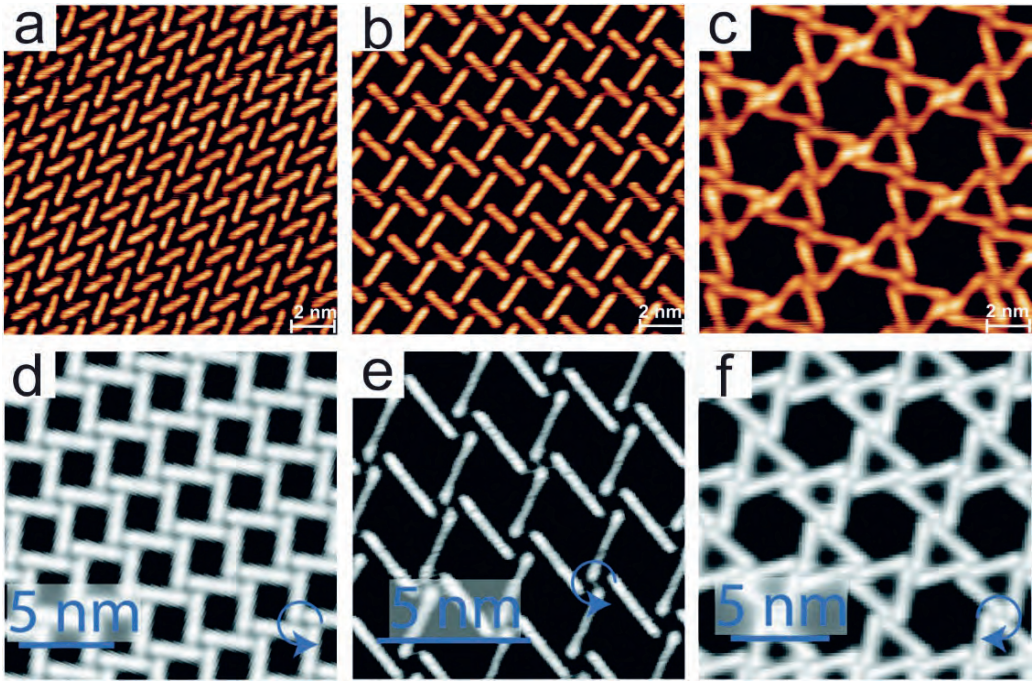

Figure 3.9. STM images of linear ditopic dicarbonitrile-polyphenyl molecules on Ag(111). *Top:* (a) Molecule **8** aligned in a densely-packed fashion, (b) molecule **9** assembled in an open rhombic network, and (c) molecule **10** arranged as a kagomé network.[34] *Bottom*: Assembly of molecule **11** in a (d) rectangular, (e) rhombic, and (f) kagomé network (scale bars are displayed within the images).[35]

3.3.2 Self-assemblies based on metal-ligand interactions

This section focuses on the self-assembly of 2D networks from cyano-substituted molecules stabilized by metal-ligand bonding. Depending on the

type of metallic atom, the coordination number, i.e. the number of ligands attached to the atom, can vary resulting in the formation of structurally different assemblies for the same molecular building block. The metal-ligand bonding can be induced either by deposition of metallic atoms onto a previously formed network of molecules or by generating – for example by annealing - native atoms that belong to the metallic substrate.

Figure 3.10 summarizes the various assembly structures observed for metal-coordinated networks from the rod-like polyphenyl derivatives **8** – **11** and different metal-atoms. As substrate, Ag(111) was used, except for the combination of **9** and Eu-atoms which was investigated on Au(111) (Figure 3.10f). The STM images of Figures 3.10a-d have a common 2D arrangement, a honeycomb nanomesh formed by metal-ligand bonding between Co-atoms and the cyano groups of molecules **8** – **11**, respectively. The Co-atoms are positioned at the nodes and coordinate to a total of three molecular units (Figure 3.10h). The electronegative nitrogen atom of the terminal cyano group interacts via metal-ligand bonding with the Co-atom (orange sphere). The Co-N bond length was reported to be 1.6 Å for the nanomeshes of molecules **8** - **10** and slightly increases to 1.9 Å for the network formed by molecule **11**. Density functional theory (DFT) calculations showed a strong hybridization between the Co-atom and the Ag surface suggesting that the Ag substrate takes the role of a fourth ligand.[37,38] The cavities of the nanomeshes vary in size according to the length of the employed rod-like molecule. For the network of molecule **8** (Figure 3.10a) the hexagonal cavity size is approximately 10 nm^2, meanwhile for molecule **9** through **11** it is 15, 20 and 23.7 nm^2, respectively.

Replacing the Co-atoms by Ce ones results in a change of the coordination number.[39] Now, exclusively a fivefold coordination is present

(Figures 3.10e, g). Barth and co-workers gradually varied the ratio between molecules **8** or **9** and Ce-atoms starting with 5:1. For this ratio, only individual pentameric units were formed. Increasing the ratio to 4:1 resulted in the formation of a hexagonal network composed of dodecameric units. In each of these units only 3 molecules are involved with both terminal cyano groups in metal-ligand bonding while the other 9 molecules are only singly coordinated. For a ratio of 5:2 (molecules:Ce) all terminal cyano groups are involved in metal-ligand bonding. Now a surface tessellation consisting of squares and triangles and corresponding to the semiregular Archimedean snub square tiling was formed. The Ce-N bond length for this network was only slightly different for molecules **9** (2.7 Å) compared to molecules **8** (2.4 Å). This indicates, since the linker length has only a marginal influence, that the assembly protocol should be of more general validity.

The metal-organic coordination networks described so far follow a certain degree of periodicity or long-range structural orientation. A completely different scenario happens for co-deposition of **9** and Eu-atoms on Au(111) (Figure 3.10f). In dependence of the ratio between molecules and Eu-atoms, the metal-organic coordination networks can even exhibit quasicrystallinity. This is only possible because molecules **9** and Eu-atoms can be involved in four-, five- and sixfold metal-ligand bonding, a prerequisite for the expression of quasicystallinity.[40]

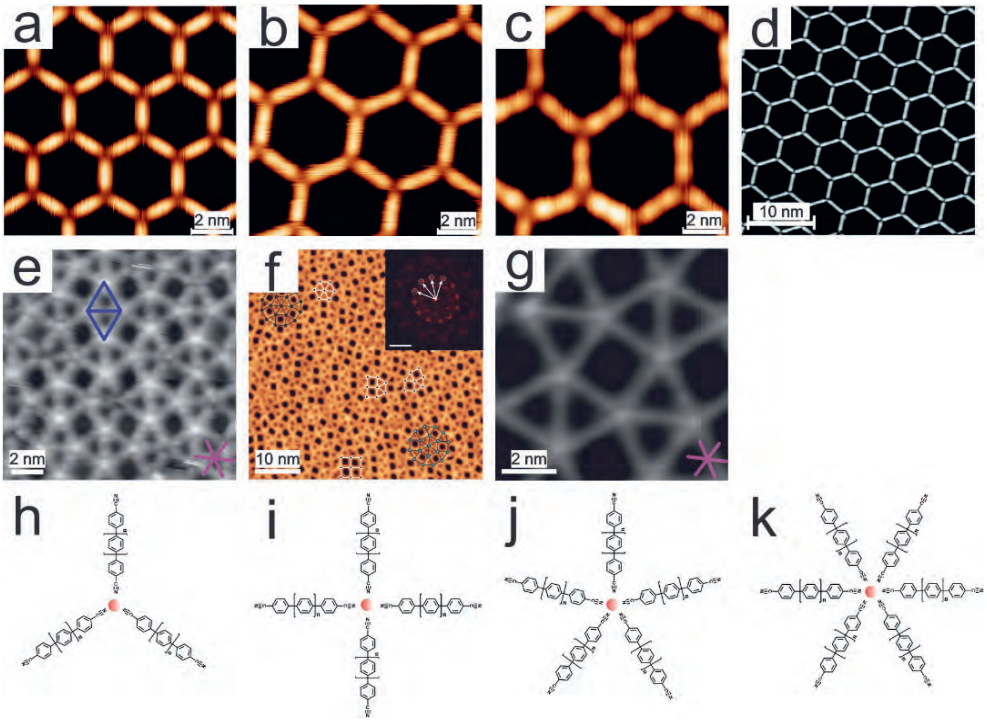

Figure 3.10. STM images of metal-coordinated organic networks from dicarbonitrile-polyphenyl molecules. Co-coordinated networks on Ag(111) from: (a) Molecule **8**, (b) molecule **9**, (c) molecule **10**,[37] and (d) molecule **11**.[38] Ce-coordinated networks on Ag(111) from: (e) molecule **8** and (g) molecule **9**.[39] (f) Eu-coordinated network on Au(111) from molecule **9**.[40] *Bottom:* Tentative structural models for the (h) three, (i) four, (j) five, and (k) sixfold coordination nodes.

For a cyano-functionalized triarylamine derivative (molecule **12**, Figure 3.11) the interplay between molecule-substrate and intermolecular interactions was studied in detail for their adsorption on the (111)-oriented coinage metal surfaces Ag, Au and Cu.[41] Figure 3.11 summarizes the assembly structures, which were observed with STM on the different surfaces, along with their structural models.

The self-assembly of **12** on Au(111) (Figure 3.11a) at a coverage of one monolayer (ML) generates a hexagonal close-packed network labeled as

phase α. The unit cell of phase α is highlighted with a green rhombus in the tentative structural model on the right of Figure 3.11a, with a size of 1.32 x 1.32 nm^2 and internal angle of 120°. Molecules **12** exhibit two different orientations rotated by 180° with respect to one another what enables their participation in three interaction motifs. These are antiparallel dipolar coupling given by the interaction between cyano groups from neighboring molecules that align parallel to each other (red oval in the structural model of Figure 3.11a), single H-bonding between the N-atom of the cyano group with a H-atom of a neighboring molecule (light blue oval in the structural model) and the trimeric motif governed by cyclic H-bonding (dark blue circle in the structural model). The herringbone reconstruction of the Au(111) surface was unaffected after molecular deposition. However, the molecular orientations were found to exhibit a correlation with the periodicity of the herringbone reconstruction.

For a coverage smaller than 1 ML, **12** formed two different phases on Au(111) both exhibiting organizational chirality (Figures 3.11b-c). Porous phase α (Figure 3.11b) is exclusively stabilized by dipolar coupling and the molecules are alternatingly rotated by 180°. The second one is the partial porous phase β (Figure 3.11c). The pores are arranged by six molecules coupled by dipolar interactions and they interact via metal-ligand bonding between one another (blue circle in the tentative model of Figure 3.11c). The metal-ligand bonding is given by one Au-atom coordinating with three cyano groups from different molecules. The unit cell size of phase β (3.77 x 3.77 nm^2 with an internal angle of 120°) is larger compared to the one of the close-packed phase α.[42]

By replacement of the substrate from Au(111) to Ag(111), a similar hexagonal close-packed pattern is formed for coverages ≤ 1ML of molecule

12 on Ag(111) (Figure 3.11d), i.e. only one type of assembly structure was observed. Almost all the molecules are oriented in one direction while only a very few are found that are rotated by 180° (black circles in the STM image in Figure 3.11d). The molecules (almost) exclusively interact via the trimeric H-bonding motif what is in contrast to situation on Au(111). The unit cell of this network is 1.32 x 1.32 nm^2 with an internal angle of 120°. These values overlap to those of the close-packed phase α on Au(111). Despite the very similar lattice constant for Ag(111) and Au(111), the influence of the substrate (with respect to the rotational adsorption position) is large enough to slightly modify the balance between molecule-substrate and intermolecular interactions. This results in the development of different phases on Au(111) because of the flexibility of the cyano group to be involved in different interaction motifs.

The deposition of a submonolayer of molecule **12** on Cu(111) (Figure 3.11e) forms a very distinct network in terms of packing and distribution of the molecules compared to the results shown for Au(111) and Ag(111). Only small islands were formed and also some disordered areas where molecules assemble in short-range rows and pores were observed. The disordered parts of the assembly are stabilized by dipolar coupling. Within the ordered close-packed islands (Figure 3.11e), the molecules are all aligned in one direction. But this time, they are involved in metal-ligand bonding occurring between the cyano groups and native Cu-atoms. The close-packed islands on Cu(111) have a unit cell (1.4 x 1.4 nm^2) larger than the one on Au(111) or Ag(111). Since the molecules point towards each other (different to the cases on Ag and Au) as revealed by the STM image, the repulsion between the electronegative N-atoms would not favor the formation of a network without Cu-atoms incorporated. The missing long-range order evident from the

disordered areas and the patches of close-packed structures is a sign for a relatively strong molecule-substrate interaction between **12** and Cu(111), also stronger compared to Au(111) and Ag(111). This can be associated with the lattice mismatch between the Cu(111) unit cell and the one of the regular hexagonal porous network.[41]

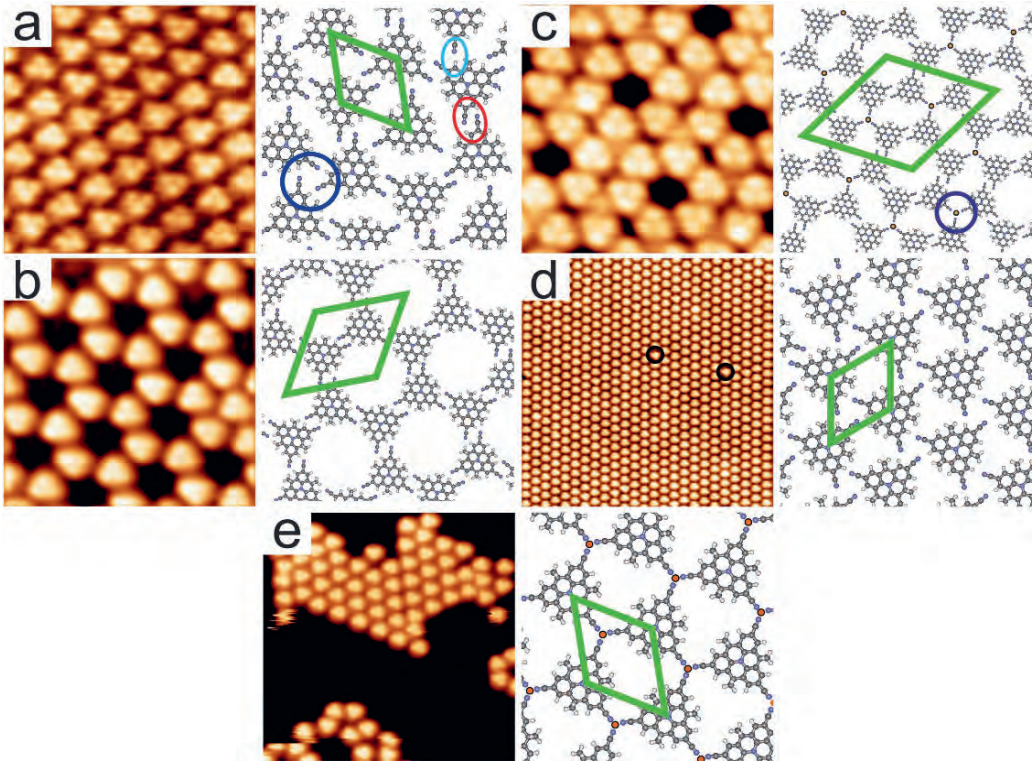

Figure 3.11. STM images of the self-assembly of molecule **12** on coinage metal substrates. Self-assembly on Au(111) (scan area = 7 x 7 nm^2): (a) close-packed phase α, (b) porous phase α, (c) phase β,[42] (d) close-packed arrangement on Ag(111) (scan area = 25 x 25 nm^2), and (e) close-packed islands on Cu(111) (scan area = 20 x 20 nm^2).[41] *Images on the right-hand of each STM image:* Tentative structural models for each network with the unit cells highlighted in green and the bonding motifs marked by circles and ovals.

The effect of annealing the sample at elevated temperatures was studied for the porphyrin derivative **7** on both Cu(111) and Au(111). For both substrates it is known that raising their temperature results in the creation of adatoms which can be involved in the formation of metal-organic coordination networks.

Annealing **7** adsorbed on Cu(111) above 150°C led to the formation of dimers (Figure 3.12a) while no other oligomeric structures were anymore observed. The cyanobiphenyl substituents flex towards each other forming a 60° angle between them and each cyanobiphenyl substituent bends by 15° (Figure 3.12d) to coordinate to one Cu-atom. The saddle-shape conformation of the porphyrin core caused by the strong interaction between Cu(111) and **12** together with the possibility of bending the single C-C bonds of the cyanobiphenyl substituents by around 5° allows the substituents to become closer.[33]

The self-assembly of molecule **7** on Au(111) after annealing at 160°C bears the formation of metal-coordinated 1D flexible polymeric chains (Figure 3.12b). Three cyanobiphenyl substituents from three molecules face each other and undergo metal-ligand bonding to a native Au-atom, thereby forming a threefold node. Compared to the dimer of Figure 3.12a, the coordination motif is now threefold instead of twofold. The 1D polymer is arranged by a set of threefold nodes as depicted in the structural model of Figure 3.12e. Similar to the dimers, the angle between the cyanobiphenyl substituents can deviate from 90° (it can be both larger and smaller). This confers a certain degree of flexibility to the polymer chains as it can be observed in the STM image of Figure 3.12b. By increasing the annealing temperature to 210°C a tetrameric bonding motif develops at the step edges of the Au(111) substrate (Figure 3.12c). The tetramers are stabilized by a

fourfold coordination motif between one native Au-atom and four cyano groups of four neighboring molecules **7** (Figure 3.12f). The *tert*-butyl groups of the porphyrins align directly along the step edge as revealed by the bright lobes in the STM image.[43]

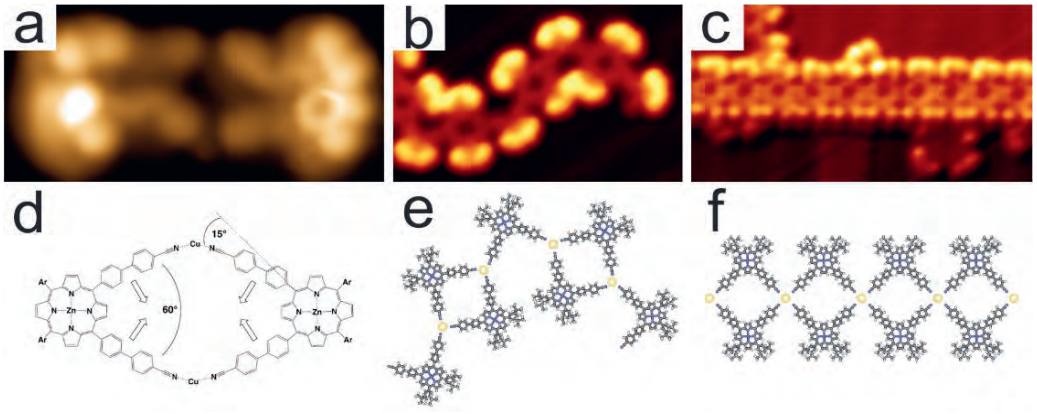

Figure 3.12. STM images of the self-assembly of molecule **7** at different experimental conditions. (a) Self-assembled dimer structure coordinated by native Cu-atoms on Cu (111) after annealing at 150 °C (scan area = 5.7 x 2.7 nm^2),[33] (b) metal-coordinated 1D molecular chain on Au(111) after annealing at 160 °C (scan area = 16 x 10 nm^2), and (c) 1D molecular chain formed upon annealing at 210 °C on Au(111) (scan area = 25 x 12.4 nm^2).[43] *Bottom* (d–f): Tentative structural models for each molecular arrangement shown in (a–c), respectively.

3.4 Conclusions

In summary, we have described the fundamental aspects involved in the self-assembly of organic molecules on coinage metal surfaces, where the different energetic contributions required for the formation of 2D networks were addressed. Furthermore, an introduction to the work that has been published for the usage of porphyrins as molecular building blocks in 2D networks and 2D MOCNs was presented and exemplified with STM images. Finally, the self-assembly of cyano-functionalized molecules on coinage metal surfaces under the modification of parameters such as the substrate and molecular coverage was discussed. The variety of bonding motifs cyano groups participate with was illustrated by STM images. For instance, polyphenyl derivatives substituted with cyano groups formed densely-packed arrangements by H-bonding and by deposition of Co-atoms porous-networks stabilized by metal-ligand bonding were formed. Similarly, the influence of the molecule-substrate interaction on the resulting assembly structure was illustrated on the basis of a porphyrin derivative, where dipolar coupling and trimeric bonding motifs were observed on Au(111) and Cu(111). On the basis of the presented examples, it becomes clear that cyano-functionalized molecules can undergo a variety of different intermolecular interactions having diverse geometries. Thus, using cyano groups for steering the self-assembly process towards the formation of a specific and predictable supramolecular arrangement can be a challenging endeavor. The reason is that the cyano groups are mainly involved in weak interactions having similar bonding strengths, the exception is metal-ligand bonding. In addition to these weak cyano interactions, molecule-substrate interactions as well as further intermolecular interactions resulting from other functional groups attached to

the molecule have to be considered. In order to properly make use of a particular cyano interaction motif for designing supramolecular architectures, all other competing factors have to be carefully evaluated beforehand. Competing factors are the influence of the substrate, molecular coverage, temperature, size and shape of the molecule and if the molecule has further substituents. On the other hand, the flexibility of the cyano group to be involved in different interaction motifs may ensure adaptation of the system to changing environments or external parameters. It is very likely that the system will keep its long-range order based on another cyano interaction motif instead of disintegrating itself.

3.5 References

1. Baker Cortés, B. D.; Stöhr, M. Role of Cyano Groups in the Self-Assembly of Organic Molecules on Metal Surfaces. In *Encyclopedia of Interfacial Chemistry*; Wandelt, K., Ed.; Elsevier, **2018**; *Vol. 4*, pp 153–165.
2. Lehn, J.-M. Supramolecular Chemistry: Receptors, Catalysts, and Carriers. *Science*, **1975**, *227*, 849–856.
3. Lehn, J.-M. Supramolecular Chemistry. *Proc. Indian Acad. Sci. (Chem. Sci)*, **1994**, *106*, 915–922.
4. Whitesides, G. M.; Mathias, J. P. Seto, C. T. Molecular Self-Assembly and Nanochemistry: A Chemical Strategy for the Synthesis of Nanostructures. *Science* **1991**, *254*, 1312–1319.
5. Gutzler, R.; Stepanow, S.; Grumelli, D.; Lingenfelder, M.; Kern, K. Mimicking Enzymatic Active Sites on Surfaces for Energy Conversion Chemistry. *Acc. Chem. Res*. **2015**, *48*, 2132–2139.
6. Barth, J. V. Molecular Architectonic on Metal Surfaces. *Annu. Rev. Phys. Chem*. **2007**, *58*, 375–407.
7. Stepanow, S.; Lin, N.; Barth, J. V. Modular Assembly of Low-Dimensional coordination architectures on metal surfaces. *J. Phys.: Condens. Matter* **2008**, *20*, 184002.
8. Dong, L.; Gao, Z. A.; Lin, N. Self-Assembly of Metal-Organic Coordination Structure on Surfaces. *Prog. Surf. Sci.* **2016**, *91*, 101–135.
9. Kuang, G.; Zhang, Q.; Lin. T.; Shi, X.; Xu, H.; Lin, N. Mechanically-Controlled Reversible Spin Crossover of Single Fe-Porphyrin Molecules. *ACS Nano* **2017**, *11*, 6295–6300.
10. Moreno Pineda, E.; Komeda, T.; Katoh, K.; Yamashita, M.; Ruben, M. Surface Confinement of $TbPc_2$-SMMs: Structural, Electronic and Magnetic Properties. *Dalton Trans*. **2016**, *45*, 18417–18433.
11. Ishikawa, N.; Sugita, M.; Ishikawa, T.; Koshihara, S.-Y., Kaizu, Y. Lanthanide Double-Decker Complexes Functioning as Magnets at the Single-Molecular Level. *J. Am. Chem. Soc*. **2003**, *125*, 8694–8695.
12. Sosa-Vargas, L.; Kim, E.; Attias, A.-J. Beyond ‘‘Decorative’’ 2D Supramolecular Self-Assembly: Strategies Towards Functional Surfaces for Nanotechnology. *Mater. Horiz*. **2017**, *4*, 570.
13. Barth, J. V.; Constantini, G.; Kern, K. Engineering Atomic and Molecular Nanostructures at Surfaces. *Nature* **2005**, *437*, 671–679.
14. Kühnle, A. Self-Assembly of Organic Molecules at Metal Surfaces. *Curr. Opin. Colloid Interface Sci*. **2009**, *14*, 157–168.

15. Gottfried, J. M. Surface Chemistry of Porphyrins and Phthalocyanines. *Surf. Sci. Rep*. **2015**, *70*, 259–379.
16. Auwärter, W.; Écija, D.; Klappenberger, F.; Barth, J. V. Porphyrins at Interfaces. *Nat. Chem*. **2015**, *7*, 105–120.
17. Auwärter, W.; Seufert, K.; Klappenberger, F.; Reichert, J.; Weber-Bargioni, A.; Verdini, A.; Cvetko, D.; Dell'Angela, M.; Floreano, L.; Cossaro, A.; et al. Site-Specific Electronic and Geometric Interface Structure of Co-Tetraphenyl-Porphyrin Layers on Ag(111). *Phys. Rev. B: Condens. Matter Mater. Phys*. **2010**, *81*, 245403.
18. Marbach, H. Surface-Mediated *in Situ* Metalation of Porphyrins at the Solid−Vacuum Interface. *Acc. Chem. Res*. **2015**, *48*, 2649–2658.
19. Diller, K.; Papageorgiou, A. C.; Klappenberger, F.; Allegretti, F.; Barth, J. V.; Auwärter. W. *In vacuo* interfacial tetrapyrrole metallation. *Chem. Soc. Rev*. **2016**, *45*, 1629.
20. Auwärter. W.; Weber-Bargioni, A.; Brink, S.; Riemann, A.; Schiffrin, A.; Ruben, M.; Barth, J. V. Controlled Metalation of Self-Assembled. *ChempPhysChem* **2007**, *8*, 250–254.
21. Doyle. Ni–Cu Ion Exchange Observed for Ni(II)-porphyrins on Cu(111). *Chem. Commun.* **2014**, *50*, 3447–3449.
22. Rieger, A.; Schnidrig, S.; Probst, B.; Ernst, K. H.; Wäckerlin, C. Ranking the Stability of Transition-Metal Complexes by On-Surface Atom Exchange. *J. Phys. Chem. Lett.* **2017**, *8*, 6193–6198.
23. Shen, K.; Narsu, B.; Ji, G.; Sun, H.; Hu, J.; Liang, Z.; Gao, X.; Li, H.; Li, Z.; Song, B.; et al. On-Surface Manipulation of Atom Substitution Between Cobalt Phthalocyanine and the Cu(111) Substrate. *RSC Advances*. **2017**, *7*, 13827–13835.
24. Furukawa, H.; Cordova, K. E.; O'Keeffe, M.; Yaghi, O. M. The Chemistry and Applications of Metal-Organic Frameworks. *Science* **2013**, *341*, 1230444.
25. Li, H.; Eddaoudi, M.; O'Keeffe, M.; Yaghi, O. M. Design and Synthesis of an Exceptionally Stable and Highly Porous Metal-Organic Framework. *Nature* **1999**, *402*, 276–279.
26. Li, Y.; Xiao, J.; Shubina, T. E.; Chen, M.; Shi, Z.; Schmid, M.; Steinrück, H.-P.; Gottfried, J. M.; N. Lin. Coordination and Metalation Bifunctionality of Cu with 5,10,15,20-Tetra(4-pyridyl)porphyrin: Toward a Mixed-Valence Two-Dimensional Coordination Network *J. Am. Chem. Soc.* **2012**, *134*, 6401–6408.

27. Baker Cortés B. D.; Schmidt, N.; Enache, M.; Stöhr, M. Coverage-Dependent Structural Transformation of Cyano-Functionalized Porphyrin Networks on Au(111) via Addition of Cobalt Atoms. *J. Phys. Chem. C* **2019**, *123*, 19681–19687.
28. Maly, K. E.; Maris, T.; Gagnon, E.; Wuest, J. D. Inclusion Compounds of Hexakis(4-cyanophenyl)benzene: Open Networks Maintained by C–HdN Interactions. *J. Am. Chem. Soc.* **2006**, *6*, 461–466.
29. Klyatskaya, S.; Klappenberger, F.; Schlickum, U.; Kühne, D.; Marschall, M.; Reichert, J.; Decker, R.; Krenner, W.; Zoppellaro, G.; Brune, H.; Barth, J. V.; Ruben, M. Surface-Confined Self-Assembly of Di-Carbonitrile Polyphenyls. *Adv. Funct. Mater.* **2011**, *21*, 1230–1240.
30. Yokoyama, T.; Yokoyama, S.; Kamikado, T.; Okuno, Y.; Mashiko, S. Selective Assembly on a Surface of Supramolecular Aggregates with Controlled Size and Shape. *Nature* **2001**, *413*, 619–621.
31. Wintjes, N.; Bonifazi, D.; Cheng, F.; Kiebele, A.; Stöhr, M.; Jung, T.; Spillmann, H.; Diederich, F. A Supramolecular Multiposition Rotary Device. *Angew. Chem. Int. Ed*. **2007**, *46*, 4089–4092.
32. Wintjes, N.; Hornung, J.; Lobo-Checa, J.; Voigt, T.; Samuely, T.; Thilgen, C.; Stöhr, M.; Diederich, F.; Jung, T. A. Supramolecular Synthons on Surfaces: Controlling Dimensionality and Periodicity of Tetraarylporphyrin Assemblies by the Interplay of Cyano and Alkoxy Substituents. *Chem. Eur. J*. **2008**, *14*, 5794–5802.
33. Fendt, L.; Stöhr, M.; Wintjes, N.; Enache, M.; Jung, T.; Diederich, F. Modification of Supramolecular Binding Motifs Induced by Substrate Registry: Formation of Self-Assembled Macrocycles and Chain-Like Patterns. *Chem. Eur. J*. **2009**, *15*, 11139–11150.
34. Schlickum, U.; Decker, R.; Klappenberger, F.; Zoppellaro, G.; Klyatskaya, S.; Auwärter, W.; Neppl, S.; Kern, K.; Brune, H.; Ruben, M.; Barth, J. Chiral Kagomé Lattice from Simple Ditopic Molecular Bricks. *J. Am. Chem. Soc*. **2008**, *130*, 11778–11782.
35. Kühne, D.; Klappenberger, F.; Decker, R.; Schlickum, U.; Brune, H.; Klyatskaya, S.; Ruben, M.; Barth, J. V. Self-Assembly of Nanoporous Chiral Networks With Varying Symmetry From Sexiphenyl-Dicarbonitrile on Ag(111). *J. Phys. Chem. C* **2009**, *113*, 17851–17859.
36. Arras, E.; Seitsonen, A. P.; Klappenberger, F.; Barth, J. V. Nature of the Attractive Interaction Between Proton Acceptors and Organic Ring Systems. *Phys. Chem. Chem. Phys.* **2012**, *14*, 15995–16001.

37. Schlickum, U.; Decker, R.; Klappenberger, F.; Zoppellaro, G.; Klyatskaya, S.; Ruben, M.; Silanes, I.; Arnau, A.; Kern, K.; Brune, H.; Barth, J. V. Metal–Organic Honeycomb Nanomeshes With Tunable Cavity Size. *Nano Lett.* **2007**, *7*, 3812–3817.
38. Kühne, D.; Klappenberger, F.; Decker, R.; Schlickum, U.; Brune, H.; Klyatskaya, S.; Ruben, M.; Barth, J. V. High-Quality 2D Metal–Organic Coordination Network Providing Giant Cavities Within Mesoscale Domains. *J. Am. Chem. Soc.* **2009**, *131*, 3881–3883.
39. Écija, D.; Urgel, J.; Papageorgiou, A. C.; Joshi, S.; Auwärter, W.; Seitsonen, A. P.; Klyatskaya, S.; Ruben, M.; Fischer, S.; Vijayaraghavan, S.; Reichert, J.; Barth, J. V. Five Vertex Archimedean Surface Tessellation by Lanthanide-Directed Molecular Self-Assembly. *Proc. Natl. Acad. Sci. U. S. A*. **2013**, *110*, 6678–6681.
40. Urgel, J. I.; Écija, D.; Lyu, G.; Zhang, R.; Palma, C. A.; Auwärter, W.; Lin, N.; Barth, J. V. Quasicrystallinity Expressed in Two-Dimensional Coordination Networks. *Nat. Chem*. **2016**, *8*, 657–662.
41. Müller, K.; Moreno-López, J. C.; Gottardi, S.; Meinhardt, U.; Yildirim, H.; Kara, A.; Kivala, M.; Stöhr, M. Cyano-Functionalized Triarylamines on Coinage Metal Surfaces: Interplay of Intermolecular and Molecule–Substrate Interactions. *Chem. Eur. J.* **2016**, *22*, 581–589.
42. Gottardi, S., Müller, K., Moreno-López, J. C., Yildirim, H., Meinhardt, U., Kivala, M., Kara, A., Stöhr, M. Cyano-Functionalized Triarylamines on Au(111): Competing Intermolecular Versus Molecule/Substrate Interactions. *Adv. Mater. Interfaces* **2014**, *1*, 1300025.
43. Pham, T. A.; Song, F.; Alberti, M. N.; Nguyen, M. T.; Trapp, N.; Thilgen, C.; Diederich, F.; Stöhr, M. Heat-Induced Formation of One-Dimensional Coordination Polymers on Au(111): An STM Study. *Chem. Commun.* **2015**, *51*, 14473–14476.


Chapter 4

4 Coverage-Dependent Structural Transformation of Cyano-Functionalized Porphyrin Networks on Au(111) via Addition of Cobalt Atoms[2]

The self-assembly process of a cobalt-porphyrin derivative (Co-TCNPP) containing cyanophenyl substituents at all four meso positions on Au(111) was studied by means of scanning tunneling microscopy (STM) and low energy electron diffraction (LEED) under ultra-high vacuum conditions (UHV). Deposition of Co-TCNPP onto Au(111) gave rise to the formation of a close-packed H-bonded network, which was independent of coverage as revealed by STM and LEED. However, a coverage-dependent structural transformation took place upon the deposition of Co-atoms. At monolayer coverage, a reticulated long-range ordered network exhibiting a distinct fourfold Co coordination was observed. By reduction of the molecular coverage, a second metal−organic coordination network (MOCN) was formed in coexistence with the fourfold Co-coordinated network, that is, a chevron structure stabilized by a simultaneous expression of H-bonding and threefold Co coordination. We attribute the coverage-dependent structural transformation to the in-plane compression pressure exerted by the molecules deposited on the surface. Our study shows that a subtle interplay between the chemical nature of the building blocks (molecules and metallic atoms) and

[2] The results presented in this chapter have been published as Baker Cortés B. D.; Schmidt, N.; Enache, M.; Stöhr, M. Coverage-Dependent Structural Transformation of Cyano-Functionalized Porphyrin Networks on Au(111) via Addition of Cobalt Atoms. *J. Phys. Chem. C* **2019**, *123*, 19681–19687.

molecular coverage can steer the formation of structurally different porphyrin-based MOCNs.

4.1 Introduction

The possibility of fabricating metal–organic frameworks (MOFs) in three-dimensions (3D) possessing remarkable functional properties – also in view of applications – by applying concepts of supramolecular chemistry has eventually granted protocols for the construction of low-dimensional nanoarchitectures on surfaces.[1,2] That is, two-dimensional (2D) metal-organic coordination networks (MOCNs) on surfaces have been realized by means of self-assembly and possess promising applications in gas storage, catalysis and energy conversion chemistry.[3–6] The formation of structurally different MOCNs can be achieved by carefully selecting the organic building blocks and metallic species to which they coordinate to.[7–9] Especially, porphyrins have been shown to be stable and versatile building blocks for the construction of MOCNs displaying different coordination geometries, as their backbone can be tailored with specific functional endgroups.[10–13] Despite the extensive literature available for MOCNs on surfaces, there are only a few studies focused on the influence of molecular coverage on the self-assembly of such structures upon varying the molecule-metal ratio.[14,15] This is in contrast to the abundance of reports discussing coverage-dependent phenomena for low-dimensional purely organic arrangements on surfaces.[16–21] Similar to these findings, the in-plane compression pressure built by the molecules on the surface, which increases with molecular coverage, is expected to result in changes of the MOCNs with respect to its structure, molecular conformation and/or coordination environment.

Herein we present a study of the influence of molecular coverage on the self-assembly process of cobalt(II) 5,10,15,20-(tetra-4-cyanophenyl)porphyrin (Co-TCNPP) before and after coordination with Co-atoms on Au(111) by means of scanning tunneling microscopy (STM) and low energy electron diffraction (LEED). Co-TCNPP, as shown in Figure 4.1, is a tetrapyrrolic macrocycle functionalized at all four meso positions by cyanophenyl substituents, with each cyano endgroup pointing outwards and its core contains a Co-atom. The STM and LEED measurements showed that deposition of Co-TCNPP on Au(111) gave rise to a long-range ordered close-packed H-bonded network that is invariant to changes of in-plane compression pressure exerted by molecular coverage. After deposition of Co-atoms with a fixed molecule to metal ratio (~1:1 with a slight excess of metal), a coverage-dependent structural transformation took place that modified the coordination geometry of the Co-atoms located at the coordination nodes. At monolayer coverage, the formation of a distinct long-range ordered fourfold MOCN was observed in which the Co-atoms adopted a rare square planar coordination geometry. Upon decreasing the molecular coverage of Co-TCNPP and keeping the stoichiometric ratio between molecules and metal-atoms constant, a second MOCN formed in coexistence with the fourfold MOCN, i.e., a chevron structure stabilized by a simultaneous expression of H-bonding and threefold metal-coordination. In such structure, the Co-atoms arranged in a distorted tetrahedral coordination geometry. Based on the premise of in-plane compression pressure built from the molecules on the surface, the subtle balance between the cyanophenyl-substituents and molecular coverage makes the self-assembly of this porphyrin-based MOCN an interesting alternative to investigate the adsorption behavior of structurally different MOCNs on metal surfaces. To the best of our knowledge, we present

the first coverage-dependent long-range ordered porphyrin-based MOCN on a bare metal surface, while keeping the molecule-metal atom ratio constant.

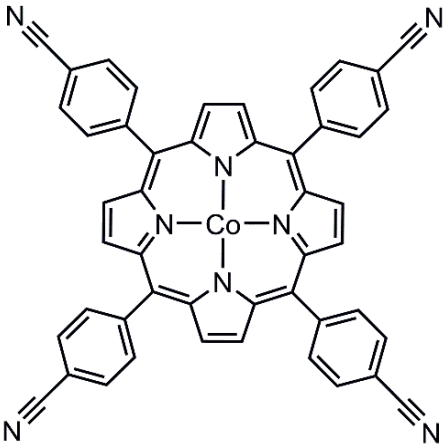

Figure 4.1. Chemical structure of cobalt(II) 5,10,15,20-(tetra-4-cyanophenyl)porphyrin (Co-TCNPP).

4.2 Experimental Methods

All experiments were carried out in an ultra-high vacuum (UHV) system (with a base pressure in the low 10^{-10} mbar regime) equipped with different chambers for sample preparation and characterization. The Au(111) single crystal was cleaned by repeated cycles of Ar^+ sputtering and annealing at 720 K. The porphyrin derivatives (PorphyChem) were thermally sublimed at 820 K onto the Au(111) surface held at room temperature (RT) by means of a Knudsen cell evaporator (OmniVac). Cobalt-atoms were deposited onto the organic layer from a cobalt rod using an e-beam evaporator (Oxford Applied Research). During metal deposition the substrate was held at 410 K. For comparison, the deposition of Co-atoms was also performed at RT (Figure 4.5). The molecule-metal ratio was kept fixed (~1:1 with a slight excess of metal). A quartz crystal microbalance was used to monitor the molecule and

metal-atom deposition rates. STM measurements were conducted with a commercial low-temperature STM (Scienta Omicron GmbH) operated at RT with a mechanically cut Pt/Ir wire as a tip in constant current mode. All bias voltages are given with respect to a grounded tip. The STM images were processed with WSxM software.[22] In addition, the LEED patterns were acquired using a microchannel plate LEED (Scienta Omicron GmbH) and simulated with the LEEDPat4.2 software.[23]

4.3 Results

Co-TCNPP on Au(111)

The deposition of a monolayer of Co-TCNPP on Au(111) held at RT gave rise to a close-packed network displaying the long-range order as evidenced in the overview STM image of Figure 4.2a. The molecules arranged in a square-like fashion. The high-resolution STM image in Figure 4.2b unveils in detail the molecular appearance of Co-TCNPP and its orientation with respect to neighboring porphyrin units. Individual porphyrins (highlighted in yellow) can be distinguished by four bright lobes attributed to the peripheral phenyl moieties. Such an appearance is typical for phenyl-substituted porphyrins on metallic substrates.[24–27] It should be noted that the cyano endgroups did not contribute to the STM contrast.[28,29] The metallic center in the porphyrin core is not visible in the STM image under the given tunneling conditions.[24–26,30,31] Furthermore, the varying brightness between consecutive molecules is induced by the underlying herringbone reconstruction of the Au substrate, which was well preserved underneath the molecular layer (Figure 4.3a). Based on our STM and LEED measurements, we propose a square unit cell (depicted in green in Figure 4.2b) with lengths

$a = b = 1.68 \pm 0.05$ nm and an internal angle of $\alpha = 90° \pm 2°$. The molecular density for this arrangement is equal to 0.35 Co-TCNPP molecules per nm^2. Moreover, our STM and LEED measurements (Appendix Figure A4.1) suggest that the unit cell (cf. dotted green line in Figure 4.2c) is rotated 7.5° with respect to the principal Au directions. The incommensurability of the close-packed network with the underlying Au substrate was confirmed by the absence of integer matrix elements in the superstructure matrix of the simulated LEED pattern (Appendix Figure A4.1). This adsorption behavior might be induced when the molecule-molecule interactions outweigh over site-specific interactions with the substrate.[32,33]

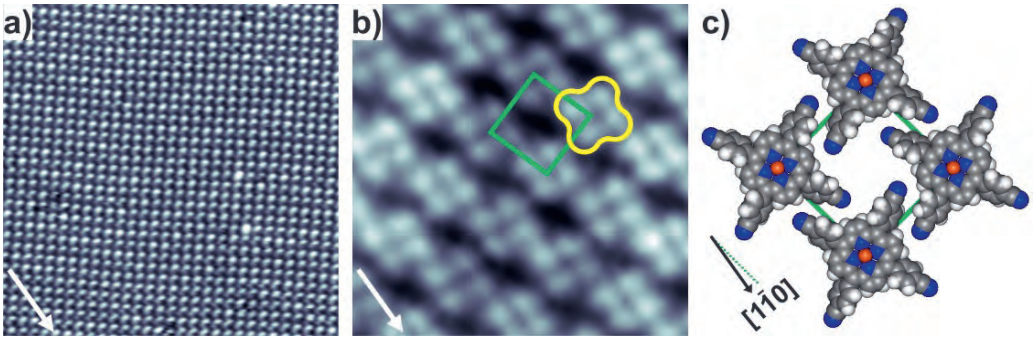

Figure 4.2. Self-assembly of the close-packed H-bonded network of Co-TCNPP on Au(111). (a) Overview STM image showing the long-range order of the 2D network stabilized by H-bonding (50 x 50 nm^2, U_{bias} = 1.6 V, I_{set} = 20 pA). (b) High-resolution STM image in which the phenyl moieties of the macrocycle are discernible (7.5 x 7.5 nm^2, U_{bias} = 2 V, I_{set} = 15 pA). The yellow outline and green square highlight one porphyrin and the unit cell, respectively. (c) Tentative structural model of the H-bonded close-packed network. Cobalt, nitrogen, carbon and hydrogen atoms are shown in orange, blue, gray and white, respectively. The unit cell of the network is shown in green. In (c) the dotted green line is parallel to a unit cell direction and the black arrow indicates a principal direction of the Au substrate. In (a) and (b) the white arrow at the bottom denotes a principal crystallographic direction of the Au substrate.

In addition to the molecular appearance (Figure 4.2b), the lateral molecular orientation with respect to neighboring porphyrin units can also be discerned. The corresponding tentative structural model is depicted in Figure 4.2c. The molecules are rotated 19° with respect to the unit cell axis (shown in green) and align their cyanophenyl substituents towards the pyrrole moieties of neighboring Co-TCNPP units. Such a configuration allows the formation of a H-bond between the electronegative N-atom of the terminal cyano endgroup and a hydrogen bonded to a sp^2-hybridized carbon atom from a pyrrole moiety of an adjacent molecule. The projected H–N distance is

approximately 3.2 Å and falls within typical H-bond distances (1.5-3.5 Å).[4,14] The Co-TCNPP molecules also assembled into the aforementioned close-packed H-bonded network at submonolayer coverage (Figure 4.3b). Such an arrangement is similar to the previously reported 2D assembly of a free-base tetracyanophenyl porphyrin (2H-TCNPP) on Ag(111).[26]

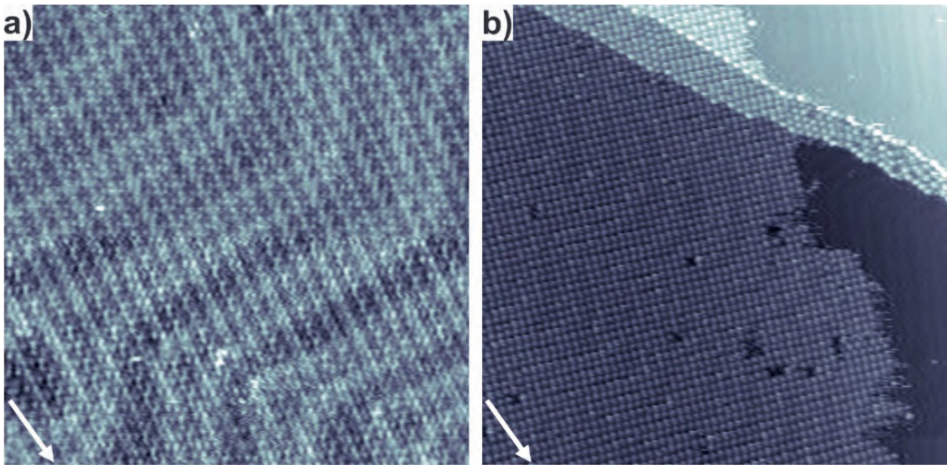

Figure 4.3. STM images of the self-assembly of Co-TCNPP on Au(111). (a) STM image displaying the herringbone reconstruction of Au(111) well preserved underneath the molecular layer (40 x 40 nm^2, U_{bias} = -1.9 V, I_{set} = 20 pA). (b) Overview STM image of (100 x 100 nm^2, U_{bias} = -1.6 V, I_{set} = 20 pA). The long-range order of the close-packed H-bonded network prevails at submonolayer coverage. In (a) and (b) the white arrow at the bottom denotes a principal crystallographic direction of the Au substrate.

Co-TCNPP on Au(111) After Co-coordination – Monolayer case

The deposition of the required amount of Co-TCNPP followed by addition of Co-atoms (while keeping the substrate at 410 K) for a full monolayer of fourfold MOCN (maintaining a fixed ~1:1 molecule-metal ratio with a slight excess of metal) gave rise to a well-ordered 2D network as shown in the overview STM image of Figure 4.4a. The molecules arranged into a network displaying a grid-like appearance. The herringbone reconstruction of the Au(111) surface translates through the molecular layer, similar to the observations described for the close-packed H-bonded network (see Figures 4.2b and 4.3). The long-range order of the network with domains that extend over >100 nanometers is supported by LEED measurements (Appendix Figure A4.2). Nonetheless, domain boundaries stabilized by H-bonding between islands of the 2D network were infrequently found (Figure 4.5a).

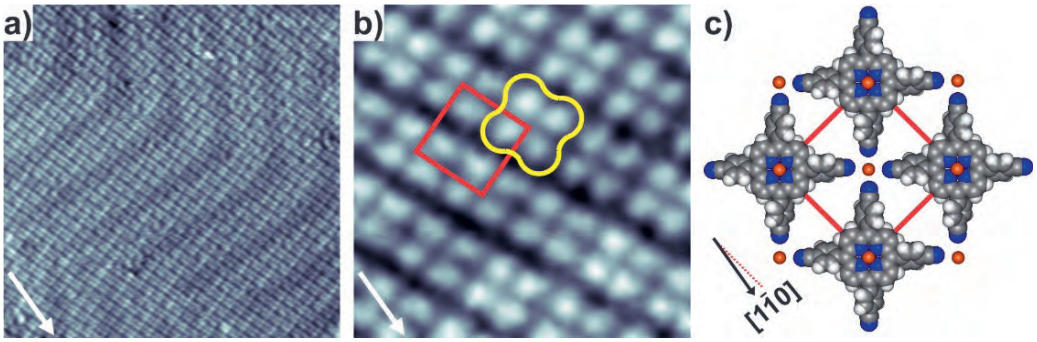

Figure 4.4. Self-assembly of the fourfold Co-coordinated network at monolayer coverage of Co-TCNPP with Co-atoms on Au(111). (a) Overview STM image showing the long-range order of the 2D network stabilized by metal-coordination (50 x 50 nm^2, U_{bias} = 2 V, I_{set} = 15 pA). The Au herringbone reconstruction is visible through the molecular ad-layer. (b) High-resolution STM image in which the phenyl moieties of the macrocycle are discernible (7.5 x 7.5 nm^2, U_{bias} = 2 V, I_{set} = 15 pA). The yellow outline and red square highlight one porphyrin and the unit cell, respectively. (c) Tentative structural model of the fourfold Co-coordinated network. Cobalt, nitrogen, carbon and hydrogen atoms are shown in orange, blue, gray and white, respectively. The unit cell of the network is shown in red. In (c) the dotted red line is parallel to a unit cell direction and the black arrow indicates a principal direction of the Au substrate. In (a) and (b) the white arrow at the bottom denotes a principal crystallographic direction of the Au substrate.

The high-resolution STM image in Figure 4.4b reveals features of the network structure. Within the envelope of a single Co-TCNPP unit (highlighted in yellow) the phenyl moieties are again imaged as bright lobes,[24–27] as previously discussed for the H-bonded network. The metallic center in the porphyrin core is not imaged at positive bias as shown in Figure 4.4b. Once again, the varying brightness between consecutive molecules is given by the underlying herringbone reconstruction of the Au substrate. From our STM and LEED measurements, we determined a square unit cell

(depicted in red) with dimensions a = b = 1.79 ± 0.02 nm and an internal angle of α = 90° ± 3°. The molecular density now amounts to 0.31 Co-TCNPP molecules per nm^2. Our STM and LEED measurements (Appendix Figure A4.2) suggest that the unit cell (cf. dotted red line in Figure 4.4c) is rotated 7.5° with respect to the principal Au directions. In contrast to the lateral molecular orientation with respect to neighboring porphyrins in the H-bonded network (Figure 4.2b), the molecules no longer align their cyanophenyl substituents towards the phenyl moieties of a neighboring molecule but rather arrange in a head-to-head configuration pointing to a common fourfold node. By taking into consideration the repulsive nature between nucleophilic species, the formation of a fourfold node between the terminal N-atoms without a coordinating metal-atom can be ruled out. Hence, such configuration gives evidence of a metal-ligand bonding. Indeed, the lone pair electrons provided by the N-atoms of the cyano endgroups possess high binding affinity towards transition metals.[34-36] Therefore, as illustrated in the tentative structural model (Figure 4.4c), we propose that this network is a MOCN stabilized by a fourfold coordination node with one Co-atom (orange sphere) coordinating to a total of four molecules, resulting in a 1:1 stoichiometric ratio between Co-TCNPP and Co-atoms as evidenced by STM. The electronegative N-atom of the terminal cyano endgroup interacts via metal-ligand bonding with the Co-atom, with a projected Co–N distance of approximately 2.5 Å. The common invisibility of 3d transition metals within 2D MOCNs on metallic surfaces prevails for the Co-atoms located at the coordinating nodes (Figures 4.4a and b).[8,9,34]

Co-TCNPP on Au(111) After Co-coordination at Room Temperature

The deposition of Co-atoms in Figure 4.4 was performed while annealing the sample to enhance surface diffusion. Since the latter is a thermally activated process, we also conducted experiments of Co-deposition at room temperature to study the influence of temperature in the self-assembly of the MOCN at monolayer coverage. As evidenced by the STM measurements (Figure 4.5b), the fourfold Co-coordinated network coexisted with the close-packed H-bonded network. The non-coordinated Co-atoms clustered into metallic islands. Subsequent thermal annealing favored the formation of the fourfold Co-coordinated network.

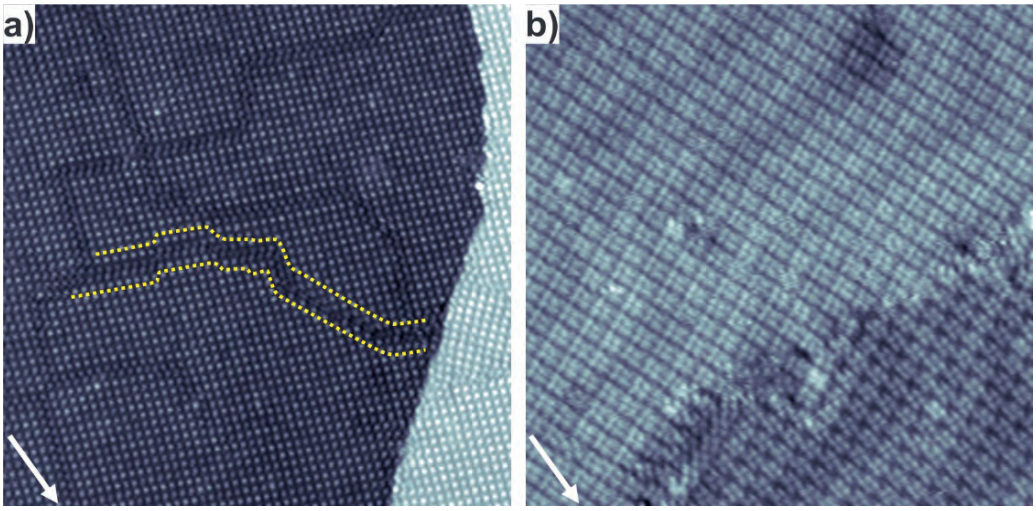

Figure 4.5. STM image of the self-assembly formed by Co-TCNPP on Au(111) after deposition of Co-atoms: (a) Overview STM image of the long-range ordered metal-organic coordination network (100 x 100 nm^2, U_{bias} = 1.2 V, I_{set} = 20 pA). The domain boundaries between islands of the fourfold Co-coordinated network can be distinguished. A pair of dotted yellow lines acts as a guide to the eye to highlight one domain boundary. The domain boundaries are stabilized by H-bonding, following the same molecular arrangement of the close-packed H-bonded network. Self-assembly of Co-TCNPP on Au(111) after deposition of Co-atoms at room-temperature: (b) STM image displaying the coexistence between the fourfold Co-coordinated (top) and close-packed H-bonded (bottom) networks (40 x 40 nm^2, U_{bias} = 2 V, I_{set} = 15 pA). In (a) and (b) the white arrow at the bottom denotes a principal crystallographic direction of the substrate.

Co-TCNPP on Au(111) After Co-coordination – Submonolayer case

To assess the adsorption behavior of Co-TCNPP in terms of molecular coverage, we deposited a submonolayer coverage of molecules on Au(111), followed by Co-deposition with the sample kept at 410 K. The stoichiometric ratio between molecules and metal-atoms was fixed (~1:1 with a slight excess

of metal) throughout all our experiments to only focus on the influence of molecular coverage in the self-assembly of Co-TCNPP. As evidenced by the overview STM image in Figure 4.6a, the formation of a second different network took place, i.e., a chevron structure (highlighted with black text) coexisted with the fourfold Co-coordinated network (highlighted with red text) in the lower and upper half, respectively. The higher molecular density of the fourfold Co-coordinated network with respect to the chevron structure is clearly noticeable. The herringbone reconstruction of the Au(111) substrate was still intact as seen in Figure 4.6a.

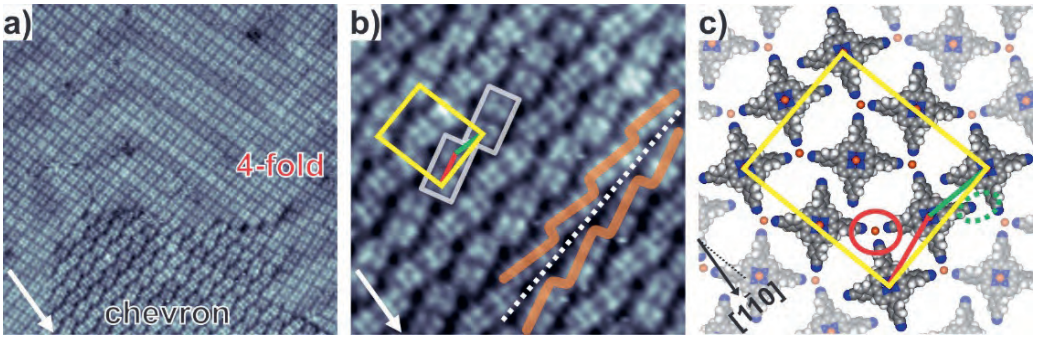

Figure 4.6. Self-assembly of submonolayer coverage of Co-TCNPP on Au(111) after deposition of Co-atoms. (a) Overview STM image (50 x 50 nm^2, U_{bias} = 2 V, I_{set} = 15 pA). The molecules and Co-atoms assembled into two MOCNs: a fourfold Co-coordinated network (text in red) and a close-packed chevron structure (text in black). (b) Zoom-in STM image of the close-packed chevron structure (17 x 17 nm^2, U_{bias} = 2 V, I_{set} = 15 pA). The yellow rectangle highlights the unit cell, while the red and green lines resemble the lengths highlighted in the structural model in (c). The grey rectangles enclose two pairs of Co-TCNPP molecules within a single row of molecules. The white dotted line guides the eye between two mirrored rows of molecules (denoted by the orange zig zag lines). (c) Tentative structural model of the chevron structure. Cobalt, nitrogen, carbon and hydrogen atoms are shown in orange, blue, gray and white, respectively. The unit cell of the network is shown in yellow. The red and green line are equal in length to the unit cell axes of the fourfold Co-coordinated network and to the close-packed H-bonded network, respectively. Analogously, the solid red and dotted green ovals highlight the Co-coordination and H-bonding motifs, respectively. In (c) the dotted black line is parallel to a unit cell direction and the black arrow indicates a principal direction of the Au substrate. In (a) and (b) the white arrow at the bottom denotes a principal crystallographic direction of the Au substrate.

A closer inspection of the chevron structure is shown in Figure 4.6b. The common bright lobe contrast given by the phenyl moieties prevails for

each Co-TCNPP molecule and the varying brightness between consecutive porphyrins is given by the herringbone reconstruction of the Au substrate. From our STM measurements, we determined a unit cell (depicted in yellow) with dimensions a = 3.54 ± 0.03 nm and b = 4.26 ± 0.04 nm and an internal angle of α = 90° ± 3°. The molecular density of this structure is equal to 0.27 Co-TCNPP molecules per nm^2. The Co-TCNPP molecules arranged in pairs following a tail-to-tail configuration as outlined by the grey rectangles (two Co-TCNPP molecules per rectangle). The tiling of successive pairs formed rows of molecules as depicted by the orange zigzag lines. A peculiarity of the chevron structure is its chirality (the white dotted line guides the eye between two mirrored rows). Accordingly, as depicted in the tentative structural model (Figure 4.6c), we propose that the network is stabilized by a simultaneous expression of H-bonding and metal-ligand interactions:[14,15] (i) a threefold metal-coordination (solid red oval) between the cyano endgroups from three different Co-TCNPP molecules and one Co-atom and (ii) H-bonding (dashed green oval) between consecutive porphyrin pairs following the geometry of a T-type interaction.[37] Interestingly, the 1:1 stoichiometric ratio between molecules and Co-atoms prevailed for the chevron structure. The solid red and green lines in Figure 4.6b and c are in agreement with the unit cell vector values reported for the fourfold Co-coordinated and the close-packed H-bonded networks, respectively. Furthermore, the threefold metal-coordination node is distorted, i.e., the angle between the Co-TCNPP molecules is not symmetrical and deviates from the previously reported values of 120° for Co-coordinated MOCNs.[6,7] The chevron structure coexisted as a minority phase with the fourfold Co-coordinated network in a ca. 30:70 coverage ratio for samples prepared at submonolayer coverage on the range of around 0.75 ML. However, the chevron structure did not form as

one exclusive phase and post-annealing treatments did not promote the formation of one exclusive phase. These results confirm that the chevron and fourfold Co-coordinated assemblies are coverage-dependent and the latter is formed as one exclusive phase at monolayer coverage.

4.4 Discussion

Over the last decades, numerous studies on the formation of metal-organic frameworks (MOFs) in three-dimensions (3D) have been realized and explained with concepts of supramolecular chemistry.[1,2] In cases where Co-atoms are used as metallic centers within the MOF, they are known to prefer coordinating with organic ligands in an octahedral or tetrahedral coordination geometry in 3D crystalline structures.[38–41] However, the coordination geometry of metal-atoms is likely to be modified on a surface, since the underlying substrate takes away one dimension. Consequently, the number of coordination sites available to interact with the organic ligands is reduced. Additionally, the substrate can either take the role of a ligand or not. In particular, on noble metal surface, threefold coordination motifs are known to prevail for Co-atoms with cyano-functionalized molecules.[6,7,34,38] In our study, the chevron structure observed at submonolayer coverage is stabilized by a distorted threefold coordination motif present in the 2D plane parallel to the Au(111) substrate. We reason that such configuration could only occur if a hybridization between the Co-atoms (located at the coordination nodes) and the Au substrate takes place. Therefore, the Co-atoms at the nodes might have adopted a distorted tetrahedral coordination geometry with the three cyano endgroups located in the plane of the MOCN and the Au substrate acting as the fourth ligand. Our reasoning is based on the findings for linear

dicarbonitrile-polyphenyl molecules and Co-atoms adsorbed on Ag(111) for which a hybridization between the Co and Ag-atoms was concluded, which prompted the formation of a metal-organic nanomesh stabilized by threefold Co-coordination nodes.[7]

As described above, the chevron structure always coexisted as a minority phase with the fourfold Co-coordinated network at submonolayer coverage. In a previous study, a similar grid-like MOCN formed on a non-interacting substrate (hBN) and allowed the formation of fourfold Co-coordination motifs.[27] In contrast, we observed the formation of such coordination motif on a bare metal surface, namely Au(111). In comparison to the chevron structure and in analogy to the fourfold coordinated MOCN on hBN,[27] we conclude that the Co-atoms located at the nodes of the fourfold Co-coordinated network are no longer hybridized with the Au substrate and interact with four cyano endgroups via a square planar coordination geometry. Obviously, the introduction of the Au(111) substrate modified the expected coordination geometry encountered for Co-atoms in 3D crystalline structures. Similarly, we deposited a nickel analogue of Co-TCNPP on Au(111) and the results are in line with the here discussed fourfold Co-coordinated network (Appendix Figure A4.3, A4.4 and A4.5).

Furthermore, the coverage-dependent behavior of Co-TCNPP upon coordination became evident at monolayer coverage, where the fourfold Co-coordinated network formed as one exclusive phase. The influence of molecular coverage on the self-assembly of organic networks[16-21] and MOCNs[14,15] has been previously reported to lead to the transformation of one type of structure into a second, mostly more densely packed structure. Such transformation is driven by so-called intrinsic in-plane compression pressure, which is built up from the molecules adsorbed on the surface and increases

with molecular coverage. Literature describing the coverage-dependent adsorption behavior of porphyrin-based networks has been rarely reported.[20,21] In our study, the higher molecular density of the fourfold Co-coordinated network compared to the chevron structure (0.31 and 0.27 Co-TCNPP molecules per nm^2, respectively) increases the in-plane compression pressure in the 2D plane of the MOCN. This promotes a dense molecular packing between the Co-TCNPP molecules and Co-atoms following a square planar coordination geometry, which has been so far only reported for Co-coordinated MOCNs on non-interacting surfaces like hBN[27,42] and 3D crystalline structures.[43–45] To our knowledge, we present the first coverage-dependent long-range ordered MOCN stabilized by a fourfold Co-coordination motif observed for a tetracyanophenylporphyrin derivative on a bare metal surface.

Along with the in-plane compression pressure, the different energetic contributions must be considered to better understand the coverage-dependent behavior of Co-TCNPP upon coordination with Co-atoms. To compare both MOCNs in terms of Gibbs free energy we will consider the following factors: (i) the intermolecular interactions in the MOCN, (ii) the molecule substrate interactions and (iii) the surface area covered by the molecules (molecular density). The chevron structure is stabilized by a combination of H-bonding and metal-ligand interactions, whereas only metal-ligand interactions are present in the fourfold Co-coordinated network. In general, metal-ligand interactions are stronger than H-bonds and should bring the system to a lower energetic state. With respect to the molecule substrate interactions, we assume that they are similar for both the threefold and the fourfold Co-coordinated structures despite the identified different rotational arrangement of the molecules with respect to the principal Au directions. We arrive at that

conclusion since both structures are not commensurate to the substrate and thus, the molecules do not favor a specific adsorption position. Furthermore, the overall energy of the system can also be lowered by increasing the number of molecules per surface area. Such is the case of the fourfold Co-coordinated network that minimizes the surface area occupied per molecule.

However, the threefold coordination motif of the chevron structure should be preferred according to the coordination geometries reported for 3D structures. Thus, to assemble the molecules in the fourfold coordination motif, the fourfold MOCN pays an energetic penalty through its higher molecular density observed with respect to the chevron structure. In general, we can conclude that the overall energy is considered to be small (based on the above arguments) due to the observed coexistence of both MOCNs and that is the reason why the fourfold Co-coordinated network can be promoted as one exclusive phase at monolayer coverage.

4.5 Conclusions

In summary, we investigated the influence of molecular coverage on the self-assembly of Co-TCNPP before and after coordination with Co-atoms on Au(111) by STM and LEED under UHV conditions. The deposition of Co-TCNPP on Au(111) gave rise to a close-packed H-bonded network that showed to be invariant to changes in molecular coverage. However, upon metal-coordination with Co-atoms a coverage-dependent structural transformation took place, which also modified the coordination geometry of the Co-atoms located at the coordination nodes. At monolayer coverage, the in-plane compression pressure exerted by the molecules on the surface steered the formation of a fourfold Co-coordinated network that exhibited a distinct

square planar coordination geometry for the Co-atoms located at the coordination nodes. By reducing the molecular coverage, a second MOCN was formed in coexistence with the fourfold MOCN, i.e., a chevron structure stabilized by a simultaneous expression of H-bonding and threefold Co-coordination. In this MOCN, the Co-atoms adopted a distorted tetrahedral coordination geometry, which is the coordination geometry expected in 3D structures. Furthermore, the fourfold MOCN paid an energetic penalty to have all Co-TCNPP molecules in the square planar coordination geometry by, among others, reducing the surface area occupied per molecule. In addition, as observed at monolayer coverage, a MOCN stabilized by only metal-ligand interactions such as the fourfold Co-coordinated network will bring the system to a lower energetic state compared to MOCNs that contain weaker bonding motifs like the H-bonding found in the chevron structure. Therefore, a subtle interplay between the chemical nature of the building blocks and molecular coverage can steer the formation of structurally different MOCNs.

4.6 References

1. Furukawa, H.; Cordova, K. E.; O'Keeffe, M.; Yaghi, O. M. The Chemistry and Applications of Metal-Organic Frameworks. *Science* **2013**, *341*, 1230444/1-1230444/12.
2. Li, H.; Eddaoudi, M.; O'Keeffe, M.; Yaghi, O. M. Design and Synthesis of an Exceptionally Stable and Highly Porous Metal-Organic Framework. *Nature*. **1999**, *402*, 276–279.
3. Gutzler, R.; Stepanow, S.; Grumelli, D.; Lingenfelder, M.; Kern, K. Mimicking Enzymatic Active Sites on Surfaces for Energy Conversion Chemistry. *Acc. Chem. Res*. **2015**, *48*, 2132–2139.
4. Barth, J. V. Molecular Architectonic on Metal Surfaces. *Annu. Rev. Phys. Chem*. **2007**, *58*, 375–407.
5. Stepanow, S.; Lin, N.; Barth, J. V. Modular Assembly of Low-Dimensional Coordination Architectures on Metal Surfaces. *J. Phys.: Condens. Matter* **2008**, *20*, 184002.
6. Dong, L.; Gao, Z.; Lin, N. Self-Assembly of Metal-Organic Coordination Structures on Surfaces. *Prog. Surf. Sci*. **2016**, *91*, 101–135.
7. Schlickum, U.; Decker, R.; Klappenberger, F.; Zoppellaro, G.; Klyatskaya, S.; Ruben, M.; Silanes, I.; Arnau, A.; Kern, K.; Brune, H.; et al. Metal-Organic Honeycomb Nanomeshes with Tunable Cavity Size. *Nano Lett.* **2007**, *7*, 3813–3817,
8. Björk, J.; Matena, M.; Dyer, M. S.; Enache, M.; Lobo-Checa, J.; Gade, L. H.; Jung, T. A.; Stöhr, M.; Persson, M. STM Fingerprint of Molecule–Adatom Interactions in a Self-Assembled Metal–Organic Surface Coordination Network on Cu(111). *Phys. Chem. Chem. Phys.* **2010**, *12*, 8815–8821.
9. Matena, M.; Björk, J.; Wahl, M.; Lee, T.-L.; Zegenhagen, J.; Gade, L. H.; Jung, T. A.; Persson, M.; Stöhr, M. On-Surface Synthesis of a Two-Dimensional Porous Coordination Network: Unraveling Adsorbate Interactions. *Phys. Rev. B*. **2014**, *90*, 125408/1-125408/8.
10. Pham, T. A.; Song, F.; Alberti, M. N.; Nguyen, M.-T.; Trapp, N.; Thilgen, C.; Diederich, F.; Stöhr, M. Heat-Induced Formation of One-Dimensional Coordination Polymers on Au(111): An STM Study. *Chem. Commun*. **2015**, *51*, 14473–14476.
11. Fendt, L. A.; Stöhr, M.; Wintjes, N.; Enache, M.; Jung, T. A.; Diederich, F. Modification of Supramolecular Binding Motifs Induced by Substrate Registry: Formation of Self-Assembled Macrocycles and Chain-like Patterns. *Chem. - Eur. J.* **2009**, *15*, 11139–11150.
12. Auwärter, W.; Écija, D.; Klappenberger, F.; Barth, J. V. Porphyrins at Interfaces. *Nat. Chem*. **2015**, *7*, 105–120.
13. Gottfried, J. M. Surface Chemistry of Porphyrins and Phthalocyanines. *Surf. Sci. Rep*. **2015**, *70*, 259–379.

14. Liu, J.; Lin, T.; Shi, Z.; Xia, F.; Dong, L.; Liu, P. N.; Lin, N. Structural Transformation of Two-Dimensional Metal-Organic Coordination Networks Driven by Intrinsic In-Plane Compression. *J. Am. Chem. Soc*. **2011**, *133*, 18760–18766.
15. Vijayaraghavan, S.; Ecija, D.; Auwärter, W.; Joshi, S.; Seufert, K.; Drach, M.; Nieckarz, D.; Szabelski, P.; Auriscchio, C.; Bonifazi, D.; et al. Supramolecular Assembly of Interfacial Nanoporous Networks with Simultaneous Expression of Metal-Organic and Organic-Bonding Motifs. *Chem. -Eur. J*. **2013**, *19*, 14143–14150.
16. Enache, M.; Maggini, L.; Llanes-Pallas, A.; Jung, T. A.; Bonifazi, D.; Stöhr, M. Coverage-Dependent Disorder-to-Order Phase Transformation of a Uracil Derivative on Ag(111). *J. Phys. Chem. C.* **2014**, *118*, 15286–15291.
17. Samuely, T.; Liu, S.-X.; Wintjes, N.; Haas, M.; Decurtins, S.; Jung, T. A.; Stöhr, M. Two-Dimensional Multiphase Behavior Induced by Sterically Hindered Conformational Optimization of Phenoxy-Substituted Phthalocyanines. *J. Phys. Chem. C* **2008**, *112*, 6139-6144.
18. Schmidt, N.; Enache, M.; Maggini, L.; Havenith, R. W. A.; Bonifazi, D.; Stöhr, M. Coverage-Controlled Polymorphism of H-Bonded Networks on Au(111). *J. Phys. Chem. C* **2019**, *123*, 7151-7157.
19. Xu, B.; Tao, C.; Williams, E. D.; Reutt-Robey, J. E. Coverage Dependent Supramolecular Structures: C60:ACA Monolayers on Ag(111). *J. Am. Chem. Soc.* **2006**, *128*, 8493–8499.
20. Lepper, M.; Zhang, L.; Stark, M.; Ditze, S.; Lungerich, D.; Jux, N.; Hieringer, W.; Steinrück, H. P.; Marbach, H. Role of Specific Intermolecular Interactions for the Arrangement of Ni(II)-5, 10, 15, 20-Tetraphenyltetrabenzoporphyrin on Cu(111). *J. Phys. Chem. C.* **2015**, *119*, 19897–19905.
21. Zhang, L.; Lepper, M.; Stark, M.; Lungerich, D.; Jux, N.; Hieringer, W.; Steinrück, H.; Marbach, H. Self-Assembly and Coverage Dependent Thermally Induced Conformational Changes of Ni(II)-Meso-Tetrakis (4-Tert-Butylphenyl) Benzoporphyrin on Cu(111). *Phys. Chem. Chem. Phys.* **2015**, *17*, 13066–13073.
22. Horcas, I.; Fernández, R.; Gómez-Rodríguez, J. M.; Colchero, J.; Gómez-Herrero, J.; Baro, A. M. WSXM: A Software for Scanning Probe Microscopy and a Tool for Nanotechnology. *Rev. Sci. Instrum.* **2007**, *78*, 013705.
23. Hermann, K.; van Hove, M. A. LEEDpat4 (LEED pattern analyzer). http://www.fhi-berlin.mpg.de/KHsoftware/LEEDpat/index.html (accessed January 8, 2021).

24. Brede, J.; Linares, M.; Kuck, S.; Schwöbel, J.; Scarfato, A.; Chang, S. H.; Hoffmann, G.; Wiesendanger, R.; Lensen, R.; Kouwer, P. H. J.; et al. Dynamics of Molecular Self-Ordering in Tetraphenyl Porphyrin Monolayers on Metallic Substrates. *Nanotechnology.* **2009**, *20*, 275602/1-275602/10.
25. Auwärter, W.; Seufert, K.; Klappenberger, F.; Reichert, J.; Weber-Bargioni, A.; Verdini, A.; Cvetko, D.; Dell'Angela, M.; Floreano, L.; Cossaro, A.; et al. Site-Specific Electronic and Geometric Interface Structure of Co-Tetraphenyl-Porphyrin Layers on Ag(111). *Phys. Rev. B*. **2010**, *81*, 245403/1-245403/14.
26. Lepper, M.; Schmitt, T.; Gurrath, M.; Raschmann, M.; Zhang, L.; Stark, M.; Hölzel, H.; Jux, N.; Meyer, B.; Schneider, M. A.; et al. Adsorption Behavior of a Cyano-Functionalized Porphyrin on Cu(111) and Ag(111): From Molecular Wires to Ordered Supramolecular Two-Dimensional Aggregates. *J. Phys. Chem. C*. **2017**, *121*, 26361–26371.
27. Urgel, J. I.; Schwarz, M.; Garnica, M.; Stassen, D.; Bonifazi, D.; Ecija, D.; Barth, J. V.; Auwärter, W. Controlling Coordination Reactions and Assembly on a Cu(111) Supported Boron Nitride Monolayer. *J. Am. Chem. Soc*. **2015**, *137*, 2420–2423.
28. Bischoff, F.; He, Y.; Seufert, K.; Stassen, D.; Bonifazi, D.; Barth, J. V.; Auwärter, W. Tailoring Large Pores of Porphyrin Networks on Ag(111) by Metal–Organic Coordination. *Chem. - Eur. J.* **2016**, *22*, 15298–15306.
29. Gottardi, S.; Müller, K.; Moreno-Lõpez, J. C.; Yildirim, H.; Meinhardt, U.; Kivala, M.; Kara, A.; Stöhr, M. Cyano-Functionalized Triarylamines on Au(111): Competing Intermolecular versus Molecule/Substrate Interactions. *Adv. Mater. Interfaces.* **2014**, *1*, 1300025/1-1300025/10.
30. Scudiero, L.; Barlow, D. E.; Hipps, K. W. Physical Properties and Metal Ion Specific Scanning Tunneling Microscopy Images of Metal(II) Tetraphenylporphyrins Deposited from Vapor onto Gold (111). *J. Phys. Chem. B* **2000**, *104*, 11899–11905.
31. Buchner, F.; Warnick, K.-G.; Wölfle, T.; Görling, A.; Steinrück, H.-P.; Hieringer, W.; Marbach, H. Chemical Fingerprints of Large Organic Molecules in Scanning Tunneling Microscopy: Imaging Adsorbate - Substrate Coupling of Metalloporphyrins. *J. Phys. Chem. C.* **2009**, *113*, 16450–16457.
32. Buchner, F.; Zillner, E.; Röckert, M.; Gläßel, S.; Steinrück, H.-P.; Marbach, H. Substrate-Mediated Phase Separation of Two Porphyrin Derivatives. *Chem. - Eur. J.* **2011**, *17*, 10226–10229.
33. Yanagi, H.; Mukai, H.; Ikuta, K.; Shibutani, T.; Kamikado, T.; Yokoyama, S.; Mashiko, S. Molecularly Resolved Dynamics for Two-Dimensional Nucleation of Supramolecular Assembly. *Nano Lett*. **2002**, *2*, 601–604.
34. Henningsen, N.; Rurali, R.; Limbach, C.; Drost, R.; Pascual, J. I.; Franke, K. J. Site-Dependent Coordination Bonding in Self-Assembled Metal-Organic Networks. *J. Phys. Chem. Lett.* **2011**, *2*, 55–61.

35. Kuznetsov, M. L. Is the Charge on the Nitrile Carbon Atom a Driving Force of the Nucleophilic Addition to Coordinated Nitriles? *J. Mol. Struct*. **2004**, *674*, 33–42.
36. Baker Cortés, B. D.; Stöhr, M. Role of Cyano Groups in the Self-Assembly of Organic Molecules on Metal Surfaces. In *Encyclopedia of Interfacial Chemistry*; Wandelt, K., Ed.; Elsevier, **2018**; *Vol. 4*, pp 153–165.
37. Buchner, F.; Kellner, I.; Hieringer, W.; Görling, A.; Steinrück, H. P.; Marbach, H. Ordering Aspects and Intramolecular Conformation of Tetraphenylporphyrins on Ag(111). *Phys. Chem. Chem. Phys.* **2010**, *12*, 13082–13090.
38. Hosseini, M. W. Molecular Tectonics: From Simple Tectons to Complex Molecular Networks Inclusion Networks: An Interplay Between. *Acc. Chem. Res.* **2005**, *38*, 313–323.
39. Castaldelli, E.; Jayawardena, K. D. I.; Cox, D. C.; Clarkson, G. J.; Walton, R. I.; Le-Quang, L.; Chauvin, J.; Silva, S. R. P.; Demets, G. J. F. Electrical Semiconduction Modulated by Light in a Cobalt and Naphthalene Diimide Metal-Organic Framework. *Nat. Commun.* **2017**, *8*, 2139/1-2139/8.
40. Jouaiti, A.; Hosseini, M. W.; Cian, A. De. Design, Synthesis and Structural Investigation of a 1-D Directional Coordination Network Based on the Self-Assembly of an Unsymmetrical Mono-Tridentate Ligand and Cobalt Cation. **2000**, *Chem. Commun.*1863–1864.
41. Venkataraman, D.; Du, Y.; Wilson, S. R.; Hirsch, K. A.; Zhang, P.; Moore, J. S. A Coordination Geometry Table of the D-Block Elements and Their Ions. *J. Chem. Educ*. **1997**, *8*, 915-918.
42. Reichert, J.; Marschall, M.; Seufert, K.; Ecija, D.; Auwärter, W.; Arras, E.; Klyatskaya, S.; Ruben, M.; Barth, J. V. Competing Interactions in Surface Reticulation with a Prochiral Dicarbonitrile Linker. *J. Phys. Chem. C.* **2013**, *117*, 12858–12863. Cibian, M.; Derossi, S.; Hanan, G. S. Synthesis and Crystal Structure of a Rare Square-Planar Co(II) Complex of a Hydroxyamidinate Ligand. *Dalt. Trans* **2011**, *40*, 1038–1040.
43. Cibian, M.; Derossi, S.; Hannan, G. S. Synthesis and Crystal Structure of a Rare Square-Planar Co(II) Complex of a Hydrox-yamidinate Ligand. *Dalton Trans.* **2011**, *40*, 1038–1040.
44. Corona, T.; Company, A. Nitrous Oxide Activation by a Cobalt(II) Complex for Aldehyde Oxidation under Mild Conditions. *Dalt. Trans*. **2016**, *45*, 14530–14533.
45. Cibian, M.; Langis-Barsetti, S.; Gomes De Mendonça, F.; Touaibia, S.; Derossi, S.; Spasyuk, D.; Hanan, G. S. Influence of Ligand Substitution Pattern on Structure in Cobalt(II) Complexes of Bulky N,N'-Diarylformamidinate N-Oxides. *Eur. J. Inorg. Chem*. **2015**, 73–82.

4.6 Appendix

LEED data of Co-TCNPP before and after coordination with Co-atoms on Au(111)

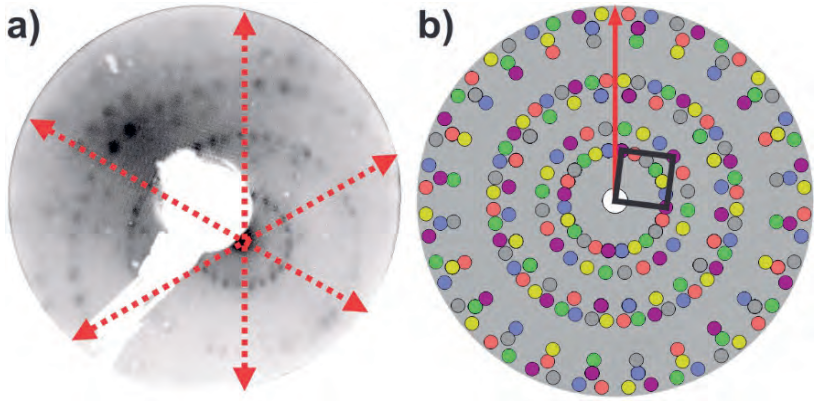

Figure A4.1. (a) LEED pattern of the close-packed H-bonded network formed by Co-TCNPP on Au(111) (E_{beam}= 24.5 eV). The red dotted arrows indicate the principal directions of the Au(111) surface. (b) Simulated LEED pattern of the close-packed H-bonded network illustrating a unit cell (shown in black). The circles in different colors indicate rotationally equivalent and mirrored domains. The red solid arrow indicates the principal direction of the Au(111) surface. The superstructure of the simulated LEED pattern is described by the matrix notation $\begin{pmatrix} 6.2 & 0.9 \\ 2.6 & 6.7 \end{pmatrix}$.

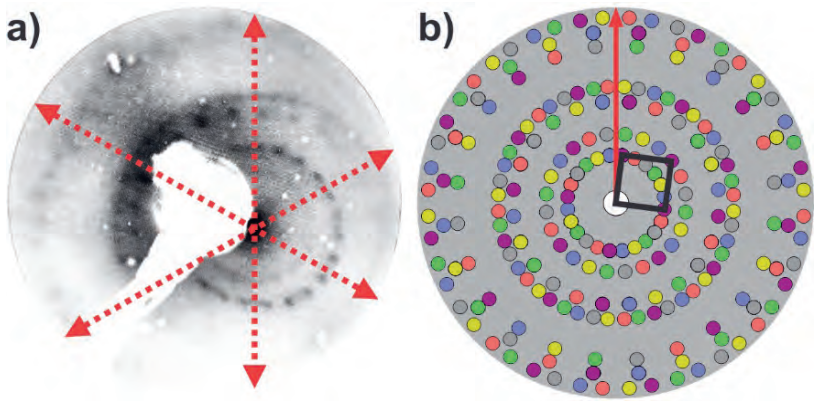

Figure A4.2. (a) LEED pattern of the fourfold Co-coordinated network formed by Co-TCNPP on Au(111) after deposition of Co-atoms (E_{beam}= 15.3 eV). The red dotted arrows indicate the principal directions of the Au(111) surface (b) Simulated LEED pattern of the fourfold Co-coordinated network illustrating a unit cell (shown in black). The circles in different colors indicate rotationally equivalent and mirrored domains. The red solid arrow indicates the principal direction of the Au(111) surface. The superstructure of the simulated LEED pattern is described by the matrix notation $\begin{pmatrix} 6.6 & 0.9 \\ 2.7 & 7.1 \end{pmatrix}$.

STM and LEED data of Ni-TCNPP after coordination with Co-atoms on Au(1111)

Ni-TCNPP on Au(111) after Co-coordination. To study the influence of a different metal center on the self-assembly of the herein discussed porphyrin, we used a nickel-substituted porphyrin (Ni-TCNPP) with identical chemical structure as Co-TCNPP (Figure A4.3). As evidenced by STM and LEED measurements (Figure A4.4 and A4.5) the self-assembly of Ni-TCNPP on Au(111) upon deposition of Co-atoms gave rise to a MOCN stabilized by fourfold Co-coordination, similar to the previously discussed MOCN formed by Co-TCNPP. Therefore, we suggest that the metal center in the porphyrin core of either Co-TCNPP or Ni-TCNPP, does not play a decisive role on the molecular orientation within the MOCN.

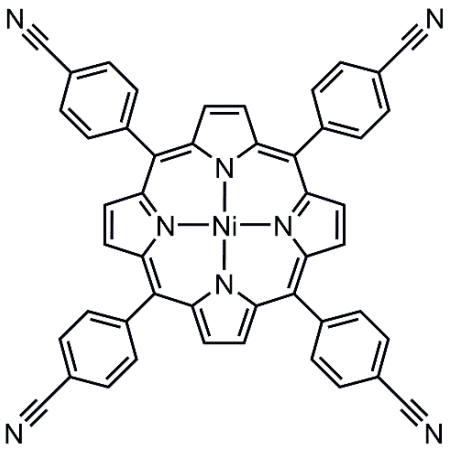

Figure A4.3. Chemical structure of nickel(II) 5,10,15,20-(tetra-4-cyanophenyl)porphyrin (Ni-TCNPP).

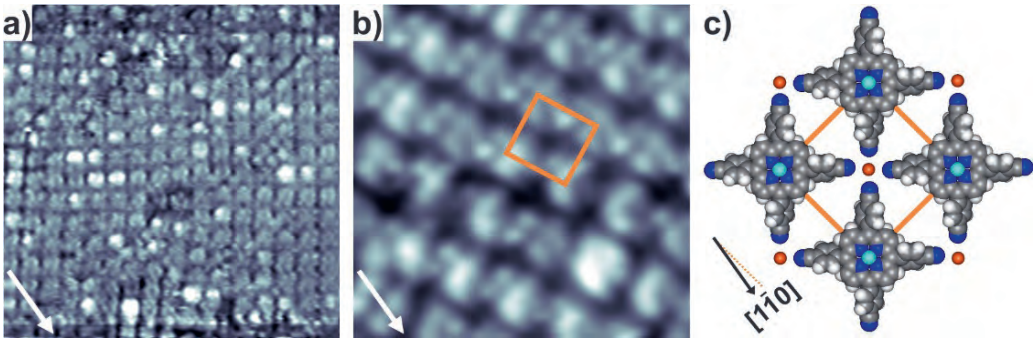

Figure A4.4. Self-assembly of monolayer coverage of the fourfold Co-coordinated of Ni-TCNPP on Au(111). (a) Overview STM image showing the long-range order of the 2D network stabilized by metal-coordination (30 x 30 nm^2, U_{bias} = 2 V, I_{set} = 12 pA). The orange square highlights the unit cell. (b) High-resolution STM image of the 2D network (10 x 10 nm^2, U_{bias} = 2.2 V, I_{set} = 15 pA). (c) Tentative structural model of the network. The unit cell of the network is shown in orange. Nickel, cobalt, nitrogen, carbon and hydrogen atoms are shown in turquoise blue, orange, blue, gray and white, respectively. The unit cell of the network is shown in orange. The dotted orange line is parallel to a unit cell direction and the black arrow indicates a principal direction of the substrate. In (a) and (b) the white arrow at the bottom denotes a principal crystallographic direction of the Au substrate.

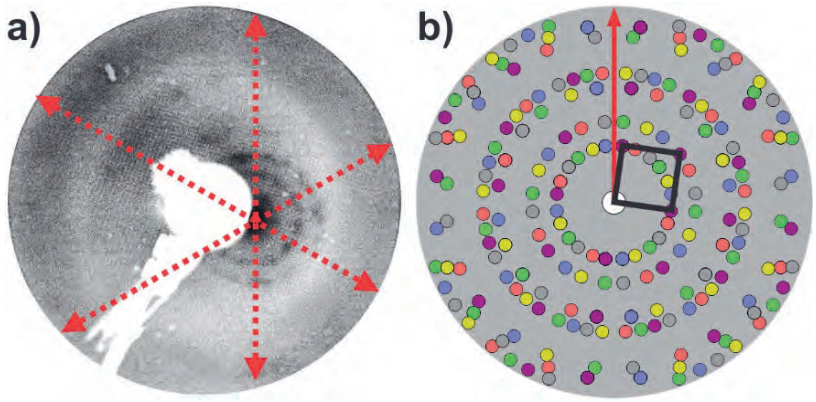

Figure A4.5. (a) LEED pattern of the fourfold Co-coordinated network formed by Ni-TCNPP on Au(111) after deposition of Co-atoms (E_{beam}= 21.7 eV). The red dotted arrows indicate the principal directions of the Au(111) surface (b) Simulated LEED pattern of the fourfold Co-coordinated network illustrating a unit cell (shown in black). The circles in different colors indicate rotationally equivalent and mirrored domains. The red solid arrow indicates the principal direction of the Au(111) surface. The superstructure of the simulated LEED pattern is described by the matrix notation $\begin{pmatrix} 6.6 & 0.9 \\ 2.7 & 7.1 \end{pmatrix}$.


chapter 5

5 Comparing Cyanophenyl and Pyridyl Ligands in the Formation of Porphyrin-Based Metal-Organic Coordination Networks

In recent studies, porphyrins derivatives have been frequently used as building blocks for the fabrication of metal-organic coordination networks (MOCNs) on metal surfaces under ultra-high vacuum conditions (UHV). The porphyrin core can host a variety of 3d transition metals which are usually incorporated in solution. However, the replacement of a preexisting metal atom in the porphyrin core by a different metallic species has been rarely reported under UHV. Herein, we report on the influence of cyanophenyl and pyridyl functional endgroups in the self-assembly of structurally different porphyrin-based MOCNs by the deposition of Fe-atoms on tetracyanophenyl (Co-TCNPP) and tetrapyridyl-functionalized (Zn-TPPyP) porphyrins under UHV on Au(111) by means of scanning tunneling microscopy (STM). A comparative analysis of the influence of the cyano and pyridyl endgroups in the formation of different in-plane coordination motifs is addressed. Each porphyrin derivative formed two structurally different Fe-coordinated MOCNs stabilized by three and fourfold in-plane coordination nodes, respectively. In addition, the co-deposited Fe-atoms did not only bind to the functional endgroups but also reacted with the porphyrin core of the Zn-substituted porphyrin (Zn-TPyP), i.e., an atom exchange reaction took place in the porphyrin core where the co-deposited Fe-atoms replaced the Zn-atoms. This was evidenced by the appearance of molecules with an enhanced (centered) STM contrast compared with the appearance of Zn-TPyP, which suggested the formation of a new molecular species, i.e., Fe-TPPyP.

Furthermore, the porphyrin core of the Co-substituted porphyrin (Co-TCNPP) displayed an off-centered STM contrast after the deposition of Fe-atoms, which was attributed to the binding of the Fe-atoms on a top-site of the Co-substituted porphyrin core. In summary, the deposition of metal-atoms onto organic layers can steer the formation of structurally different MOCNs and may replace preexisting metal-atoms contained in the porphyrin core.

5.1 Introduction

Porphyrins are a class of macrocyclic organic molecules that play an essential role in biological processes but can be also utilized in technological applications, such as solar cells, sensors and catalysis.[1–6] The porphyrin core – which is composed by four pyrrole moieties – can host a variety of metal atoms or remain in its free base version.[7,8] The incorporation of the metal atom in the porphyrin core and its replacement – also known as transmetalation or atom exchange – by a different metallic species has been performed extensively in solution.[9–12] On the other hand, metalation is also possible on a surface and even under dry conditions. Several studies have reported the metalation of free-base porphyrins on noble metal surfaces under ultrahigh vacuum (UHV) conditions as well as at the solid-liquid interface by means of the co-deposition of metal atoms or coordination to substrate atoms, also known as selfmetalation.[8,13–15] However, there are very few studies addressing atom exchange reactions under UHV conditions for porphyrin and porphyrin-like macrocycles, such as phthalocyanines and pyrphyrins.[16–20] In addition, most of the atom exchange studies under UHV conditions make use of X-ray absorption and photoemission spectroscopies to support their findings and few attention has been given to the imaging capabilities of

scanning tunneling microscopy (STM).[16–20] Furthermore, the porphyrin backbone can be tailored with numerous functional endgroups that grants them the possibility to form structurally different two-dimensional (2D) nanostructures that are driven by molecular self-assembly on a surface – either through directional intermolecular interactions or metal-ligand interactions in the case of metal-organic coordination networks (MOCNs).[7,8,21,22] In the latter case, the functional endgroups play an essential role in the formation of different in-plane coordination motifs that stabilize the structure of the MOCNs, for instance, the subtle balance between the overall shape and chemistry of the functional endgroup along with the chemical nature of the coordinating metal-atoms will dictate the 2D structure of the MOCN.[7,8,21,22] In previous studies, the self-assembly of cyano-functionalized porphyrins on Au(111)[21,23,24] and Ag(111)[25–27] as well as pyridyl-functionalized porphyrins on Au(111)[5,28–32] and Ag(111)[27,33,34] has been reported.

Herein, we present a comparative study on the deposition of Fe-atoms onto self-assembled networks from cobalt(II) 5,10,15,20-(tetra-4-cyanophenyl)porphyrin (Co-TCNPP) and zinc(II) 5,10,15,20-(tetra-4-pyridyl)-21H,23H-porphyrin (Zn-TPyP) on Au(111). It was the aim to investigate which of the following processes would occur: MOCN formation, atom exchange reaction and bonding of the Fe-atoms on top of the porphyrin core. Comparing the influence of cyanophenyl and pyridyl ligands as well as Co and Zn contained in the porphyrin core on the above processes gives valuable additional information on the reactivities.

The chemical structures of both porphyrin derivatives are shown in Figure 5.1. For Co-TCNPP (Figure 5.1a), the tetrapyrrolic macrocycle is functionalized at all four meso positions by cyanophenyl endgroups and its

core contains one Co-atom. On the other hand, the macrocycle of Zn-TPyP (Figure 5.1b) is functionalized at all four meso positions by pyridyl endgroups and its core contains one Zn-atom. As revealed by STM, the deposition of Co-TCNPP on Au(111) and subsequent deposition of Fe-atoms with a fixed molecule to metal ratio (~1:1 with a slight excess of metal) gave rise to the coexistence of two structurally different MOCNs stabilized by fourfold (grid-like network) and threefold Co-coordination nodes (chevron structure), respectively. The presence of porphyrins with a different appearance after the deposition of Fe-atoms – compared with the molecular appearance shown for Co-substituted porphyrins (Co-TCNPP) in our previous work on Au(111) – suggested that a different molecular species was formed by two possibilities: (i) an atom exchange reaction between the Fe- and Co-atoms or (ii) the binding of one Fe-atom on top of the porphyrin core, with the latter being the most probable possibility.[21] Furthermore, Zn-TPyP also formed two structurally different MOCNs upon coordination with Fe-atoms, where threefold Fe-coordination nodes (chain-like network) were favored over the fourfold nodes (grid-like network). In contrast to the findings for Co-TCNPP, an atom exchange reaction took place where the Fe-atoms replaced most of the Zn-atoms in the porphyrin core of Zn-TPyP. To the best of our knowledge, we present the first detailed STM study of an atom exchange reaction under UHV conditions for long-range ordered porphyrin-based MOCNs on metal surface.

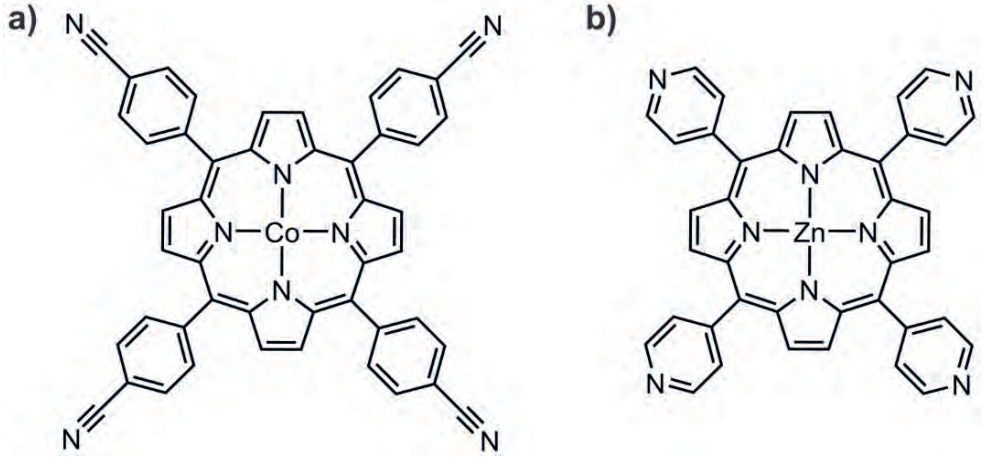

Figure 5.1. Chemical structure of a) cobalt(II) 5,10,15,20-(tetra-4-cyanophenyl)porphyrin (Co-TCNPP) and b) zinc(II) 5,10,15,20-(tetra-4-pyridyl)-21H,23H-porphyrin (Zn-TPyP).

5.2 Experimental Methods

An ultra-high vacuum (UHV) system (with a base pressure in the low 10^{-10} mbar range) with different chambers for sample preparation and characterization was used to perform all the experiments. The Au(111) single crystal was cleaned by repeated cycles of Ar^+ sputtering and annealing to 720 K. Co-TCNPP (PorphyChem) was thermally sublimed at 820 K and Zn-TPyP (Sigma-Aldrich) at 785 K onto the Au(111) surface held at RT by means of a Knudsen cell evaporator (OmniVac). Iron atoms were deposited onto the organic layers from an iron rod using an e-beam evaporator (Oxford Applied Research), while keeping the sample at 410 K. On the other hand, for Zn-TPyP adsorbed on Au(111), iron atoms were deposited while maintaining the sample at room temperature (RT), followed by a post-annealing treatment at 440 K. The molecule-metal ratio was kept fixed (~1:1 with a slight excess of metal) for all experiments. A quartz crystal microbalance was used to monitor

the molecule and metal-atom deposition rates. The STM (Scienta Omicron GmbH) measurements were performed at room temperature in the constant current mode. A mechanically cut Pt/Ir wire was used as a tip. All bias voltages are given with respect to a grounded tip. The STM images were processed with the WSxM software.[35] In addition, the low energy electron diffraction (LEED) patterns were acquired using a micro-channel plate LEED (Scienta Omicron GmbH) and simulated with the LEEDPat4.2 software.[36]

5.3 Results

Co-TCNPP on Au(111) after Fe-coordination. As shown in our previous study, the deposition of up to one monolayer of Co-TCNPP (Figure 5.1a) on Au(111) prompted the formation of a close-packed H-bonded network (Figure 5.2a). By addition of Co-atoms, the formation of both a three- and fourfold MOCN was formed in dependence of the initial Co-TCNPP coverage (Figure 5.2c–e).[21] It should be already noted that in both assemblies, independently of the applied bias, the appearance of the porphyrin core in the STM images remained uniformly distributed among consecutive molecules, since only one type of porphyrin was present, i.e., Co-TCNPP. These results serve as a reference for our present work, where the deposition of Fe-atoms onto a submonolayer of Co-TCNPP molecules while annealing the sample at 410 K and keeping a fixed molecule-metal ratio (~1:1 with a slight excess of metal), gave rise to the coexistence of two different 2D networks as shown in Figure 5.3 and Figure 5.6: (i) a grid-like network (Figure 5.3 and Figure 5.4) and (ii) chevron structure (Figure 5.6).

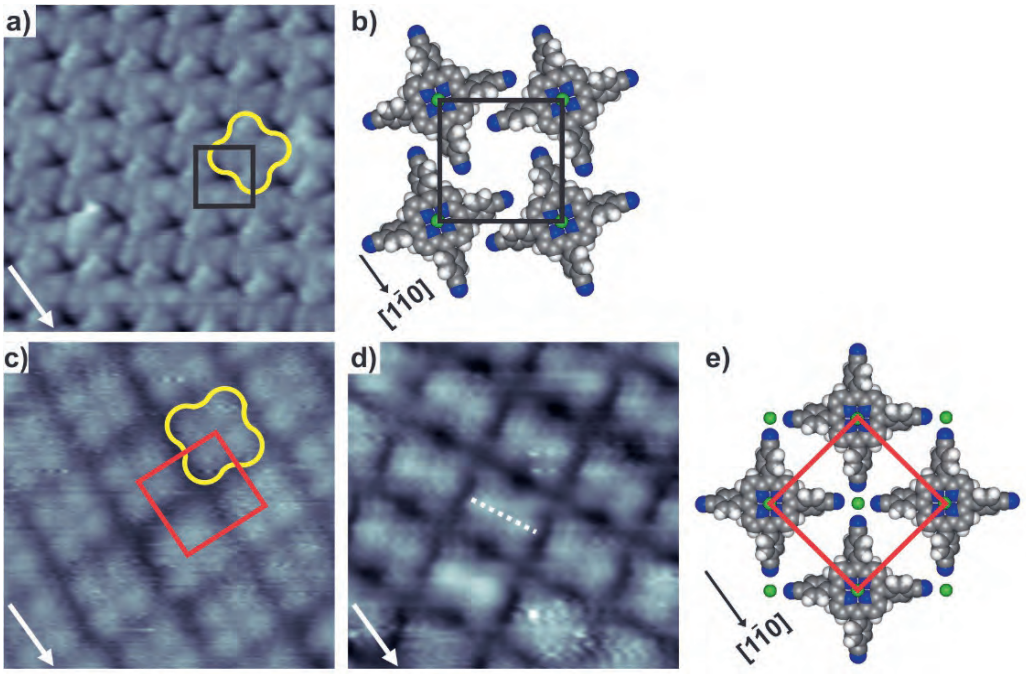

Figure 5.2. (a) STM image of the close-packed H-bonded network of Co-TCNPP on Au(111) (10 x 10 nm^2, U_{bias} = 1.3 V, I_{set} = 15 pA). The black square and yellow outline highlight the unit cell and one porphyrin, respectively. (b) Tentative structural model of the close-packed H-bonded network with the unit cell shown in black. STM images of the fourfold Co-coordinated network of Co-TCNPP on Au(111) acquired at: (c) positive bias (7.5 x 7.5 nm^2, U_{bias} = 1.7 V, I_{set} = 18 pA) and (d) negative bias (7.5 x 7.5 nm^2, U_{bias} = -2.4 V, I_{set} = 15 pA). In (c), the red square and yellow outline highlight the unit cell and one porphyrin, respectively. In (d) the white dotted line highlights the long symmetry axis of Co-TCNPP. (e) Tentative structural model of the fourfold Co-coordinated network with the unit cell shown in red. In (b) and (e) the cobalt, nitrogen, carbon and hydrogen atoms are shown in green, blue, gray and white, respectively. The white arrow at the bottom of each STM image denotes the [1$\bar{1}$0] crystallographic direction of the substrate. The black arrow at the bottom of (b) and (e) indicates the [1$\bar{1}$0] direction of the Au substrate.

Firstly, we will describe the observations found for the grid-like network. In the overview STM image (Figure 5.3a) a densely packed array of porphyrins is shown with molecular islands that were observed to spread over 100s of nanometers (Figure 5.4). Individual Co-TCNPP molecules within the grid-like network can be clearly distinguished in Figure 5.3b. A single Co-TCNPP molecule (highlighted in yellow) appears with four bright lobes that correspond to the phenyl moieties.[25,26,37,38] The Co-atom contained in the porphyrin core is not imaged at positive sample bias.[21] In addition, the herringbone reconstruction of the Au(111) surface does not translate through the molecular layer at the given imaging conditions. However, it should be noted that the herringbone reconstruction was observed on bare areas of the Au(111) surface at submonolayer coverage (Figure 5.5a) entering the molecular islands and not avoiding them – which is an indication that it is preserved underneath the molecular layer.

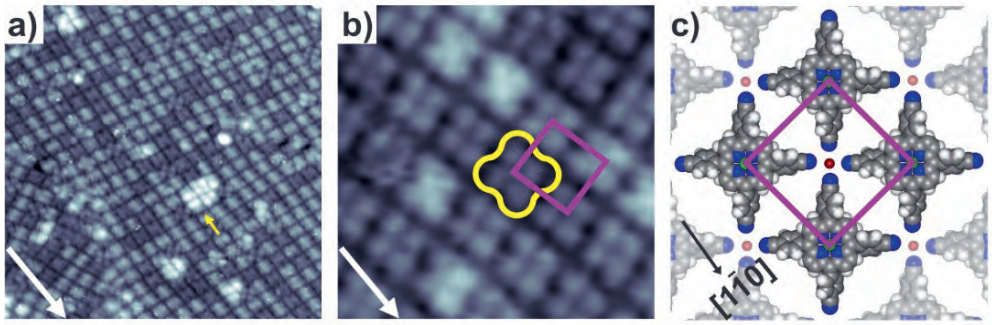

Figure 5.3. Self-assembly of submonolayer coverage of Co-TCNPP on Au(111) after deposition of Fe-atoms: (a) STM image displaying the long-range ordered grid-like MOCN (35 x 35 nm^2, U_{bias} = -1.8 V, I_{set} = 15 pA). The yellow arrow indicates a metallic island composed by Fe-atoms. (b) High-resolution STM image of the grid-like MOCN (10 x 10 nm^2, U_{bias} = 2.2 V, I_{set} = 15 pA). The purple square and yellow outline highlight the unit cell and one Co-TCNPP molecule, respectively. (c) Tentative structural model of the fourfold Fe-coordinated network with the unit cell depicted in purple. In (c) the cobalt, iron, nitrogen, carbon and hydrogen atoms are shown in green, red, blue, gray and white, respectively. In (a) and (b) the white arrow at the bottom denotes the [1$\bar{1}$0] crystallographic direction of the Au substrate. The black arrow at the bottom in (c) denotes the [1$\bar{1}$0] crystallographic direction of the Au substrate.

From the STM and LEED measurements, a molecular overlayer (see Figure A5.1 in the Supporting Information) incommensurate with the Au(111) surface and having a square unit cell (shown in purple in Figure 5.3b and c with lengths a = b = 1.7 ± 0.1 nm and an internal angle of α = 90° ± 1° was deduced. Furthermore, the unit cell is rotated 7.5° with respect to the principal Au directions (see Figure A5.1 in the Supporting Information). A total of one porphyrin is contained in the unit cell, giving a molecular density of 0.31 molecules per nm^2. As observed within a single unit cell, the porphyrins are pointing their cyano endgroups to a common fourfold node.

Due to the repulsive interaction between electronegative N-atoms from the cyano endgroups, the formation of a common fourfold node between them can be ruled out. Thus, as illustrated in the tentative structural model (Figure 5.3c), the grid-like network is a MOCN stabilized by metal-ligand interactions between the Fe-atoms (red sphere) and porphyrins. The porphyrins form a fourfold coordination node through the terminal N-atoms of the cyano endgroups and one Fe-atom (Fe–N distance ~2.5 Å). The metal atoms at the coordination nodes do not contribute to the STM contrast (Figure 5.3), which is common for 3d transition metals in MOCNs on metallic surfaces.[39,40] Porphyrin-based MOCNs exhibiting fourfold coordination nodes have been previously reported for tetracyanophenyl porphyrin derivatives coordinated to Co-atoms supported on a boron nitride/Cu(111) template and to Cu-atoms on Cu(111), respectively.[27,38] Moreover, Co-TCNPP molecules rotated by 45° with respect to neighboring molecules were infrequently found in the fourfold Fe-coordinated network (Figure 5.4b and c). In addition, the large bright islands observed in Figure 5.3a (indicated by the yellow arrow) and Figure 5.5a can be explained by the formation of metal clusters underneath the grid-like network from the surplus of Fe-atoms.[41]

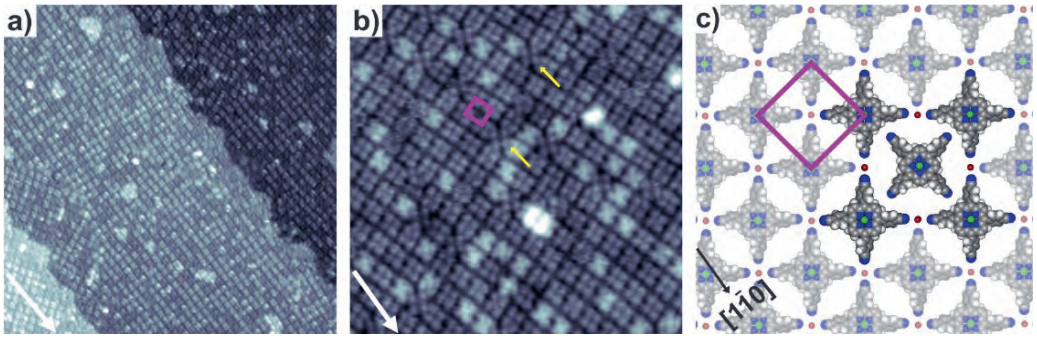

Figure 5.4. STM images of the grid-like MOCN formed by Co-TCNPP on Au(111) after deposition of Fe-atoms. (a) Overview STM image of the long-range ordered MOCN (80 x 80 nm^2, U_{bias} = -1.8 V, I_{set} = 15 pA). The fourfold coordination motif prevails even after exceeding the stoichiometric number of Fe-atoms required for fourfold coordination and atom exchange of the metallic center in the porphyrin core. The excess of iron was found in the form of clusters (large bright regions in the STM image) underneath the 2D plane of the MOCN.[29] (b) STM image of the grid-like network (28 x 28 nm^2, U_{bias} = 2.2 V, I_{set} = 15 pA). The purple square highlights the unit cell, and the yellow arrows denote rotated Co-TCNPP molecules within the MOCN. (c) Tentative structural model of the fourfold Fe-coordinated network with the unit cell depicted in purple. A rotated molecule is added to match the molecular arrangement observed in (b). In (c) the cobalt, iron, nitrogen, carbon and hydrogen atoms are shown in green, red, blue, gray and white, respectively. The black arrow indicates the [1$\bar{1}$0] direction of the Au substrate.

In contrast to the molecular appearance observed in the Co-coordinated fourfold MOCN (Figure 5.2c-e),[21] the main observable peculiarity within the Fe-coordinated grid-like network (Figure 5.3a and b) is the brightness difference between consecutive molecules. The presence of bright and dim molecules at both polarities of the bias voltages – negative (Figure 5.3a) and positive (Figure 5.3b) – may be attributed to two possibilities: (i) an axial ligation of the co-deposited Fe-atoms with the Co-

atom contained in the porphyrin core and/or (ii) an atom exchange reaction between Co and Fe-atoms at the porphyrin core, i.e., the deposited Fe-atoms replaced some of the Co-atoms that were already contained in the starting molecule (Co-TCNPP). Therefore, the grid-like network (Figure 5.3a and b) is composed by two different porphyrins: (i) the starting molecule (Co-TCNPP) and (ii) a molecular species formed after deposition of Fe-atoms. The bright molecules in Figure 5.3b correspond to the newly formed porphyrin by comparing their appearance with Co-TCNPP when imaged at same positive bias (Figure 5.2), where the Co-atom inside the porphyrin core does not contribute to the STM contrast and only four bright lobes can be distinguished.[21] Our results are comparable to the findings reported for a Co-substituted tetraphenyl porphyrin on Ag(111), where the bright protrusions were attributed to Fe-atoms adsorbed on top of the porphyrin core.[42] Furthermore, the studies focusing on the axial ligation of the porphyrin core under UHV conditions have been mainly performed with gaseous diatomic molecules (e.g. CO and NO),[43–48] whereas the interaction with individual atomic species has been rarely addressed.[42] In addition, atom exchange reactions in the porphyrin core are well-known in solution and have also been reported under UHV conditions for porphyrin-like molecules where the Cu-substituted molecules were replaced by Ni- and Fe-atoms, respectively.[13,17]

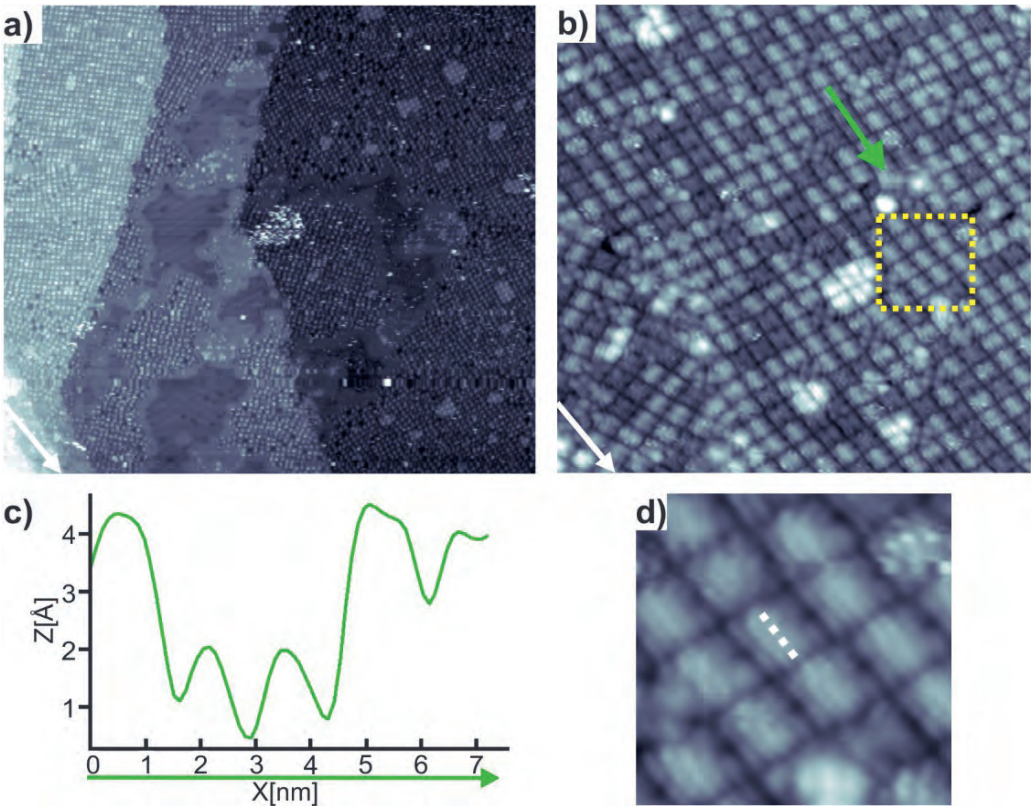

Figure 5.5. (a) Overview STM image of the long-range ordered MOCN (180 x 160 nm^2, U_{bias} = -1.8 V, I_{set} = 15 pA). The clusters of iron formed underneath the MOCN after dosing the sample with excess of Fe-atoms are clearly observable. (b) STM image of the grid-like MOCN with a green line that highlights the line profile shown in (c) (35 x 35 nm^2, U_{bias} = -1.8 V, I_{set} = 15 pA). The yellow dotted square highlights the enlarged area shown in (d). The white arrows at the bottom left of each STM image denote the [1$\bar{1}$0] crystallographic direction of the Au substrate. (c) Height profile of the line scan shown in green in (b), where the apparent heights of the Fe-atoms that sit on top of Co-TCNPP and bare Co-TCNPP are approximately ~4.2 Å and 2 Å, respectively. The direction of the green arrow resembles the direction shown in (b). (d) Enlarged view of the area highlighted by the yellow dotted square in (b) (7 x 7 nm^2, U_{bias} = -1.8 V, I_{set} = 15 pA). The bright protrusion along the long symmetry axis (follow the dashed line) of the porphyrin core is observable

The grid-like network always coexisted with a second 2D network, i.e., the chevron structure shown in Figure 5.6a. The molecular appearance of the porphyrins in the chevron structure (Figure 5.6b) is dominated by four bright lobes. Once again, the herringbone reconstruction of the Au(111) surface remained invisible underneath the 2D network. Based on the STM data, a rectangular unit cell (shown in yellow in Figure 5.6b and c) was obtained with dimensions a = 3.5 ± 0.2 nm and b = 4.2 ± 0.2 nm an internal angle of α = 90° ± 3°. A total of four porphyrins are contained in the unit cell, giving a molecular density of 0.27 molecules per nm^2. The porphyrins are grouped in pairs that gave rise to rows of molecules, in which the pairs from neighboring rows are chiral images of each other as highlighted by the orange and white rectangles in Figure 5.6b. The bonding motifs that stabilize the chevron structure are shown in the tentative structural model (Figure 5.6c) and will be explained by looking at a single porphyrin molecule and its surroundings. Three cyano endgroups of one porphyrin molecule are coordinating to one Fe-atom (solid red oval), while the fourth cyano endgroup interacts via H-bonding (dashed green oval) with a H-atom from the phenyl moiety of a neighboring porphyrin. By repetition of such arrangement, the chevron structure is a MOCN stabilized by a distorted threefold metal-coordination (solid red oval) and H-bonding (dashed green oval). Furthermore, the distortion of the threefold coordination node arises from an asymmetrical arrangement of the porphyrins involved in metal-coordination, i.e., the angle between the porphyrins involved in threefold metal-coordination diverges from 120°, which is the value reported for threefold coordination motifs on metal surfaces.[49] The typical invisibility of 3d transition metals at the coordination nodes of MOCNs prevails for the chevron structure at both, positive and negative bias (Figure 5.7).[39,40] Similar

to the Fe-coordinated grid-like network (Figure 5.3a and b), the varying contrast between dim and bright molecular species is also present in the chevron structure (Figure 5.6a and b), which suggests the presence of Co-TCNPP and some porphyrins with a Fe-atom as an axial ligand on the porphyrin core and/or substituting the initial Co-atom by means of an atom exchange reaction. To gain deeper insight into this aspect, a bias-dependent experiment for the chevron structure was performed (Figure 5.7). The four bright lobe contrast is present at positive bias and a square-like shape of the porphyrin macrocycle dominates at negative bias for Co-TCNPP. By analogy with the results obtained for Co-TCNPP with Co-atoms on Au(111),[21] the porphyrin core within the Co-coordinated structure remained dim for all molecules at positive bias (Figure 5.2), which is opposite to the observed brightness difference in the chevron structure stabilized by Fe-atoms (Figure 5.6b). The porphyrins that contain one bright protrusion (highlighted by the white arrow in Figure 5.7) at all voltages can be attributed to Co-TCNPP species that contain one Fe-atom as an axial ligand on top of its core (Figure 5.7). The possibility of having one Fe-atom as an axial ligand on the porphyrin core and/or substituting the Co-atom of the starting molecule will be addressed in the discussion section (*vide infra*).

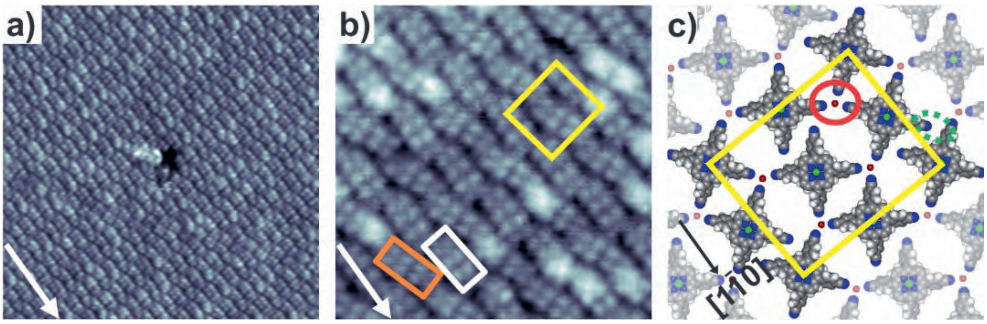

Figure 5.6. Self-assembly of submonolayer coverage of Co-TCNPP on Au(111) after deposition of Fe-atoms: (a) STM image of the chevron structure (50 x 50 nm^2, U_{bias} = 2 V, I_{set} = 15 pA). The black region in the center of the image corresponds to missing Co-TCNPP molecules. (b) Close-up STM image of the chevron structure (18 x 18 nm^2, U_{bias} = 3 V, I_{set} = 15 pA). The yellow rectangle highlights the unit cell, while the white and orange rectangles highlight two mirrored pairs of Co-TCNPP molecules between two rows of molecules. (c) Tentative structural model of the chevron structure with the unit cell depicted in yellow. The solid red and dotted green ovals highlight the Co-coordination and H-bonding motifs, respectively. In (c) the cobalt, iron, nitrogen, carbon and hydrogen atoms are shown in green, red, blue, gray and white, respectively. In (a) and (b) the white arrow at the bottom denotes the [1$\bar{1}$0] crystallographic direction of the Au substrate. The black arrow at the bottom in (c) denotes the [1$\bar{1}$0] crystallographic direction of the Au substrate.

The chevron structure always coexisted as a minority phase with the grid-like network. A 20:80 coverage ratio was found between both MOCNs for samples prepared at submonolayer coverage (~0.85 ML). It should be noted that the chevron structure did not form as one exclusive phase irrespective of the molecular coverage. In contrast, the grid-like network formed as one exclusive phase upon deposition of the required stoichiometric amount of Co-TCNPP and Fe-atoms for a full monolayer of fourfold MOCN. The 2D structure and bonding motifs of the Fe-coordinated MOCNs of Co-

TCNPP are in agreement with our previous results obtained for Co-TCNPP on Au(111) upon coordination with Co-atoms.[21]

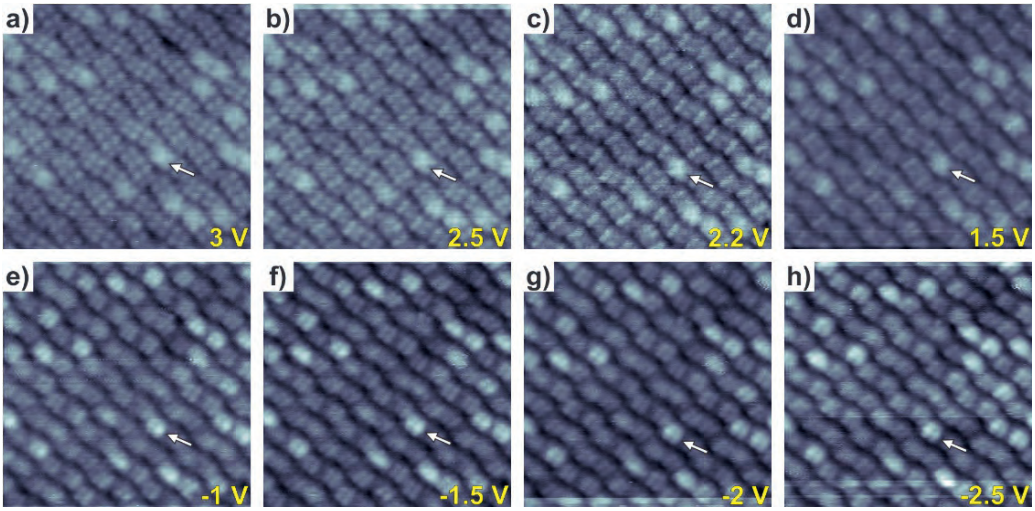

Figure 5.7. (a)-(h) Bias-dependent STM images of the chevron structure of Co-TCNPP on Au(111) (20 x 20 nm^2, I_{set} = 15 pA). The appearance of the functional endgroups and metal atoms in the porphyrin core is strongly bias-dependent. The typical invisibility of 3d transition metals at the coordination nodes of MOCNs prevails at positive and negative bias. The Co-TCNPP molecules with a Fe-atom on top are imaged as a brighter species compared with bare Co-TCNPP molecules. The bias voltage (U_{bias}) is indicated in yellow in the bottom right of each STM image. The white arrows serve as a reference to one specific porphyrin (see text).

Zn-TPyP on Au(111) after Fe-coordination. The deposition of submonolayer coverage of Zn-TPyP molecules (Figure 5.1b) on Au(111) and subsequent addition of Fe-atoms followed by post-annealing at 440 K and keeping a fixed molecule-metal ratio (~1:1 with a slight excess of metal), gave rise to the coexistence of two different 2D networks as shown in Figure 5.8: (i) a chain-like network (Figure 5.8a) and (ii) grid-like network (Figure 5.8c). We will focus on the long-range ordered chain-like network first (Figure

5.12). The STM image in Figure 5.8a shows details of the molecular appearance and orientation of the Zn-TPyP molecules within the chain-like network. At first glance, the molecules arrange in two types of parallelly oriented rows (highlighted by the solid and dashed orange lines). Within one type of row, the yellow outline highlights the rectangular shape of a single Zn-TPyP molecule with its pyridyl endgroups imaged as four small dim lobes located at the surrounding of each molecule (emphasized by the green dots in Figure 5.8a). The rectangular shape is given by the saddle-shape conformation adopted by Zn-TPyP upon adsorption, which creates two different side lengths by tilting upwards one pair of opposing pyrrole moieties (long symmetry axis), while tilting downwards the remaining pair due to steric hindrance between the H-atoms of the pyrrole moieties from the porphyrin core and the pyridyl endgroups, with the latter being tilted ~60° out of the plane of the porphyrin macrocycle, as previously reported for the pyridyl endgroups of tetrapyridyl porphyrin derivatives on Ag(111) and Au(111), respectively.[28,33] This shape is representative of pyridyl substituted porphyrins by imaging its occupied states at negative bias voltage.[28,33] Furthermore, the molecules appear to be alternately rotated by 90° with respect to their long symmetry axis (highlighted by the yellow and white lines in Figure 5.8a) within a single row of molecules, this arrangement is given by steric repulsion between the H-atoms from neighboring molecules.[28,33] Based on the STM data, a unit cell (shown in blue) with lengths $a = 1.4 \pm 0.2$ nm and $b = 4.0 \pm 0.1$ nm and an internal angle of $\alpha = 57° \pm 3°$ was obtained. There are two Zn-TPyP molecules per unit cell giving a molecular density of 0.40 molecules per nm^2.

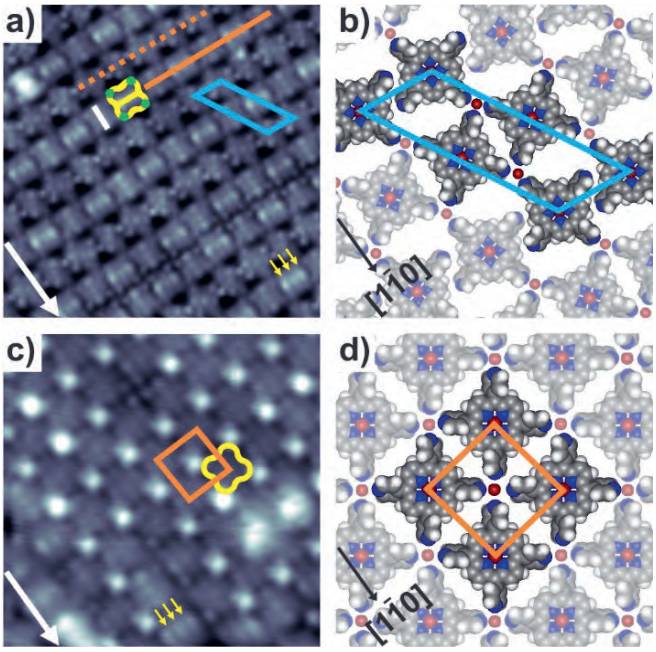

Figure 5.8. Self-assembly of Zn-TPyP on Au(111) after deposition of Fe-atoms: (a) High-resolution STM image of the threefold Fe-coordinated chain-like network (15 x 15 nm^2, U_{bias} = -0.9 V, I_{set} = 20 pA). The blue parallelogram depicts the oblique unit cell. The yellow and white outlines highlight two alternating Zn-TPyP molecules given by the saddle-shape conformation of the porphyrin macrocycle. The solid and dashed orange lines correspond to two different parallel rows of molecules. (b) Tentative structural model of the threefold Fe-coordinated chain-like network with the unit cell depicted in blue. (c) High-resolution STM image of the fourfold Fe-coordinated network (10 x 10 nm^2, U_{bias} = -1.6 V, I_{set} = 15 pA). The orange square and yellow outline highlight the unit cell and one Zn-TPyP molecule, respectively. (d) Tentative structural model of the fourfold Fe-coordinated network with the unit cell depicted in orange. In (b) and (d) the iron, nitrogen, carbon, and hydrogen atoms are shown in red, blue, gray, and white, respectively. In (a) and (c) the white arrow at the bottom denotes the [1$\bar{1}$0] crystallographic direction of the Au substrate. The black arrow at the bottom in (b) and (d) denotes the [1$\bar{1}$0] crystallographic direction of the Au substrate.

Herein, the intermolecular interactions of the porphyrins within the two types of parallelly oriented rows (highlighted by the orange lines in Figure 8a) will be addressed. The solid orange line highlights a row of alternating porphyrins that follow a head-to-head configuration pointing their pyridyl endgroups towards each other, similar to the molecular orientation reported for Fe-coordinated one-dimensional chains of H_2-TPyP molecules on Au(111).[28] The dashed orange line is added to distinguish the second type of molecular row, in which the alternating molecules are pointing their pyridyl endgroups towards the macrocycle of a neighboring molecule. This orientation is comparable to the one described for H_2-TPyP on Ag(111).[33] The interaction between consecutive (parallel) rows creates a common threefold node between the pyridyl endgroups from three different porphyrins. By taking steric repulsion into consideration, a threefold node between the N-atoms of the pyridyl endgroups without a metallic atom between them can be neglected. Therefore, as illustrated in the tentative structural model (Figure 5.8b) the chain-like network is a MOCN stabilized by two types of interactions: (i) a distorted threefold Fe-coordination motif between the pyridyl endgroups from three different molecules and one Fe-atom (red sphere) with a Fe–N distance of ~2.3 Å and (ii) H-bonding between the pyridyl's terminal N-atom and a H-atom from a neighboring pyrrole moiety (H-bonding occurs along the molecular row that is highlighted by the dashed orange line).

One relevant observable feature within the chain-like network is the long bright protrusion composed by three maxima (highlighted by the three yellow arrows) along the main symmetry axis of each molecule. The STM image of the H-bonded network of Zn-TPyP on Au(111) (Figure 5.9) serves as a comparison for the contrast observed at the porphyrin core in the absence

of Fe-atoms and has been previously reported.[50] The dark spot or depression in the porphyrin core is given by the fully occupied d-orbital ($3d^{10}$) of the Zn-atom which does not contribute to the STM contrast (Figure 5.9).[51] However, as shown in Figure 5.8a and in the bias-dependent STM images of the chain-like network (Figure 5.10a-d), the contrast of the three bright maxima (the white arrows mark a reference point to guide the eye) is resilient at various voltages (within the range of -0.9 to -2 V as mentioned in the STM data), which is an indication of an atom exchange reaction between Zn and Fe-atoms in the porphyrin core. The observed brightness in the porphyrin core is well in line with previous literature of Fe-substituted tetrapyridyl and tetraphenyl porphyrin networks on Au(111) and Ag(111).[30,34,52–55] The formation of the three maxima can be explained by a combination between the saddle-shape conformation of Zn-TPyP on the Au(111) surface and the replacement of Zn-atoms by Fe-atoms, where the maxima located at the edges of the porphyrin core (Figure 5.8a) can be assigned to the two upper tilted pyrrole moieties and the central maximum is given by a Fe-atom that replaced the Zn-atoms of Zn-TPyP. Such molecular appearance has been reported for Fe-TPyP molecules on metal surfaces.[34,52] It should be noted that the long bright protrusion is only observed on the long symmetry axis of the molecule.

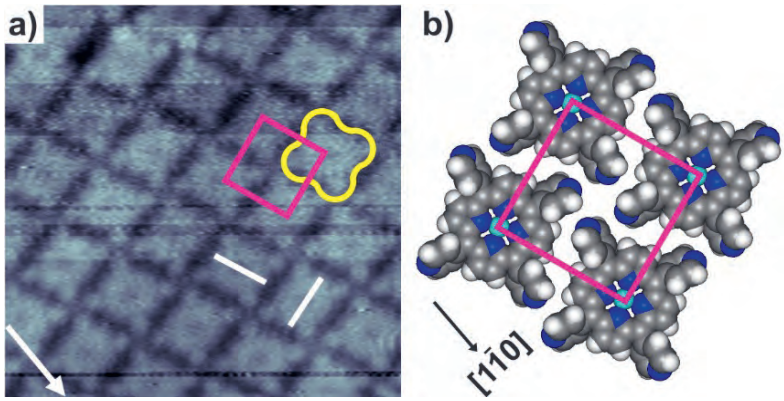

Figure 5.9. (a) STM image of the close-packed H-bonded network of Zn-TPyP on Au(111) (8 x 8 nm^2, U_{bias} = 2 V, I_{set} = 20 pA). The pink square and yellow outline highlight the unit cell and one porphyrin, respectively. The set of white lines highlight two alternating Zn-TPyP molecules given by the saddle-shape conformation of the porphyrin macrocycle. The white arrow at the bottom left denotes the [1$\bar{1}$0] crystallographic direction of the Au substrate. (b) Tentative structural model of the close-packed H-bonded network with the unit cell shown in pink. The zinc, nitrogen, carbon and hydrogen atoms are shown in turquoise, blue, gray and white, respectively. The black arrow indicates the [1$\bar{1}$0] direction of the Au substrate.

The chain-like network coexisted with a second 2D network which will be referred as the grid-like network (Figure 5.8c). The STM image (Figure 5.8c) shows tightly packed porphyrins. Similar as in the chain-like network, a single porphyrin (highlighted in yellow) is imaged as a rectangle and the pyridyl endgroups are imaged as small dim lobes located at the edges of each porphyrin. Once again, the saddle-shape conformation and alternating out of plane rotation of the pyridyl endgroups (~60°) create two different side lengths that lead to the rectangular shape of the porphyrin macrocycle. This adsorption conformation of the porphyrin core is in line with previous reports

of tetrapyridyl porphyrin assemblies on Ag(111) and Au(111), respectively.[28,33] The STM contrast observed in the porphyrin core is outweighed by the bright spots located in its periphery. These bright spots might correspond to Fe-atoms, which is not typical for 3d transition metals found in MOCNs (*vide infra*). We attribute this appearance to a tip-induced effect, i.e., a functionalized tip. Furthermore, the herringbone reconstruction of the Au(111) surface is preserved underneath the molecular layer (Figure 5.11).

From the STM measurements, a unit cell (shown in orange) with lengths a = 1.4 ± 0.1 nm and b = 1.4 ± 0.2 nm and an internal angle of α = 90° ± 2° was proposed. The unit cell contains one molecule giving a molecular density of 0.47 molecules per nm^2. The Zn-TPyP molecules align their pyridyl endgroups towards a common fourfold node which suggests the presence of a metal-ligand interaction between Fe-atoms (bright spots in Figure 5.8c) and pyridyl endgroups. We rule out the possibility of a common fourfold node between the N-atoms of the pyridyl endgroups due to steric repulsion. Thus, as depicted in the tentative structural model (Figure 5.8d), the grid-like network can be regarded as a MOCN stabilized by a fourfold Fe-coordination node formed between the terminal N-atoms from four pyridyl endgroups belonging to different porphyrin molecules and one Fe-atom (red sphere) acting as the coordination node with a Fe–N distance of ~2.2 Å. The molecular arrangement of the grid-like network is in agreement with the assembly described for pyridyl-substituted porphyrins after coordination with Fe-atoms on Au(111).[5,28,29]

The set of bias-dependent STM images (Figure 5.10e-h) justify the presence of the fourfold Fe-coordination motif in the grid-like network. The white arrows mark a reference point to guide the eye. At low negative bias

voltage (Figure 5.10e), the pyridyl endgroups are imaged as dim protrusions in the periphery of the Zn-TPyP molecules and the Fe-atoms do not contribute to the STM contrast. As the negative bias voltage approaches to higher negative values (Figure 5.10f-h), the contrast of the Fe-atoms at the coordination nodes increases and overcomes the contribution of the pyridyl endgroups. At the highest negative bias voltage (Figure 5.10h), the Fe-atoms appear as bright spots and the pyridyl endgroups are barely visible. The STM contrast of the porphyrin core was not able to outweigh the contribution given by the coordinating Fe-atoms, most likely because of the tip-induced effect caused during data acquisition. By taking a closer look at the porphyrin core (Figure 5.8c), the three maxima (highlighted by the yellow arrows) along the molecular axis are reminiscent of the appearance encountered in the chain-like network, which confirms that the atom exchange reaction between Zn and Fe-atoms also holds for the grid-like network.

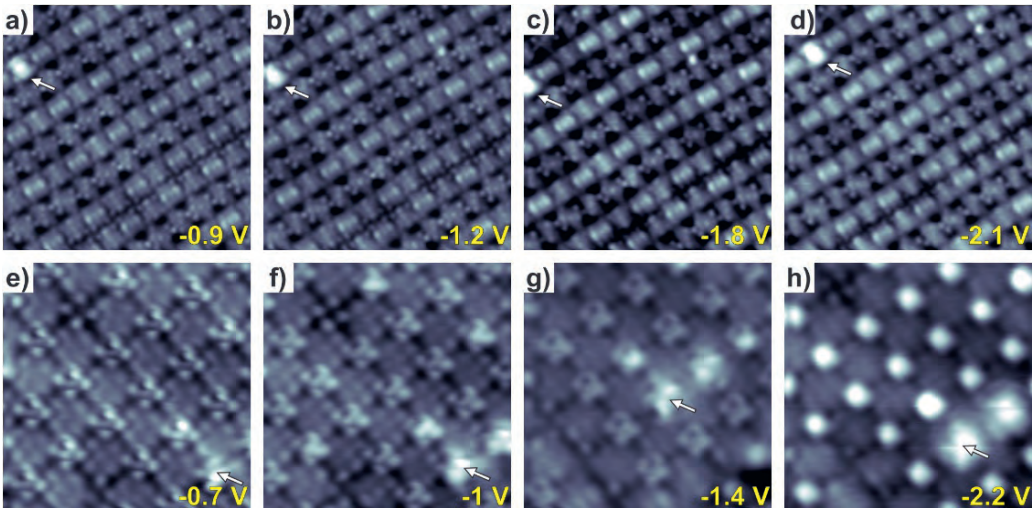

Figure 5.10. Bias-dependent STM images of the MOCNs formed by Zn-TPyP on Au(111) after deposition of Fe-atoms: (a)-(d) threefold Fe-coordinated network (15 x 15 nm^2, I_{set} = 20 pA). The porphyrin core is distinguished by three protrusions attributed to a central Fe-atom and two upward tilt pyrrole moieties due to the saddle-shape conformation of Zn-TPyP. (e)-(h) Fourfold Fe-coordinated network (7 x 7 nm^2, I_{set} = 20 pA). The appearance of the functional endgroups and iron atoms at the coordination nodes is strongly bias-dependent. The Fe-coordination nodes are observed as bright spots. The bias voltage (U_{bias}) for each STM image is indicated in yellow in the bottom right of each STM image. The white arrows serve as a guide to the eye to one specific feature (see text).

The grid-like network always coexisted as a minority phase with the chain-like network in a 10:90 coverage ratio (for the given preparation conditions) between both MOCNs formed by Zn-TPyP molecules. Both MOCNs of Zn-TPyP were also stable at low molecular coverage (Figure 5.11 and Figure 5.12). However, the grid-like network did not form as one exclusive phase. In addition, a fourfold coordination motif can be seen in the lower half of the STM image (Figure 5.8a) shown for the chain-like network. The presence of such motif can be regarded as a kinetically trapped phase

since annealing the Au(111) substrate at 420 K while depositing Fe-atoms prompted the formation of the chain-like network as one exclusive phase (Figure 5.12a).

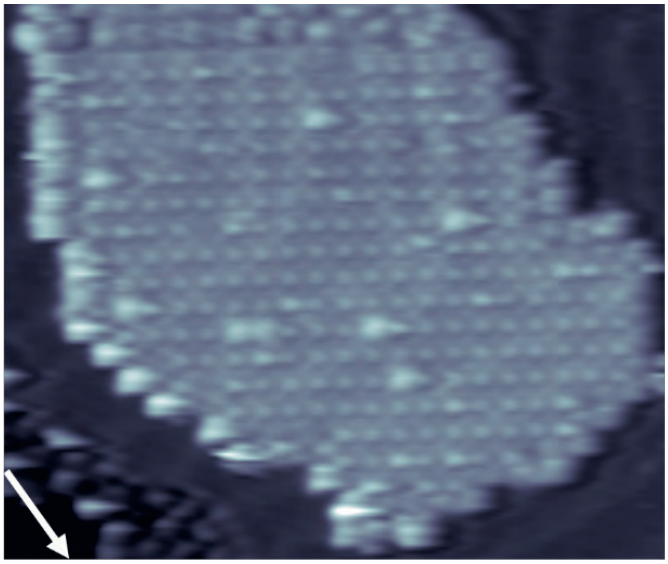

Figure 5.11. STM image of an island of the fourfold Fe-coordinated network of Zn-TPyP on Au(111) (35 x 30 nm^2, U_{bias} = -1.5 V, I_{set} = 15 pA). The Fe-coordination nodes are imaged as bright spots. The white arrow at the bottom left denotes the $[1\bar{1}0]$ direction of the Au substrate.

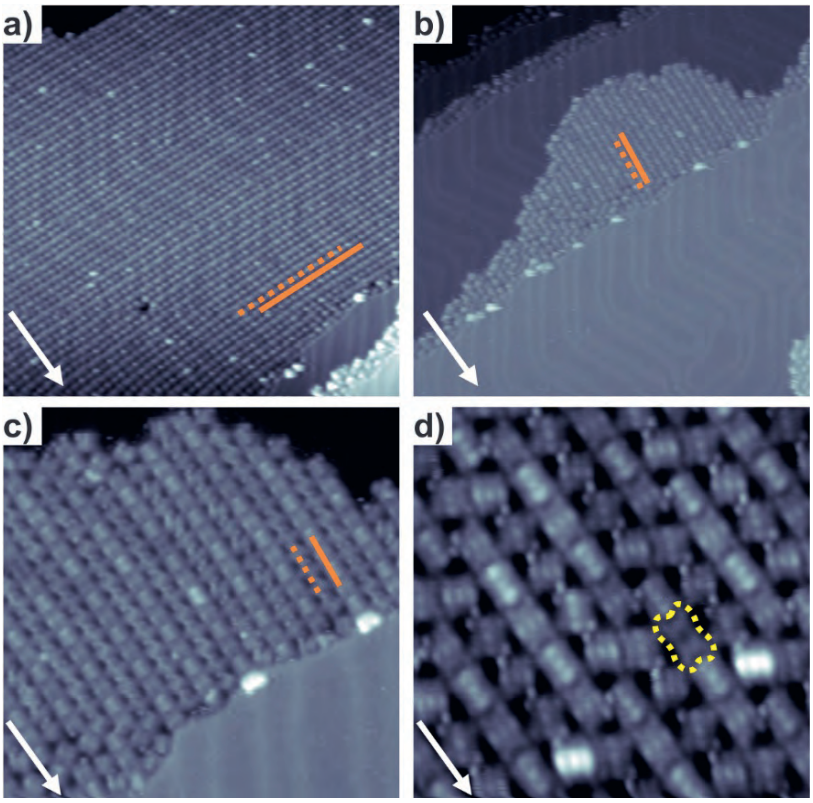

Figure 5.12. STM images of the threefold Fe-coordinated network of Zn-TPyP on Au(111) showing: (a) the long-range order of the MOCN (80 x 80 nm^2, U_{bias} = -1.5 V, I_{set} = 20 pA), (b) the growth of the MOCN from a step edge (80 x 80 nm^2, U_{bias} = -1.5 V, I_{set} = 20 pA) and (c) zoom-in of the same region in (b) (30 x 30 nm^2, U_{bias} = -1.5 V, I_{set} = 20 pA). In (a)-(c) the solid and dashed orange lines highlight two different parallel rows of molecules: the solid line is superimposed on a row of molecules that follow an arrangement similar to a 1-D coordinated chain, while the dashed line highlights a parallel row of molecules linked by H-bonding. (d) STM image of an infrequently found arrangement of the threefold Fe-coordinated network (15 x 15 nm^2, U_{bias} = -1.5 V, I_{set} = 20 pA). The dashed yellow outline is added on a porphyrin that contains a dark depression in its center, which is attributed to the absence of a metallic atom in its core. The white arrows at the bottom left of each STM image denote the [1$\bar{1}$0] direction of the Au substrate.

5.4 Discussion

Our discussion is aimed to explain two relevant topics in the following order: (I) the influence of the co-deposited Fe-atoms on the porphyrin core of Co-TCNPP and Zn-TPyP in view of either triggering an atom exchange reaction or the formation of an axial ligand on the porphyrin core. (II) A comparison of the influence of the functional endgroups from each porphyrin in the formation of different Fe-coordinated MOCNs.

(Ia) Influence of the co-deposited Fe-atoms on the porphyrin core of Co-TCNPP. Since the STM contrast in metalloporphyrins is strongly mediated through the orbitals of 3d transition metals contained in the porphyrin core, the varying brightness between consecutive molecules within the MOCNs was the observable fingerprint available to determine if an atom exchange reaction or axial ligation occurred in the porphyrin core after the deposition of the Fe-atoms.[34,53,54,56,57] The STM contrast observed for Co-TCNPP in the absence of Fe-atoms (Figure 5.2) is in line with the reported appearance for Co-substituted porphyrins; the typical four bright lobe contrast at positive bias and the long bright protrusion along the long molecular axis (highlighted by the white dotted line in Figure 5.2d) at negative bias.[25,53,56,58] However, for the Fe-coordinated networks of Co-TCNPP (grid-like network and chevron structure in Figure 5.3a and Figure 5.6a, respectively), the increased STM contrast stemming from the core of some molecules – in comparison with the appearance of Co-TCNPP with Co-atoms (Figure 5.2) – suggested a modification in the porphyrin core induced by the co-deposited Fe-atoms either as an (i) axial ligand on the core or (ii) atom exchange reaction.

We will first address the possibility of an axial ligation on top of the porphyrin core. The position of the bright centers in the porphyrin core of both networks (grid-like network and chevron structure in Figure 5.3b and Figure 5.6b, respectively) is off-centered and remained unaffected even when imaged at positive bias. In order to gain further insight, we performed bias-dependent imaging (ranging from positive to negative bias) for the chevron structure (Figure 5.7). The molecules with enhanced STM contrast (one marked by the white arrow in Figure 5.7) remained bright irrespective of the bias polarity. As previously reported, the porphyrin core of Fe-substituted porphyrins on metal substrates does not contribute to the STM contrast depending on the value of the applied positive bias as its LUMO does not mediate electron tunneling.[34,48] In addition, the bright STM contrast independent of the applied bias does not convey the overall emblem that is characteristic for Fe-substituted porphyrins when imaged at negative bias, i.e., three maxima along the long molecular axis of the porphyrin backbone or a dumbbell-like appearance depending on the applies bias.[34,52,53] On the other hand, the appearance of the other (dim) molecules was modified with the applied bias and even displayed the typical four bright lobe contrast when imaged at positive bias (Figure 5.7a and b), which is in line with the appearance of Co-TCNPP molecules. The enhanced STM contrast of the molecules displaying an off-centered brightness with respect to the porphyrin core can be explained by the bonding of one Fe-atom as an axial ligand on top of the porphyrin core. Therefore, the increased height of the Fe-atoms with respect to the molecular plane of the 2D MOCNs confers them a brighter STM contrast than its surrounding, i.e., the Fe-atom bonded on top of the porphyrin core sits higher than any other adsorbate on the Au(111) surface. These findings are well in line with a previous report of the adsorption of Fe-

atoms as axial ligands on the porphyrin core of Co-substituted tetraphenylporphyrins on Ag(111).[42] In this study, the Fe-atoms were not adsorbed centered and occupied one of four equivalent positions of the porphyrin core, for which each equivalent position is composed by the hexamer formed by two neighboring pyrrole moieties of the porphyrin core, i.e., the Co–N–C–C–C–N cyclic subunit.[42] Within our study, we attribute a similar adsorption geometry to the co-deposited Fe-atoms (observed in Figure 5.3b and Figure 5.6b). In addition, the height profiles (Figures 5.5b and c) of bare Co-TCNPP and Fe on top of Co-TCNPP are ~2 Å and 4.2 Å, respectively and are in line with the previously reported values of Fe-atoms sitting on top of Co-substituted tetraphenyl porphyrins on Ag(111).[42]

Based on these arguments, an atom exchange reaction between the co-deposited Fe-atoms and Co-atoms in Co-TCNPP seems unlikely. However, we do not fully rule out this possibility since some of these molecules do not resemble the off-centered brightness which was attributed to the axial ligation of Fe-atoms bonded on top of the porphyrin core. Instead, they display a very bright protrusion along their long symmetry axis after Fe-deposition (as observed in Figure 5.3a, Figure 5.4a and Figure 5.5d), which is in line with the previously reported appearance of Fe-substituted porphyrins when imaged at negative bias.[34,52,53] The difference in STM contrast between Co-TCNPP and the (possibly) Fe-substituted porphyrins can be explained by the population of the d-orbital of the Co and Fe-atoms contained in the porphyrin core, respectively. The Co-atom has a $3d^7$ electronic configuration with its energy levels distributed far enough from each other that allows them to be resolved by changing the polarity of the applied bias (Figure 5.2).[53,59] In contrast, the Fe-atom has a $3d^6$ electronic configuration with its energy levels too close to each other, which makes it complicated to resolve different

energy levels in Fe-substituted porphyrins within the same polarity of the applied bias, i.e., for Fe-substituted porphyrins a four bright lobe contrast prevails at positive bias, while a long bright protrusion is observed at negative bias.[34,53,60]

Despite that enough Fe-atoms were added to cover or replace all the Co-atoms contained in the Co-TCNPP molecules deposited on the Au(111) surface, the yield of brighter molecules after Fe-deposition was around one third as revealed by the STM images (Figure 5.3). Although, the detailed mechanisms of an axial ligation or atom exchange reaction in the porphyrin core are beyond the scope of this publication and the capabilities of a typical STM measurement, we assume that a similar value of binding energies for the Co and Fe-atoms can explain why most Fe-atoms bonded to the porphyrin core in an off-centered configuration on top of the porphyrin core instead of replacing the Co-atoms.[61] In summary, most bright molecules possess a Fe-atom bonded on top of its core, while some molecules might have experienced an atom exchange reaction where the Co-atom of the starting molecules was replaced by one of the co-deposited Fe-atoms.

(Ib) Influence of the co-deposited Fe-atoms on the porphyrin core of Zn-TPyP. A slightly different scenario was observed for both MOCNs of Zn-TPyP (Figure 5.8) in comparison with the MOCNS of Co-TCNPP. As previously mentioned, the long bright protrusion composed by three maxima along the main symmetry axis of the porphyrin correlates to the fingerprint observed for Fe-substituted porphyrins functionalized with pyridyl endgroups when imaged at negative bias.[34,52,53] This molecular appearance was present for all the porphyrins in the chain-like and grid-like networks and differs completely from the dark depression observed for Zn-substituted porphyrins (Figure 5.9).[50,51,62] The fully occupied d-orbital ($3d^{10}$) of Zn-atoms in

combination with the larger calculated HOMO-LUMO gap for Zn-substituted porphyrins compared to Fe-substituted porphyrins (*vide supra*) explains its dark appearance under STM.[61] The atom exchange reaction between Zn and Fe-atoms was fully efficient as revealed by the STM images (Figure 5.8 and Figure 5.12) and correlates to the lower binding energy towards the porphyrin core found for Zn-atoms with respect to Fe-atoms.[61] Therefore, the energy barrier that a Fe-atom must overcome to replace a Zn-atom must be lower than the barrier to replace the Co-atom and agrees with the universal stability order found for metal porphyrins, where metals with an increased occupation of the d-orbital – such as Zn-atoms – have lower stability within the porphyrin core.[17,61,63]

(II) Fe-coordinated MOCNs: influence of the functional endgroups. Herein, the influence of the functional endgroups (e.g., cyano and pyridyl) of each porphyrin in the formation of different bonding motifs will be addressed along with the coordination geometries of the Fe-atoms stabilizing each MOCN. In 3D crystalline structures Fe-atoms prefer tetrahedral and octahedral coordination geometries.[64] However, MOCNs on surfaces were found to be stabilized by two, three and fourfold in-plane Fe-coordination motifs.[5,28–32,65]

(IIa) Co-TCNPP. For the MOCNs formed by Co-TCNPP, the grid-like network (Figure 5.3a) was stabilized by a fourfold Fe-coordination motif and the chevron structure (Figure 5.6a) by a distorted threefold Fe-coordination motif as well as H-bonding. These results are structurally equivalent to the results obtained in our previous study of Co-TCNPP on Au(111) upon coordination with Co-atoms (Figure 5.2).[21] However, the herringbone reconstruction of the Au(111) surface did not translate through the molecular layer of the Fe-coordinated MOCNs (Figure 5.3), which might

suggest a stronger molecule-substrate interaction compared with our results of the Co-coordinated MOCNs of Co-TCNPP on Au(111), where the herringbone reconstruction remained visible through the 2D network after depositing Co-atoms.[21] However, as previously mentioned, the herringbone reconstruction was observed on bare areas of the Au(111) surface at submonolayer coverage (Figure 5.5a) entering the molecular islands and not avoiding them – which is an indication that it is preserved underneath the molecular layer. Furthermore, we propose that the Fe-atoms located at the coordination nodes of the grid-like network are interacting through a square planar coordination geometry with four (in-plane) cyano endgroups.[28,29] On the other hand, the Fe-atoms stabilizing the chevron structure adopted a distorted tetrahedral coordination geometry between three cyano endgroups and the Au substrate that acts as the fourth ligand. Furthermore, no site-specific interactions were observed for the Fe-coordinated MOCNs of Co-TCNPP (Figure 5.3) as supported by the absence of integer matrix elements in the superstructure matrix of the simulated LEED pattern (see Figure A5.1 in the Supporting Information).[66,67]

(IIb) Zn-TPyP. For the MOCNs formed by Zn-TPyP, the chain-like network (Figure 5.8a) exhibited a combination of an in-plane threefold Fe-coordination motif and H-bonding. In this arrangement, the Fe-atoms bonded to the pyridyl endgroups and Au substrate follow a tetrahedral coordination geometry, as expected for Fe-atoms in 3D structures. However, in-plane threefold Fe-coordination has not been reported up to now for long-range ordered MOCNs formed by tetrapyridyl-porphyrins on metal surfaces, where two and fourfold coordination motifs prevail.[5,28–30] The second MOCN of Zn-TPyP, i.e, the grid-like network of Zn-TPyP (Figure 5.8c) was a minority phase in which the Fe-atoms arranged in an in-plane fourfold node following

a square planar coordination geometry.[28,29] This can be explained by the fact that the pyridyl endgroups on a surface possess less degrees of freedom than a smaller and linear cyano endgroup. Furthermore, the herringbone reconstruction remained intact for both of these MOCNs (Figure 5.11 and Figure 5.12), meaning that the intermolecular interactions (between molecules and Fe-atoms) are most likely stronger than the molecule-substrate interactions.

By comparing the structure of the MOCNs formed by both molecules (Figure 5.1), they were able to form similar coordination environments (three- and fourfold motifs) with the Fe-atoms through their terminal N-atoms. However, as observed by the STM images (Figure 5.3, 5.6 and 5.8), the structural differences between the cyanophenyl and pyridyl endgroups either allowed or obstructed the formation of higher coordination motifs within the 2D plane of the MOCN. For instance, the linear conformation of the cyano endgroups of Co-TCNPP in the grid-like network (Figure 5.3a) favored the formation of a higher coordination motif (e.g. fourfold Fe-coordination) in the 2D plane of the MOCN compared with the threefold motif of the chain-like network of Zn-TPyP (Figure 5.8a). The spatial constraints that pyridyl endgroups introduce has been previously reported, where they favored two and threefold coordination motifs.[27,68–70] For obvious reasons, the low preference of the fourfold motif encountered for Zn-TPyP (Figure 5.8c) was corroborated when only threefold nodes were formed by annealing the Au substrate during Fe-deposition. Therefore, the grid-like network of Zn-TPyP can be considered as a kinetically trapped phase that can transform into the thermodynamically favored chain-like network. As for the cyano endgroups in Co-TCNPP, their reduced steric hindrance compared with its pyridyl analogue, favored the formation of fourfold nodes. This was confirmed by the

formation of the grid-like network as a majority phase over the chevron structure. In summary, the cyano endgroups preferred coordinating with the Fe-atoms in an in-plane fourfold geometry, whereas the pyridyl endgroups adopted a threefold node due to steric repulsion.

The aforementioned MOCNs can be compared in terms of Gibbs free energy since self-assembly is a thermodynamically driven process.[71] For Co-TCNPP, the grid-like network minimizes the surface area through its higher molecular density compared with the chevron structure and allows the formation of the square planar coordination geometry for the Fe-atoms, which differs from the coordination geometry expected for Fe-atoms in 3D structures.[64] In addition, the grid-like network lowers the energy of the system since only metal-ligand interactions take place in comparison with the chevron structure that possesses H-bonding along with metal-ligand interactions. Furthermore, the molecule-substrate interactions are most likely comparable for both MOCNs since no site-specific positions were observed, i.e., the MOCNs are not commensurate with the Au substrate.

In the case of Zn-TPyP (Figure 5.8a), the chain-like network, despite its lower molecular density and the presence of H-bonding in comparison with the grid-like network (Figure 5.8c), lowers the overall energy of the system by having the Fe-atoms arranged in the coordination geometry expected for 3D structures (favored due to the spatial constraints of the pyridyl endgroups) and is observed as one exclusive phase upon annealing. Similar to the MOCNs of Co-TCNPP, the molecule-substrate interactions for both MOCNs of Zn-TPyP are comparable since no preferential orientation with respect to the surface was observed.

Therefore, the functional endgroups in porphyrins can steer the formation of structurally different MOCNs. In addition, the atom exchange reaction between 3d transition metals in the porphyrin core on metal surfaces is achievable under UHV and its degree of exchange depends on the chemical nature of the metal atoms involved.

5.5 Conclusions

In the present study, the influence of the deposition of Fe-atoms on the self-assembly of two porphyrin derivatives (Co-TCNPP and Zn-TPyP) was investigated by STM under UHV conditions. Special attention was given to the possibility of 2D MOCN formation, atom exchange reaction in the porphyrin core and bonding of the Fe-atoms on top of the porphyrin core. Upon deposition of Fe-atoms, each porphyrin gave rise to the coexistence of two structurally different Fe-coordinated MOCNs stabilized by three- or fourfold Fe-coordination nodes. However, the structural differences between both functional endgroups (cyano and pyridyl endgroups in Co-TCNPP and Zn-TPyP, respectively) strictly determined the formation of a specific in-

plane coordination motif. As evidenced by STM, the linear conformation of the cyano endgroups (Co-TCNPP) allowed the formation of a higher in-plane coordination motif as the majority phase, i.e., fourfold Fe-coordination (grid-like network) over threefold Fe-coordination (chevron structure). In contrast, the steric hindrance that pyridyl endgroups (Zn-TPyP) encounter in higher coordination motifs favored the formation of threefold Fe-coordination nodes (chain-like network) over fourfold Fe-coordination (fourfold coordinated network). In the case of Co-TCNPP, the grid-like network reduced the overall energy of the system, i.e., by densely packing the molecules (reducing surface area covered by Co-TCNPP) and forming metal-ligand interactions only, the grid-like network was favored over the chevron structure. In the case of Zn-TPyP, the higher surface area of the chain-like network was compensated by the reduction of steric hindrance between neighboring pyridyl endgroups and by having the Fe-atoms in a tetrahedral coordination geometry, which is the coordination geometry expected for Fe-atoms in 3D-structures.

In addition, within each MOCN, the presence of molecules with a brighter STM contrast in each MOCN – compared with their 2D assemblies prior to Fe-deposition – served as the fingerprint to determine if the Fe-atoms interacted with the porphyrin core either by: (i) bonding as an axial ligand on the core or (ii) replacing the preexisting metal atom via an atom exchange reaction. The yield of brighter molecules was lower for Co-TCNPP (~one third of the molecules on the surface) than for Zn-TPyP (~100%). However, the molecular appearance of the bright Co-TCNPP molecules differed from that of the bright Zn-TPyP molecules, i.e., an off-centered brightness in some Co-TCNPP molecules suggested that the Fe-atoms did not replace the Co-atom but instead bonded on top of the porphyrin core. On the other hand, the bright Zn-TPyP molecules resembled the molecular appearance of Fe-TPyP

– meaning that the Fe-atoms atoms replaced the Zn-atoms via an atom exchange reaction. This behavior was explained by the lower binding energy that Zn-atoms possess towards the porphyrin core in comparison with Co-atoms. On the other hand, despite that Fe and Co-atoms possess similar binding energies towards the porphyrin core, the Fe-atoms were not able to replace the Co-atoms and instead bonded on top of the porphyrin core. However, based on the STM contrast of some bright Co-TCNPP molecules, we did not rule out the possibility of having some Co-atoms replaced by Fe-atoms when enough thermal energy was supplied to the system through the post-annealing treatment during Fe-deposition. In summary, the choice of the functional endgroups in metalloporphyrins will strongly influence the coordination geometry for the metal-atoms stabilizing the MOCN. In addition, atom exchange reactions are achievable under UHV and their yield is dependent on, among others, the chemical nature of the metal atoms involved, i.e., their binding energy towards the porphyrin core. In the present study, both metal-ligand interactions and atom exchange reactions were observed. Further studies are required to address which of these reactions takes place first.

5.6 References

1. Oohora, K.; Hayashi, T. Hemoprotein-Based Supramolecular Assembling Systems. *Curr. Opin. Chem. Biol.* **2014**, *19*, 154–161.
2. Chae, S. H.; Yoo, K.; Lee, Y. S.; Cho, M. J.; Kim, J. H.; Ko, M. J.; Lee, S. J.; Choi, D. H. Novel π-Extended Porphyrin Derivatives for Use in Dye-Sensitized Solar Cells. *J. Porphyrins Phthalocyanines* **2014**, *18*, 569–578.
3. Hadmojo, W. T.; Lee, U.-H.; Dajeong, Y.; Kim, H. W.; Jang, W.-D.; Yoon, S. C.; Jung, I. H.; Jang, S. High-Performance Near-Infrared Absorbing n-Type Porphyrin Acceptor for Organic Solar Cells. *ACS Appl. Mater. Interfaces* **2018**, *10*, 41344–41349.
4. Lvova, L.; Mastroianni, M.; Pomarico, G.; Santonico, M.; Pennazza, G.; Di Natale, C.; Paolesse, R.; D'Amico, A. Carbon Nanotubes Modified with Porphyrin Units for Gaseous Phase Chemical Sensing. *Sens. Actuators.* **2012**, *170*, 163–171.
5. Wurster, B.; Grumelli, D.; Hötger, D.; Gutzler, R.; Kern, K. Driving the Oxygen Evolution Reaction by Nonlinear Cooperativity in Bimetallic Coordination Catalysts. *J. Am. Chem. Soc.* **2016**, *138*, 3623–3626.
6. Tempas, C. D.; Morris, T. W.; Wisman, D. L.; Le, D.; Din, N. U.; Williams, C. G.; Wang, M.; Polezhaev, A. V; Rahman, T. S.; Caulton, G.; et al. Redox-Active Ligand Controlled Selectivity of Vanadium Oxidation on Au(100). *Chem. Sci.* **2018**, *9*, 1674–1685.
7. Auwärter, W.; Écija, D.; Klappenberger, F.; Barth, J. V. Porphyrins at Interfaces. *Nat. Chem.* **2015**, *7*, 105–120.
8. Gottfried, J. M. Surface Chemistry of Porphyrins and Phthalocyanines. *Surf. Sci. Rep.* **2015**, *70*, 259–379.
9. Schneider, J.; Kollho, F.; Bernardi, J.; Kaftan, A.; Libuda, J.; Berger, T.; Laurin, M.; Diwald, O. Porphyrin Metalation at the MgO Nanocube/Toluene Interface. *ACS Appl Mater Interfaces*, **2015**, *7*, 22962-22969.
10. Lavallee, D. K. Kinetics and Mechanisms Reactions of Metalloporphyrin. *Coord. Chem. Rev.* **1985**, *61*, 55–96.
11. Hambright, P.; Batini, I.; Spasojevi, I. Phyrins : Kinetics of Copper(II) and Zinc(II) Incorporation and Zinc Porphyrin Demetalation. *J. Porphyrins Phthalocyanines* **2003**, *7*, 139–146.
12. Buchler, J. W. *Porphyrins and Metalloporphyrins*; Smith, K. M., Ed.; Asmterdam, 1975.
13. Diller, K.; Papageorgiou, A. C.; Klappenberger, F.; Allegretti, F.; Barth, J. V.; Auwärter, W. In Vacuo Interfacial Tetrapyrrole Metallation. *Chem Soc Rev* **2016**, *45*, 1629–1656.
14. Marbach, H. Surface-Mediated *in Situ* Metalation of Porphyrins at the Solid−Vacuum Interface. *Acc. Chem. Res.* **2015**, *48*, 2649–2658.
15. Doyle, C. M.; Krasnikov, S. A.; Sergeeva, N. N.; Preobrajenski, A. B.; Vinogradov, N. A.; Sergeeva, Y. N.; Senge, O. M.; Cafolla, A. A. Evidence for

the Formation Metalation of Tetra(4-Bromophenyl)-Porphyrin on the Cu(111) Surface. *Chem. Commun.* **2011**, *47*, 12134–12136.
16. Doyle. Ni–Cu Ion Exchange Observed for Ni(II)-porphyrins on Cu(111). *Chem. Commun.* **2014**, 50, 3447–3449.
17. Rieger, A.; Schnidrig, S.; Probst, B.; Ernst, K. H.; Wäckerlin, C. Ranking the Stability of Transition-Metal Complexes by On-Surface Atom Exchange. *J. Phys. Chem. Lett.* **2017**, *8*, 6193–6198.
18. Shen, K.; Narsu, B.; Ji, G.; Sun, H.; Hu, J.; Liang, Z.; Gao, X.; Li, H.; Li, Z.; Song, B.; et al. On-Surface Manipulation of Atom Substitution Between Cobalt Phthalocyanine and the Cu(111) Substrate. *RSC Adv*. **2017**, *7*, 13827–13835.
19. Hötger, D.; Abufager, P.; Morchutt, C.; Alexa, P.; Grumelli, D.; Dreiser, J.; Stepanow, S.; Gambardella, P.; Busnengo, H. F.; Etzkorn, M.; et al. On-Surface Transmetalation of Metalloporphyrins. *Nanoscale* **2018**, *10*, 21116–21122.
20. Hötger, D.; Etzkorn, M.; Morchutt, C.; Wurster, B.; Dreiser, J.; Stepanow, S.; Grumelli, D.; Gutzler, R.; Kern, K. Stability of Metallo-Porphyrin Networks under Oxygen Reduction and Evolution Conditions in Alkaline Media. *Phys. Chem. Chem. Phys.* **2019**, *21*, 2587–2594.
21. Baker Cortés, B. D.; Schmidt, N.; Enache, M.; Stöhr, M. Coverage-Dependent Structural Transformation of Cyano- Functionalized Porphyrin Networks on Au(111) via Addition of Cobalt Atoms. *J. Phys. Chem. C* **2019**, *123*, 19681–19687.
22. Baker Cortés, B. D.; Stöhr, M. Role of Cyano Groups in the Self-Assembly of Organic Molecules on Metal Surfaces. In *Encyclopedia of Interfacial Chemistry*; Wandelt, K., Ed.; Elsevier, **2018**; Vol. 4, pp 153–165.
23. Yokoyama, T.; Yokoyama, S.; Kamikado, T.; Okuno, Y.; Mashiko, S. Selective Assembly on a Surface of Supramolecular Aggregates with Controlled Size and Shape. *Nature* **2001**, 413, 619–621.
24. Pham, T. A.; Song, F.; Alberti, M. N.; Nguyen, M.-T.; Trapp, N.; Thilgen, C.; Diederich, F.; Stöhr, M. Heat-Induced Formation of One-Dimensional Coordination Polymers on Au(111): An STM Study. *Chem. Commun.* **2015**, 51, 14473−14476.
25. Lepper, M.; Schmitt, T.; Gurrath, M.; Raschmann, M.; Zhang, L.; Stark, M.; Hölzel, H.; Jux, N.; Meyer, B.; Schneider, M. A.; et al. Adsorption Behavior of a Cyano-Functionalized Porphyrin on Cu(111) and Ag(111): From Molecular Wires to Ordered Supramolecular Two-Dimensional Aggregates. *J. Phys. Chem. C* **2017**, *121*, 26361–26371.
26. Urgel, J. I.; Ecija, D.; Auwärter, W.; Stassen, D.; Bonifazi, D.; Barth, J. V. Orthogonal Insertion of Lanthanide and Transition-Metal Atoms in Metal–Organic Networks on Surfaces. *Angew. Chemie. Int. Ed.* **2015**, *127*, 6261–6165.
27. Bischoff, F.; He, Y.; Seufert, K.; Stassen, D.; Bonifazi, D.; Barth, J. V.; Auwärter, W. Tailoring Large Pores of Porphyrin Networks on Ag(111) by Metal–Organic Coordination. *Chem. Eur. J.* **2016**, *22*, 15298–15306.
28. Wang, Y.; Zhou, K.; Ma, Y. Structural Reconstruction and Spontaneous

Formation of Fe Polynuclears: A Self-Assembly of Fe–Porphyrin Coordination Chains on Au (111) Revealed by Scanning Tunneling Microscopy. *Phys. Chem. Chem. Phys.* **2016**, *18*, 14273–14278.

29. Lin, T.; Kuang, G.; Wang, W.; Lin, N. Two-Dimensional Lattice of Out-of-Plane Dinuclear Iron Centers Exhibiting Kondo Resonance. *ACS Nano* **2014**, *8*, 8310–8316.
30. Liu, B.; Fu, H.; Guan, J.; Shao, B.; Meng, S.; Guo, J. An Iron-Porphyrin Complex with Large Easy-Axis Magnetic Anisotropy on Metal Substrate. *ACS Nano* **2017**, *11*, 11402–11408.
31. Shi, Z.; Lin, N. Structural and Chemical Control in Assembly of Multicomponent Metal–Organic Coordination Networks on a Surface. *J. Am. Chem. Soc.* **2010**, *132*, 10756–10761.
32. Mao, X. F.; Lin, T.; Adisoejoso, J.; Shi, Z.; Shang, X. S.; Liu, P. N.; Lin, N. Coordination Self-Assembly of Bromo-Phenyl and Pyridyl Functionalized Porphyrins with Fe on an Au(111) Surface. *Phys. Chem. Chem. Phys.* **2013**, *15*, 12447–12450.
33. Auwärter, W.; Weber-Bargioni, A.; Riemann, A.; Schiffrin, A.; Gröning, O.; Fasel, R.; Barth, J. V. Self-Assembly and Conformation of Tetrapyridyl-Porphyrin Molecules on Ag(111). *J. Chem. Phys.* **2006**, *124*, 194708/1-194708/6.
34. Auwärter, W.; Weber-Bargioni, A.; Brink, S.; Riemann, A.; Schiffrin, A.; Ruben, M.; Barth, J. V. Controlled Metalation of Self-Assembled Porphyrin Nanoarrays in Two Dimensions. *ChemPhysChem* **2007**, *8*, 250–254.
35. Horcas, I.; Fernández, R.; Gómez-Rodríguez, J. M.; Colchero, J.; Gómez-Herrero, J.; Baro, A. M. WSXM: A Software for Scanning Probe Microscopy and a Tool for Nanotechnology. *Rev. Sci. Instrum* **2007**, *78*, 013705.
36. Hermann, K.; van Hove, M. A. LEEDpat4.2 (LEED pattern analyzer). http://www.fhi-berlin.mpg.de/KHsoftware/LEEDpat/index.html (accessed Sep 21, 2018).
37. Auwärter, W.; Seufert, K.; Klappenberger, F.; Reichert, J.; Weber-Bargioni, A.; Verdini, A.; Cvetko, D.; Dell'Angela, M.; Floreano, L.; Cossaro, A.; et al. Site-Specific Electronic and Geometric Interface Structure of Co-Tetraphenyl-Porphyrin Layers on Ag(111). *Phys. Rev. B* **2010**, *81*, 245403/1-245403/14.
38. Urgel, J. I.; Schwarz, M.; Garnica, M.; Stassen, D.; Bonifazi, D.; Ecija, D.; Barth, J. V.; Auwärter, W. Controlling Coordination Reactions and Assembly on a Cu(111) Supported Boron Nitride Monolayer. *J. Am. Chem. Soc.* **2015**, *137*, 2420–2423.
39. Björk, J.; Matena, M.; Dyer, M. S.; Enache, M.; Lobo-checa, J.; Gade, L. H.; Jung, T. A.; Stöhr, M.; Persson, M. STM Fingerprint of Molecule–Adatom Interactions in a Self-Assembled Metal–Organic Surface Coordination Network on Cu(111). *Phys. Chem. Chem. Phys.* **2010**, *12*, 8815–8821.
40. Henningsen, N.; Rurali, R.; Limbach, C.; Drost, R.; Pascual, J. I.; Franke, K. J. Site-Dependent Coordination Bonding in Self-Assembled Metal–Organic

Networks. *J. Phys. Chem. Lett.* **2011**, *2*, 55–61.
41. Buchner, F.; Kellner, I.; Steinrück, H-.P.; Marbach. H. Modification of the Growth of Iron on Ag(111) by Predeposited Organic Monolayers. *Z. Phys. Chem.* **2009**, *223*, 131–144.
42. Vijayaraghavan, S.; Auwärter, W.; Ecija, D.; Seufert, D.; Rusponi, S.; Houwaart, T.; Sautet, P.; Bocquet, M.-L.; Thakur, P.; Stepanow, S.; Schlickum, U.; Etzkorn, M.; Brune, H.; Barth, J. V. Restoring the Co Magnetic Moments at Interfacial Co-Porphyrin Arrays by Site-Selective Uptake of Iron. *ACS Nano* **2015**, 9, 3605–3616.
43. Seufert, K.; Auwärter, W.; Barth, J. V. Discriminative Response of Surface-Confined Metalloporphyrin Molecules to Carbon and Nitrogen Monoxide. *J. Am. Chem. Soc.* **2010**, 132, 18141–18146.
44. Wäckerlin, C.; Chylarecka, D.; Kleibert, A.; Müller, K.; Lacovita, C.; Nolting, F.; Jung, T. A.; Ballav, N. Controlling Spins in Adsorbed Molecules by a Chemical Switch. *Nat. Commun*. **2010**, 1, 1–7.
45. Hieringer, W.; Flechtner, K.; Kretschmann, A.; Seufert, K.; Auwärter, W.; Barth, J. V.; Görling, A.; Steinrück, H.-P.; Gottfried, J. M. The Surface Trans Effect: Influence of Axial Ligands on the Surface Chemical Bonds of Adsorbed Metalloporphyrins. *J. Am. Chem. Soc.* **2011**, 133, 6206–6222.
46. Miguel, J.; Hermanns, C. F.; Bernien, M.; Krüger, A.; Kuch, W. Reversible Manipulation of the Magnetic Coupling of Single Molecular Spins in Fe-Porphyrins to a Ferromagnetic Substrate. *J. Phys. Chem. Lett.* **2011**, 2, 1455–1459.
47. Kim, H.; Chang, Y. H.; Lee, S.-H.; Kim, Y.-H.; Kahng, S.-J. Switching and Sensing Spin States of Co-Porphyrin in Bimolecular Reactions on Au(111) Using Scanning Tunneling Microscopy. *ACS Nano* **2013**, 7, 9312–9317.
48. Wäckerlin, C.; Nowakowski, J.; Liu, S.-X.; Jaggi, M.; Siewert, D.; Girovsky, J.; Shchyrba, A.; Hählen, T.; Kleibert, A.; Oppeneer, P. M.; Nolting, F.; Decurtins, S.; Jung, T. A.; Ballav, N. Two-Dimensional Supramolecular Electron Spin Arrays. *Adv. Mater*. **2013**, 25, 2404–2408.
49. Schlickum, U.; Decker, R.; Klappenberger, F.; Zoppellaro, G.; Klyatskaya, S.; Ruben, M.; Silanes, I.; Arnau, A.; Kern, K.; Brune, H.; et al. Metal–Organic Honeycomb Nanomeshes with Tunable Cavity Size. *Nano Lett.* **2007**, *7*, 3813–3817.
50. Shi, Z.; Lin, N. Self-Assembly of a Two-Dimensional Bimetallic Coordination Framework and Dynamic Control of Reversible Conversions to Homo-Metallic Hydrogen-Bond Arrays. *ChemPhysChem* **2010**, *11*, 97–100.
51. Yoshimoto, S.; Tsutsumi, E.; Suto, K.; Honda, Y.; Itaya, K. Molecular Assemblies and Redox Reactions of Zinc (II) Tetraphenylporphyrin and Zinc (II) Phthalocyanine on Au(111) Single Crystal Surface at Electrochemical Interface. *Chem. Phys.* **2005**, *319*, 147–158.
52. Zotti, L. A.; Teobaldi, G.; Hofer, W. A.; Auwa, W.; Barth, J. V. Ab-Initio Calculations and STM Observations on Tetrapyridyl and Fe(II)-Tetrapyridyl-

Porphyrin Molecules on Ag(111). *Surf. Sci.* **2007**, *601*, 2409–2414.
53. Buchner, F.; Warnick, K.; Wo, T.; Go, A.; Hieringer, W.; Marbach, H. Chemical Fingerprints of Large Organic Molecules in Scanning Tunneling Microscopy: Imaging Adsorbate–Substrate Coupling of Metalloporphyrins. *J. Phys. Chem. C* **2009**, 16450–16457.
54. Wang, W.; Pang, R.; Kuang, G.; Shi, X.; Shang, X.; Liu, P. N.; Lin, N. Intramolecularly Resolved Kondo Resonance of High-Spin Fe(II)-Porphyrin Adsorbed on Au(111). *Phys. Rev. B: Condens. Matter Mater. Phys.* **2015**, *91*, No. 045440.
55. Buchner, F.; Schwald, V.; Comanici, K.; Steinrück, H.-P.; Marbach, H. Microscopic Evidence of the Metalation of a Free-Base Porphyrin Monolayer with Iron. *ChemPhysChem* **2007**, *8*, 241–243.
56. Houwaart, T.; Le Bahers, T.; Sautet, P.; Auwärter, W.; Seufert, K.; Barth, J. V; Bocquet, M.-L. Surface Science Scrutinizing Individual CoTPP Molecule Adsorbed on Coinage Metal Surfaces from the Interplay of STM Experiment and Theory. *Surf. Sci.* **2015**, *635*, 108–114.
57. Comanici, K.; Buchner, F.; Flechtner, K.; Lukasczyk, T.; Gottfried, J. M.; Steinrück, H. P.; Marbach, H. Understanding the Contrast Mechanism in Scanning Tunneling Microscopy (STM) Images of an Intermixed Tetraphenylporphyrin Layer on Ag(111). *Langmuir* **2008**, *24*, 1897–1901.
58. Brede, J.; Linares, M.; Kuck, S.; Schwöbel, J.; Scarfato, A.; Chang, S. H.; Hoffmann, G.; Wiesendanger, R.; Lensen, R.; Kouwer, P. H. J.; et al. Dynamics of Molecular Self-Ordering in Tetraphenyl Porphyrin Monolayers on Metallic Substrates. *Nanotechnology* **2009**, *20*, 275602/1-275602/10.
59. Lu, X.; Hipps, K. W.; Wang, X. D.; Mazur, U. Scanning Tunneling Microscopy of Metal Phthalocyanines: d^7 and d^9 Cases. *J. Am. Chem. Soc.* **1996**, *118*, 7197–7202.
60. Lu, X.; Hipps, K. W. Scanning Tunneling Microscopy of Metal Phthalocyanines: d^6 and d^8 Cases. *J. Phys. Chem. B* **1997**, *101*, 5391–5396.
61. Liao, M.-S.; Scheiner, S. Electronic Structure and Bonding in Metal Porphyrins, Metal=Fe, Co, Ni, Cu, Zn. *J. Chem. Phys.* **2002**, *117*, 205–219.
62. Ruggieri, C.; Rangan, S.; Bartynski, R. A.; Galoppini, E. Zinc(II) Tetraphenylporphyrin Adsorption on Au(111): An Interplay between Molecular Self-Assembly and Surface Stress. *J. Phys. Chem. C* **2015**, *119*, 6101–6110.
63. Feixas, F.; Sola, M.; Swart, M. Chemical Bonding and Aromaticity In Metalloporphyrins. *Can. J. Chem.* **2009**, *87*, 1063–1073.
64. Venkataraman, D.; Du, Y.; Wilson, S. R.; Hirsch, K. A.; Zhang, P.; Moore, J. S. A Coordination Geometry Table of the d-Block Elements and Their Ions. *J. Chem. Educ.* **1997**, *8*, 915–918.

65. Shi, Z.; Liu, J.; Lin, T.; Xia, F.; Liu, P. N.; Lin, N. Thermodynamics and Selectivity of Two-Dimensional Metallo-Supramolecular Self-Assembly Resolved at Molecular Scale. *J. Am. Chem. Soc.* **2011**, *133*, 6150–6153.
66. Buchner, F.; Zillner, E.; Röckert, M.; Gläßel, S.; Steinrück, H.-P.; Marbach, H. Substrate-Mediated Phase Separation of Two Porphyrin Derivatives on Cu(111). *Chem. Eur. J.* **2011**, *17*, 10226–10229.
67. Yanagi, H.; Mukai, H.; Ikuta, K.; Shibutani, T.; Kamikado, T.; Yokoyama, S.; Mashiko, S. Molecularly Resolved Dynamics for Two-Dimensional Nucleation of Supramolecular Assembly. *Nano Lett.* **2002**, *2*, 601–604.
68. Li, Y.; Xiao, J.; Shubina, T. E.; Chen, M.; Shi, Z.; Schmid, M.; Steinrück, H.-P.; Gottfried, J. M.; Lin, N. Coordination and Metalation Bifunctionality of Cu with 5,10,15,20-Tetra(4- Pyridyl)Porphyrin: Toward a Mixed-Valence Two-Dimensional Coordination Network. *J. Am. Chem. Soc.* **2012**, *134*, 6401–6408.
69. Heim, D.; Seufert, K.; Auwärter, W.; Aurisicchio, C.; Fabbro, C.; Bonifazi, D.; Barth, J. V. Surface-Assisted Assembly of Discrete Porphyrin-Based Cyclic Supramolecules. *Nano Lett.* **2010**, *10*, 122–128.
70. Heim, D.; Écija, D.; Seufert, K.; Auwärter, W.; Aurisicchio, C.; Fabbro, C.; Bonifazi, D.; Barth, J. V. Self-Assembly of Flexible One-Dimensional Coordination Polymers on Metal Surfaces. *J. Am. Chem. Soc.* **2010**, *132*, 6783–6790.
71. Enache, M.; Maggini, L.; Llanes-Pallas, A.; Jung, T. A.; Bonifazi, D.; Stöhr, M. Coverage-Dependent Disorder-to-Order Phase Transformation of a Uracil Derivative on Ag(111). *J. Phys. Chem. C* **2014**, *118*, 15286–15291.

5.7 Appendix

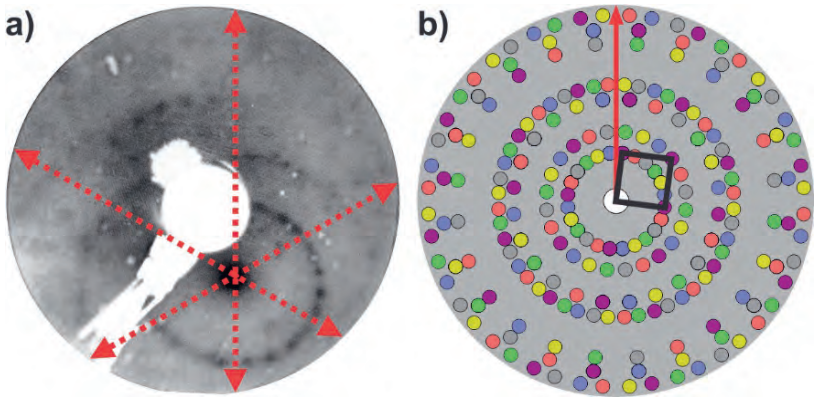

Figure A5.1. (a) LEED pattern of the fourfold Fe-coordinated network formed by Co-TCNPP on Au(111) after deposition of Fe-atoms (E_{beam} = 14.6 eV). The red dotted arrows indicate the principal directions of the Au(111) surface (b) Simulated LEED pattern of the fourfold Fe-coordinated network illustrating a unit cell (shown in black). The circles in different colors indicate rotationally equivalent and mirrored domains. The red solid arrow indicates the principal direction of the Au(111) surface. The superstructure of the simulated LEED pattern is described by the matrix notation $\begin{pmatrix} 6.6 & 0.9 \\ 2.7 & 7.1 \end{pmatrix}$.

Chapter 6

6 Structural Transformation of Surface-Confined Porphyrin Networks via Addition of Co-atoms

The self-assembly process of a nickel-porphyrin derivative (Ni-DPPyP) containing two pyridyl coordinating sites and two pentyl chains at trans *meso* positions under ultrahigh vacuum on Au(111) was studied with scanning tunneling microscopy (STM), X-ray photoelectron spectroscopy (XPS) and low energy electron diffraction (LEED). Deposition of Ni-DPPyP onto Au(111) gave rise to a close-packed network for coverages smaller or equal to one monolayer as revealed by STM and LEED. The molecular arrangement of this two-dimensional network is stabilized via hydrogen bonds formed between the pyridyl's nitrogen and hydrogen atoms from the pyrrole groups of neighboring molecules. Subsequent deposition of cobalt atoms onto the close-packed network and post-deposition annealing at 423 K led to the formation of a Co-coordinated hexagonal porous network. As confirmed by XPS measurements, the porous network is stabilized by metal-ligand interactions between one cobalt atom and three pyridyl ligands, each pyridyl ligand coming from a different Ni-DPPyP molecule.

6.1 Introduction

The well-established protocols of supramolecular chemistry have opened an alternate pathway for the bottom-up fabrication of nanostructures on surfaces.[1–3] In particular, the possibility of designing self-assembled two-dimensional (2D) networks on noble metal surfaces formed by a countless variety of organic building blocks interconnected by metal-ligand interactions – better known as metal-organic coordination networks (MOCNs) – have

been a subject of study due to their intriguing properties and prospective usage in technological applications.[4–8] To this end, porphyrins are known to be highly versatile building blocks for the construction of metal-directed 2D assemblies since their macrocycle can be decorated with different substituents that can coordinate to metal atoms in a variety of distinctive coordination geometries.[7,9–13] However, the formation of porphyrin-based MOCNs exhibiting a porous structure, *i.e.*, with cavities in the order of a few nm, have been rarely reported.[14–16] Furthermore, the (structural) properties of porous MOCNs allows them to be used as hosts for guest molecules and for the fabrication of quantum corrals. Moreover, porous MOCNs can possess intriguing magnetic properties by the inclusion of magnetic centers within their structure, *e.g.*, through metalation of the porphyrin core. [6,14,15,17– 20]

The characterization of MOCNs on noble metal surfaces has been achieved, in most of the cases, by means of scanning tunneling microscopy (STM) owing to its supreme imaging capabilities under ultra-high vacuum (UHV) conditions. Surprisingly, the use of photoemission spectroscopies, that is X-ray photoelectron spectroscopy (XPS) – which does not only provide information about the elements present on the surface but also about their chemical state – has been rarely used to characterize MOCNs, *i.e.*, to investigate the fingerprint of the metal-ligand interactions.[21] Furthermore, XPS measurements can be used to determine if the metal-ligand interaction only affects the chemical state of the coordinating atom or if it influences additional atoms such as the entire coordinating group or molecule.

Herein, we report the self-assembly process of nickel(II) 5,15-dipentyl-10,20-(4-yl-pyridine)porphyrin (Ni-DPPyP)[16] before and after coordination with Co-atoms on Au(111) by means of STM, XPS and low-energy electron diffraction (LEED). As shown in Scheme 1, Ni-DPPyP is a Ni-substituted porphyrin derivative functionalized at *trans meso* positions by two pyridyl and two pentyl chains. As revealed by STM and LEED measurements, the deposition of Ni-DPPyP on Au(111) gave rise to the formation of long-range ordered close-packed assemblies stabilized by H-bonds. The C 1s and N 1s core level XPS spectra were acquired to give insight to the chemical composition of the Ni-DPPyP on Au(111) prior to Co-deposition. The binding energy (BE) values for both core levels were in agreement with the previously reported peak positions for N-atoms involved in H-bonding.[21–23] The deposition of Co-atoms at room-temperature (RT) and post-deposition annealing at 423 K prompted a structural transformation, *i.e.*, the close-packed assembly rearranged into a hexagonal porous network as observed with STM and LEED. This hexagonal network contains pores that are arranged by a total of six molecules and each pore is interconnected by three-fold Co-coordination nodes. The transformation from a H-bond to a metal-ligand interaction by deposition of the Co-atoms was corroborated by the marked chemical shifts of the N 1s and C 1s XPS signals toward higher BE. Our results are in agreement with the 2D assemblies reported in our previous study of the free-base version of Ni-DPPyP on Ag(111).[16]

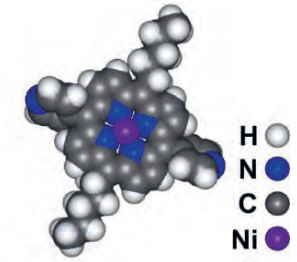

Scheme 1. Schematic molecular structure of nickel(II) 5,15-dipentyl-10,20-(4-yl-pyridine)porphyrin (Ni-DPPyP).

6.2 Experimental Methods

The experiments were carried out in two ultra-high vacuum (UHV) systems (with a base pressure in the 5 x 10^{-10} mbar regime) equipped with different chambers for sample preparation and characterization. The UHV systems host a STM (Scienta Omicron GmbH) that was either operated at (i) room temperature and (ii) 77 K. The Au(111) single crystal was cleaned by repeated cycles of Ar^+ sputtering and annealing at 750 K. The porphyrin derivatives (Ni-DPPyP)[16] were sublimed at 460 K onto the Au(111) surface using a home-built evaporator. Cobalt atoms were deposited onto the Ni-DPPyP layer from a cobalt rod using an e-beam evaporator (Oxford Applied Research). During both depositions (molecule and metal) the Au(111) substrate was held at RT. The molecule and metal deposition rates were monitored with a quartz crystal microbalance. The STM measurements were performed in the constant current mode with a tip which was mechanically cut from a Pt/Ir (90/10 chemical composition) wire. All bias voltages are given with respect to a grounded tip. The STM images were processed with WSxM software.[24] Additionally, the LEED patterns were acquired using a commercial LEED setup (Specs ErLEED 150) and simulated with LEEDPat4.2 software.[25] Furthermore, the XPS measurements were

performed at the I09 beam line at the Diamond Light Source (Oxfordshire, UK). Sample preparation and measurements were performed *in situ* under UHV conditions. As confirmed by the LEED measurements at the I09 beam line, the structural arrangement of both networks (close-packed and porous) was successfully reproduced. The analysis chamber contained a VG Scienta EW4000 HAXPES hemispherical photoelectron analyzer. The C 1s and N 1s core level spectra were acquired using a photon energy of 500 eV, while the Ni $2p_{3/2}$ spectra were acquired with a photon energy of 2.67 keV. The BE scale of the XPS data was calibrated to the $Au4f_{7/2}$ peak at 84.0 eV. For all the spectra a linear background was subtracted. The XPS spectra were fitted with Voigt profiles (convolution of a Gaussian and a Lorentzian).

6.3 Results and Discussion

Upon deposition of a submonolayer of Ni-DPPyP on Au(111) at RT, a close-packed assembly was formed as shown in the overview STM image of Figure 6.1. Two different rotational domains (I and II) of the network can be observed on each side of the step edge of the Au substrate. In addition, the intact herringbone reconstruction of the Au substrate beneath the organic layer implies a weak molecule-substrate interaction (Appendix Figure A6.1). The dotted white square in Figure 6.1a corresponds to the area from which the bias dependent STM images of Ni-DPPyP (Figure 6.1b) were acquired. The pyridyl and pentyl endgroups are imaged as bright round and long protrusions (at all given biases), respectively. One Ni-DPPyP molecule is added to guide the eye. The out-of-plane rotation of the pyridyl endgroups with respect to the porphyrin macrocycle confers them with an enhanced STM contrast over the

remnant moieties of Ni-DPPyP.[16,26,27]

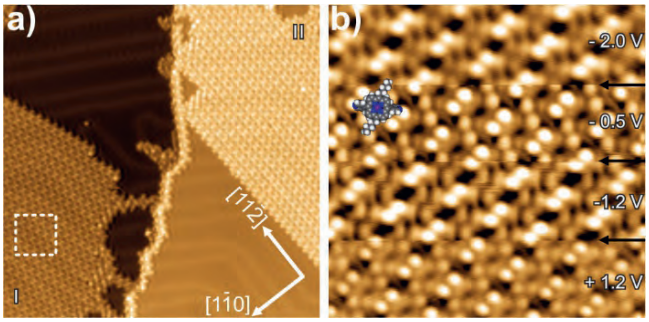

Figure 6.1. For submonolayer coverage of Ni-DPPyP on Au(111) a close-packed arrangement develops. (a) Overview STM image (42 x 42 nm^2, U = -1.2 V, I = 20 pA, 77K) in which two rotational domains (labelled I and II) of the close-packed assembly are visible. The substrate directions are denoted by the white arrows. (b) Bias voltage-dependent close-up STM image (10 x 10 nm^2, I = 20 pA, 77K) for the area indicated by the white dashed square in (a). The intramolecular features of Ni-DPPyP (pyridyl units, alkyl chains as well as the porphyrin core) can be discerned. For clarity, a molecule is superimposed on the STM image. The black arrows indicate the scan lines where the bias is changed. The corresponding bias voltages are indicated in the image.

The porphyrin macrocycle remained dim at both bias polarities and the Ni-atom did not contribute to the STM contrast. The long-range order of the network was confirmed by our LEED measurements (Figure 6.2) and in combination with the STM data, we constructed a unit cell with dimensions a = 14.1 ± 0.1 Å, b = 14.9 ± 0.1 Å, and an internal angle of α = 88° ± 2°. The molecular density amounts to 0.48 Ni-DPPyP molecules per nm^2. The unit cell is rotated by 15° with respect to the principal Au directions. The close-packed network is incommensurate with respect to the underlying Au substrate as supported by the absence of integer matrix elements in the superstructure matrix of the simulated LEED pattern (Figure 6.2b). The

presence of three rotationally equivalent and three mirror domains was corroborated by the LEED measurements (Figure 6.2a). This was supported by the simulated LEED pattern (Figure 6.2b), which shows the unit cell (black square) with the rotationally equivalent and mirror domains of the assembly depicted by the spots in different colors. Furthermore, the molecular orientation between the molecules can be discerned within the unit cell (black square) overlaid in Figure 6.2c, where the pyridyl endgroups align parallel to the pyridyl endgroups from neighboring Ni-DPPyP molecules. This arrangement is similar to the orientation observed for tetraphenyl and tetrapyridyl porphyrins on metal substrates.[28,29,30] As shown in the tentative structural model (Figure 6.2d) the 2D network is stabilized by H-bonding between the electronegative N-atom of the pyridyl endgroup and one H-atom from a neighboring pyrrole moiety.[28,30] Additionally, the pentyl chains interact with the neighboring pentyl and pyrrolic moieties via van der Waals forces.[16]

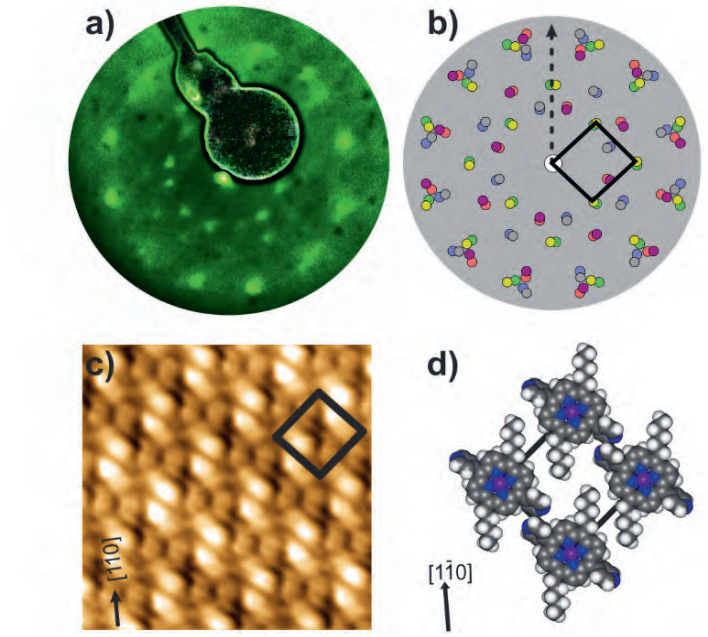

Figure 6.2. (a) Experimentally obtained LEED pattern for submonolayer coverage of
Ni-DPPyP on Au(111) taken at a beam energy of 12.2 eV. (b) Simulated LEED pattern. The different colors mark the rotationally equivalent and mirrored domains. The black square indicates the molecular unit cell for one of the domains of the molecular adlayer. The dotted black arrow shows the close-packed [1$\bar{1}$0] direction of the Au(111) surface. The superstructure of the simulated LEED pattern is described by the matrix notation $\begin{pmatrix} 5.5 & 1.5 \\ 1.7 & 5.8 \end{pmatrix}$. (c) High resolution STM image (6.4 x 6.4 nm^2, U = -3 V, I = 20 pA, 77K) for the close-packed arrangement where the unit cell is marked by the black rectangle. (d) Tentative model for the molecular arrangement of Ni-DPPyP on Au(111). The black arrows at the bottom left corner in (c) and (d) indicate the close-packed [1$\bar{1}$0] direction of the Au(111) surface.

The deposition of Co-atoms onto a submonolayer of the close-packed network followed by post-deposition annealing at 423 K led to the formation

of a porous 2D network (Figure 6.3). The presence of two mirror domains with respect to each other at a principal Au direction is highlighted by the green and black rhombuses (Figure 6.3a). In contrast to the close-packed network, the herringbone reconstruction of the Au substrate was no longer visible through the molecular layer. It could be that this has to be ascribed to the imaging parameters and tip condition but we do not rule out the possibility that the herringbone reconstruction might have been partially lifted by the formation of the Co-coordinated porous network, i.e., the interaction of the Co-atoms with the Au surface might be stronger than compared to the molecule-substrate interactions in the close-packed network. The close-up STM image (inset in Figure 6.3a) unveils details of the molecular network; where the pentyl chains point their main axis towards the center of each pore following a star-like shape and appear as fuzzy long protrusions due to their mobility at RT.[16] The pyridyl endgroups are imaged as small bright protrusions and point to a common three-fold node, which can also be seen as the vertex formed between three adjacent pores. Once again, the Ni-atom in the porphyrin core did not contribute to the STM contrast. Combining our STM and LEED data (Figure 6.3) we constructed a rhombic unit cell (black rhombus in Figure 6.3a and c) with dimensions $a = b = 32 \pm 0.2$ Å, and an internal angle of $\alpha = 60° \pm 2°$. The molecular density now amounts to 0.34 Ni-DPPyP molecules per nm^2. In addition, the unit cell is rotated by 15° with respect to the principal Au directions. The incommensurability of the porous network with the underlying Au substrate was supported by the absence of integer matrix elements in the superstructure matrix of the simulated LEED pattern (Figure 6.3c). The simulated LEED pattern (Figure 6.3c) displays both mirror domains of the network in gray and green, respectively. Furthermore, the common three-fold node formed between the pyridyl endgroups could not

be possible without an additional linker between them due to steric repulsion between the electronegative N-atoms. Therefore, as illustrated in the tentative structural model (Figure 6.3d), the three-fold node is formed by metal-ligand interactions between one Co-atom (orange circles) bonded to the N-atoms (blue circles) from three different pyridyl endgroups, resulting in a 1.5:1 molecule-to-metal ratio.[16] It is well known that 3d transition metals located at the coordination nodes on metal substrates often remain invisible under STM.[31–33] Nevertheless, our study supports the preference that Co-atoms have towards (in-plane) three-fold coordination on noble metal surfaces,[6,16,18,33–36] despite the fact that such coordination motifs have been rarely reported for pyridyl-substituted porphyrins.[16] It is worth to mention that the three-fold Co-coordinated node prevailed independently of: (i) the Ni-atom in the porphyrin core, since our results (Figure 6.3) are structurally comparable to our findings shown in our previous report of the free-base version (DPPyP) of Ni-DPPyP on Ag(111)[16] and (ii) the length of the alkyl endgroup, as the deposition of another analogue of Ni-DPPyP containing hexyl instead of pentyl chains gave rise to a structurally equivalent porous network after coordinating to Co-atoms on Au(111) (Appendix Figure A6.2).

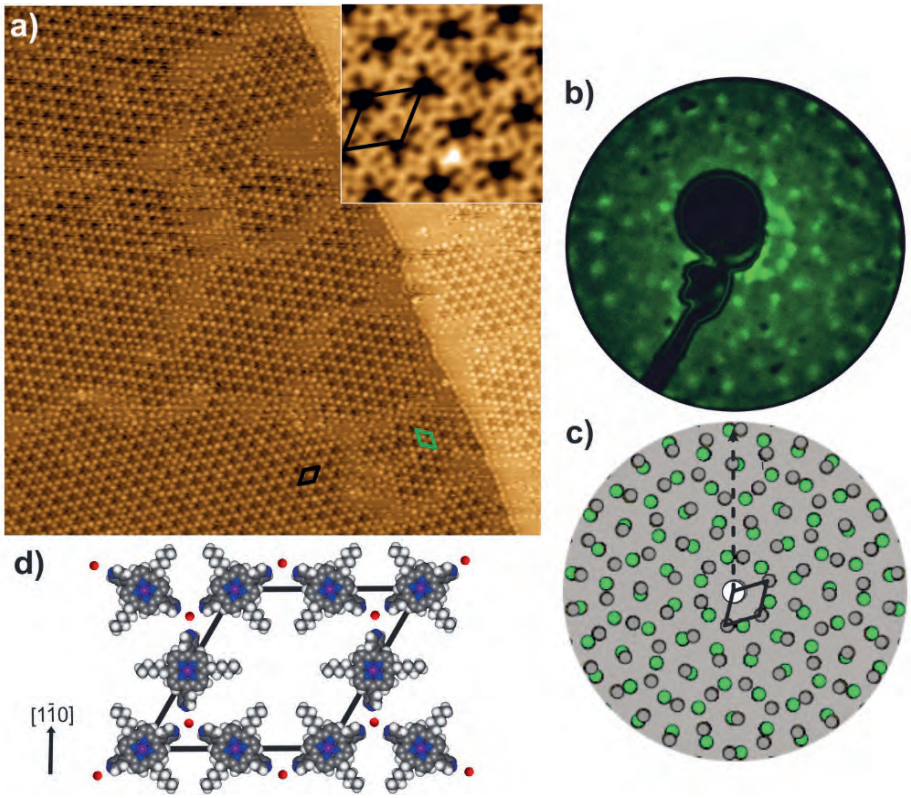

Figure 6.3. Cobalt-coordinated porous network of Ni-DPPyP on Au(111). (a) Overview STM image (113 x 113 nm^2, U = 2 V, I = 20 pA, RT). The mirror domains are marked by the black and green rhombic unit cell. The inset shows a close-up STM image (10.8 x 10.8 nm^2, U = -3.5 V, I = 20 pA, RT) of the porous network. (b) Experimentally obtained LEED pattern for the porous network of Ni-DPPyP on Au(111) taken at a beam energy of 8.3 eV. (c) Simulated LEED pattern. The different colors mark the two mirror domains. The black square indicates the unit cell for one of the domains of the molecular adlayer. The dotted black arrow shows the close-packed [1$\bar{1}$0] direction of the Au(111) surface. The superstructure of the simulated LEED pattern is described by the matrix notation $\begin{pmatrix} 9.1 & 3.3 \\ -3.3 & 12.4 \end{pmatrix}$. (d) Tentative structural model for the cobalt-coordinated porous Ni-DPPyP network with the unit cell in black. One cobalt atom (orange circles) coordinates to three pyridyl ligands. The black arrow indicates the close-packed [1$\bar{1}$0] direction of the Au(111) surface.

In light of studying the formation of metal-ligand interactions in MOCNs on noble metal surfaces, the shift in the binding energies (BE) of a core level spectrum serve as a measure – through so-called chemical shifts – of the chemical environment of a particular atom prior to and after metal coordination.[8,32,37–40] Therefore, in addition to our STM and LEED data, we measured XPS spectra for the C 1s, N 1s and Ni $2p_{3/2}$ core levels to check both the chemical composition and possible changes of the electronic structure of Ni-DPPyP on Au(111) before and after coordination with Co-atoms. Ni-DPPyP contains a total of six N-atoms and forty C-atoms distributed in two and five chemically different environments, respectively. Each group of chemically different atoms is properly labelled and color coded in the ball and stick model shown in Figure 6.4. The two different chemical states of the N-atoms are given by: N1 (iminic N-atom coordinating to the central Ni-atom) and N2 (located in the pyridyl endgroup). On the other hand, the C-atoms are grouped as follows: four types of sp^2-hybridized C-atoms can be found as C1 (bonded to only C-atoms), C3 (located inside the pyrrole and pyridyl moieties bonded to C- and H-atoms), C4 (bonded to N1), C5 (bonded to N2); and one type of sp^3-hybdrized C-atoms labelled as C2 (placed along the pentyl chains and connected to C- and H-atoms).

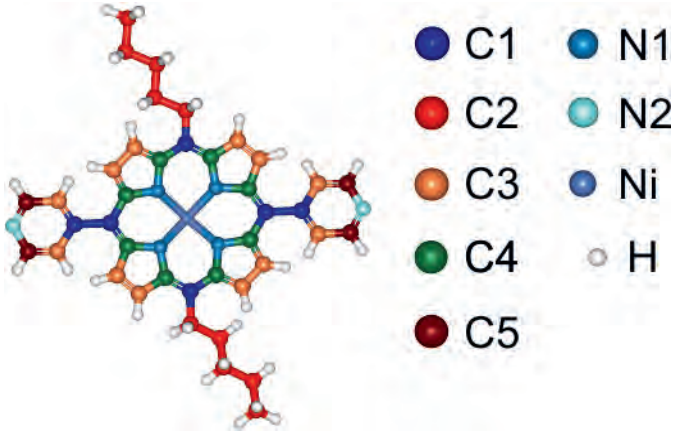

Figure 6.4. Ball and stick molecular model of Ni-DPPyP where the chemically different carbon and nitrogen species are color coded. The C 1s components (C1 – C5) are correlated with the carbon components in Figure 6.5a and b.

The C 1s core level spectrum of the close-packed network (Figure 6.5a) was fitted with five components. For fitting the C 1s spectra, the FWHMs of the components were allowed to vary between 0.5 eV and 0.7 eV, whereas the area ratios were left free. The assignment of the components was done with respect to the stoichiometry of the molecule: C1 : C2 : C3 : C4 : C5 = 6 : 10 : 12 : 8 : 4. The BE for each component of the C 1s core level spectra can be found in Table 6.1. The main component (orange peak) located at 284.71 eV was attributed to C3 and is in line with the BE values reported for aromatic carbons.[41–46] The second largest contribution (red peak) located at 284.23 eV belongs to C2 and agrees with the peak positions reported for sp^3-hybdrized C-atoms in alkyl chains.[47–49] The green peak (285.20 eV) corresponds to C4 which is bonded to the N-atoms from the porphyrin core. C4 appears at a higher BE as compared with C1, C2, and C3 due to its near proximity to the N-atom (N1), which possesses an increased electronegativity as compared with the C-atom. Thus, the N1-atom pulls the carbon valence

electrons strongly away from the C4-atoms lowering its electron density, which leads to an effective increase of its nuclear charge and it therefore increases the BE observed in the C 1s spectrum.[23,44,45] The contribution at the lowest BE (283.80 eV) was attributed to C1 and resembles the C-C bonds along the porphyrin backbone.[50] Finally, the smallest contribution (brown peak) was given to C5 and is located at the highest BE (285.77 eV) because it is bonded to the pyridylic N-atoms (N2) involved in H-bonding.[23] Thus, similarly to the case of C4, the N-atoms (N2) bonded to H-atoms pull electron density away from C5.

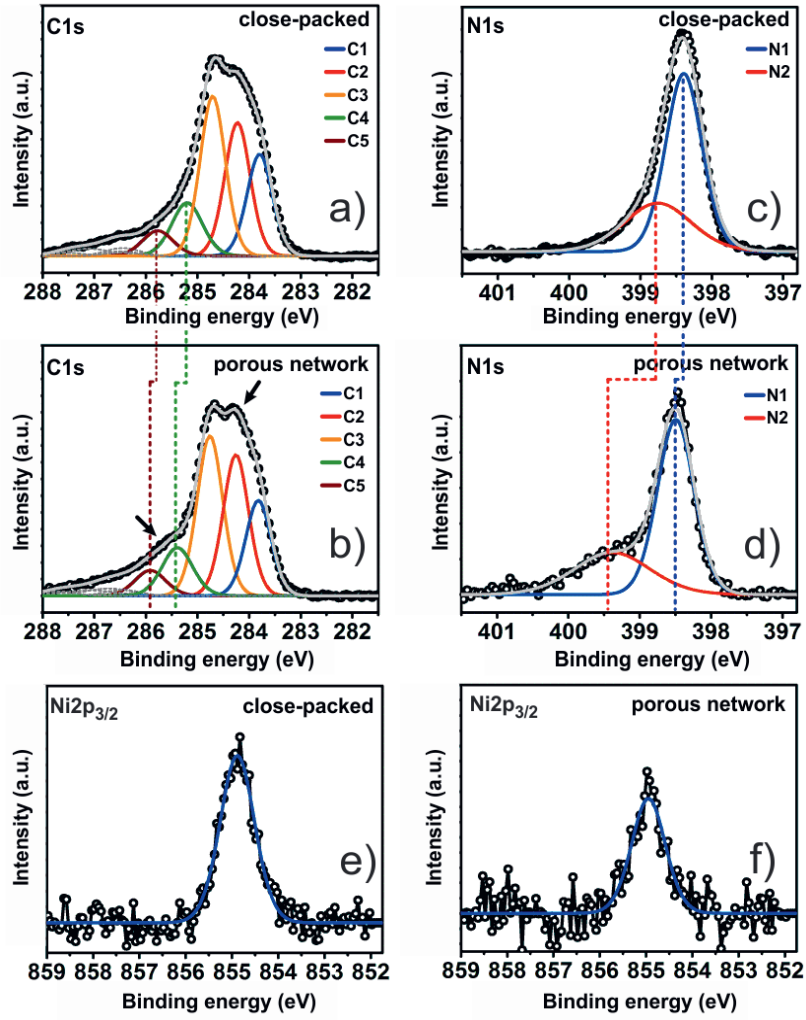

Figure 6.5. (a), (c), (e) C 1s, N 1s and Ni $2p_{3/2}$ core level spectra of Ni-DPPyP on Au(111) for the close-packed structure. (b), (d), (f) C 1s, N 1s and Ni $2p_{3/2}$ core level spectra of Ni-DPPyP on Au(111) for the cobalt-coordinated porous network. The black arrows in (b) point to the new features in the C 1s envelope of the porous network structure. Due to the metal coordination, a peak shift towards higher binding energies of the C4, C5, N1 and N2 components was observed and is emphasized by the vertical dotted lines. For peak positions see Table 6.1 and Table 6.2. The C 1s and N 1s spectra were acquired with a photon energy $h\upsilon$ = 500 eV, while the Ni $2p_{3/2}$ spectra were acquired with a photon energy $h\upsilon$ = 2.67 keV.

Table 6.1. Binding energies (BE) and FWHMs in eV for the C 1s core level signal of Ni-DPPyP on Au(111) for the close-packed and porous network assemblies.										
	C1		**C2**		**C3**		**C4**		**C5**	
Assembly	BE	FWHM (%Area)	BE	FWHM (%Area)	BE	FWHM (%Area)	BE	FWHM (%Area)	BE	FWHM (%Area)
CP	283.80	0.58 (19.3)	284.23	0.58 (25.3)	284.71	0.59 (30.1)	285.20	0.69 (12.1)	285.77	0.69 (5.7)
PN	283.82	0.58 (18.0)	284.26	0.58 (26.7)	284.76	0.59 (30.6)	285.39	0.69 (11.0)	285.91	0.69 (5.8)

Table 6.1. Binding energies and FWHMs in eV and area ratios between components of the C 1s core level signal of Ni-DPPyP on Au(111) for the close-packed and porous network assemblies. For fitting the C 1s spectrum of the close-packed structure the FWHMs of the components were allowed to vary between 0.5 eV and 0.7 eV. No area (ratio) constraints between components were imposed. The FWHMs obtained after fitting the C 1s spectrum for the close-packed structure were used for fitting the C 1s spectrum of the porous network structure. The labels *CP* and *PN* are the acronyms of the close-packed and porous networks, respectively. In addition, two satellite peaks were fitted for the C 1s core level spectra of the close-packed network around 286.5 and 287 eV, respectively.

The N 1s core level spectrum of the close-packed network (Figure 6.5c) was fitted with two components. For fitting the N 1s spectra, the area ratios were fixed to 4:2 and the FWHMs were left free. The energy position for each component of the N 1s spectrum can be found in Table 6.2. The peak located at 398.75 eV was attributed to N2, since the pyridylic N-atom (N2) is bonded to a H-atom and consequently, appears at a slightly higher BE than the N-atoms (N1) contained in the porphyrin core which are bonded to a Ni-

atom. This peak position is consistent with the one obtained for pyridylic N-atoms in tetrapyridyl-substituted porphyrins.[21] In addition, in previous reports for free-base porphyrins, the N-atoms bonded to H-atoms in the porphyrin core have been assigned to higher BE than their iminic counterparts (N-atoms in the porphyrin core with an electron lone pair) and can be compared to the chemical environment that N2 has while being bonded to a neighboring H-atom.[22,51–53] Therefore, the peak at lower BE (398.39 eV) was assigned to N1 as compared with the values reported for iminic N-atoms in Ni-substituted porphyrins[53–55] and in various metal-substituted porphyrins on noble metal surfaces.[21,22,52,56]

Table 6.2. Binding energies (BE) and FWHMs in eV for the N 1s and Ni $2p_{3/2}$ core level signals of Ni-DPPyP on Au(111) for the close-packed and porous network assemblies. Area constraints between the components were imposed only on the N 1s spectra.

	N1		**N2**		**Ni $2p_{3/2}$**	
Assembly	BE	FWHM	BE	FWHM	BE	FWHM
Close-packed	398.39	0.6	398.75	1.1	854.88	0.88
Porous network	398.49	0.6	399.42	1.14	854.95	0.86

Table 6.2. Binding energies and FWHMs in eV and area ratios between components of the N 1s and Ni $2p_{3/2}$ core level signals of Ni-DPPyP on Au(111) for the close-packed and porous network assemblies. Area constraints between the components were imposed only on the N 1s spectra.

The deposition of Co-atoms and subsequent annealing led to the formation of a porous 2D network as previously mentioned. The C 1s core level spectrum of the porous 2D network (Figure 6.3) is shown in Figure 6.5b. Similar to the C 1s spectrum of the close-packed network, the intensity ratio between the components is in line with the stoichiometric ratio of C-atoms (see Table 6.1). However, new features (marked by the black arrows) appeared in the C 1s envelope (Figure 6.5b) of the porous 2D network which are correlated to the change in chemical environment of the C-atoms in Ni-DPPyP after the deposition of Co-atoms. This is supported by the chemical shift (highlighted by the vertical green line) of 0.19 eV and the spectral shift of 0.14 eV (highlighted by the vertical brown dotted line) towards higher BE of the C4 (green peak) and C5 (brown peak) components, respectively. Similarly, the N 1s envelope (Figure 6.5d) of the porous 2D network presented new features that were given by a marked shift (highlighted by the vertical blue and red dotted lines) of 0.10 eV and 0.67 eV towards higher BE of the N1 (blue peak) and N2 (red peak) components, respectively. The most pronounced chemical shift was observed for N2 at 399.49 eV and can be explained by the Co-directed structural transformation going from H-bonding (Figure 6.1) to metal-ligand coordination (Figure 6.3) where the nuclear charge of N2 increases after donating charge to the Co-atoms.[21,32,57] Consequently, N2 withdraws charge from C5 which leads to a spectral shift (brown peak) of 0.14 eV. Similar chemical shifts have been reported for the pyridylic N 1s signal of tetrapyridyl-porphyrins coordinating to Cu-atoms and linear bis-pyridyl molecules coordinating to Fe-atoms on Au(111).[21,57]

On the other hand, the smaller spectral shifts of C4 (0.19 eV) and N1 (0.10 eV) might be an indication of a possible conformational change of the porphyrin core due to the metal coordination observed between the pyridyl

endgroups and Co-atoms. We hypothesize that upon MOCN formation the central Ni-atom of the porphyrin might be slightly lifted (away) from the Au surface as compared with the close-packed structure. Thus, a possible weakened interaction between the Ni-atoms and the Au surface results in an increased interaction between the Ni-atoms with the N-atoms of the porphyrin core, which translates into a shift towards higher BE for N1 and C4. Similar conformational adaptations of the porphyrin core that modify its distance to the underlying surface by the dihedral rotation of the aromatic endgroups have been previously reported.[46] Thus, we consider the possibility that the pyridyl endgroups of the Ni-DPPyP derivatives are tilted with a large dihedral angle with respect to the Au surface, which elevates the porphyrin core.[46] In addition, the Ni $2p_{3/2}$ core level spectra taken before (Figure 6.5e) and after (Figure 6.5f) metal-coordination can be taken as support for our assumption. Even if the chemical shift (0.07 eV) is small, it can be an indication that the Ni-atom could have increased its charge after being separated from the Au surface. Additionally, the BE of the Ni $2p_{3/2}$ core level is in agreement with the reported values for a nickel-substituted tetraphenyl porphyrin (NiTPP) on Au(111) and a nickel-substituted tetrabromophenyl porphyrin (NiTBrPP) on Cu(111).[54,58]

6.4 Conclusions

We have presented a complementary study of the influence of Co-deposition on the self-assembly process of a Ni-substituted porphyrin derivative (Ni-DPPyP) on Au(111) by means of STM, LEED and XPS. As revealed by STM, the deposition of Ni-DPPyP for coverages < 1 monolayer on Au(111) formed a well-ordered close-packed network stabilized by H-bonding between the N-atoms of the pyridyl endgroups and the H-atoms from neighboring pyrrole moieties. The long-range order of this 2D network was corroborated by LEED measurements. In addition, the chemical state of the C and N-atoms – prior to Co-deposition – was investigated with XPS, which agreed with the previously reported BE for the C 1s and N 1s core levels in porphyrin-based 2D networks stabilized by H-bonding on metal surfaces.

The deposition of Co-atoms onto the close-packed network led to a structural transformation, i.e., the formation of a Co-coordinated hexagonal porous network. The long-range order of the network was revealed by LEED measurements. The presence of metal-ligand interactions was confirmed by XPS with a marked chemical shift (0.67 eV) towards higher BE of the pyridylic N 1s XPS signal of the hexagonal porous network. While, STM measurements allow studying the structure of metal-organic coordination networks and give insight to the lateral interactions within these structures. XPS can provide complementary information of the chemical environment of the atomic species within the MOCN in order to confirm the nature of the lateral interactions stabilizing the network.

6.5 References

1. Goronzy, D. P.; Ebrahimi, M.; Rosei, F.; Arrmael, Fang, Y.; De Feyter, S.; Tait, S. L.; Wang, C.; Beton, P. H.; Wee, A. T. S.; Weiss, P. S.; Perepichka, D. F. Supramolecular Assemblies on Surfaces: Nanopatterning, Functionality, and Reactivity. *ACS Nano* **2018**, *12*, 7445–7481.
2. Furukawa, H.; Cordova, K. E.; O'Keeffe, M.; Yaghi, O. M. The Chemistry and Applications of Metal-Organic Frameworks. *Science* **2013**, *341*, 1230444.
3. Bétard, A.; Fischer, R. A. Metal-Organic Framework Thin Films: From Fundamentals to Applications. *Chem. Rev* **2012**, *112*, 1055–1083.
4. Barth. J. V. Fresh Perspectives for Surface Coordination Chemistry. *Surf. Sci*. **2009**, *603*, 1533–1541.
5. Gutzler, R.; Stepanow, S.; Grumelli, D.; Lingenfelder, M.; Kern, K. Mimicking Enzymatic Active Sites on Surfaces for Energy Conversion Chemistry. *Acc. Chem. Res*. **2015**, *48*, 2132–2139.
6. Dong, L.; Gao, Z. A.; Lin, N. Self-Assembly of Metal-Organic Coordination Structures on Surfaces. *Prog. Surf. Sci.* **2016**, *91*, 101–135.
7. Baker Cortés, B. D.; Stöhr, M. Role of Cyano Groups in the Self-Assembly of Organic Molecules on Metal Surfaces. In *Encyclopedia of Interfacial Chemistry;* Wandelt, K., Ed.; Elsevier, **2018**, Vol. *4*, pp 153–165.
8. Klappenberger, F. Two-Dimensional Functional Molecular Nanoarchitectures – Complementary Investigations with Scanning Tunneling Microscopy and X-ray Spectroscopy. *Prog. Surf. Sci.* **2014**, *89*, 1–55.
9. Baker Cortés B. D.; Schmidt, N.; Enache, M.; Stöhr, M. Coverage-Dependent Structural Transformation of Cyano-Functionalized Porphyrin Networks on Au(111) via Addition of Cobalt Atoms. *J. Phys. Chem. C* **2019**, *123*, 19681–19687.
10. Auwärter, W.; Écija, D.; Klappenberger, F.; Barth, J. V. Porphyrins at Interfaces. *Nat. Chem*. **2015**, *7*, 105–120.
11. Gottfried, J. M. Surface Chemistry of Porphyrins and Phthalocyanines. *Surf. Sci. Rep*. **2015**, *70*, 259–379.
12. Pham, T. A.; Song, F.; Alberti, M. N.; Nguyen, M. T.; Trapp, N.; Thilgen, C.; Diederich, F.; Stöhr, M. Heat-Induced Formation of One-Dimensional Coordination Polymers on Au(111): An STM Study. *Chem. Commun.* **2015**, *51*, 14473–14476.
13. Fendt, L.; Stöhr, M.; Wintjes, N.; Enache, M.; Jung, T.; Diederich, F. Modification of Supramolecular Binding Motifs Induced by Substrate Registry: Formation of Self-Assembled Macrocycles and Chain-Like Patterns. *Chem. Eur. J*. **2009**, *15*, 11139–11150.

14. Shi, Z.; Lin. N. Porphyrin-Based Two-Dimensional Coordination Kagome Lattice Self-Assembled on a Au(111) Surface. *J. Am. Chem. Soc.* **2009**, *131*, 5376–5377.
15. Mao, X. F.; Lin, T.; Adisoejoso, J.; Shi, Z.; Shang, X. S.; Liu, P. N.; Lin. N. Coordination Self-Assembly of Bromo-Phenyl and Pyridyl Functionalized Porphyrins with Fe on an Au(111) surface. *Phys. Chem. Chem. Phys.* **2013**, *15*, 12447.
16. Studener, F.; Müller, K.; Marets, N.; Bulach, V.; Hosseini, M. W.; Stöhr. M. From Hydrogen Bonding to Metal Coordination and Back: Porphyrin-Based Networks on Ag(111). *J. Chem. Phys*. **2015**, *142*, 101296-1/101296-6.
17. Kühne, D.; Klappenberger, F.; Decker, R.; Schlickum, U.; Brune, H.; Klyatskaya, S.; Ruben, M.; Barth, J. V. High-Quality 2D Metal–Organic Coordination Network Providing Giant Cavities Within Mesoscale Domains. *J. Am. Chem. Soc.* **2009**, *131*, 3881–3883.
18. Schlickum, U.; Decker, R.; Klappenberger, F.; Zoppellaro, G.; Klyatskaya, S.; Ruben, M.; Silanes, I.; Arnau, A.; Kern, K.; Brune, H.; Barth, J. V. Metal–Organic Honeycomb Nanomeshes With Tunable Cavity Size. *Nano Lett.* **2007**, *7*, 3812–3817.
19. Umbach, T. R.; Bernien, M.; Hermanns, C. F.; Krüger, A.; Sessi, V.; Fernandez-Torrente, I.; Stoll, P.; Pascual, J. I.; Franke, K. J.; Kuch. W. Ferromagnetic Coupling of Mononuclear Fe Centers in a Self-Assembled Metal-Organic Network on Au(111). *Phys. Rev. Lett*. **2012**, *109*, 267207.
20. Jiang, W.; Ni, X.; Liu, F. Exotic Topological Bands and Quantum States in Metal-Organic and Covalent-Organic Frameworks. *Acc. Chem. Res.* **2021**, *54*, 416–426.
21. Li, Y.; Xiao, J.; Shubina, T. E.; Chen, M.; Shi, Z.; Schmid, M.; Steinrück, H.-P.; Gottfried, J. M.; N. Lin. Coordination and Metalation Bifunctionality of Cu with 5,10,15,20-Tetra(4-pyridyl)porphyrin: Toward a Mixed-Valence Two-Dimensional Coordination Network *J. Am. Chem. Soc.* **2012**, *134*, 6401–6408.
22. Gottfried, J. M.; Flechtner, K.; Kretschmann, A.; Lukasczyk, T.; Steinrück, H.-P. Direct Synthesis of a Metalloporphyrin Complex on a Surface. *J. Am. Chem. Soc.* **2006**, *128*, 5644–5645.
23. Cohen. M. R. HREELS, ARUPS, and XPS of Pyridine on Ni(110). *Surf. Sci.* **1991**, *245*, 1–11.
24. Horcas, I.; Fernández, R.; Gómez-Rodríguez, J. M.; Colchero, J.; Gómez-Herrero, J.; Baro, A. M. WSXM: A Software for Scanning Probe Microscopy and a Tool for Nanotechnology. *Rev. Sci. Instrum*. **2007**, *78*, 013705.
25. Hermann, K.; van Hove, M. A. LEEDpat4 (LEED pattern analyzer). http://www.fhi-berlin.mpg.de/KHsoftware/LEEDpat/index.html (accessed January 19, 2021).

26. Auwärter, W.; Weber-Bargioni, A.; Riemann, A.; Schiffrin, A. Self-Assembly and Conformation of Tetrapyridyl-Porphyrin Molecules on Ag(111). *J. Chem. Phys.* **2006**, *124*, 194708.
27. Wang, Y.; Zhou, K.; Shi, Z.; Ma. Y.-Q. Structural Reconstruction and Spontaneous Formation of Fe Polynuclears: A Self-Assembly of Fe-Porphyrin Coordination Chains on Au(111) Revealed by Scanning Tunneling Microscopy. *Phys. Chem. Chem. Phys.* **2016**, *18*, 14273–14278.
28. Rolf, D.; Lotze, C.; Czekelius, C.; Heinrich, B. W.; Franke. K. J. Visualizing Intramolecular Distortions as the Origin of Transverse Magnetic Anisotropy. *J. Phys. Chem. Lett.* **2018**, *9*, 6563–6567.
29. Buchner, F.; Kellner, I.; Hieringer, W.; Görling, A.; Steinrück, H.-P.; Marbach, H. Ordering Aspects and Intramolecular Conformation of Tetraphenylporphyrins on Ag(111). *Phys. Chem. Chem. Phys.* **2010**, *12*, 13082–13090.
30. Auwärter. W.; Weber-Bargioni, A.; Brink, S.; Riemann, A.; Schiffrin, A.; Ruben, M.; Barth, J. V. Controlled Metalation of Self-Assembled Porphyrin Nanoarrays in Two Dimensions. *ChempPhysChem* **2007**, *8*, 250–254.
31. Björk, J.; Matena, M.; Dyer, M. S.; Enache, M.; Lobo-Checa, J.; Gade, L. H.; Jung, T. A.; Stöhr, M.; Persson, M. STM Fingerprint of Molecule-Adatom Interactions in a Self-Assembled Metal-Organic Surface Coordination Network on Cu(111). *Phys. Chem. Chem. Phys.* **2010**, *12*, 8815–8821.
32. Matena, M.; Björk, J.; Wahl, M.; Lee, T.-L.; Zegenhagen, J.; Gade, L. H.; Jung, T. A.; Persson, M.; Stöhr, M. On-Surface Synthesis of a Two-Dimensional Porous Coordination Network: Unraveling Adsorbate Interactions. *Phys. Rev. B* **2014**, *90*, 125408-1/125408-8.
33. Henningsen, N.; Rurali, R.; Lumbach, C.; Drost, R.; Pascual, J. I.; Franke. K. J. Site-Dependent Coordination Bonding in Self-Assembled Metal-Organic Networks. *J. Phys. Chem. Lett.* **2011**, *2*, 55–61.
34. Hosseini. M. W. Molecular Tectonics: From Simple Tectons to Complex Molecular Networks. *Acc. Chem. Res.* **2005**, *38*, 313–323.
35. Stepanow, S.; Lin, N.; Payer, D.; Schlickum, U.; Klappenberger, F.; Zoppellaro, G.; Ruben, M.; Brune, H.; Barth, J. V.; Kern. K. Surface-Assisted Assembly of 2D Metal-Organic Networks That Exhibit Unusual Threefold Coordination Symmetry. *Angew. Chem. Int. Ed.* **2007**, *46*, 710–713.
36. Pham, T. A.; Song, F.; Alberti, M. N.; Nguyen, M.-T.; Trapp, N.; Thilgen, C.; Diederich, F.; Stöhr, M. Heat-Induced Formation of One-Dimensional Coordination Polymers on Au(111): An STM Study. *Chem. Commun*. **2015**, *51*, 14473–14476.
37. Gelius, U. Binding Energies and Chemical Shifts in ESCA. *Phys. Scr.* **1974**, *9*, 133–147.

38. Tempas, C. D.; Skomski, D.; Cook, B. J.; Le, D.; Smith, K. A.; Rahman, T. S.; Caulton, K. G.; Tait, S. L. Redox Isomeric Surface Structures Are Preferred over Odd-Electron Pt^{1+}. *Chem. Eur. J.* **2018**, *24*, 15852–15858.
39. Shen, Q.; Larkin, E. J.; Delaney, C.; Cheng, Y.; Miao, C.; Zhou, X.; Liu, L; Huang, W.; Gao, H.; Draper, S. M.; Fuchs, H. Coordination Reactions of 5-(2-(4-Bromophenyl)ethynyl)pyrimidine in On-Surface Synthesis. *J. Phys. Chem. C* **2018**, *122*, 8954–8959.
40. Müller, K.; Moreno-López, J. C.; Gottardi, S.; Meinhardt, U.; Yildirim, H.; Kara, A.; Kivala, M.; Stöhr, M. Cyano-Functionalized Triarylamines on Coinage Metal Surfaces: Interplay of Intermolecular and Molecule–Substrate Interactions. *Chem. Eur. J.* **2016**, *22*, 581–589.
41. Lukasczyk, T.; Flechtner, K.; Merte, L. R.; Jux, N.; Maier, F.; Gottfried, J. M.; Steinrück, H.-P. Interaction of Cobalt(II) Tetraarylporphyrins with a Ag(111) Surface Studied with Photoelectron Spectroscopy. *J. Phys. Chem. C* **2007**, *111*, 3090–3098.
42. Ronning, C.; Feldermann, H.; Merk, R.; Hofsass, H. Carbon Nitride Deposited Using Energetic Species: A Review on XPS studies. *Phys. Rev. B* **1998**, *4*, 2207–2215.
43. Ektessabi, A. M.; Hakamata, S. XPS Study of Ion Beam Modified Polyimide Films. *Thin Solid Films* **2000**, *377-378*, 621–625.
44. Shen, K.; Narsu, B.; Ji, G.; Sun, H.; Hu, J.; Liang, Z.; Gao, H.; Li, H.; Li, Z.; Song, B.; Jiang, Z.; Huang, H.; Wells, J. W.; Song, F. On-Surface Manipulation of Atom Substitution Between Cobalt Phthalocyanine and The Cu(111) Substrate. *RSC Adv.* **2017**, *7*, 13827–13835.
45. Peisert, H.; Knupfer, M.; Fink, J. Electronic Structure of Partially Fluorinated Copper Phthalocyanine ($CuPCF_4$) and its interface to Au(100). *Surf. Sci.* **2002**, *515*, 491–498.
46. Xiao, J.; Ditze, S.; Chen, M.; Buchner, F.; Stark, M.; Drost, M.; Steinrück, H.-P.; Gottfried, J. M.; Marbach, H. Temperature-Dependent Chemical and Structural Transformations from 2H-tetraphenylporphyrin to Copper(II)-Tetraphenylporphyrin on Cu(111). *J. Phys. Chem. C* **2012**, *116*, 12275–12282.
47. Cecchet, F.; Pilling, M.; Hevesi, L.; Schergna, S.; Wong, J. K. Y.; Clarkson, G. J.; Leigh, D. A.; Rudolf, P. Grafting of Benzylic Amide Macrocycles onto Acid-Terminated Self-Assembled Monolayers Studied by XPS, RAIRS, and Contact Angle Measurements. *J. Phys. Chem. B* **2003**, *107*, 10863–10872.
48. Wilson, D.; Langell, M. A. XPS Analysis of Oleylamine/Oleic Acid Capped Fe_3O_4 Nanoparticles as a Function of Temperature. *Appl. Surf. Sci.* **2014**, *303*, 6–13.
49. Graf, N.; Yegen, E.; Gross, T.; Lippitz, A.; Weigel, W.; Krakert, S.; Terfort, A.; Unger, W. E. S. XPS and NEXAFS Studies of Aliphatic and Aromatic Amine Species on Functionalized Surfaces. *Surf. Sci.* **2009**, *603*, 2849–2860.

50. Bürker, C.; Franco-Cañellas, A.; Broch, K.; Lee, T.-L.; Gerlach, A.; Schreiber, F. Self-Metalation of 2H-Tetraphenylporphyrin on Cu(111) Studied With XSW: Influence of the Central Metal Atom on the Adsorption Distance. *J. Phys. Chem. C* **2014**, *118*, 13659–13666.
51. Buchner, F.; Xiao, J.; Zillner, E.; Chen, M.; Röckert, M.; Ditze, S.; Stark, M.; Steinrück, H.-P.; Gottfried, J. M.; Marbach, H. Diffusion, Rotation, and Surface Chemical Bond of Individual 2H-Tetraphenylporphyrin Molecules on Cu(111). *J. Phys. Chem. C* **2011**, *115*, 24172–24177.
52. Kretschmann, A.; Walz, M.-M.; Flechtner, K.; Steinrück, H.-P.; Gottfried, J. M. Tetraphenyl Porphyrin Picks Up Zinc Atoms from a Silver Surface. *Chem. Commun.* **2007**, 568–570.
53. Shubina, T. E.; Marbach, H.; Flechtner, K.; Kretschmann, A.; Jux, N.; Buchner, F.; Steinrück, H.-P.; Clark, T.; Gottfried, J. M. Principle and Mechanism of Direct Porphyrin Metalation: Joint Experimental and Theoretical Investigation. *J. Am. Chem. Soc.* **2007**, *129*, 9476–9483.
54. Chen, M.; Feng, X.; Zhang, L.; Ju, H.; Xu, Q.; Zhu, J.; Gottfried, J. M.; Ibrahim, K.; Qian, H.; Wang, J. Direct Synthesis of Nickel(II) Tetraphenylporphyrin and Its Interaction With a Au(111) Surface: A Comprehensive Study. *J. Phys. Chem. C* **2010**, *114*, 9908–9916.
55. Wang, C.; Fan, Q.; Han, Y.; Martínez, J. I.; Martín-Gago, J. A.; Wang, W.; Ju, H.; Gottfried, J. M.; Zhu, J. Metalation of Tetraphenylporphyrin with Nickel on a TiO_2(110)-1 x 2 Surface. *Nanoscale* **2016**, *8*, 1123–1132.
56. Di Santo, G.; Castellarin-Cudia, C.; Fanetti, M.; Taleatu, B.; Borghetti, P.; Sangaletti, L.; Floreano, L.; Magnano, E.; Bondino, F.; Goldoni, A. Conformational Adaptation and Electronic Structure of 2H-Tetraphenylporphyrin on Ag(111) during Fe Metalation. *J. Phys. Chem. C* **2011**, *115*, 4155–4162.
57. Hötger, D.; Carro, P.; Gutzler, R.; Wurster, B.; Chandrasekar, R.; Klyatskaya, S.; Ruben, M.; Salvarezza, R. C.; Kern, K.; Grumelli, D. Polymorphism and Metal-Induced Structural Transformation in 5,5'-Bis(4-Pyridyl)(2,2'-Bispyrimidine) Adlayers on Au(111). *Phys. Chem. Chem. Phys.* **2018**, *20*, 15960–15969.
58. Doyle, C. M.; Cunniffe, J. P.; Krasnikov, S. A.; Preobrajenski, A. B.; Li, Z.; Sergeeva, N. N.; Senge, M. O.; Cafolla, A. A. Ni–Cu Exchange Observed for Ni(II)-Porphyrins on Cu(111). *Chem. Commun.* **2014**, *50*, 3447.

6.7 Appendix

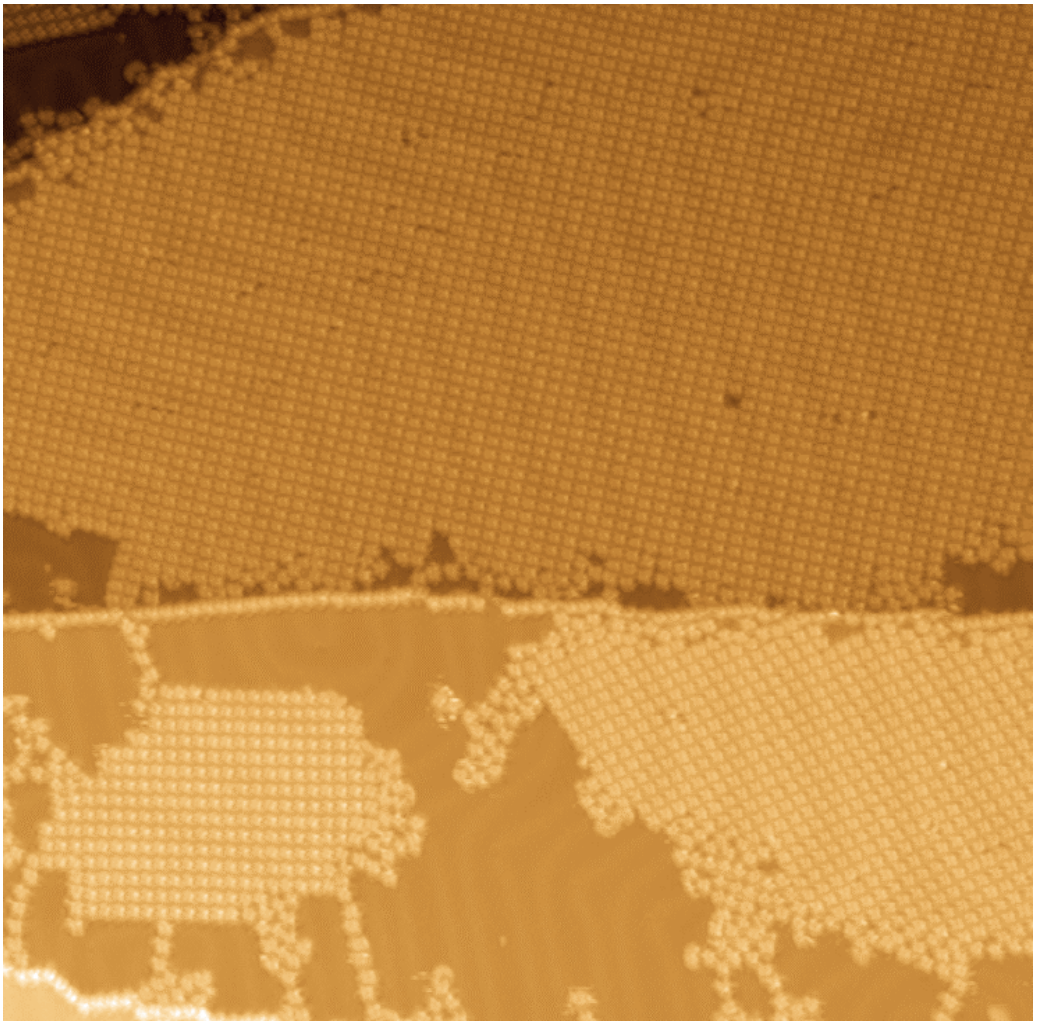

Figure A6.1. Overview STM image of the close-packed network formed by the deposition of a submonolayer of Ni-DPPyP on Au(111) at RT (100 x 100 nm^2, U = -1 V, I = 41 pA, RT). The network displays long-range order and the herringbone reconstruction of the Au(111) surface is well preserved underneath the molecular layer.

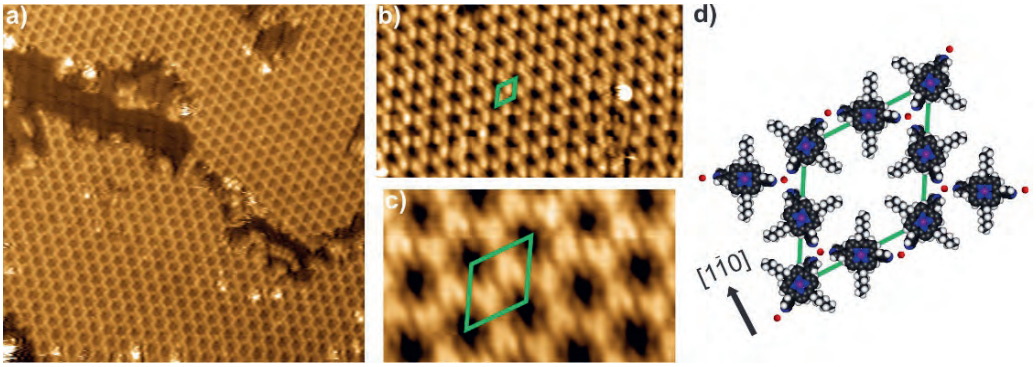

Figure A6.2. Cobalt-coordinated porous network of the analogue of Ni-DPPyP having hexyl chains (Ni-DHPyP) on Au(111). (a) Overview STM image (90 x 90 nm^2, U = 1.7 V, I = 20 pA, RT) of the porous network. (b) Close-up STM image (50 x 28 nm^2, U = 1.7 V, I = 20 pA, RT) of the cobalt-coordinated porous network. (c) Additional close-up STM image where individual Ni-DHPyP molecules can be distinguished. A single pore contains a group of six porphyrins (16.6 x 10 nm^2, U = 1.7 V, I = 20 pA, RT). In (b) and (c) the rhombic unit cell is shown in green. (d) Tentative structural model for the cobalt-coordinated porous Ni-DHPyP network. Cobalt, nickel, carbon, nitrogen and hydrogen atoms are depicted in red, purple, black, blue and white, respectively. One cobalt atom is coordinated to three pyridyl ligands. The unit cell is indicated by the green rhombus. The black arrow indicates the close-packed [1$\bar{1}$0] direction of the Au(111) surface.

Chapter 7

7 Pyrimidinyl-Functionalized Triarylamines on Cu(111): Temperature-Assisted Formation of a Porous Metal-Organic Coordination Network

The influence of post-deposition annealing on the self-assembly process of a pyrimidinyl-functionalized triarylamine derivative (molecule **1**) was studied under ultra-high vacuum (UHV) by means of scanning tunneling microscopy (STM) and X-ray photoelectron spectroscopy (XPS). The deposition of molecule **1** on Cu(111) held at room-temperature (RT) gave rise to a close-packed network as measured by STM. This two-dimensional (2D) network was simultaneously stabilized by H-bonds and twofold metal-coordination motifs via the peripheral N-atoms bonded to H-atoms from neighboring molecules and Cu-native atoms, respectively. Upon annealing the close-packed network at 150°C, the molecules rearranged into a metal-organic coordination network (MOCN) exhibiting a hexagonal porous structure that was stabilized by twofold metal-coordination motifs between the peripheral N-atoms and Cu-native atoms. The XPS measurements confirmed the presence of metal-coordination motifs in both networks and that upon annealing, the MOCN was exclusively stabilized by Cu-coordination motifs.

7.1 Introduction

The study of two-dimensional (2D) molecular networks steered by self-assembly on metal surfaces is of paramount interest owing to their potential usage in devices for electronic, catalytical and sensor applications.[1–4] The synthesis of these networks is based on the concepts provided by supramolecular chemistry, which utilizes non-covalent interactions to construct intricate nanostructures by linking a wide range of organic molecules together.[5] A promising class of organic molecules for the fabrication of 2D networks on surfaces are so-called heterotriangulenes due to their promising applications in (opto)electronic devices.[6–11] Heterotriangulenes are characterized by containing a heteroatom in their center and their periphery can be tailored with a variety of functional endgroups.[9,10] Furthermore, N-substituted heterotriangulenes – also known as *N*-heterotriangulenes or triarylamines – have gained salient attention in the last decade for fundamental research and usage as dyes in solar cells.[8–10]

Herein, we present a complementary study of the influence of post-deposition annealing on the self-assembly process of the pyrimidinyl-functionalized triarylamine derivative 4,4,8,8,12,12-hexamethyl-2,6,10-tri(pyrimidin-5-yl)-8,12-dihydro-4*H*-benzo[9,1]quinolizino[3,4,5,6,7-*defg*]acridine (referred as molecule **1** in scheme 1) on Cu(111) by means of scanning tunneling microscopy (STM) and X-ray photoelectron spectroscopy (XPS) under ultra-high vacuum (UHV) conditions. The self-assembly of a submonolayer of molecule **1** on Cu(111) at room-temperature (RT) formed a long-range ordered close-packed network that coexisted with a minority phase, i.e., a windmill structure, as observed in our STM measurements. Both networks were stabilized by H-bonds and twofold metal-ligand interactions

between the pyrimidinyl endgroups and Cu-native atoms. Annealing the sample at 150°C steered the formation of a metal-organic coordination network (MOCN) displaying a long-range ordered hexagonal porous structure stabilized by twofold metal-ligand interactions between the pyrimidinyl endgroups and Cu-native atoms.

The N 1s core level XPS spectra were acquired to investigate the chemical composition of molecule **1** on Cu(111) at RT and after annealing at 150°C, respectively. The binding energy (BE) values in the XPS spectra obtained for the samples prepared at RT are in line with our observations established from the STM measurements and the BE values reported for N-atoms bonded to H-atoms and Cu-native atoms, respectively. Furthermore, the XPS spectra acquired after annealing the sample at 150°C supported the presence of only metal-ligand interactions between the N-atoms from the pyrimidinyl endgroups and Cu-native atoms.

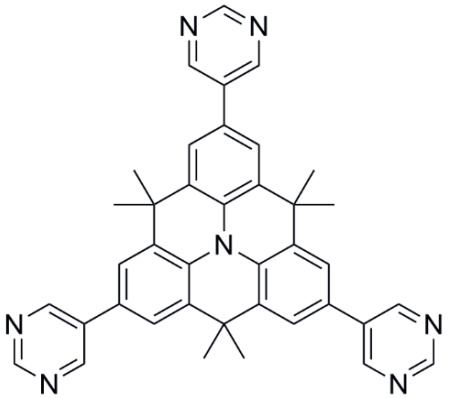

Scheme 1. Schematic molecular structure of 4,4,8,8,12,12-hexamethyl-2,6,10-tri(pyrimidin-5-yl)-8,12-dihydro-4*H*-benzo[9,1]quinolizino[3,4,5,6,7-*defg*]acridine (molecule **1**).

7.2 Experimental Methods

All experiments were carried out in a UHV system (with a base pressure in the low 10^{-10} mbar regime) equipped with different chambers for sample preparation and characterization. The Cu(111) single crystal was cleaned by repeated cycles of Ar^+ sputtering and annealing at 495°C. The triarylamine derivatives (molecule **1**) were thermally sublimed onto the Cu(111) surface held at RT by means of a Knudsen cell evaporator (CreaPhys). A quartz crystal microbalance was used to monitor the molecule deposition rates. The STM measurements were conducted with a commercial variable-temperature (VT) STM (Scienta Omicron GmbH) operated at RT with a mechanically cut Pt/Ir wire as a tip in constant current mode. All bias voltages are given with respect to a grounded tip. The STM images were processed with WSxM software.[12] Furthermore, the XPS measurements (Thermo Scientific) were performed in the same analysis chamber which also houses the STM. The XPS core level spectra were acquired using Al K_α X-rays with a photon energy of 1486.6 eV. The energy positions of the N 1s core level data were calibrated to the Au $4f_{7/2}$ peak of Au(111). For evaluating the measured data, a linear background was first subtracted from the spectrum. Then the spectrum was fitted with Voigt profiles (convolution of a Gaussian and a Lorentzian) using CasaXPS.

7.3 Results and Discussion

The self-assembly of a submonolayer of molecule **1** (shown in scheme 1) on Cu(111) at RT is shown in Figure 7.1. The overview STM image (Figure 7.1a) shows a long-range ordered, close-packed network that is composed by hexagon-like building blocks (highlighted by the green and purple hexagons).

The intramolecular features of molecule **1** can be distinguished in the high-resolution STM image (Figure 7.1b), where a single molecule (marked by the white outline) has its methyl and pyrimidinyl endgroups highlighted by orange and black dots, respectively. It should be noted that the out-of-plane rotation of the methyl endgroups confers them a brighter STM contrast compared with the pyrimidinyl groups.[13,14] By carefully measuring the intermolecular distances from the STM data, we constructed a unit cell (shown in red in Figure 7.1a) with lengths a = 6.5 ± 0.2 nm, b = 3.8 ± 0.1 nm, and an internal angle of α = 85° ± 2°. As highlighted by the green and purple hexagons (Figure 7.1a), the molecules are grouped in six-membered rings. The molecules within a six-membered ring point one of their pyrimidinyl endgroups towards the center of the ring with an offset between opposing molecules (highlighted by the dotted red lines in Figure 7.1b), i.e., the bottom molecule is placed either on the right- or left-hand side with respect to the top molecule. This arrangement of the molecules within a hexagon exhibits organizational chirality, which is triggered by the adsorption of achiral molecules (such as molecule **1**) on a surface that induces a specific alignment with respect to the neighboring molecules.[13–16] This type of chirality is only expressed at a local level which can be clearly distinguished in Figure 7.1b by analyzing the position of the central pair of molecules (highlighted by the dotted red lines) within each six-membered ring: in the green hexagon the central bottom molecule is aligned to the right with respect to the top molecule, while the opposite case is present in the purple hexagon, i.e., the bottom molecule is placed on the left with respect to the top molecule. Furthermore, the pyrimidinyl endgroups located at the periphery of the six-membered ring point towards one side of the pyrimidinyl endgroups from the neighboring molecules (depicted by the dotted black lines in Figure 7.1b).

Therefore, by following the arrangement of the molecules pointing at the center of the green hexagon in Figure 7.1b, the pair of N-atoms from the pyrimidinyl endgroups interact via H-bonds with the H-atoms from the pyrimidinyl endgroups of neighboring molecules. Similarly, by following the dotted black lines in Figure 7.1b, one of the N-atoms from each pyrimidinyl endgroups located at the periphery of the six-membered ring also interact via H-bonds with the H-atoms from the pyrimidinyl endgroups of neighboring molecules.

Additionally, the remaining N-atom (highlighted by the white lines and circles in Figure 7.1b) from each of the pyrimidinyl endgroups located at the periphery of the six-membered ring interacts via a metal-ligand interaction with one Cu-native atom (shown in orange in Figure 7.1c). It should be noted that each ring of molecules has six neighboring rings and hence, only one molecule per ring is available for interaction with its neighboring ring. However, two N-atoms from neighboring rings could not be bonded to each other due to steric repulsion. In addition, it is worth to mention that we ruled out the possibility of having H-bonds between the N-atoms and H-atoms from the neighboring six-membered rings since the H–N distance would amount to ~4.2 Å, which is beyond typical H-bond distances.[2] Therefore, the interaction between neighboring six-membered rings (highlighted by the green and purple hexagons) could only be possible by the presence of twofold Cu-coordination motifs formed between the pyrimidinylic N-atoms that are facing outwards, i.e., the N-atom from one ring interacts with a single Cu-atom that is bonded (on the opposite side) to the N-atom from the neighboring ring. The projected bond distances for the abovementioned H-bonds (i.e., H–N interaction) and Cu-coordination motifs (i.e., Cu–N interaction) are 2.8 and 2.1 Å, respectively, which fall within typical values for H–N[2,17,18] and Cu–N

bond distances[2,18–22]. Based on the previously mentioned 2D arrangement, the molecular and metal densities amount to 0.49 molecules and 0.49 Cu-atoms per nm^2, respectively. Furthermore, the usage of pyrimidinyl-functionalized molecules for the fabrication of 2D networks on metal surfaces has scarcely been reported and usually an annealing step above RT was required to induce metal-coordination.[18,20,21,23] The close-packed network coexisted with a second network at RT, i.e., a windmill structure, which was encountered as a minority phase (see Figure A7.5, A7.6 and A7.7 in the Supporting Information). The structure of the close-packed network remained stable after annealing to 80 °C (see Figure A7.1 in the Supporting Information).

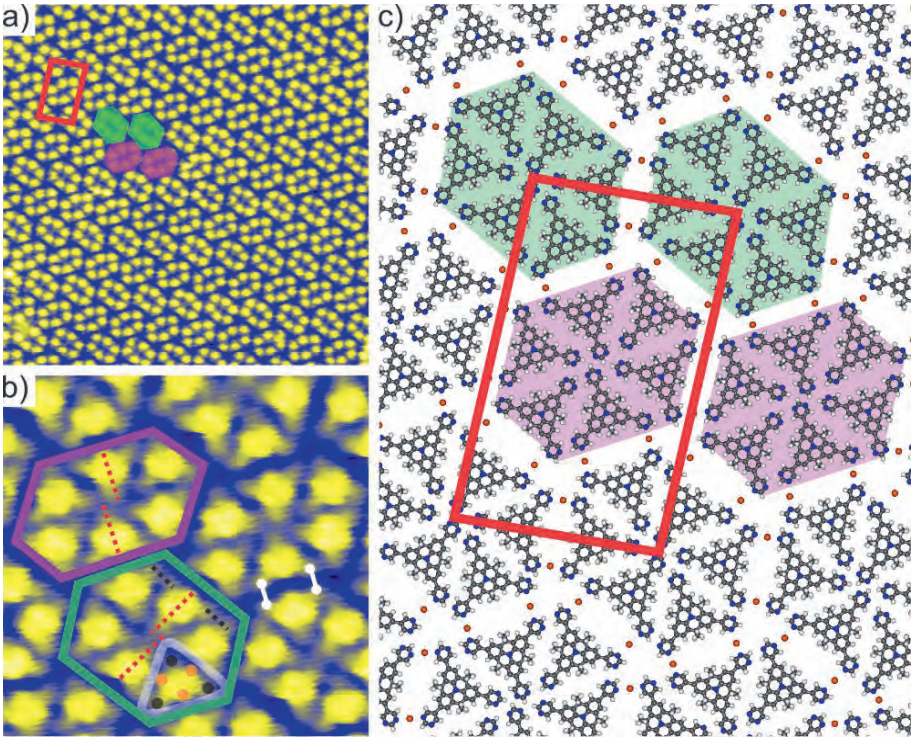

Figure 7.1. Self-assembly of molecule **1** on Cu(111) at RT. (a) Overview STM image of the close-packed network (38 x 38 nm^2, U_{bias} = -1.6 V, I_{set} = 20 pA). The structure (unit cell in red) is composed by six-membered rings, i.e., groups of six molecules highlighted in green and purple. (b) High-resolution STM image where a single molecule is highlighted by the white outline (8 x 8 nm^2, U_{bias} = -1.6 V, I_{set} = 20 pA). The black and orange circles highlight the pyrimidinyl and methyl endgroups, respectively. The green and purple hexagons resemble the ones shown in (a) and the dotted red lines depict the offset between opposing molecules. The dotted black lines guide the eye through the H-bonds between neighboring pyrimidinyl endgroups, while the white lines and circles highlight the half of the pyrimidinyl endgroup that is engaged in metal-coordination. (c) Tentative structural model of the close-packed network stabilized by H-bonds and twofold Cu-coordination motifs. Copper, nitrogen, carbon and hydrogen atoms are shown in orange, blue, gray and white, respectively. The unit cell is shown in red. The purple and green hexagons resemble the six-membered rings shown in (a).

The formation of a long-range ordered porous hexagonal network was observed by STM after annealing the sample at 150°C (Figure 7.2a). The presence of rotational molecular domains separated by 10° was evidenced by STM (see Figure A7.4 in the Supporting Information). The detailed STM image (Figure 7.2b) displays the molecular arrangement within the porous network, in which a single molecule is highlighted by the orange outline. The structure is characterized by pores that are formed by groups of six molecules. From our STM measurements we constructed a rhombic unit cell (shown in green in Figure 7.2b) with lengths a = b = 2.2 ± 0.1 nm and an internal angle of α = 120° ± 2°. Furthermore, the molecular orientation can be discerned in Figure 7.2, where each molecule has three nearest neighbors that are rotated 60° with respect to the central molecule. Within such an arrangement, the pyrimidinyl endgroups seem to be parallelly aligned to each other and this could only be possible with a linker between them, i.e., a metal-atom provided by the Cu(111) surface. Therefore, since steric repulsion would not allow a direct interaction between the N-atoms from neighboring pyrimidinyl endgroups, we propose that the porous network is stabilized by twofold Cu-coordination motifs between the N-atoms from two neighboring pyrimidinyl endgroups and one Cu-native atom as depicted in the tentative structural model (Figure 7.2c). It should be noted that the Cu-native atoms were not resolved in our STM images, which is in agreement with the common invisibility for 3d transition metals on metal surfaces.[18,20,21,24,25] The projected Cu–N bond distance is 2.1 Å and agrees with previously reported values for Cu–N bond lengths.[18,21,22,26] In addition, by taking these intermolecular interactions into account, the molecular and metal densities amount to 0.48 molecules and 1.43 Cu-atoms per nm^2, respectively. Furthermore, compared with the twofold Cu-coordination observed in the porous network in the

present study, similar coordination geometries in porous 2D networks have been achieved for pyrimidinyl-functionalized perylene derivatives coordinated to Cu-native atoms after annealing at 150°C on Cu(111).[18,20,21,23] Furthermore, the structure of the porous network persisted after annealing at 245°C (see Figure A7.2 in the Supporting Information) and thermal decomposition of the molecules was observed after annealing in the vicinity of 260 °C (see Figure A7.3 in the Supporting Information).

The generation of Cu-native atoms on the Cu(111) surface will be addressed in the following to better understand the influence that the post-deposition annealing step had on the self-assembly of molecule **1**. It is well known that Cu-native atoms on Cu surfaces are generated at RT[18,25,27] and elevated temperatures (≥150°C) by the detachment of Cu-atoms from step edges and that the detachment rate is a thermally activated process.[18,28–30] In addition, despite the low concentration of Cu-native atoms expected at RT, pyrimidinyl endgroups have shown to possess an affinity for the detachment of Cu-atoms from step edges on Cu(111) at this temperature.[18] Thus, the presence of Cu-native atoms is not only dependent on temperature but also on the molecule-substrate interactions.[18,29,30] These findings support the correlation found between the sample temperature and Cu-native atom concentration in the 2D networks described in the present work, where at RT the lower concentration of Cu-native atoms favored the formation of the close-packed network (0.49 Cu-atoms per nm^2) as the majority phase since it required ~33% less Cu-atoms than the windmill network (0.74 Cu-atoms per nm^2). However, the post-deposition annealing step at 150°C led to an increased detachment of Cu-atoms from the step edges that promoted the formation of the porous MOCN as one exclusive phase that contained ~191% higher Cu-atom concentration than the close-packed network.

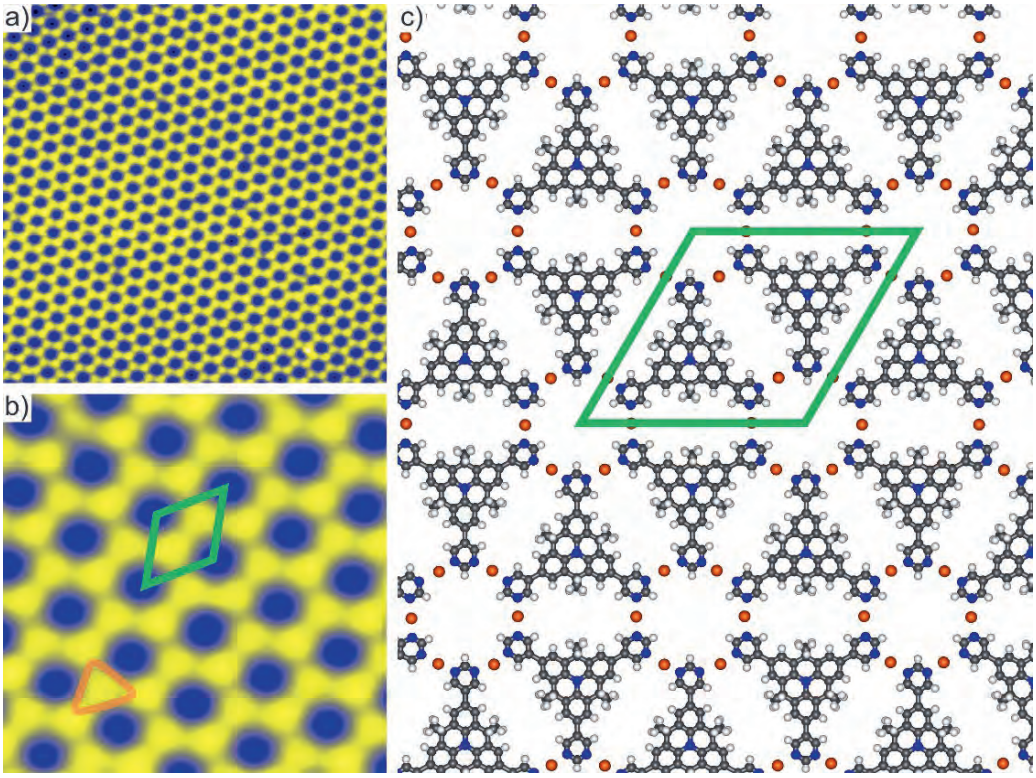

Figure 7.2. Self-assembly of molecule **1** on Cu(111) after post-deposition annealing at 150°C. (a) Overview STM image of the hexagonal porous network (38 x 38 nm^2, U_{bias} = -1.6 V, I_{set} = 25 pA). (b) Detailed STM image where a single molecule is highlighted by the orange outline (10 x 10 nm^2, U_{bias} = -1.6 V, I_{set} = 25 pA). (c) Tentative structural model of the porous network stabilized by twofold Cu-coordination motifs. Copper, nitrogen, carbon and hydrogen atoms are shown in orange, blue, gray and white, respectively. The unit cell is shown in green.

The XPS spectra for the N 1s core level were measured to shed light on the chemical state of molecule **1** on Cu(111) at RT and after annealing at 150°C. As shown in the ball and stick model (Figure 7.3), molecule **1** contains seven N-atoms (shown in blue) that are categorized in two chemically different species: N1 (six pyrimidinylic N-atoms) and N2 (one central aminic N-atom). The N 1s core level spectra shown in Figure 7.4 correspond to

samples of molecule **1** on Cu(111) prepared at different molecule coverage and post-deposition annealing temperature in order to obtain the following phases: (a) organic phase (5.5 ML at RT), (b) close-packed network (0.9 ML at RT) and (c) hexagonal porous network (0.9 ML at 150°C). Furthermore, all N 1s spectra were fitted with Gaussian functions after subtracting a linear background.

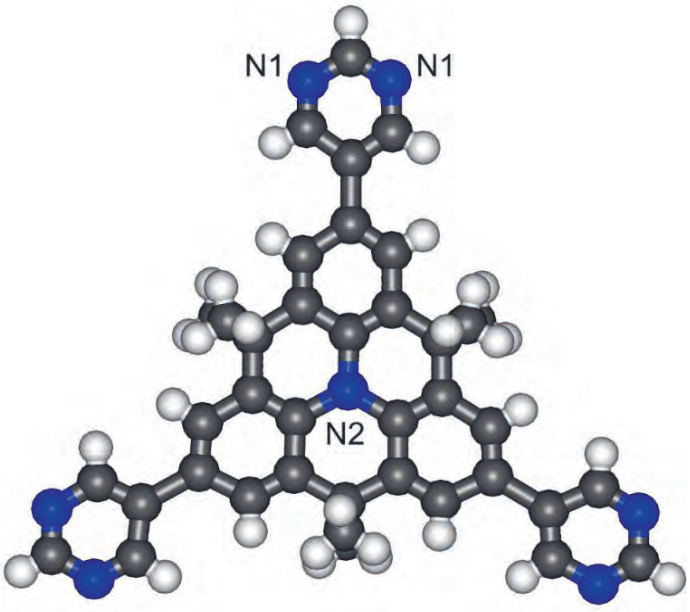

Figure 7.3. Ball and stick model of molecule **1** with the chemically different N-atoms (N1 and N2) indicated by numbers. The carbon, nitrogen and hydrogen atoms are shown in gray, blue and white, respectively.

The binding energy (BE) positions for each component of the N 1s spectra (Figure 7.4) are contained in Table 7.1. We will firstly describe the XPS spectrum for the multilayer phase (Figure 7.4a), i.e., the organic phase, since it serves as a reference for the other networks by neglecting the molecule-substrate interactions. The spectrum (in Figure 7.4a) was fitted with two Gaussian peaks (located at 399.4 and 400.7 eV, respectively), as the molecule contains two chemically different species (pyrimidinylic N1-atom and aminic N2-atom). The peak area ratio found between N1 and N2 is 5.7 : 1, which is in line with the stoichiometric ratio of the N-atoms in molecule **1** (see Table A7.1 in the Supporting Information). In agreement with the previously reported peak positions between peripheral N-atoms and central aminic N-atoms in multilayer samples of cyano-functionalized triarylamines on Cu(111), we assigned the red peak (Figure 7.4a) located at lower BE (399.4 eV) to the pyrimidinylic N-atoms (N1), while the blue peak located at higher BE (400.7 eV) was attributed to the aminic N-atoms (N2).[14] In addition, the peak position of N1 is similar to the previously reported value for pyridylic N-atoms in multilayer samples of tetrapyridyl-functionalized porphyrins on Cu(111).[26]

Table 7.1. Binding energies for the N 1s chemical components of molecule **1** on Cu(111) in the purely organic phase (multilayer), close-packed and porous networks.

Network	**N1**		**N2**
	H-bonded	**Cu-coordinated**	
Organic phase (multilayer)	399.4	n/a	400.7
Close-packed	399.1	398.1	400.3
Porous	n/a	398.3	400.2

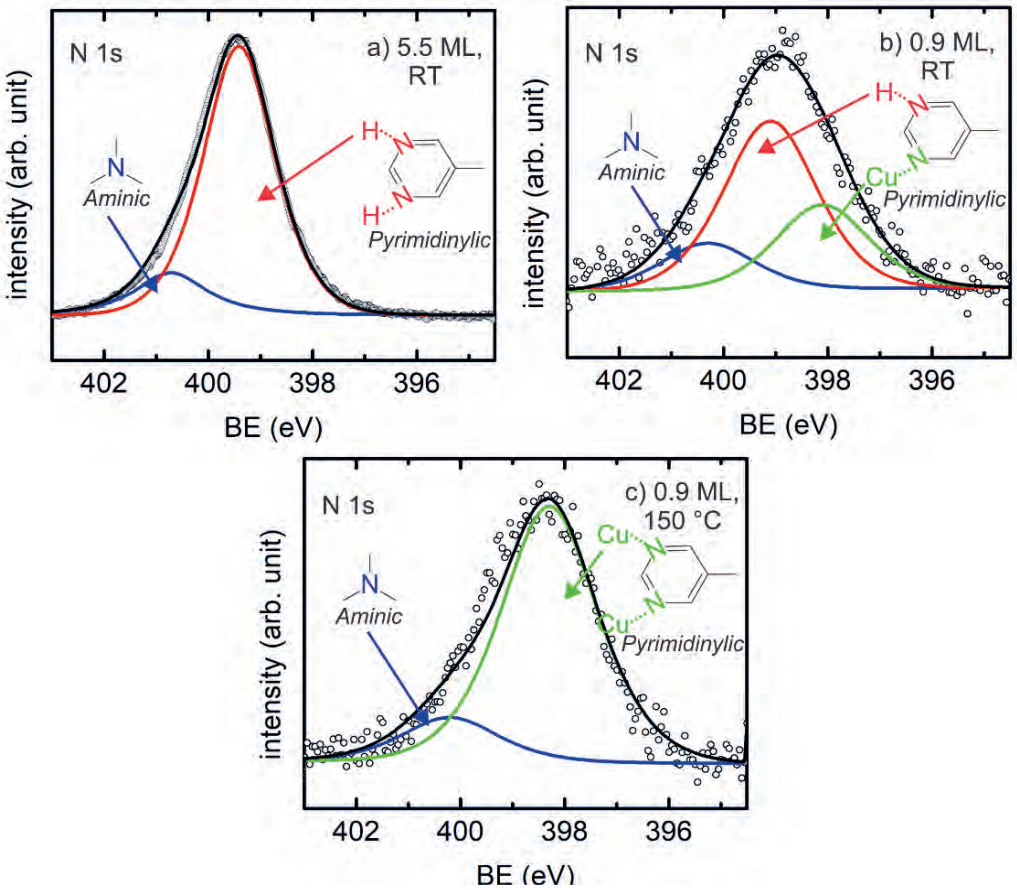

Figure 7.4. N 1s core level spectra of molecule **1** on Cu(111) for samples prepared at varying molecule coverage and annealing temperature after molecule deposition: (a) 5.5 ML of molecule **1** at RT, (b) 0.9 ML of molecule **1** at RT, and (c) 0.9 ML of molecule **1** followed by post-deposition annealing at 150°C. The spectrum in (a) corresponds to the multilayer case of the purely organic phase of molecule **1**, while the spectrum in (b) belongs to the close-packed network and (c) is the Cu-coordinated porous network. The chemically different components are color-labelled for the aminic (N2) and pyrimidinylic (N1) N-atoms as follows: blue for the component of the N 1s core level for the aminic N2-atoms, while for the pyrimidinylic N1-atoms, the components are color-labelled according to their bonding motif, red for H-bonding and green for Cu-coordination. The peak positions are given in Table 7.1.

The N 1s core level spectrum in Figure 7.4b belongs to the close-packed network and its envelope appears broader with respect to the multilayer phase.[14] By taking this and the analysis obtained from the STM measurements into consideration, the fitting of the spectrum was only possible by using three components located at 398.1, 399.1 and 400.3 eV, respectively. The peak area ratio between them is 3.9: 1.9: 1 = (red peak): (green peak): (blue peak). Compared to the spectrum of the multilayer phase, the red and blue peaks shifted towards lower BE, while the main difference resides in the appearance of a third component, i.e., indicating a chemically different N-atom. Therefore, in agreement with our STM findings and the previously reported peak positions for Cu-coordinated N-atoms in pyrimidinyl-functionalized perylene derivatives and cyano-functionalized triarylamines on Cu(111), respectively, the green peak (398.1 eV) located at the lowest BE was assigned to the pyrimidinylic N-atoms (N1) bonded to Cu-native atoms.[14,18] On the other hand, the red peak (399.1 eV) was once again attributed to the pyrimidinylic N-atoms (N1) bonded to H-atoms since its position is comparable to the one observed in the spectrum of the multilayer sample and its BE is in agreement with the previously reported peak positions for H-bonded N-atoms in cyano-functionalized tetrahydroanthracene molecules on Ag(111) and in cyano-functionalized triarylamines on Cu(111), respectively.[14,31] Similarly to the spectrum of the multilayer sample, the blue peak (400.3 eV) located at the highest BE was also attributed to the aminic N-atom (N2) and is in full agreement with the previously reported peak position for aminic N-atoms in submonolayer samples of cyano-functionalized triarylamines on Cu(111).[14] Additionally, the trend observed between the peak positions of the H-bonded pyrimidinylic N1 and aminic N2 components in the spectrum of the multilayer phase of molecule **1** – that is

N1 at lower and N2 at higher BE, respectively – also persisted for the spectrum of the close-packed network and agrees with the previously reported peak positions between peripheral and central N-atoms in triarylamines on Cu(111) and Au(111).[14] Furthermore, the peak position distribution between both pyrimidinylic N-atoms, i.e., the Cu-coordinated N1-atoms (green peak) at lower BE and H-bonded N1-atoms (red peak) at higher BE, is also in line with the previously reported peak position trend between Cu-bonded and H-bonded N-atoms in cyano-functionalized triarylamines on Cu(111).[14] In addition, a similar trend between the peak positions for Cu-coordinated pyridylic N-atoms and H-bonded pyrrolic N-atoms was previously reported in tetrapyridyl-functionalized porphyrins on Au(111).[32] It should be noted that the peak area ratio (see Table A7.1 in the Supporting Information) between the H-bonded and Cu-coordinated N1 components (3.9 : 1.9) in the N 1s spectra of the close-packed network supports the 2 : 1 stoichiometric ratio between H and Cu-bonds suggested in the corresponding structural model (Figure 7.1c).

By comparing the peak positions in the N 1s core level spectrum of the close-packed network with respect to the multilayer case, a shift of 0.3 and 0.4 eV towards lower BE was observed for the H-bonded N1-atoms (red peak in Figure 7.4b) and aminic N2-atoms (blue peak in Figure 7.4b), respectively. Such a decrease in BE when going from a multilayer to monolayer sample can be attributed to a core-hole screening and possible modification of the metal work function.[14] Similar shifts towards lower BE were reported for N-atoms in cyano-functionalized triarylamines and tetrapyridyl as well as tetraphenyl-functionalized porphyrins on Cu(111).[14,26,33]

Finally, the N 1s core level spectrum of the hexagonal porous network (Figure 7.4c) appears at a lower BE compared with the close-packed phase (Figure 7.4b), which can be correlated to the influence that the post-deposition annealing step had on the chemical state of molecule **1**. Therefore, based on this and the observations obtained from the STM measurements the spectrum was fitted with two components: one green (398.3 eV) and blue (400.2 eV) peak, respectively. The peak area ratio (see Table A7.1 in the Supporting Information) between them (5.8 : 1 = N1 (green peak) : N2 (blue peak)) is in agreement with the molecular stoichiometry of molecule **1**. It should be noted that compared to the peak positions observed in the spectrum of the close-packed network, the N1 and N2 components only shifted slightly. However, the peak of the H-bonded N1-atoms (red peak in Figure 7.4b) observed in the spectrum of the close-packed network is no longer present in the spectrum of the porous network (Figure 7.4c), which supports – along with the STM measurements – that the yield of metal-coordination between the pyrimidinylic N-atoms and Cu-native atoms is fully efficient after annealing at 150°C. Indeed, previous studies of pyrimidinyl-functionalized perylene derivatives have shown that annealing at 150°C or higher increases the concentration of Cu-atoms on the Cu(111) surface which steers the formation of MOCNs exclusively stabilized by Cu-coordination.[18,23,24] Therefore, the green peak (398.3 eV) belongs to the pyrimidinylic N-atoms (N1) bonded to Cu-native atoms, which is in line with previously reported peak positions for N-atoms involved in metal-coordination with Cu and Fe-atoms.[14,18,32–35] On the other hand, the blue peak (400.2 eV) corresponds to the aminic N-atoms (N2) as it agrees with the BE reported for aminic N-atoms in cyano-functionalized triarylamines on Cu(111).[14] Similarly, to the multilayer and close-packed network case, the overall trend for the peak

positions between the N1 (lower BE) and N2 (higher BE) components also persisted for the spectrum of the porous network.[14]

In comparison with the peak positions observed in the spectrum of the close-packed network, the N1 component shifted (0.2 eV) towards higher BE, while the N2 component shifted (0.1 eV) towards lower BE. A possible explanation for both shifts is a change in adsorption conformation of molecule **1** upon metal-coordination.[13,14] Following such an assumption, molecule **1** in the close-packed network adopted an arched adsorption conformation to be able to interact with the Cu surface and consequently the methyl groups were tilted upwards. However, when the concentration of Cu-native atoms was increased by the post-deposition annealing step and the porous network was formed, molecule **1** became flatter on the Cu(111) surface, which lead to a closer interaction of the aminic N2-atoms with the metal surface, while the pyrimidinylic N1-atoms were placed further away since they are anchored to Cu-native atoms resulting in a reduced interaction with the Cu surface. Therefore, the aminic N2-atoms and pyrimidinylic N1-atoms experienced an increased and lowered core hole screening from the Cu(111) surface, that is reflected in the peak shift towards lower and higher BE, respectively. A similar transition from an arched to a flattened adsorption conformation mediated by Cu-coordination was previously reported for an amino-functionalized perylene molecule on Cu(111).[24]

7.4 Conclusion

In summary, we presented a complementary study of the influence of annealing on the self-assembly process of a pyrimidinyl-functionalized triarylamine (molecule **1**) on Cu(111) by means of STM and XPS under UHV. As observed by STM, molecule **1** self-assembled into a close-packed network at submonolayer coverage that was simultaneously stabilized by H-bonds between neighboring molecules and Cu-coordination between the N-atoms from the pyrimidinyl endgroups and Cu-native atoms provided by the underlying Cu(111) surface. In addition, a windmill structure stabilized by H-bonds and Cu-coordination coexisted as a minority phase with the close-packed network. After annealing at 150°C, a transition from the close-packed phase to a hexagonal porous network was evidenced by STM. Such a network was stabilized by twofold Cu-coordination motifs between the pyrimidinylic N-atoms and Cu-native atoms.

The samples were measured with XPS to further support and study the chemical composition of molecule **1** prior to and after annealing. Firstly, a multilayer sample was measured to gain insight of the purely organic phase of molecule **1** by neglecting the molecule-substrate interactions. The N 1s XPS spectrum of the multilayer phase was composed by two components, i.e., N1 (H-bonded pyrimidinylic N1-atoms) and N2 (central aminic N2-atoms) and their peak positions were in good agreement with the previously reported BE for multilayer samples of triarylamine derivatives on Cu(111). Furthermore, in the N 1s spectrum of the close-packed network, a shift towards lower BE was observed for the N1 and N2 components which is typical when going from multilayer to submonolayer samples due to core-hole screening. In addition, the formation of Cu-coordination motifs in the

close-packed network was confirmed by the presence of a third component (Cu-bonded pyrimidinylic N1). Finally, the N 1s spectrum of the porous network exhibited only two components, Cu-bonded pyrimidinylic N1 and aminic N2, while the H-bonded pyrimidinylic N1 was completely absent. These findings were in line with the results assumed after carefully analyzing the STM measurements, which fully supported the presence of only Cu-coordination motifs within the porous network.

7.5 References

1. Gutzler, R.; Stepanow, S.; Grumelli, D.; Lingenfelder, M.; Kern, K. Mimicking Enzymatic Active Sites on Surfaces for Energy Conversion Chemistry. *Acc. Chem. Res*. **2015**, *48*, 2132−2139.
2. Barth. J. V. Molecular Architectonic on Metal Surfaces. *Annu. Rev. Phys. Chem*. **2007**, *58*, 375–407.
3. Stepanow, S.; Lin, N.; Barth, J. V. Modular Assembly of Low-Dimensional Coordination Architectures on Metal Surfaces. *J. Phys.: Condens. Matter* **2008**, *20*, 184002.
4. Dong, L.; Gao, Z. A.; Lin, N. Self-Assembly of Metal-Organic Coordination Structures on Surfaces. *Prog. Surf. Sci.* **2016**, *91*, 101−135.
5. Furukawa, H.; Cordova, K. E.; O'Keeffe, M.; Yaghi, O. M. The Chemistry and Applications of Metal-Organic Frameworks. *Science* **2013**, *341*, 1230444.
6. Kim, D.; Kim, C.; Choi, H.; Song, K.; Kang, M.-S.; Ko, J. A New Class of Organic Sensitizers with Fused Planar Triphenylamine for Nanocrystalline Dye Sensitized Solar Cells. *J. Photochem. Photobiol., A* **2011**, *219*, 122–131.
7. Liu, C.; Zhang, Y.; Yang, C.; Wu, H.; Qin, J.; Cao, Y. Solution-Processed, Undoped, Deep-Blue Organic Light-Emitting Diodes Based on Starburst Oligofluorenes with a Planar Triphenylamine Core. *Chem. Eur. J*. **2012**, *18*, 6928–6934.
8. Meinhardt, U.; Lodermeyer, F.; Schaub, T. A.; Kunzmann, A.; Dral, P. O.; Sale, A. C.; Hampel, F.; Guldi, D. M.; Costa, R. D.; Kivala, M. *N*-Heterotriangulene Chromophores with 4-Pyridyl Anchors for Dye-Sensitized Solar Cells. *RSC. Adv.*, **2016**, *6*, 67372–67377.
9. Hammer, N.; Schaub, T. A.; Meinhardt, U.; Kivala, M. *N*-Heterotriangulenes: Fascinating Relatives of Triphenylamine. *Chem. Rec.* **2015**, *15*, 1119–1131.
10. Schaub, T. A.; Padberg, K.; Kivala, M. Bridged Triarylboranes, -Silanes, -Amines, and -Phosphines as Minimalistic Heteroatom-Containing Polycyclic Aromatic Hydrocarbons: Progress and Challenges. *J. Phys. Org. Chem.* **2020**, *33*, 1–27.
11. Field, J. E.; Venkataraman, D. Heterotriangulenes–Structure and Properties. *Chem. Mater.* **2002**, *14*, 962–964.
12. Horcas, I.; Fernández, R.; Gómez-Rodríguez, J. M.; Colchero, J.; Gómez-Herrero, J.; Baro, A. M. WSXM: A Software for Scanning Probe Microscopy and a Tool for Nanotechnology. *Rev. Sci. Instrum.* **2007**, *78*, 013705.
13. Gottardi, S.; Müller, K.; Moreno-Lopez, J. C..; Yildirim, H.; Meinhardt, U.; Kivala, M..; Kara, A.; Stöhr, M. Cyano-Functionalized Triarylamines on Au(111): Competing Intermolecular versus Molecule/Substrate Interactions. *Adv. Mater. Interfaces* **2014**, *1*, 1300025.
14. Müller, K.; Moreno-López, J. C.; Gottardi, S.; Meinhardt, U.; Yildirim, H.; Kara, A.; Kivala, M.; Stöhr, M. Cyano-Functionalized Triarylamines on Coinage

Metal Surfaces: Interplay of Intermolecular and Molecule–Substrate Interactions *Chem. Eur. J* **2016**, *22*, 581-589.
15. Barlow, S. M.; Raval. R. Complex Organic Molecules at Metal Surfaces: Bonding, Organisation and Chirality. *Surf. Sci. Rep.* **2003**, *50*, 201–341.
16. Ernst, K.-H. Molecular Chirality at Surfaces. *Phys. Status Solidi B* **2012**, *249*, 2057–2088.
17. Baker Cortés, B. D.; Schmidt, N.; Enache, M.; Stöhr, M. Coverage-Dependent Structural Transformation of Cyano-Functionalized Porphyrin Networks on Au(111) via Addition of Cobalt Atoms. *J. Phys. Chem. C* **2019**, *123*, 19681-19687.
18. Matena, M.; Stöhr, M.; Riehm, T.; Björk, J.; Martens, S.; Dyer, M. S.; Persson, M.; Lobo-Checa, J.; Müller, K.; Enache, M.; Wadepohl, H.; Zegenhagen, J.; Jung, T. A.; Gade, L. H. Aggregation and Contingent Metal/Surface Reactivity of 1,3,8,10-Tetraazaperopyrene (TAPP) on Cu(111). *Chem. Eur. J.* **2010**, *16*, 2079-2091.
19. Liu, J.; Lin, T.; Shi, Z.; Xia, F.; Dong, L.; Liu, P. N.; Lin, N. Structural Transformation of Two-Dimensional Metal–Organic Coordination Networks Driven by Intrinsic In-Plane Compression. *J. Am. Chem. Soc*. **2011**, *133*, 18760–18766.
20. Matena, M.; Riehm, T.; Stöhr, M.; Jung. T. A.; Gade, L. H. Transforming Surface Coordination Polymers into Covalent Surface Polymers: Linked Polycondensed Aromatics through Oligomerization of N-Heterocyclic Carbene Intermediates. *Angew. Chem. Int. Ed.* **2008**, *47*, 2414–2417.
21. Björk, J.; Matena, M.; Dyer, M. S.; Enache, M.; Lobo-Checa, J.; Gade, L. H.; Jung, T. A.; Stöhr, M.; Persson, M. STM Fingerprint of Molecule–Adatom Interactions in a Self-Assembled Metal–Organic Surface Coordination Network on Cu(111). *Phys. Chem. Chem. Phys.* **2010**, *12*, 8815-8821.
22. Zhang, X.; Li, N.; Wang, H.; Yuan, C.; Gu, G.; Zhang, Y.; Nieckarz, D.; Szabelski, P.; Hou, S.; Teo, B. K.**;** Wang. Y. Influence of Relativistic Effects on Assembled Structures of V-Shaped Bispyridine Molecules on M(111) Surfaces Where M = Cu, Ag, Au. *ACS Nano* **2017**, *11*, 8511-8518.
23. Enache, M. (2016). *Surface-confined molecular assembly: Investigations with local and non-local probes*. [Groningen]: University of Groningen.
24. Matena, M.; Björk, J.; Wahl, M.; Lee, T.-L.; Zegenhagen, J.; Gade, L. H.; Jung, T. A.; Persson, M.; Stöhr. M. On-surface synthesis of a two-dimensional porous coordination network: Unraveling adsorbate interactions. *Phys. Rev. B* **2014**, *90*, 125408-1/125408-8.
25. Lin. N.; Dmitriev, A.; Weckesser, J.; Barth, J. V.; Kern. K. Real-Time Single-Molecule Imaging of the Formation and Dynamics of Coordination Compounds. *Angew. Chem. Int. Ed.* **2002**, *41*, 4779–4783.
26. Klappenberger, F.; Weber-Bargioni, A.; Auwärter, W.; Marschall, M.; Schiffrin, A.; Barth, J. V. Temperature Dependence of Conformation, Chemical State, and

Metal-Directed Assembly of Tetrapyridyl-Porphyrin on Cu(111). *J. Chem. Phys*. **2008**, *129*, 214702.

27. Schunack, M.; Rosei, F.; Naitoh, Y.; Jiang, P.; Gourdon, A.; Laegsgaard, E.; Stensgaard, I.; Joachim, C.; Besenbacher, F. Adsorption behavior of Lander Molecules oon Cu(110) Studied by Scanning Tunneling Microscopy. *J. Chem. Phys.* **2002**, *117*, 6259–6259.
28. Barth, J. V.; Weckesser, J.; Lin, N.; Dmitriev, A.; Kern. K. Supramolecular Architectures and Nanostructures at Metal Surfaces. *Appl. Phys. A* **2003**, *76*, 645–652.
29. Giesen. M. Equilibrium Fluctuations and Decay of Step Bumps on Vicinal Cu(111) Surfaces. *Surf. Sci.* **1998**, *412/413*, 645– 656.
30. Giesen. M. Scaling Transition of the Time Dependence of Step Fluctuations on Cu(111). *Surf. Sci.* **1999**, *442*, 543–549.
31. Fan, Q.; Luy, J.-N.; Liebold, M.; Greulich, K.; Zugermeier, M.; Sundermeyer, J.; Tonner, R.; Gottfried, J. M. Template-Controlled On-Surface Synthesis of a Lanthanide Supernaphthalocyanine and its Open-Chain Polycyanine Counterpart. *Nat Commun.* **2019**, *10*, 5049.
32. Li, Y.; Xiao, J.; Shubina, T. E.; Chen, M.; Shi, Z.; Schmid, M.; Steinrück, H.-P.; Gottfried, J. M.; Lin, N. Coordination and Metalation Bifunctionality of Cu with 5,10,15,20-Tetra(4-pyridyl)porphyrin: Toward a Mixed-Valence Two-Dimensional Coordination Network. *J. Am. Chem. Soc.* **2012**, *134*, 6401-6408.
33. Diller, K.; Klappenberger, F.; Marschall, M.; Hermann, K.; Nefedov, A.; Wöll, Ch.; Barth, J. V. Self-Metalation of 2H-tetraphenylporphyrin on Cu(111): An X-ray Spectroscopy Study. *J. Chem. Phys*. **2012**, *136*, 014705.
34. Hötger, D.; Carro, P.; Gutzler, R.; Wurster, B.; Chandrasekar, R.; Klyatskaya, S.; Ruben, M.; Salvarezza, R. C.; Kern, K.; Grumelli, D. Polymorphism and Metal-Induced Structural Transformation in 5,5'-bis(4-pyridyl)(2,2-bispyrimidine) Adlayers on Au(111). *Phys. Chem. Chem. Phys*. **2018**, *20*, 15960-15969.
35. Di Santo, G.; Castellarin-Cudia, C.; Fanetti, M.; Taleatu, B.; Borghetti, P.; Sangaletti, L.; Floreano, L.; Magnano, E.; Bondino, F.; Goldoni, A. Conformational Adaptation and Electronic Structure of 2H-Tetraphenylporphyrin on Ag(111) during Fe Metalation. *J. Phys. Chem. C* **2011**, *115*, 4155-4162.

7.6 Appendix

Additional STM images of the close-packed, porous and windmill networks

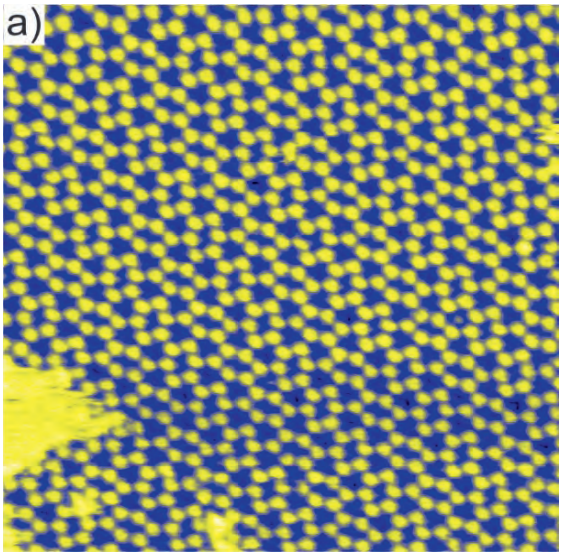

Figure A7.1. (a) STM image of the close-packed network after post-deposition annealing at 80°C (38 x 38 nm^2, U_{bias} = -1.6 V, I_{set} = 15 pA).

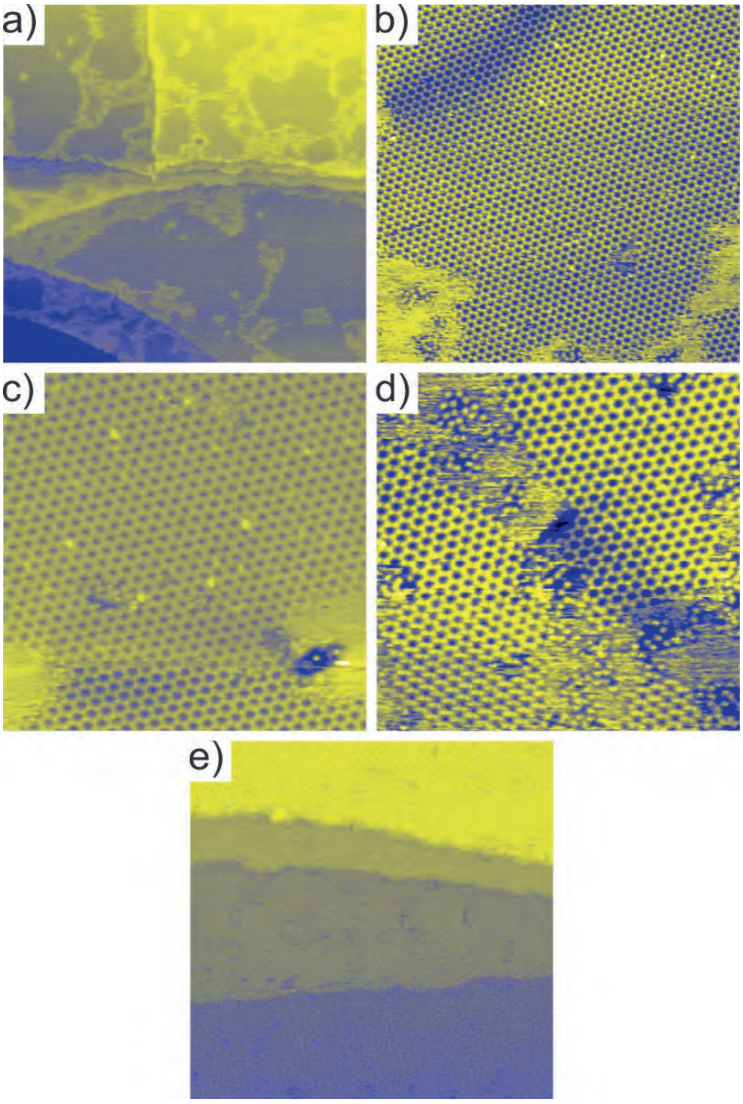

Figure A7.2. STM images of the self-assembly of molecule **1** on Cu(111) after annealing at different temperatures. The porous network was formed at 150°C as shown in (a) (200 x 200 nm^2, U_{bias} = -1.6 V, I_{set} = 20 pA) and (b) (80 x 80 nm^2, U_{bias} = -1.6 V, I_{set} = 25 pA). The structure of the porous network persisted after increasing the post-deposition annealing temperature to (c) 190°C (50 x 50 nm^2, U_{bias} = -1.6 V, I_{set} = 30 pA) and (d) 225°C (55 x 50 nm^2, U_{bias} = -1.6 V, I_{set} = 30 pA). (e) The structure of the porous network persisted even at a smaller coverage (0.42 ML) up to an annealing temperature of 245°C (100 x 100 nm^2, U_{bias} = -1.6 V, I_{set} = 20 pA).

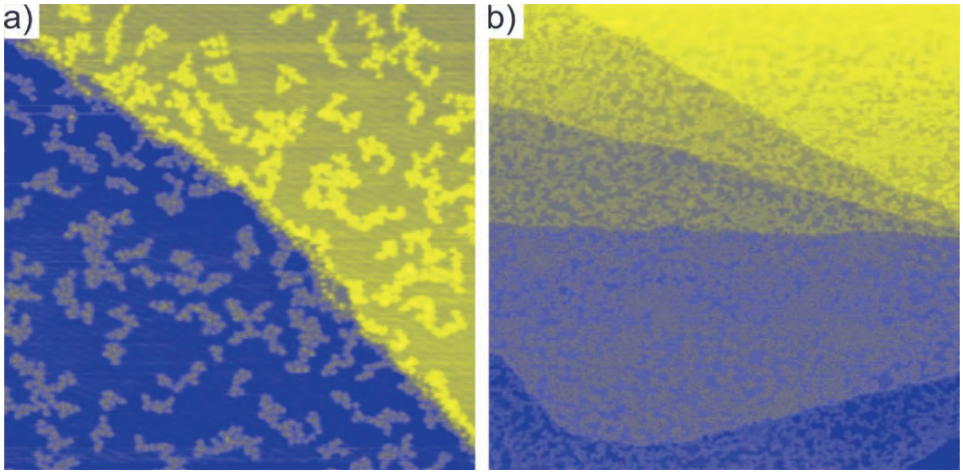

Figure A7.3. Thermal decomposition was observed in the range of 250 – 260°C: (a) 260°C (100 x 100 nm^2, U_{bias} = -1.6 V, I_{set} = 15 pA) and (b) 250°C (200 x 200 nm^2, U_{bias} = -1.6 V, I_{set} = 15 pA).

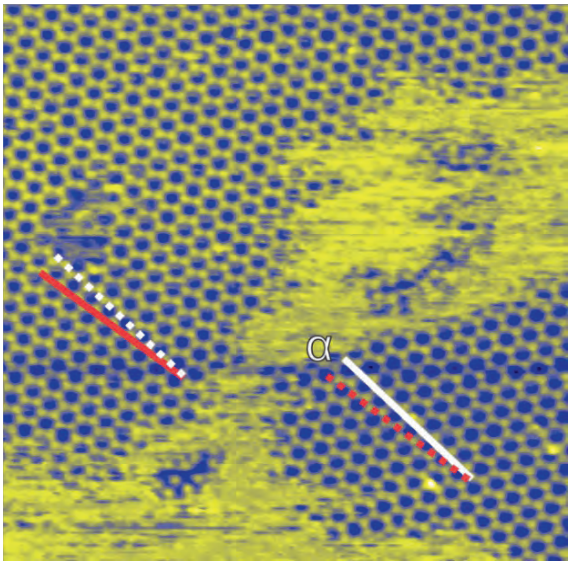

Figure A7.4. Overview STM image of the porous network (50 x 50 nm^2, U_{bias} = -1.6 V, I_{set} = 25 pA). The red and white solid lines highlight two rotationally equivalent domains, while the red and white dotted lines are added to show the rotational angle (α = 10°) between them.

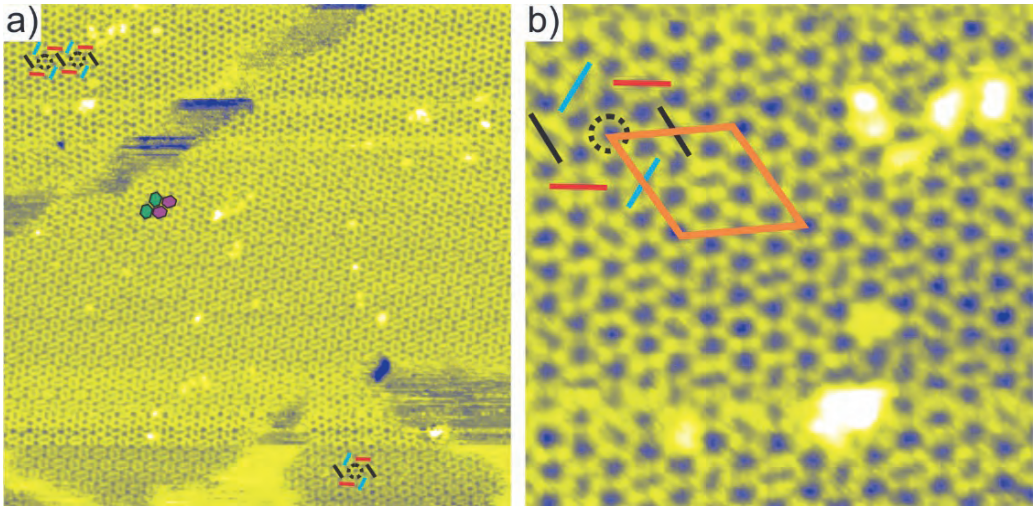

Figure A7.5. Self-assembly of molecule **1** on Cu(111) at RT. STM image of: (a) the close-packed network (highlighted by the green and purple hexagons) in coexistence with the windmill structure (120 x 120 nm^2, U_{bias} = -1.6 V, I_{set} = 20 pA) and (b) the windmill structure where the unit cell is shown in orange (30 x 30 nm^2, U_{bias} = -1.6 V, I_{set} = 20 pA). In (a) and (b) the black dotted circle highlights a pore that is bonded to six groups of the (six-membered) rings (highlighted by blue, red and black lines).

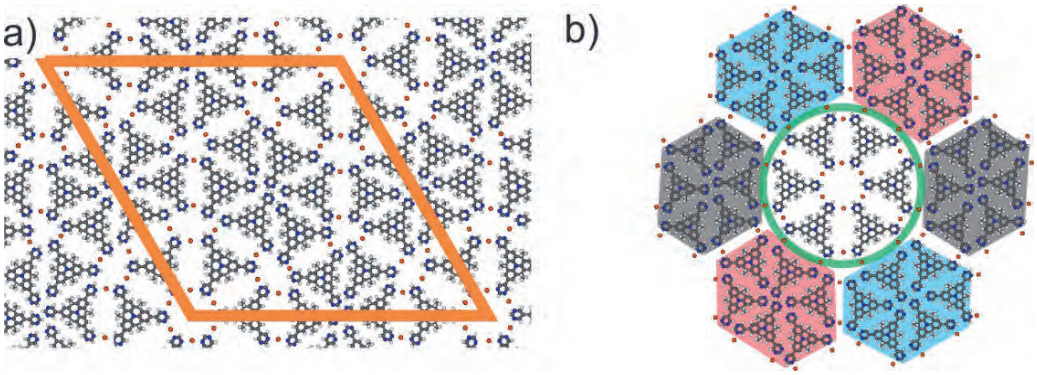

Figure A7.6. (a) Tentative structural model of the windmill structure stabilized by H-bonds and twofold Cu-coordination motifs. Copper, nitrogen, carbon and hydrogen atoms are shown in orange, blue, gray and white, respectively. The unit cell is shown in orange. (b) Structural model of a single windmill, where the green circle highlights the twofold Cu-coordination motifs between the central pore and six neighboring (six-membered) rings. The color-code of the hexagons under the (six-membered) rings resembles that of the one shown in Figure A7.5a and b. Windmill network: unit cell a = b = 7.5 ± 0.2 nm, internal angle = 60° ± 4°, with a Cu-N bond distance = 2.1 Å. The molecular and metal densities are 0.49 molecules per nm^2 and 0.74 Cu-atoms per nm^2, respectively. These values give a 1 : 1.5 molecule-to-metal ratio.

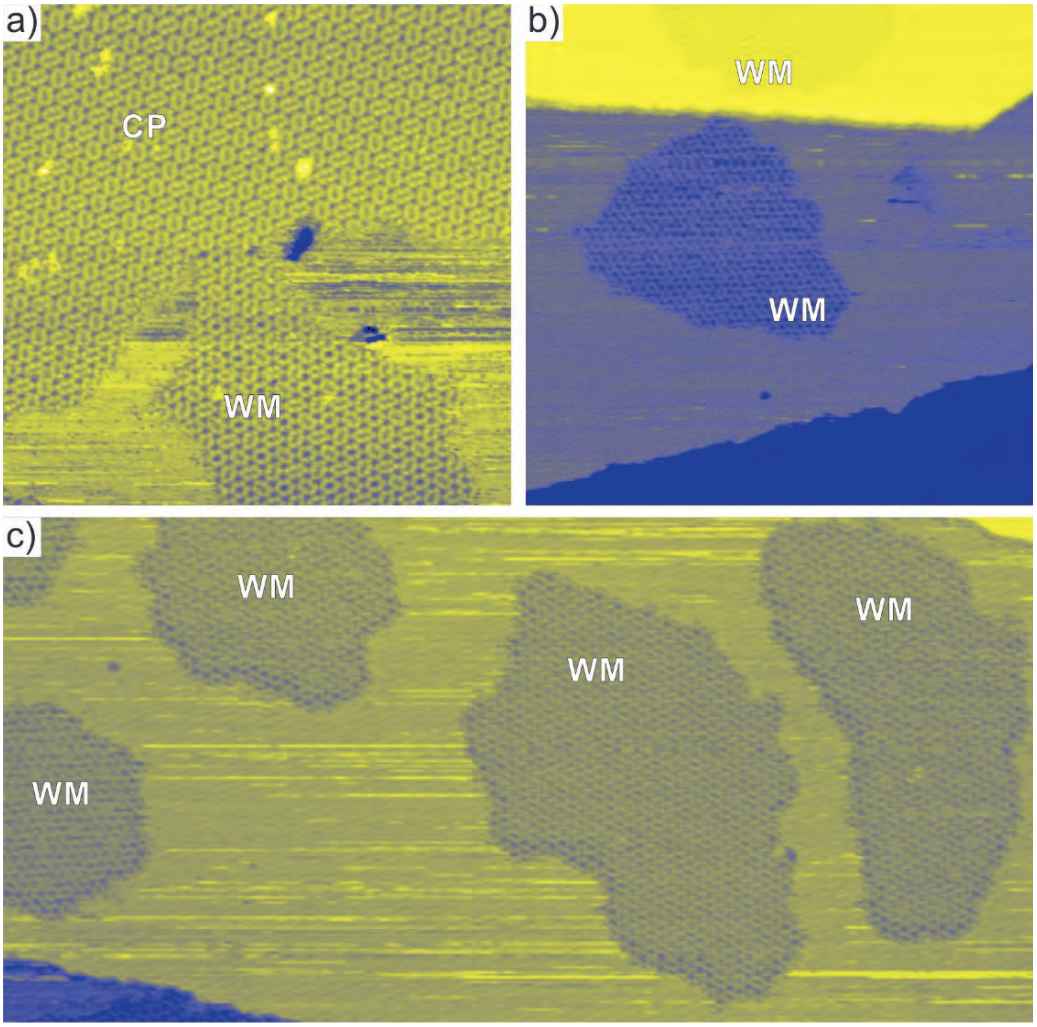

Figure A7.7. Self-assembly of molecule **1** on Cu(111) at RT. The windmill structure is observed in coexistence with the close-packed network in (a) (85 x 85 nm^2, U_{bias} = -1.6 V, I_{set} = 20 pA) and molecular islands of several windmill building blocks are observed in (b) (120 x 120 nm^2, U_{bias} = -1.6 V, I_{set} = 20 pA) and (c) (200 x 100 nm^2, U_{bias} = -1.6 V, I_{set} = 15 pA). In (a) – (c), the labels WM and CP highlight the molecular islands of the windmill and close-packed networks, respectively.

Table A7.1. FWHM (unit: eV) for the different N 1s chemical components in the purely organic phase (multilayer), close-packed and porous networks.

Network	N1		N2
	H-bonded	Cu-coordinated	
Organic phase (multilayer)	1.6	n/a	1.6
Close-packed	2.1	2.1	2.1
Porous	n/a	2.1	2.1

Peak area ratio for the different N 1s chemical components in each network.

Network	N1		N2
	H-bonded	Cu-coordinated	
Organic phase (multilayer)	5.7	n/a	1
Close-packed	3.9	1.9	1
Porous	n/a	5.8	1

Table A7.2. Peak area (arb. unit) for the different N 1s chemical components in the different networks.

Network	N1		N2
	H-bonded	Cu-coordinated	
Organic phase (multilayer)	5250.7	n/a	921.2
Close-packed	2841.9	1421	728.7
Porous	n/a	2162.3	372.5

8 Summary and Outlook

The self-assembly of organic molecules on surfaces is a promising route within the bottom-up approach for the fabrication of nanoscale structures which can find application in nanoscale devices. By being able to custom tailor organic molecules with functional endgroups that allow them to interact through non-covalent interactions on a surface, we can form well-ordered two-dimensional (2D) networks supported on (metallic) surfaces. Within the framework of this thesis, we fabricated and studied 2D nanoscale networks formed by the self-assembly of porphyrin and triarylamine derivatives on metallic surfaces. In order to properly characterize and study the self-assembly of these nanoscale systems, we made use of the surface sensitive techniques presented in Chapter 2. The structure of these 2D nanoscale networks was studied by means of scanning tunneling microscopy (STM) and low-energy electron diffraction (LEED), while the influence of the chemical environment on the electronic properties of these networks was studied by X-ray photoelectron spectroscopy (XPS). In Chapter 3 we provided an overview of the fundamental aspects involved in molecular self-assembly on surfaces. As it was presented in Chapters 4 through 7, the incorporation of metal-atoms into the 2D networks steered the formation of long-range ordered metal-organic coordination networks (MOCNs) by linking the organic building blocks with metal-atoms. A brief summary of the relevant aspects of the research presented in this thesis is provided in the following.

In Chapter 4, the influence of molecular coverage on the self-assembly of a tetracyanophenyl porphyrin bearing a Co-atom in its core (Co-TCNPP) was studied before and after the addition of Co-atoms on Au(111)

by means of STM and LEED. The formation of a close-packed network was evidenced by STM and its long-range order was corroborated by LEED. The close-packed network was stabilized by H-bonds formed between the neighboring Co-TCNPP molecules. The deposition of Co-atoms allowed the formation of a MOCN that showed to be coverage-dependent – that is – dependent on the amount of molecules adsorbed on the Au(111) surface. At submonolayer coverage, the coexistence of two structurally different MOCNs was observed under STM, i.e., a fourfold Co-coordinated MOCN and a second MOCN simultaneously stabilized by threefold Co-coordination motifs and H-bonds. However, when the molecular coverage was increased to a monolayer, only the fourfold MOCN was observed. Therefore, the formation of MOCNs stabilized by different in-plane coordination motifs can be steered by the molecular coverage on a surface when the interplay between the molecular building blocks and coordination chemistry of the metal-atoms allow it.

In Chapter 5, the influence of Fe-position on the self-assembly porphyrin-based MOCNs under UHV conditions was studied by means of STM. This study investigated the adsorption of a Co-substituted tetracyanophenyl (Co-TCNPP) and Zn-substituted tetrapyridyl (Zn-TPyP) porphyrin on Au(111). The deposition of Fe-atoms onto a submonolayer of either of the porphyrin derivatives allowed the formation of two structurally different Fe-coordinated MOCNs that were stabilized by three and fourfold in-plane coordination nodes, respectively. In addition, the rarely studied atom-exchange reaction in the porphyrin core was observed by STM. The atom-exchange reaction within the porphyrin core of Zn-TPyP was evidenced by the presence of a molecular species with an enhanced STM contrast compared with the appearance of bare Zn-TPyP, i.e., the brighter species was

attributed to Fe-TPyP. However, in the case of Co-TCNPP, the Fe-atom did not replace the Co-atom in the porphyrin core as evidenced by the off-centered brightness of it observed under STM, i.e., the Fe-atom bonded on top of the core. This study highlighted the relevance of the imaging capabilities of the STM in studying the atom exchange reactions within porphyrin-based MOCNs under UHV conditions and provided insight of the interaction between the central metal atom and the porphyrin core, e.g., the Zn-atoms were less bound to the core compared to the Fe-atoms.

In Chapter 6, a complementary study on the self-assembly process of a nickel porphyrin (Ni-DPPyP) before and after the deposition of Co-atoms under UHV conditions on Au(111) was presented by means of STM, XPS and LEED. The deposition of Ni-DPPyP on Au(111) gave rise to a close-packed network as revealed by STM and LEED. The addition of Co-atoms onto the close-packed network led to a structural transformation, i.e., the formation of a hexagonal porous network was observed with STM. Furthermore, the electronic structure of the networks was studied by XPS. The XPS measurements confirmed – along with the assumptions proposed from the STM measurements – that the close-packed network was stabilized by H-bonding, while the hexagonal porous network was a MOCN stabilized by threefold Co-coordination motifs formed between one Co-atom and three pyridyl endgroups from three different Ni-DPPyP molecules. In this chapter, XPS was used to unveil the electronic changes of the molecules upon a structural transformation of 2D self-assembled networks on metallic surfaces when they transform from their organic phase into a MOCN.

In Chapter 7, the influence of post-deposition annealing on the self-assembly process of a pyrimidinyl-functionalized triarylamine under UHV conditions on Cu(111) was shown by means of STM and XPS. The deposition

of the triarylamine molecule on Cu(111) at room-temperature resulted in the formation of a close-packed 2D network as shown by STM. The XPS measurements showed that the close-packed network was stabilized by H-bonding and twofold Cu-coordination motifs. By applying a post-deposition annealing step of 150°C, the close-packed network rearranged into a hexagonal porous 2D network, which suggested a modification in the chemical environment of the triarylamine molecules. The STM and XPS measurements revealed that the porous network was a MOCN exclusively stabilized by twofold Cu-coordination motifs. This structural rearrangement was attributed to the annealing step (at 150°C), which led to a higher concentration of Cu-atoms on the Cu(111) surface. Furthermore, the structural properties of MOCNs, i.e., large surface area and high porosity, confers them with promising applications in organic electronics, catalysis and spintronics.

This thesis offered an overview of different parameters involved in the fabrication of MOCNs. For instance, the influence of the molecular coverage or functional endgroups in the structure of the self-assembled MOCNs was provided. Additionally, the usage of the underlying substrate as a reservoir for metal-atoms used in the fabrication of MOCNs was studied as well as the usage of XPS data to corroborate the chemical environment of the 2D networks was presented. Furthermore, it was possible to study an atom-exchange reaction within the porphyrin core under UHV due to the outstanding imaging capabilities of the STM.

MOCNs can also be used for the functionalization of surfaces to tune their electronic properties, e.g., templates such as graphene or transition metal dichalcogenides (TMDs) like molybdenum disulfide (MoS_2) are promising candidates to be studied with an adsorbed MOCN. However, there are limited

studies that focus on the influence of MOCNs on the electronic properties of these templates, i.e., graphene or MoS_2. In addition, a proper understanding of the underlying mechanisms that allow the growth of these nanomaterials on decoupling layers such as graphene is required. Furthermore, the 2D porous structure of some MOCNs is of relevance for the fabrication of host-guest systems on various surfaces and may even allow the inclusion of metal centers – as in the case of porphyrin-based MOCNs – that can possess intriguing magnetic properties. The relevance of supramolecular chemistry has translated to studies on surfaces, and it will not only serve as a method to study molecular self-assembly at a fundamental level, but it will also allow the fabrication of surfaces with a desired application.

8.1 Resumen (*Summary in Spanish*)

El autoensamblaje de moléculas orgánicas empleando el método de fabricación *bottom-up*, permite el desarrollo de superficies funcionalizadas con potenciales aplicaciones. Las moléculas orgánicas ofrecen la ventaja de poder ser sintetizadas con una gran variedad de grupos funcionales. Las interacciones presentes en la interfaz pueden modularse a través del empleo de sustituyentes de distinta naturaleza química. En particular, las interacciones moleculares no-covalentes sobre una superficie, permiten la fabricación nanoestructuras bidimensionales (2D) con excelente grado de cristalinidad.

Dentro del marco experimental de esta tesis, hemos fabricado y estudiado nanoestructuras 2D formadas por autoensamblaje molecular de derivados de porfirinas y triarilaminas sobre superficies metálicas. Con el fin de caracterizar y estudiar estas nanoestructuras, hicimos uso de distintas técnicas de caracterización superficial, las cuales fueron descritas en el Capítulo 2 (*Chapter 2*) de la presente tesis. La estructura 2D de los arreglos moleculares formados fue estudiada por medio de la microscopía por efecto túnel y por la difracción de electrones de baja energía, técnicas conocidas como *STM* y *LEED* por sus siglas en inglés, respectivamente. La influencia del entorno químico en las propiedades electrónicas de las nanoestructuras fue analizada mediante la espectroscopía fotoelectrónica de rayos X o *XPS* por sus siglas en inglés. En el Capítulo 3 (*Chapter 3*) damos información general sobre los aspectos fundamentales que influyen en el autoensamblaje molecular en superficies. Finalmente, en los Capítulos 4 al 7 (*Chapter* 4–7) cubrimos el tema de incorporación de átomos metálicos en las nanoestructuras 2D para la fabricación de redes metal-orgánicas o *MOCNs*

por sus siglas en inglés. A continuación, presentamos un breve resumen sobre los aspectos más relevantes de los resultados experimentales obtenidos en esta tesis doctoral.

En el Capítulo 4 (*Chapter 4*) se describe la adsorción de la molécula tetracianofenil-porfirina sobre la superficie Au(111). La influencia de la cantidad de moléculas (densidad molecular) en el autoensamblaje de una tetracianofenil-porfirina (Co-TCNPP) fue estudiado antes y después de la adición de átomos de cobalto sobre una superficie de Au(111) por medio *STM* y *LEED*. Las micrografías de baja y alta resolución de la interfaz Co-TCNPP sobre Au(111) mostraron la formación de una nanoestructura 2D de alta densidad cuya cristalinidad fue corroborada por *LEED*. Se determinó que esta nanoestructura estaba estabilizada por enlaces por puentes de hidrógeno formados entre las moléculas Co-TCNPP. El depósito de moléculas y átomos de cobalto en conjunto a nivel submonocapa permitió la formación de dos nanoestructuras *MOCN*. La primera estructura observada estaba estabilizada por enlaces metal-orgánicos formados por cuatro moléculas Co-TCNPP con un átomo de cobalto central, mientras que la segunda estaba simultáneamente estabilizada por enlaces de hidrógeno y enlaces metal-orgánicos formados entre tres moléculas Co-TCNPP y un átomo de cobalto. Sin embargo, al aumentar la densidad molecular a una monocapa sólo se detectó la formación de la primera estructura. Por lo tanto, la formación de nanoestructuras *MOCN* estabilizadas por diferentes enlaces químicos puede ser controlada por la densidad molecular en una superficie, siempre y cuando lo permitan la interacción entre los constituyentes moleculares y la química de coordinación de la porción metálica.

En el Capítulo 5 (*Chapter 5*), presentamos un estudio de *STM* sobre la influencia del depósito de átomos de hierro en el autoensamblaje de

nanoestructuras *MOCN* formadas por diferentes porfirinas bajo condiciones de ultra alto vacío (*UHV* por sus siglas en inglés). Este estudio presentó la adsorción de dos porfirinas sobre una superficie de Au(111): tetracianofenil-porfirina con un átomo de cobalto en su centro (Co-TCNPP) y tetrapiridil-porfirina con un átomo de zinc en su centro (Zn-TPyP). El depósito de átomos de hierro generó la formación de nanoestructuras tipo *MOCN* en ambos familias de porfirinas adoptando configuraciones estabilizadas por enlaces metal-orgánicos presentando una simetría triple y cuádruple en el mismo plano de adsorción, es decir, el plano paralelo a la superficie de Au(111). Además, se evidenció una reacción de substitución del átomo metálico en el centro de la porfirina Zn-TPyP, ya que al depositar átomos de hierro en las micrografías se observaron moléculas con un contraste mayor en comparación al observado en las moléculas que sólo contienen un átomo de zinc en su centro, es decir, las moléculas más brillantes se atribuyeron a la formación de una nueva porfirina substituida por átomos de hierro (Fe-TPyP). Sin embargo, en el caso de las moléculas Co-TCNPP, el átomo de hierro no reemplazó el átomo de cobalto ya que con el *STM* se observó un contraste descentrado en la cavidad central de la porfirina, es decir, el átomo de hierro se enlazó encima de la porfirina sin substituir al átomo de cobalto. Este trabajo destacó la relevancia de las imágenes del *STM* en el estudio de reacciones de substitución de átomos metálicos contenidos en el centro de porfirinas bajo condiciones de ultra alto vacío.

En el Capítulo 6 (*Chapter 6*), se analizó el proceso de autoensamblaje de una porfirina con un átomo de níquel en su centro (Ni-DPPyP) antes y después del depósito de átomos de cobalto bajo condiciones de ultra alto vacío, utilizando la superficie Au(111) como substrato. El estudio se llevó a cabo por medio de *STM*, *XPS* y *LEED*. El depósito de Ni-DPPyP sobre

Au(111) dio lugar a una nanoestructura densa caracterizada a través de *STM* y *LEED*. La adición de átomos de cobalto a la nanoestructura densa causó una transformación estructural, es decir, la formación de una nanoestructura porosa hexagonal. Además, la estructura electrónica de ambas nanoestructuras fue estudiada por *XPS*. Las mediciones de *XPS* confirmaron los resultados deducidos por *STM*, que la nanoestructura densa estaba estabilizada por enlaces de hidrógeno y la nanoestructura porosa hexagonal estaba estabilizada por enlaces metal-orgánicos formados por tres moléculas Ni-DPPyP y un átomo de cobalto. En este capítulo se demostró la capacidad de la técnica de *XPS* para estudiar los cambios en la estructura electrónica de moléculas al ser sometidas a una transformación estructural dentro de nanoestructuras 2D adsorbidas en superficies metálicas.

En el Capítulo 7 (*Chapter 7*), la influencia de la temperatura en el proceso de autoensamblaje de una triarilamina substituida por grupos pirimidinílicos fue estudiado bajo condiciones de ultra alto vacío. El estudio se llevó a cabo en un substrato de Cu(111) y fue caracterizado por medio de *STM* y *XPS*. El depósito de la triarilamina sobre Cu(111) a temperatura ambiente resultó en la formación de una nanoestructura que fue estudiada por medio de *STM*. Las mediciones de *XPS* demostraron que la nanoestructura estaba estabilizada por enlaces de hidrógeno y enlaces metal-orgánicos formados entre las moléculas y átomos de cobre que fueron suministrados por el substrato de Cu(111). Al aplicar un proceso de recocido a 150°C, la nanoestructura densa sufrió un reordenamiento hasta adoptar un patrón poroso hexagonal y, en consecuencia, el entorno químico de las moléculas fue modificado. Las mediciones de *STM* y *XPS* revelaron que la nanoestructura porosa era un *MOCN* que estaba estabilizado exclusivamente por enlaces metal-orgánicos entre moléculas y átomos de cobre

subministrados por el substrato de Cu(111). Este reordenamiento estructural en 2D fue atribuido al proceso de recocido (a 150°C), que causó una mayor concentración de átomos de cobre provenientes de la superficie de cobre. Además, las propiedades estructurales de nanoestructuras *MOCN* con gran área superficial y alta porosidad les confieren aplicaciones prometedoras en dispositivos organo-electrónicos y con uso catalítico y de espintrónica.

Esta tesis ofreció un panorama de los diferentes parámetros involucrados en la fabricación de nanoestructuras *MOCN*. De primera instancia, fue presentada la influencia de densidad molecular o de grupos funcionales en la estructura de los *MOCN* autoensamblados. Además, se presentó un estudio sobre el uso del substrato metálico para la producción de átomos metálicos que permiten la formación de nanoestructuras *MOCN* y, así mismo, se presentó el uso de *XPS* para corroborar el entorno químico de las nanoestructuras estudiadas. Finalmente, fue posible estudiar las reacciones de substitución de átomos metálicos en el centro de las porfirinas por medio de *STM* bajo condiciones de ultra alto vacío.

Las nanoestructuras *MOCN* también pueden ser utilizadas para la funcionalización de superficies y así sintonizar sus propiedades electrónicas, por ejemplo, el caso de grafeno o MoS_2. Además, estudios comprensivos de los mecanismos que permiten la nucleación de moléculas para formar estos nanomateriales sobre superficies de desacoplamiento como grafeno es requerido. Otra aplicación es el uso de nanoestructuras porosas 2D para la fabricación de sistemas *host-guest* sobre varias superficies y que la misma vez podrían permitir la inclusión de centros metálicos, como es el caso de nanoestructuras *MOCN* formadas por porfirinas que puede poseer propiedades magnéticas. La gran importancia de la química supramolecular se ha trasladado a estudios en superficies, y no sólo servirá como un método

para estudiar autoensamblaje molecular a un nivel fundamental, pero también permitirá la fabricación de superficies con una aplicación deseada. Este resumen en español fue escrito para que toda persona hispanohablante que lo lea pueda sentirse un poco más cercano de casa si se encuentran lejos de ella.

9 Samenvatting

Zelfassemblage van organische moleculen op oppervlaktes is een veelbelovende ‘bottum-up’ benadering om nanostructuren te bouwen die geschikt zijn voor toekomstige elektronische apparaten. Door organische moleculen met functionele eindgroepen op maat te maken, waardoor ze kunnen interageren via niet-covalente interacties op een oppervlak, kunnen we goed geordende tweedimensionale (2D) netwerken vormen op oppervlakken. In dit proefschrift bestudeerden we 2D-netwerken op nanoschaal die worden gevormd door de zelfassemblage van porfyrine en triarylaminederivaten op metalen oppervlakken. Om de zelfassemblage van deze nanoschaalsystemen goed te karakteriseren en te bestuderen, hebben we gebruik gemaakt van de oppervlaktegevoelige technieken die in hoofdstuk 2 worden gepresenteerd. De structuur van deze 2D-netwerken op nanoschaal werd bestudeerd met behulp van scanning tunneling microscopie (STM) en lage-energie elektronendiffractie (LEED). De invloed van de chemische omgeving op de elektronische eigenschappen van deze netwerken werd bestudeerd door middel van röntgenfoto-elektronspectroscopie (XPS). In hoofdstuk 3 beschrijven wij de fundamentele aspecten van moleculaire zelfassemblage op oppervlakken.Hoofdstukken 4 tot en met 7 presenteren wij hoe de metaalatomen in de 2D-netwerken de vorming van geordende metaal-organische coördinatienetwerken (of *metal-organic coordination networks*, MOCN's) op lange afstand mogelijk maken. Hieronder volgt een korte samenvatting van deze hoofdstukken.

In hoofdstuk 4 werd de invloed van moleculaire dekking op de zelfassemblage van een tetracyanofenylporfyrine met een Co-atoom in de kern (Co-TCNPP) bestudeerd voor en na de toevoeging van Co-atomen op

Au(111) door middel van STM en LEED. De vorming van een dicht opeengepakt netwerk werd bewezen door STM en de volgorde ervan werd bevestigd door LEED. Het dicht opeengepakte netwerk werd gestabiliseerd door H-bindingen die werden gevormd tussen de naburige Co-TCNPP-moleculen. De afzetting van Co-atomen maakte de vorming van een MOCN mogelijk die afhankelijk van de dekking bleek te zijn, dat wil zeggen, afhankelijk van de hoeveelheid moleculen die op het Au(111) oppervlak geadsorbeerd werden. Bij submonolaag-dekking werd het naast elkaar bestaan van twee structureel verschillende MOCN's waargenomen onder STM oftewel een viervoudige Co-gecoördineerde MOCN en een tweede MOCN die gelijktijdig werden gestabiliseerd door drievoudige Co-coördinatiemotieven en H-bindingen. Toen de moleculaire dekking echter werd verhoogd tot een monolaag, werd alleen de viervoudige MOCN waargenomen. De vorming van MOCNs die gestabiliseerd worden door verschillende coördinatiemotieven in het vlak, kan dus worden aangepast door de moleculaire dekking op een oppervlak. Mits het samenspel tussen de moleculaire bouwstenen en de coördinatiechemie van de metaalatomen dit toestaan.

In hoofdstuk 5 werd de invloed van de ijzer (Fe) atoom positie op de zelfassemblage op porfyrine gebaseerde MOCNs onder UHV-condities bestudeerd door middel van STM. Deze studie onderzocht de adsorptie van een Co-gesubstitueerde tetracyanofenyl (Co-TCNPP) en Zn-gesubstitueerde tetrapyridyl (Zn-TPyP) porfyrine op een Au(111) oppervlak. De afzetting van Fe-atomen op een submonolaag van een van de porfyrinederivaten maakte de vorming mogelijk van twee structureel verschillende Fe-gecoördineerde MOCN's. Deze werden gestabiliseerd door respectievelijk drie en viervoudige coördinatieknooppunten op het oppervlak. Bovendien werd de

zelden bestudeerde atoomuitwisselingsreactie in de porfyrinekern waargenomen door STM. De atoomuitwisselingsreactie in de porfyrinekern van Zn-TPyP werd bewezen door de aanwezigheid van een moleculaire soort met een hoger STM-contrast in vergelijking met het verschijnen van Zn-TPyP, oftewel de helderdere soort werd toegeschreven aan Fe-TPyP. In het geval van Co-TCNPP heeft het Fe-atoom het Co-atoom in de porfyrinekern echter niet vervangen, zoals blijkt uit de niet gecentreerde helderheid die werd waargenomen onder STM, oftewel het Fe-atoom dat bovenop de porfyrinekern was gebonden. Dit hoofdstuk benadrukte de relevantie van de beeldvormingsmogelijkheden van de STM bij het bestuderen van de atoomuitwisselingsreacties op porfyrine gebaseerde MOCN's onder UHV-omstandigheden en gaf inzicht in de interactie tussen het centrale metaalatoom en de porfyrinekern, zo waren bijvoorbeeld de Zn-atomen minder gebonden aan de kern in vergelijking met de Fe-atomen.

In hoofdstuk 6 werd een complementaire studie over het zelfassemblageproces van een nikkel-porfyrine (Ni-DPPyP) voor en na de afzetting van Co-atomen onder UHV-omstandigheden op Au(111) gepresenteerd door middel van STM, XPS en LEED. De afzetting van Ni-DPPyP op Au(111) gaf aanleiding tot een dicht opeengepakt netwerk, zoals onthuld door STM en LEED. De toevoeging van Co-atomen aan het dicht opeengepakte netwerk leidde tot een structurele transformatie, oftewel de vorming van een hexagonaal poreus netwerk kon worden waargenomen met STM. Verder werd de elektronische structuur van de netwerken bestudeerd door XPS. De XPS-metingen bevestigden - samen met de veronderstellingen die werden voorgesteld uit de STM-metingen - dat het dicht opeengepakte netwerk werd gestabiliseerd door H-binding, terwijl het hexagonale poreuze netwerk een MOCN was die werd gestabiliseerd door drievoudige Co-

coördinatie-motieven gevormd tussen één Co-atoom en drie pyridyl-eindgroepen van drie verschillende Ni-DPPyP-moleculen. In dit hoofdstuk werd XPS gebruikt om de elektronische veranderingen van de moleculen te onthullen na een structurele transformatie van 2D zelf-geassembleerde netwerken op metalen oppervlakken wanneer ze transformeren van hun organische fase naar een MOCN.

In hoofdstuk 7 werd de invloed van verhitten van het materiaal na het zelfassemblageproces van een pyrimidinyl-gefunctionaliseerd triarylamine onder UHV-omstandigheden op Cu(111) bestudeerd door middel van STM en XPS. De afzetting van het triarylaminemolecuul op Cu(111) bij kamertemperatuur resulteerde in de vorming van een dicht opeengepakt 2D-netwerk, zoals aangetoond door STM. De XPS-metingen toonden aan dat het dicht opeengepakte netwerk werd gestabiliseerd door H-binding en tweevoudige Cu-coördinatiemotieven. Door een verhitting van 150°C (na afzetting), herschikte het dicht opeengepakte netwerk zich tot een hexagonaal poreus 2D-netwerk, wat een wijziging in de chemische omgeving van de triarylaminemoleculen suggereerde. De STM- en XPS-metingen lieten zien dat het poreuze netwerk een MOCN was die uitsluitend werd gestabiliseerd door tweevoudige Cu-coördinatiemotieven. Deze structurele herschikking werd toegeschreven aan de verhitting (bij 150°C) die leidde tot een hogere concentratie Cu-atomen op het Cu(111)-oppervlak. Bovendien verlenen de structurele eigenschappen van MOCNs, groot oppervlak en hoge porositeit, veelbelovende toepassingen in organische elektronica, katalyse en spintronica.

Dit proefschrift bood een overzicht van verschillende parameters die betrokken zijn bij de productie van MOCN's. De invloed van onder andere de moleculaire dekkingsgraad of functionele eindgroepen in de structuur van de

zelf samengestelde MOCNs werden bepaald. Daarnaast werd de rolvan het onderliggende substraat als een reservoir voor metaalatomen die worden gebruikt bij de fabricage van MOCNs bestudeerd, evenals het gebruik van XPS-gegevens om de chemische omgeving van de 2D-netwerken te bevestigen. Bovendien was het mogelijk om een atoomuitwisselingsreactie in de porfyrinekern onder UHV te bestuderen vanwege de uitstekende beeldvormingsmogelijkheden van de STM.

MOCNs kunnen worden gebruikt om de elektronische oppervlakte-eigenschappen van materialen te veranderen. Dit is een veelbelovende toepassing op materialen zoals grafeen of overgangsmetaaldichalcogeniden (TMD's) zoals molybdeendisulfide (MoS_2). Het onderzoek naar de invloed van MOCNs op deze materialen is echter nog beperkt en er is een goed begrip van de vormings-mechanismen van MOCNs op deze materialen voor nodig. Verder is de 2D-poriën structuur van zommige MOCNs ook relevant in de fabricatie van zo genoemde "*host-guest*" systemen op verschillende oppervlakten en kunnen zij het toevoegen van metaal-elementen mogenlijk maken (zoals in het geval van de Porphyrin-MOCNs hierboven), met mogenlijk interessante magnetische eigenschappen als gevolg. Het belang van supramoleculaire chemie is zichtbaar geworden door onderzoek naar oppervlakken. Het dient niet alleen als een methode om moleculaire zelfassemblage op een fundamenteel niveau te bestuderen, maar het zal ook de productie van oppervlakken met een gewenste toepassing mogelijk maken.

10 Acknowledgements

The making of this thesis would not have been possible without the valuable support from various individuals inside and outside my research group. I would like to express my gratitude to:

Prof. Meike Stöhr for accepting me in her research group and guiding me through the course of my PhD trajectory. You always offered me help under different circumstances and granted me the opportunity to professionally develop myself within and outside the scientific world. You were very supportive in allowing me to attend relevant courses and always provided me with fruitful feedback on how to become a better version of myself. Thank you for this opportunity.

Prof. Petra Rudolf for co-supervising me. Your advice was always welcomed and had a positive impact in the elaboration of this thesis. Thank you for sharing interesting stories with the group during my stay and for offering useful advice to me.

Prof. Sabine Maier, Prof. Harold Zandvliet and Prof. George Palasantzas for being part of my assessment committee and for taking some of your time for reading my thesis.

Mihaela Enache for showing commitment to our research group and for always being deeply involved in the progress of our experiments. Thank you for offering me guidance through these years. Your scientific experience was a key player during my PhD journey, you always found time for me in your busy agenda and helped me accomplish my research goals. Thank you for your rounds of feedback, they surely pushed me forward!

Nico Schmidt for sharing your knowledge of the field and for instructing me in the beginning of my PhD. I am thankful for the work that

we put together, sometimes it felt like never-ending, but you managed to bring out a joke or two which made the ride more pleasant. I really appreciate our conversations, whether they are research or life related. Thank you for all the wise words and motivating me during this time amigo!

Leonid Solianyk for sharing your friendship and words of inspiration. I also appreciate the feedback and suggestions that you offered throughout these years. Thank you for always being up for a nice dinner and talk, it made this journey a lot nicer man!

Jun Li for teaching and instructing me in the lab during the very beginning of my PhD, your kindness was always appreciated. The beamtime at Elettra was a very pleasant experience to share with you – we both like to eat. Thank you for your patience!

Van Bay Tran for being a nice office mate and inviting me to play fun football matches during lunch time. Thank you for sharing valuable scientific knowledge with me as well!

Dario Giannotti for being my second nice office mate. I enjoyed your short visit to our research group. Thank you for your friendliness!

Wenbo Lu for being my paranymph and a very friendly and open office mate. I really enjoyed the conversations that we have had so far. Thank you for your friendship. Your personality is certainly valued amongst the group, you have brought good memories and laughter during the coffee breaks. I am still looking forward to that trip to China! You will be the oldest PhD of the group after reading this.

Joris de la Rie, Koen Houtsma, Ida Delac Marion, Qiankun Wang, Baoxin Jia, Adam Watson and Gema Navarro for sharing nice moments with me and always being attentive to provide me with valuable feedback for my manuscripts. Thank you for the interesting conversations that we established

in the office and during coffee breaks! Gema muchas gracias por haber tomado el tiempo para revisar mi resumen en español y corregirlo.

Rendong Hu for your patience and being receptive to my supervision even during the not so stable corona measures!

Hilda Riemens for being our secretary and always providing me with help when it was required. I would like to also thank our former secretary Yvonne Nagelhout.

Sumit Kumar for being an enjoyable group member and very good friend. Thank you for always being supportive and showing me some words of wisdom. You are a very friendly and caring. I also appreciate the valuable scientific knowledge that we were able to learn from each other. Thank you for the nice memories and good dinners inside and outside of work man!

Van Lam Do for being a very nice friend, you always carried along happy moments and interesting stories. Thank you for the nice conversations that we had and for your friendly company. It would have been nice to have kept you longer in the group. I am glad that we have been able to stay in touch!

Oreste De Luca for being my paranymph and a lively and energetic office mate. I enjoyed the nice conversations that we had, talking about traveling, food and sports was a pleasant activity to take our minds off from work for a while. Thank you for the nice company inside and outside the office amico! I also thank you for all the relevant scientific discussions that we had in the office. Grazie di tutti!

Yan Feng for the nice conversations and dinners that took place in the last years. Your friendliness and openness are well cherished man. I wish you the best with the final steps of your PhD!

Ali Syari'ati for your positiveness and kindness. I enjoyed our talks about future career plans and so on. I am glad that you got hold of that job!

Pascal Freyer for the talks about life and career planning. Thank you for always being open to have a chat and for reviewing my *Samenvatting*, that was very nice from your side!

Jos Noteboom for the nice lunch chats and coffee that you provided us. I am also gratefully thankful for your help at our LT lab whenever it was required, dankjewel Jos!

The current and former group members of the Surfaces and Thin Films research group: Florian Studener, Tashfeen Zehra, Wu Jiquan, Wang Zi, Giovanna Feraco, Nicola Melfi, Estela Moretón Alfonsín, Theodosis Giousis, Yiannis Georgantas, Eleni Thomou, Floris van Nyendaal, Dominic Gerlach, Hamoon Hemmatpour and Charmaine Sibanda for sharing memorable moments during lunch time and outside of work. This melting pot of diverse cultural backgrounds taught me a valuable lesson of cultural awareness – a topic that I find very interesting and extremely relevant for succeeding in an international environment. Thank you for the interesting long conversations and chats that we had along the hallway or during a coffee break.

The beamline scientists from two different synchrotrons. At Elettra synchrotron in Italy, a special thank you to Vitaliy Feyer, Giovanni Zamborlini, and Matteo Jugovac for sharing your support and knowledge during our experiments. At ESRF synchrotron in France, I thank David Betto for helping us perform our XMCD measurements.

My bachelor thesis supervisor Dr. Miguel Méndez. Muchas gracias por motivarme e inculcarme las bases de la ciencia durante mis estudios de

licenciatura en México. ¡Espero que sus planes personales y científicos vayan muy bien!

My good French friend Guillaume. Thank you for your friendship and company man! I really enjoy our dinners and talks.

My friends that are scattered all over the place. Whether it is in nearby or far away, thank you for being there.

My uncle Yuri for introducing me to the concept of nanotechnology. Muchas gracias por los buenos consejos y deseos. ¡Te recordamos con mucho cariño tío!

My niece Marina. Gracias por la bonita y divertida compañía, nos la hemos pasado muy bien contigo. Estamos felices de que podremos pasar tu cumple contigo este año. Gracias a Yara por los buenos consejos a lo largo de los años.

Mi abue Celia y tía Gaby. Muchísimas gracias por siempre estar al pendiente de mí y de la familia. Gracias por todos los buenos recuerdos que tengo de mi niñez en Pluma y sus alrededores. La buena comida, los panes tan ricos de la zona y ese café de altura.

My uncle Gary and aunt Cindy. Thank you for all the nice memories and moments that we have spent together over the years. I always enjoy going back to the peninsula to have nice summer there. Looking forward to our long stay this year!

My in-laws and Frisian family, Klaas and Jet. Thank you for your support and for always being very welcoming. I have had a very enjoyable time in Oudehaske. Thank you for sharing you culture with me as well. I also want to thank my brother in-law Arjen for his friendliness and the pleasant time that we have spent together. Tige tank foar de ynteressante gesprekken en smûke itentsjes, wêrby de taalbarrière sa no en dan gjin rol mear spiele.

My brother Jordan and my sister in-law Xochitl, thank you for your support and the nice memories that we have built together. I remember when we were kids, and I would teach you math when you were still a little kid. Thanks for the cool time in all the different places that we lived during our childhood. ¡Gracias por todo Xoch y por tu amistad!

My wife Susanna. Thank you for how you are and all the good memories that we have built together. You have shown a lot of love and support through these years. The PhD only becomes more interesting when it transcends from science to your personal life. I am more than thankful to have started this journey here. Thank you for being so helpful. I am looking forward to the plans that we have in mind!

My parents, Brian and Isabel. This thesis would not have been possible without you dad. You have always encouraged me to go further and to achieve goals in life even if they set us distant from each other. I admire the strength that you have shown through the years and the wisdom that you have taught me. Thank you for everything, the love and the good moments that we have spent together. Muchas gracias por todo el apoyo, los buenos consejos y la buena educación que me has inculcado mom. El amor, humildad y respeto que son característicos de ti. Agradezco las oraciones, cariño y buenos momentos que hemos compartido juntos. ¡Gracias por siempre motivarme a estudiar y terminar lo que emprendo!

My God, I cannot deny my faith in you. Thank you for the strength and guidance. Thank you for placing me in different places and for providing me with the right mindset to accomplish my goals. Thanks for all the blessings and opportunities. ¡Gracias Señor Jesús!

11 List of Publications

Baker Cortés, B. D.; Enache, M.; Küster, K.; Studener, F.; Lee, T.-L.; Marets, N.; Bulach, V.; Hosseini, M. W.; Stöhr, M (2021). Structural Transformation of Surface-Confined Porphyrin Networks via Addition of Co-atoms**.** *Submitted*

Baker Cortés, B. D.; Schmidt, N.; Enache, M.; Stöhr, M (2021). Comparing Cyanophenyl and Pyridyl Ligands in the Formation of Porphyrin-Based Metal-Organic Coordination Networks. *To be submitted*

Baker Cortés, B. D.; Tran, B. V.; Pham, T. A.; Mekelburg, T.; Kivala, M.; Stöhr, M (2021). Pyrimidinyl-Functionalized Triarylamines on Cu(111): Temperature-Assisted Formation of a Porous Metal-Organic Coordination Network. *To be submitted*

Wang, Q.; de la Rie, J.; Baker Cortés, B. D.; Enache, M.; Stöhr, M (2021). Graphene as an Effective Template for Tuning the Structural and Electronic Properties of Organic-Inorganic Interfaces. *To be submitted*

Baker Cortés, B. D.; Schmidt, N.; Enache, M.; Stöhr, M (2020, November). Coverage-Dependent Metal-Organic Coordination Networks on Au(111). N*evac Blad*: *Nederlandse Vacuümvereniging.* 58 (3), p. 8–13. Retrieved from https://nevac.nl/NEVAC_Blad/Archief.php

Baker Cortés, B. D.; Schmidt, N.; Enache, M.; Stöhr, M. Coverage-Dependent Structural Transformation of Cyano- Functionalized Porphyrin Networks on Au(111) via Addition of Cobalt Atoms. *J. Phys. Chem. C* **2019**, *123*, 19681–19687.

Li, J.; Solianyk, L.; Schmidt, N.; Baker, B.; Gottardi, S.; Moreno Lopez, J. C.; Enache, M.; Monjas, L.; van der Vlag, R.; Havenith, R.W.A.; Hirsch, A.K.H.; Stöhr, M. Low-Dimensional Metal-Organic Coordination Structures on Graphene. *J. Phys. Chem. C* **2019**, *123*, 12730–12735.

Baker Cortés, B. D.; Stöhr, M. Role of Cyano Groups in the Self-Assembly of Organic Molecules on Metal Surfaces. In *Encyclopedia of Interfacial Chemistry*; Wandelt, K., Ed.; Elsevier, **2018**; Vol. 4, pp 153–165.

12 Curriculum Vitae

Brian David Baker Cortés

Jan. 2017 – Jan. 2020	**PhD candidate** in Physics, Surfaces and Thin Films research group, University of Groningen, Groningen, the Netherlands Thesis: *Molecular Self-Assembly of Organic Molecules on Coinage Metal Surfaces* Supervisors: Prof. M. Stöhr & Prof. P. Rudolf.
Sep. 2014 – Jun. 2016	**M. Sc. Degree** in Materials Science Exploring Large Scale Facilities (Erasmus Mundus)
Feb. 2016 – Jun. 2016	University of Rennes 1, Rennes, France
Sep. 2015 – Jan. 2016	Ludwig Maximilian University of Munich, Munich, Germany
Sep. 2014 – Jul. 2015	University of Turin, Turin, Italy Thesis: *Control of the Macroscopic Morphologies of Peptide Fiber by Drying within Microtextured Surfaces* Supervisor: Dr. Franck Artzner

Sep. 2009 – Jun. 2014	**B. Sc. Degree** in Nanotechnology, University of the Americas Puebla, Puebla, Mexico Thesis: *Study of Amitriptyline HCl in Core-Shell Magnetite Nanospheres Functionalized with Carboxymethyl Cellulose to Evaluate its Adsorption and Liberation Properties in Aqueous Media* Supervisor: Prof. M. A. Méndez Rojas
Sep. 2006 – Jun. 2009	**High School Degree**, Instituto Juárez Lincoln, San Andrés Cholula, Puebla, México
20 Oct. 1990	Born in Puebla, Mexico